Nanomechanics and ultrastructural studies of cortical bone: Fundamental insights regarding structure-function, mineral-organic force mechanics interactions, and heterogeneity

by

Kuangshin Tai

B.S., Bioengineering, University of California, Berkeley, 1999

Submitted to the Department of Materials Science and Engineering in partial fulfillment of the requirements for the degree of

Doctor of Philosophy in Materials Science and Engineering

at the

MASSACHUSETTS INSTITUTE OF TECHNOLOGY

June 2007

Author.....
Department of Materials Science and Engineering
February 22, 2007

Certified by.....
Christine Ortiz
Associate Professor of Materials Science and Engineering
Thesis Supervisor

Accepted by.....
Samuel M. Allen
POSCO Professor of Physical Metallurgy
Chair, Departmental Committee on Graduate Students

Nanomechanics and ultrastructural studies of cortical bone: Fundamental insights regarding structure-function, mineral-organic force mechanics interactions, and heterogeneity

by

Kuangshin Tai

Submitted to the Department of Materials Science and Engineering
On February, 2007 in partial fulfillment of the
Requirements for the degree of
Doctor of Philosophy in Materials Science and Engineering

Abstract

Although the mechanics of bone has been studied extensively at the micro- and macro-scale, the nano-scopic level is perhaps the most illuminating as this is the length scale at which the individual constituents interact. Bone is made primarily up of type I collagen, hydroxyapatite mineral, a variety of non-collagenous proteins, and water. A multitechnique experimental and modeling approach methodology was used break down several of the deformation mechanisms that exist in bone at the nanoscale including the effect of mineral content, cohesive-frictional plasticity, increased ductility through mechanical heterogeneity, and intermolecular forces.

To show that mineral content had a significant effect on both nanomechanical properties and ultrastructural deformation mechanisms of bone, partial and complete demineralization was carried out to produce samples ranging from ~0-58 wt.% mineral content. Nanoindentation experiments perpendicular to the osteonal axis found a 4-6x increase in stiffness for the ~58 wt.% sample compared to the completely demineralized ~0 wt.% samples. These results are discussed in the context of *in situ* and *post-mortem* AFM imaging studies which shed light on nanoscale mechanisms of deformation including collagen fibril deformation and pressure induced structural transitions of the mineral component. A finite element elastic-plastic continuum model was able to predict the nanomechanical properties of the different samples on loading and unloading. In addition, the ultrastructural origins of the strength of bone, which is critical for proper physiological function, were also investigated. A combination of dual nanoindentation, 3-D elastic-plastic FEA using a Mohr-Coulomb cohesive-frictional strength criterion, and

angle of repose measurements was employed, suggesting that nanogranular friction is responsible for increased resistance to plasticity in compression, and that cohesion originates from within the organic matrix itself, rather than organic-mineral bonding.

Nanomechanical heterogeneity is also expected to influence elasticity, damage, fracture, and remodeling of bone. The spatial distribution of nanomechanical properties of bone was quantified for the first time at the length scale of individual collagen fibrils. The results show elaborate patterns of stiffness ranging from 2 to 35 GPa which do not correlate directly with topographical features and hence, are attributed to underlying local structural variations. A new energy dissipation mechanism is proposed arising from nanomechanical heterogeneity, offering a graceful means for ductility enhancement, damage evolution, and toughening. This hypothesis is supported by finite element simulations which incorporate the nanoscale experimental data and predict markedly different biomechanical properties compared to a uniform material, through nonuniform inelastic deformation over larger areas and increased energy dissipation. The fundamental concepts discovered here are applicable to a broad class of biological materials and may serve as a design consideration for biologically-inspired materials technologies.

Stem cell-based gene therapy and tissue engineering have been shown to be an efficient method for the regeneration of critical-size bone defects. Despite being an area of active research over the last decade, no previous knowledge of the intrinsic structural and nanomechanical properties of such bone tissue exists. The nanomechanical properties of engineered bone tissue derived from genetically engineered mesenchymal stem cells (MSCs) overexpressing the rhBMP2 gene, grown *in vivo* in an ectopic as well as a radial defect site of immunocompetent mice is compared to native bone adjacent to the transplantation sites. Supplementary experiments showed that the two types of bone had similar mineral contents, overall microstructures showing lacunae and canaliculi, chemical compositions, and nanoscale topographical morphologies. Nanoindentation experiments revealed that the small length scale mechanical properties were statistically different for the engineered bone derived from the ectopically implanted site. For data derived from the radial defect site experiments, results were both statistically similar and different, depending on the particular animal.

The intermolecular forces (i.e. electrostatics, van der Waals, hydrogen bonding, etc.) that exist in bone are also expected to play a significant role in determining its morphology, structural integrity, interaction with bone fluid and its constituent biomolecular species as well as synthetic bone implant materials. Understanding of the macromolecular mechanisms of biomineralization in bone is an area of significant interest that is widely applicable to a wide range of materials applications, both biological in origin and synthetic. High resolution force spectroscopy (HRFS) allows for direct measurement of forces between a nanosized probe tip functionalized with SAMs which are molecules of uniform structure, charge, and chemistry as a function of separation distance from the sample in fluid. This data on approach was compared to electrostatic double layer theory, and the surface charge density (σ) was estimated numerically. The normal electrostatic double layer forces were measured for the first time between a SAM functionalized probe tip and bone of varying mineral content.

Thesis Supervisor: Christine Ortiz
Title: Associate Professor of Materials Science and Engineering

Acknowledgements

Thanks so much to all, this thesis would not have been the same without the support of such a large number of people! I'd first like to thank Christine Ortiz, my advisor who has helped refine my scientific mind and never ceases to bring new vigor and excitement to each project. My collaborators had instrumental roles in my work and were very enjoyable to work with. I would have long, philosophical discussions with Franz-Josef Ulm next to his never empty white board. It never ceased to amaze me how well connected Dan Gazit and Gadi Pelled were to U.S. funding all the way from Hebrew University. Jerry (Hang) Qi started me with FEA and Ming Dao continued to hone my skills. Subra Suresh always provided thoughtful suggestions to my work. My committee members, Alan Grodzinsky, Krystyn Van Vliet, Lorna Gibson, and Myron Spector, did a wonderful job in keeping me on my toes, sharpening the work all the more, and making it "fun" in the process.

My lab-mates have been a pleasure to work with. Ben has been a cohort in crime with me for quite some time now, always great to bounce ideas off of. Jen and I started at the same time, but she beat me to it. I could always count on Laurel to be a kind and listening ear in any situation. Delphine was always the life of a party. I start salivating whenever I think of Lin's Szechuan cuisine. Miao is one of the most level headed guys I know. Cathal had a recipe for being able to laugh regardless of the situation. Thanks also to the rest of the Ortiz group. Shout outs go to Joonil, Reuben, Kristin, Monica, Jae, Bobae, Hsu-Yi, and Juha as well.

Hours of Star Trek: TNG, DS9, Voyager, and Enterprise, 24, and Lost have helped me recharge and remain motivated to finish the race. The shoddy performances of the Redskins and Wizards, on the other hand, have prompted me not to emulate their performance. Artistry from Shane and Shane, David Crowder, Jason Mraz, U2, John Mayer, Chris Rock, Russell Peters, and Triumph the Comic Dog have all helped in providing continuous fundamental insights into the research.

Friends from home and college are always great to visit in my times away from MIT. Flex has been with me for quite some time now, it seemed like yesterday I'd bike over to his house to eat chili cheese dogs and ramen. Everytime I hang out with Jimmy I feel like I've learned some random new sports fact or deep spiritual insight. Steve's transformation from caveman to gentleman is perhaps the greatest miracle of all. Henry was huge in helping me adjust to both Berkeley and Boston. Bing has got to be the most polite frat boy I've ever met.

The people at the Cambridge Community Fellowship Church have been a huge part of my life in Boston. Pastors Soong-Chan, Jason, Kevin, Elizabeth, Gary, and Larry have all taught me so much about the intersection of life and faith. It began with the mens' group lead by Jason and Jerome. Thanks for taking initiative and believing in me. Our house church has been incredible, especially Dan and Soojin, whose hospitality and culinary prowess combine with my talent for eating to form a perfect combination. Phil, Fred, Jason, and Stanley have been great guys that I've been able to commiserate with and mutually support through school, work, and church-life. Thanks to Danny and Susan for inviting us over to watch Star Trek and eat good food. Brian shares the same love for

cheap curry from the box. Warren and Melissa were consistently there as sounding boards for anything that may be on our mind. Ed, Dan, Ro, and Nate round out the list of jabronies that are irreplaceable. I'm proud to call you all spiritual mentors in my life.

What would a PhD thesis be without people to enjoy campus life with? My tennis buddies, Alessandro, Tom, Charlie, Georgios, and Jerome gave me great matches on the court. Mad props go out to all the noon ballers, especially Kariuki and Tarek, for the epic battle battles in DuPont. Chorallaries was a great experience. Sebastian and Aneal were guys that I clicked with from the beginning.

My family has been an enormous support to me. My brother, Kuangkai, has seen me through thick and thin, highs and lows. He's a real great guy to look up to. My sister, Kuangheng, who I terrorized in my youth, is the epitome of optimism and patience. It's always fun visiting you guys! Estella and Pete have been wonderful siblings in-law, people who I can easily be myself around. It's been pure joy to see my nephews and nieces, Dante, Christopher, Amanda, Emily, Norah, and Jonathan grow up before my very eyes. My new in-laws, Betty, William, and Melissa have taken me in as their own. My mother, Thelma, will always be available to lend some advice. My father, T.C., is one never to be underestimated, always having some new ideas up his sleeve. My very loving and forgiving wife, Cathy, has seen it all and knows me like none other. Lastly, I thank God for calling me out to MIT and the Boston area to grow and learn more about His heart for people. The Lord has been with me every step of the way and will surely continue now and on through the end and beyond.

This research was funded in part by the Whitaker Foundation Graduate Fellowship, the Cambridge/MIT Alliance, and the Institute for Soldier Nanotechnologies.

Contents

List of Figures

List of Tables

Chapter 1

Introduction

1.1 Motivation

Bone is the primary connective tissue which provides support, protection, and structure for the body and its organs. Bones collectively make up the skeleton of an animal, which brings about overall shape and movement. They are intimately connected to muscles, tendons, ligaments and cartilage, which all facilitate movement and support. The mechanical properties and behavior of bone has always been of interest to researchers given its biological and medical relevance. It is estimated that 20% of older Americans who suffer a hip fracture die within a year of the fracture and 20% people with a hip fracture end up in a nursing home within a year [5]. There are over 1.5 million osteoporosis related bone fractures per year, estimated to have an annual cost of $14 billion [6]. Bone is a vastly hierarchical structure from the long bone level to the osteonal/interstitial lamellar microstructure down to the individual molecular constituents. It is ultimately a nanocomposite made up of type I collagen, hydroxyapatite, water, and non-collagenous proteins. A fundamental understanding of the ultrastructural origins of deformation and mechanics that occur at the nanoscale may give further insight to overall structure, function, and dysfunction in bone as well as provide inspiration for clinical treatments, biomimicry, and architecture.

1.2 Objectives

There are four primary objectives in this thesis, one of which will be touched upon by each chapter and appendix. The first aim is to examine the effect of mineral content on the nanomechanical behavior in bone. This is put forth through leaching out mineral from the bone matrix and subsequently inspecting the nanoscale mechanics that result in samples of varying mineral content. The second objective is to investigate nanoscale mechanisms of deformation that occur in bone. The ideas generated through this objective have wide ranging implications for biological and biomimetic systems and is explored through a combination of application of novel material models and implications set forth from the direct observation of patterned nanomechanical testing. The third goal is related to developing applications to medicinal therapies in the clinic. Here, nanoscale mechanics are used as a complementary method in assessing the quality of bone generating from existing animal research models. The fourth objective is in quantifying the intermolecular forces that are present in bone, which is accomplished through high resolution force spectroscopy.

1.3 Overview

This thesis begins with a brief summary of the primary techniques involved in nanomechanical assessment along with an overview of the hierarchical structure that occurs in bone. Chapter 2, which is published in Journal of Materials Science: Materials in Medicine in 2005, describes the effect of mineral content on the deformation behavior and mechanical properties at the nanoscale in bone. Chapter 3, which is published in Nano Letters in 2006, describes the nanogranular nature of deformation in bone through the use of a pressure sensitive cohesive-frictional material model. Chapter 4, a portion of

which is currently in revision, gives details regarding a first order approximation of the importance of nanoscale mechanical heterogeneity in providing a ductile mechanism for energy dissipation in bone. Chapter 5 contains more complex fiber-composite finite element analysis nanoindentation models that show nanoscale interplay between fibrillar and extrafibrillar regions. Chapter 6 involves the direct measurement of the intermolecular forces existing in bone of varying mineral contents, including electrostatic and van der Waals. Chapter 7, a portion of which is published in Journal of Biomechanics in 2006, gives a nanomechanical analysis of osteogenic bone derived from genetically engineered stem cells in two different mouse models (ectopic and radial defect). Chapter 8 provides further application using a chitosan glutamate bone growth inducing transport mechanism for delivery of osteoblasts to an injected defect site. Appendix A summarizes macroscopic compression tests and their subsequent analyses for bone in different orientations. Appendix B lists the supplementary materials analyses used in conjunction with nanomechanical techniques for further validation of the results including X-ray diffraction, X-ray photoelectron spectroscopy, and energy dispersive X-ray analysis. Appendix C shows high resolution images of collagen fibril deformation and mechanical force-displacement behavior. Appendix D records a literature search of the effects of various chemical treatments on bone including demineralization, deorganification, and ethanol treatment. Appendix E describes the methodologies used in calibrating the AFM and nanoindenter tip for extraction of mechanical properties. Appendix F is a summarized FEA study of the effect of sloping on the overall indentation results.

1.4 Background

1.4.1 Bone Structure and Mechanics

Bone is a hierarchical composite, made up of hydroxyapatite, type I collagen, water, and non-collagenous proteins. On the macroscopic level, bone takes on various forms, but is fundamentally made up of those four components. It is either compact (cortical) or cancellous (trabecular). Cortical bone is typically 10% porous while trabecular or spongy bone is up to 80% porous. In long bones, the trabecular bone is typically found filling the ends of the epiphysis while surrounded by cortical bone. Bone is also either woven or lamellar. Woven bone is typically found in younger bone where there is no structure from which to form upon. As a result, woven bone spontaneously develops, but is more disorganized and random in appearance than the older lamellar bone, which occurs during typical growth and remodeling. Microscopically, lamellar bone consists of vascularized Haversian canals which contain blood vessels that run through the center. Lamellae are typically formed circumferentially around these canals to eventually form osteons which can range between 50 – 500 μm in diameter. Between osteonal bone, which typically is in the process of remodeling, is interstitial bone which tends to be older bone containing remnants of osteons. Along the circumferential lamellae are lacunae, which are ~ 10 μm, where osteocytes are normally housed. Canaliculi are small channels <1 μm in diameter that connect lacunae so that osteocytic processes are able to extend and sense the surrounding environment. Osteons run parallel to the long bone axis. Bone exhibits high compressive strength, but is in general weaker in tension [7].

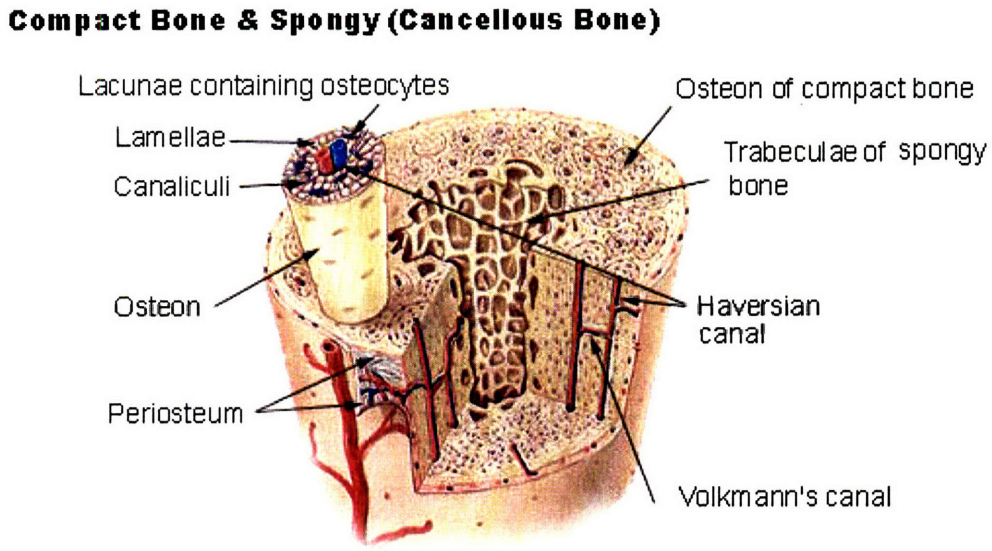

Figure 1-1. Microstructure of bone showing vasculature and osteonal network that exists throughout the mineralized matrix.
(*http://training.seer.cancer.gov/module_anatomy/unit3_2_bone_tissue.html*)

1.4.2 Type I Collagen

Type I collagen is the most abundant protein in mammals, found chiefly in connective tissues such as skin, cartilage, ligaments, tendon, bone, and teeth. Collagen takes on fibrous form, serving as a structural protein as opposed to globular proteins such as enzymes. The most prevalent amino acid residue in type I collagen is glycine, which is typically located at every third residue. There are also large amounts of proline, hydroxyproline, and hydroxylysine. The collagen molecule is called "tropocollagen" and is a left-handed trihelical polypeptide fiber, approximately 300 nm long and 1.5 nm in diameter. Bundles of tropocollagen molecules are bound together by self-assembled hydrogren bonds and cross-links to make up a collagen fibril quaternary structure array, which is characterized by a 67 nm banding periodicity. Groups of collagen fibrils together ultimately form fibers as shown in Figure 1-2.

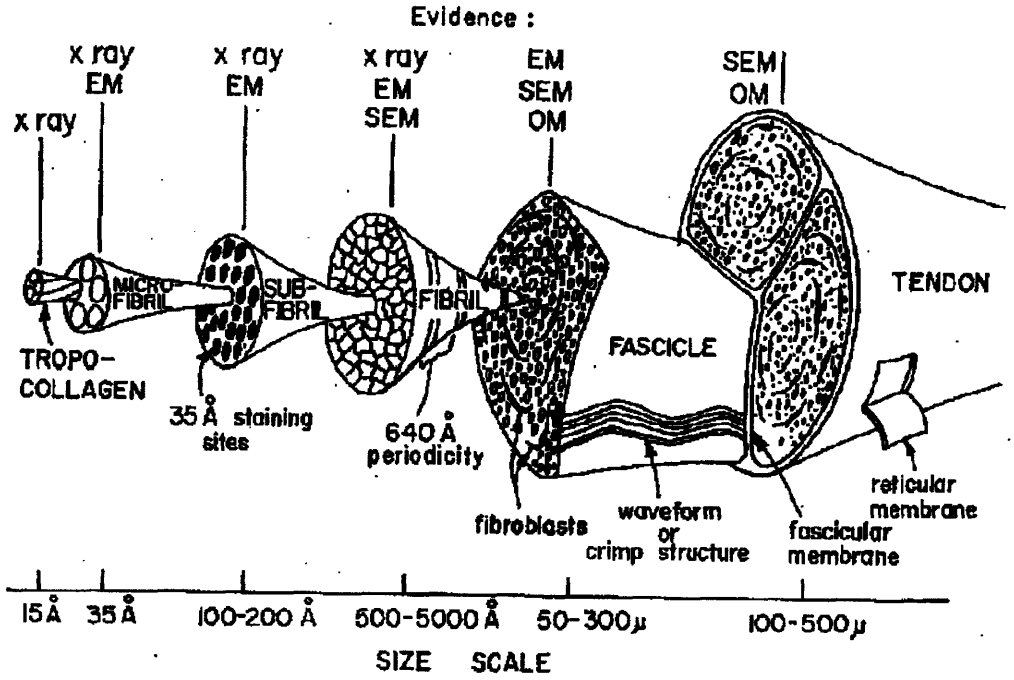

Figure 1-2. Hierarchical structure of tendon ranging from the tropocollagen molecule (1.5 nm) to the tendon (2-12 mm). (Kastelic et al, 1978)

1.4.3 Hydroxyapatite

Hydroxyapatite (HA) is the primary mineral component in bone, taking up ~70 wt.%. The molecular structure is $Ca_{10}(PO_4)_6(OH)_2$. The crystal structure of HA is hexagonal (Figure 1-3), consisting of calcium ion surrounded by phosphate and hydroxide ionic groups. Biological HA crystals take on platelet morphologies and are incorporated in "hole zones" between tropocollagen molecules as well as in and around the organic matrix. The average size of these crystals are ~50 nm x 5 nm with the c-axis parallel to the collagen fiber axis. A more detailed discussion of the morphology and size dimension of mineralite clusters are given in Appendix H.

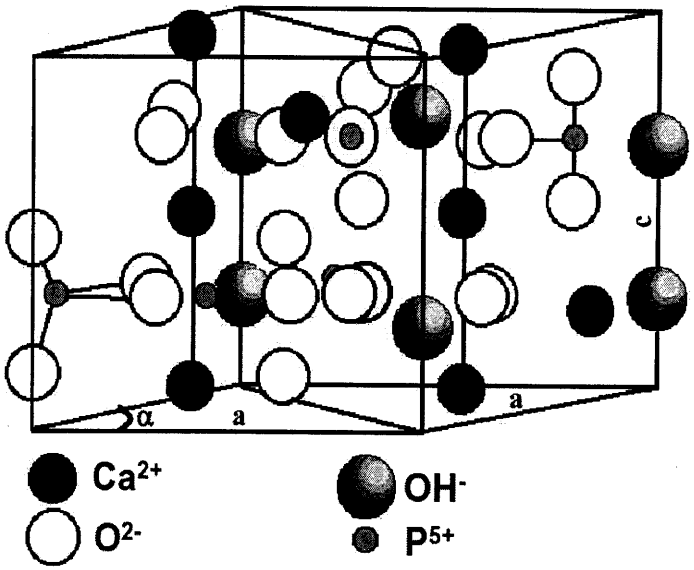

Figure 1-3. Crystal structure of hydroxyapatite.

Chapter 2

Effect of Mineral Content on the Nanoindentation Properties and Nanoscale Deformation Mechanisms of Bovine Tibial Cortical Bone

This chapter was published as a paper in Journal of Materials Science: Materials in Medicine in 2005 [8].

2.1. Introduction

Cortical or compact bone is a load-bearing hard tissue that is a well-studied complex biocomposite composed of organic and inorganic material hierarchically organized from the nanometer (nm) up to the macroscopic scale [9]. The fine details of the nano- to microscale structural organization, heterogeneity, geometry, composition, and mechanical properties are known to have a profound effect on the macroscopic mechanical function and dysfunction of the tissue [10-16]. Powerful high resolution nanotechnological methods have become more widely available and are just starting to be employed in the study of bone at these smaller length scales such as atomic force microscopy (AFM) imaging [17-20] and nanoindentation [11, 16, 17, 21-26]. In this paper, these techniques are used in combination with other multiple standard characterization methods to investigate a few specific scientific areas of interest using a model system of adult bovine tibial cortical bone, as described in detail following.

The first objective was the identification and/or elimination of the many previously suggested nanoscale mechanisms of deformation and the investigation of how

these mechanisms are related to elastic, viscoelastic, and plastic nanomechanical properties (e.g. elastic moduli, yield stress, viscoelastic relaxation, etc.) [11]. Proposed damage mechanisms in cortical bone include; debonding of mineral-organic interfaces, collagen fibril shear, crosslink scission, denaturation, and failure of collagen fibrils, crack formation and propagation, mineral displacement, deformation, and a structural phase transformation, viscous stretching of the organic component, and rupture of self-healing sacrificial bonds [2, 7, 21, 27, 28]. The second aim was to examine the effect of mineral content on ultrastructural deformation mechanisms and to establish its relation to nanomechanical properties. Mineral content is a critical parameter affecting macroscopic mechanical properties [29] that varies with disease (e.g. osteoporosis, changes in subchondral trabecular bone with osteoarthritis), prosthetic implantation, weightlessness, ethnicity, and aging [30]. Macroscopic tensile experiments performed on cortical bone have shown that increasing calcium content results in an approximately linear increase in stiffness and yield stress, a linear decrease in post-yield stress, work, ultimate strain, and strain-to-failure, and has a minimal effect on ultimate stress [29]. While the origin of the elasticity dependence on mineral content is rather intuitive from consideration of a standard rule of mixtures approximation for a composite [7, 27], the nanoscale mechanisms by which mineral content affect viscoelastic and plastic behavior are expected to be more complex and are largely unknown at this time. The third and final goal of this study was to assess the ability of two continuum models to capture the nanomechanical behavior of bone and predict its nanoscale materials properties; the first being a purely elastic contact mechanical model [2] and the second consisting of elastic-perfectly plastic finite element analysis (FEA) simulations.

To achieve these objectives, samples of varied mineral content were studied (0 wt.% - 58wt.%), including; undemineralized longitudinal sections of adult bovine tibial cortical bone (cut parallel and tested perpendicular to the long bone axis and the osteonal / Haversian canal axis), and this same sample treated with acid to remove various amounts of the mineral component. Extensive characterization of these samples was performed by Raman spectroscopy to measure the chemical composition and mineral-to-organic ratio, back-scattered electron (BSE) imaging to quantify mineral content, standard and environmental scanning electron microscopy (SEM, ESEM) to assess morphology, and AFM to image higher resolution nanoscale surface topography (down to the resolution of individual collagen fibrils). The technique of nanoindentation (controlled compression of a stiff probe tip into a softer specimen of interest while recording the load versus displacement behavior) was employed on these samples at forces ~100-1000 μN and depths ~50-500 nm corresponding to a maximum contact area at the maximum load of ~4.7 μm^2 containing ~31 collagen fibrils and maximum depths of 500 nm containing ~3 collagen fibrils. These experiments were combined with *in situ* and *post-mortem* high resolution (μm to nm-scale) AFM imaging of the indented area, to obtain information on the micro- to nanoscale deformation mechanisms, again down to the level of individual collagen fibrils. Two theoretical models were fit to the nanoindentation data to estimate material properties : *1)* the Oliver-Pharr (O-P) method [2] where the initial unloading curve was compared to continuum mechanical theory for an isotropic, elastic half-space and the elastic modulus, E, was the only fitting parameter and *2)* an elastic-perfectly plastic FEA simulations where the entire loading and unloading curves were fit using two parameters, the elastic modulus and yield stress, σ_y.

It should be noted that since the necessary sample preparation steps do not produce a model system exactly like that of native bone, a direct quantitative correlation with the mechanical properties of *in vivo* bone tissue is not valid without further theoretical developments. However, trends in nanomechanical properties with various structural parameters, such as mineral content, do provide interesting, new scientific information. In addition, the samples studied here are closer-to-physiological conditions than typically reported (e.g. no alcohol dehydration, embedding, chemical fixation, etc.) and do retain many of the nano- to microscale structural features of bone. Hence, their use should be able to provide physiologically-relevant insights into nanoscale mechanical behavior.

2.2 Materials and Methods

2.2.1 Sample Preparation

Adult compact bovine bone from between the tibial metaphysis and diaphysis was cut down to 1.5 mm thick specimens (which was also the approximate thickness of the final samples used for nanoindentation testing) using a diamond-impregnated annular wafering saw (*Buehler,* Isomet 5000) running at 400-600 rpm with constant phosphate buffered saline (PBS, IS=0.15M, pH7.4) irrigation. Longitudinal sections (cut parallel to the long bone axis) were polished down in 2-3 minute intervals using a metallographic polishing wheel (*Buehler*, at ~100 rpm) and adhesive papers with successively smaller Al_2O_3 particle grit sizes; 9 μm, 3 μm, 1 μm, 0.3 μm, 0.1 μm, and 0.05 μm (*South Bay Technologies*). Samples were rinsed copiously with DI water followed by ultrasonicatation in DI water between polishing intervals. Samples were then

immediately stored in 20°C PBS. Demineralization etches were performed using 40% H_3PO_4/60% DI water for 0, 1, 10, 40, and 120 seconds, followed by at least 48 hours of rehydration time in PBS during which time the collagen fibrils to refibrillate [28, 31]. Complete demineralization (confirmed by ash weight) was accomplished by storage in 0.5 M ethylenediaminetetraacetic acid (EDTA) for a minimum of 7 days, where the solution was changed every day. Demineralization produces both large pores on the sample surface as well as internal porosity. Nanoindentation experiments were performed only in the flatter regions between the large surface pores (as determined by optical microscopy). Energy dispersive X-ray (EDX) analysis (probe depth of ~1 □m) identified only trace amounts of Al (upper atomic percentage limit is 1.5%, *data not shown*) excluding the possibility surface contamination.

2.2.2 Sample Characterization: AFM, SEM, GSE, BSE, and Raman Spectroscopy

Tapping mode (TM)AFM imaging in ambient temperature and humidity was employed using two instruments; *1)* a *Digital Instruments* (DI, Santa Barbara, CA) Multimode SPM IIIA with an AS-130 "JV" piezoelectric scanner and DI NanoSensors TappingMode Etched Silicon Probes (TESP) cantilevers (nominal resonant frequency, ω ~ 250 kHz, nominal spring constant, k ~ 40 N/m, and nominal probe tip end radius, R_{TIP} ~ 10 nm) and *2)* a *Quesant* Q-Scope 350 with Si_3N_4 *Wavemode* NSC16 cantilevers (ω ~ 170 kHz, k ~ 40 N/m, R_{TIP} ~ 10 nm). The cantilevers were driven just below ω using a scan rate of 2 Hz and a maximum sampling size of 512 x 512 pixels. The images reported were amplitude (i.e. cantilever frequency variation which is reflective of surface topography; light areas are regions of high topography and darker areas of regions of

lower topography) and phase imaging were used the most in TMAFM. phase (i.e. cantilever oscillation phase lag from the signal at which the cantilever is driven. Along with being used to measure properties of different materials based on which is reflective of viscoelasticity, adhesion, and friction; light areas are regions of high phase lag and darker areas of regions of lower phase lag).

Samples were coated with Au-Pd 10 nm thick, and imaged using a JEOL SEM 6320FV. The working distance was 5-7 mm, the sample plane was oriented perpendicular to the electron beam incidence, and a 3 kV accelerating voltage was employed. An environmental SEM (ESEM, *Philips/FEI* XL30 FEG-SEM) was employed for sample characterization in a water vapor environment of uncoated samples. Pressed pellets of 99% pure magnesium oxide (MgO, *Merck*), 99% pure aluminum oxide (Al_2O_3, *Merck*), and 99.99% dense, phase-pure hydroxyapatite[32], undemineralized bone, and acid-treated bone were mounted on the same metal base. Electron acceleration was set to 20 kV with a 184 μA operating current. The working distance was set to 9.6 mm and the water vapor was at 0.4 Torr. Contrast and brightness levels were adjusted and held so that electron images would appear optimally for all 5 samples, allowing for feasible gray level calibration using BSE detection. A gaseous secondary electron (GSE) detector was also placed in the chamber so that regular secondary electron emissions could be detected to form images of the samples as well.

The mean gray level for BSE images was computed directly from the histogram plot of each substance was obtained and compared with that of the other substances. The average atomic number ($\overline{Z}$) for MgO, Al_2O_3, and HA are known respectively to be 10.41, 10.65, and 14.06 where $\overline{Z}$ is given by[33]:

$$\overline{Z} = \frac{\sum(NAZ)}{\sum(NA)} \quad (1)$$

where N is the number of atoms of each element with atomic weight and number A and Z, respectively. Based on the calibration of known substances and the mean gray level obtained from the BSE, it is possible to extrapolate what $\overline{Z}$ is due to the direct relationship between the voltage output from the BSE detector (gray level pixel) and the average atomic number [34, 35] [36] [37]. The image analysis software also allows for 2-Dimensional Fast Fourier Transforms (2DFFT) to be taken of images that are 256 x 256 pixels in size. Gray scale values per pixel were quantified for the images recorded by the BSE detector along with control samples of known $\overline{Z}$ where a linear scale was used to approximate the percent weight of mineral content for our samples.

Raman Spectroscopy was used for non-invasive chemical characterization of the undemineralized and acid-etched bone. Through optical microscopy, the *Kaiser Hololab* 5000R Raman Spectrometer was used to record the spectra of Raman shifts. The instrument was operated at 785 nm utilizing Coherent CW Argon/Ion and Ti/S Lasers using a 100 μm diameter optical fiber to maximize throughput

2.2.3 Nanoindentation

Nanoindentation experiments were conducted in ambient conditions using a *Hysitron, Inc.* (Minneapolis, MN) Triboindenter equipped with an AFM (*Quesant* Q-Scope) for tapping mode imaging of residual impressions. Indentations were carried out perpendicular to the plane of the Haversian canal axis. The instrument is housed in a granite frame environmental isolation chamber so as to minimize instabilities due to the

ambient background noise, with active piezoelectric vibration control stages (*Hysitron*), and a thermal drift calibration step. Load-controlled nanoindentation was performed using a Berkovich (trigonal pyramid) diamond probe tip. The applied load function was divided into four segments as follows. The first segment consisted of a 3 second hold at zero force in which the probe tip is barely kept in contact with the sample, allowing for tip-sample equilibration. Segment two was a constant loading rate of 9 ± 0.4 μN/sec and once the maximum set peak load was reached, the third segment, which was a hold period of 10 - 20 seconds. The fourth segment would conclude the experiment with a constant unloading rate of 9 ± 0.4 μN/sec. >15 experiments per maximum load were done on different sample locations for each indent. To ensure that creep effects were minimal, three different experiments were conducted. The first was to vary the third hold segment between 10 to 100 seconds. The second was to use a load function that would, after the hold period, unload to 50% of the maximum force and then reload back to the maximum force for several cycles. The third was to vary the loading/unloading rate by a 2 orders of magnitude (the limit of the machine). All three sets of experiments found that the variation in calculated elastic moduli was negligible. Load versus indentation distance curves from multiple experiments using the same maximum load and from different sample locations were averaged and standard deviations calculated and presented on the plots. The tip area function and frame compliance, were calibrated prior to each set of experiments using a fused quartz sample. Values for elastic moduli were calculated from 95% to 20% of the initial unloading curve by fitting these data to contact mechanical theory for an isotropic, elastic half-space (O-P method[2]) using n=108 number of individual curves. This tip calibration for area function and machine compliance was

employed for all of the O-P fits to the experimental data to approximate the elastic moduli. The area under the curve was calculated for each force versus distance curve to compute the energy dissipation and a force normalized value was plotted as a function of average maximum load for each case. The Q-scope AFM was used in tapping mode in air at an amplitude set point of 0.25 V in order to image residual indent impressions left by the probe tip.

2.2.4 Elastic-Plastic Finite Element Analysis (FEA) of Nanoindentation

A three dimensional elastic-perfectly plastic model was built by FEA using the software package ABAQUS (Hibbitt, Karlsson & Sorensen, Inc.) and solved numerically using the elastic modulus and yield strength as the two fitting parameters. A discussion of the applicability of this model to the samples of interest is given in later sections of this paper. To reduce computational cost and due to symmetry, only 1/6 of the tip and the surface were modeled and the corresponding boundary conditions were applied to ensure the symmetry, i.e. the nodes on the sidewalls were fixed in the direction normal to the sidewall surface (the nodal displacement in this direction is set to be zero). Since the modulus of the diamond probe tip is about 100X higher than the bone and collagen samples studied here, the indenter was modeled as a rigid surface. In practice, the indenter generally does not have an ideally sharp Berkovich geometry; instead it is rounded due to wear and can be characterized by a finite end radius, R_{TIP}, and truncate height, h (which is the distance between the apex of the rounded tip and the apex of the imaginary ideally sharp tip). In order to approximate R_{TIP} and h, nanoindentation experiments were conducted on a standard fused quartz sample. First, a Hertzian elastic

sphere-on-a-flat (SOF) model [38] was employed to determine R_{TIP} and h as a function of indentation depth, D, from the experimental nanoindentation data where the modulus of the fused quartz was set to the known value of 72 GPa [39]. These calculations yielded R_{TIP} ~ 210 nm at D ~ 5 nm and decreased to R_{TIP} ~ 140 nm at D ~ 20 nm. The spherical geometry and SOF model prediction of R_{TIP} is most accurate for $D<h^2/R_{TIP}$ and for $D>h^2/R_{TIP}$ the SOF model becomes increasingly inaccurate, underestimating R_{TIP} as the geometric transition from spherical to blunted trigonal pyramid (Berkovich) takes place. In order to more precisely determine R_{TIP} and h perfectly elastic FEA simulations were compared to the experimental nanoindentation data using R_{TIP} and h as fitting parameters taking the SOF ranges as the initial starting point for the fits, and yielded R_{TIP} ~ 180 nm and h ~ 4 nm. Hence, for all subsequent FEA simulations of bone and collagen, the indenter was modeled as a rigid surface with Berkovich geometry (inclined face angle, β = 24.7°, apex angle, γ = 77.1°) having R_{TIP} of 180 nm and truncate height of 4 nm. The samples were modeled using an 8-node linear brick element hybrid with constant pressure (C3D8H in ABAQUS element library). The mesh was refined in the vicinity of the contact region where large gradients in stress and strain prevail. Several mesh densities were analyzed and an optimal mesh was finally chosen for use in all simulations which contained 6195 nodes and 5491 elements. The element size increased with increasing distance from the indentation axis and surface. Large deformation theory and frictionless contact between the indenter and material were assumed throughout the analysis. A smaller number of individual experimental nanoindentation curves were fit (n=3) compared to the O-P method due to the longer time and computational cost required for the FEA simulations.

It should be noted that there are inherent sources of error that come with the elastic-perfectly plastic assumption. The first is that it does not take into account any sort of time-dependent behavior, which is evidenced by the slight creep effect during the experimental nanoindentation. Although visco-elastic effects are minimized to the highest degree possible, they can never be fully eliminated, which the model assumes. The second is that strain hardening and/or softening are not taken into account by the model either. In this case, the strain hardening exponent n = 0, which was independently determined (Appendix H) for both mineral content cases above (57 wt.%) and below (32 wt.%) the percolation threshold using an "inverse" computational FEA back analysis [40]. However, a more rigorous analysis is required in order to understand the effect of mineral content on the strain hardening (or softening) behavior and yield unique nanoscale mechanical parameters. This specific concern is not within the scope of this particular study.

2.3 Results

2.3.1 Sample Characterization by SEM, GSE, BSE, AFM, and Raman Spectroscopy

The microstructure of the undemineralized bone samples as revealed through SEM (Figure 2-1(a)) showed a rough surface morphology with no obvious periodic or directional trends [41]. The underlying fibrous nature of the matrix is revealed in Figure 2-1(b) through SEM of a fractured surface edge crack which presumably show mineralized collagen fibrils. A higher resolution TMAFM image taken in ambient conditions (Figure 2-2(a)) shows a similar surface morphology with topographical what

features ~10 nm in height and ~ 20-100 nm in lateral dimension and no preferred orientation or banding structure as assessed by a 2DFFT of this image (Figure 2-2(b)). The lateral topographical feature size measured here correlates well with the size of the

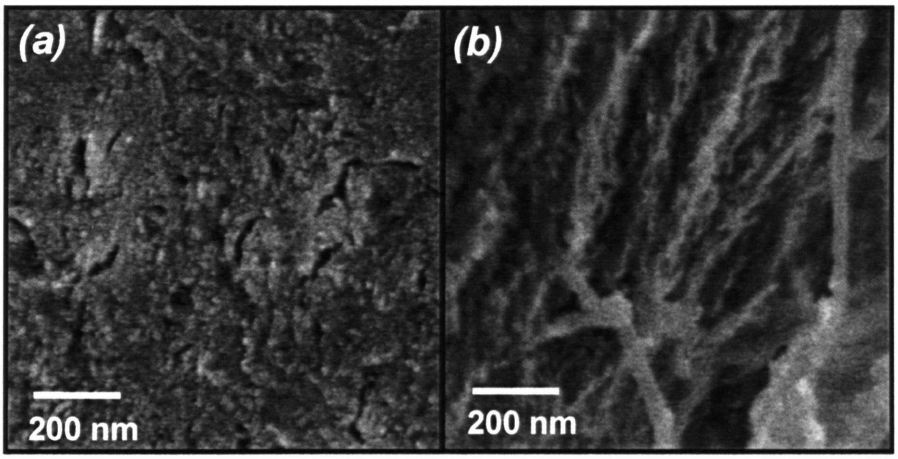

Figure 2-1. Characterization of an undemineralized longitudinal section of adult bovine cortical bone; *(a)* Scanning electron microscopy (SEM) image shows a ~10% porosity with irregular, granular-type surface features, *(b)* SEM image showing the edge along a crack fracture surface, revealing rough fibrous material indicative of collagen mineralized fibers

mineral particles observed by AFM [18, 19], TEM [10], and XRD [42] and the apparent lack of the characteristic collagen fibril banding is expected as a significant amount of mineral is expected to be located outside of the collagen fibrils [43], thus obscuring the distinct banding [19, 44]. Figure 2-3(a) is a larger scan size BSE image, which possesses

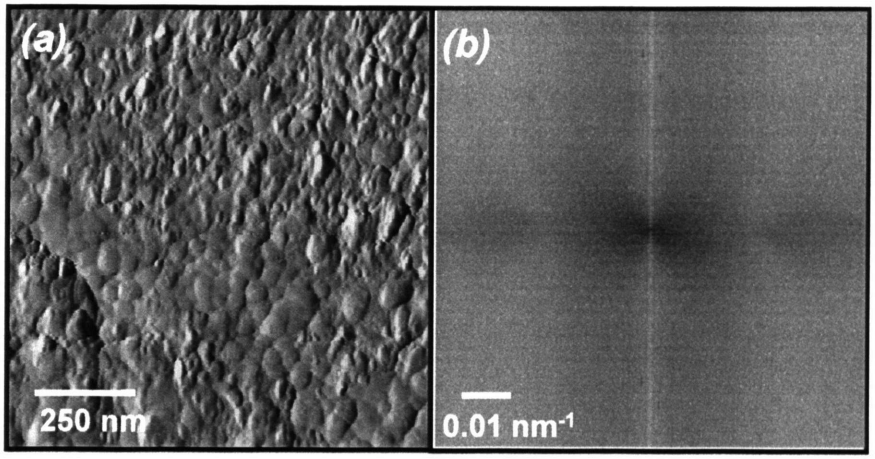

Figure 2-2. Characterization of an undemineralized longitudinal section of adult bovine cortical bone; *(a)* Tapping mode atomic force microscopy (TMAFM) image in air (taken with *DI Multimode*) showing surface morphology at higher resolution, *(b)* 2D Fast Fourier Transform (FFT) of *(a)*, which does not exhibit any noticeable peaks.

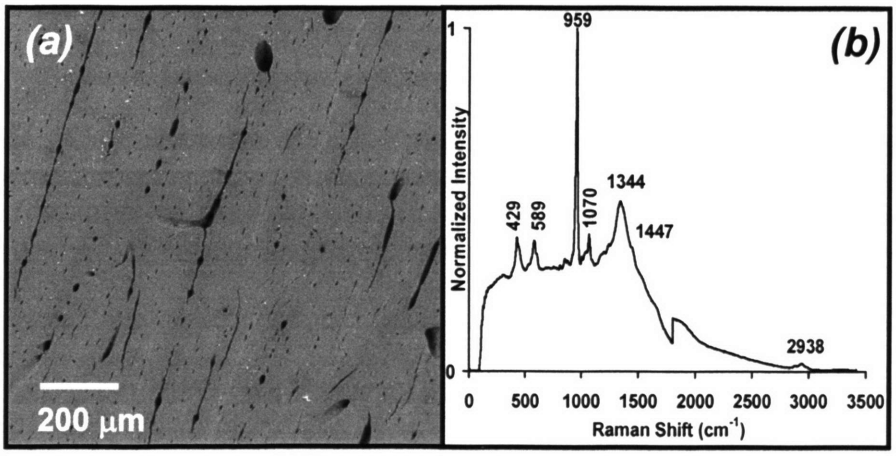

Figure 2-3. Characterization of an undemineralized longitudinal section of adult bovine cortical bone; *(a)* low vacuum, micron-scale (back-scattered electron) BSE image in water vapor, and *(b)* Raman spectrum for sample *(a)*. Peaks can be observed at specific wavenumbers that are characteristic for bone (cm^{-1}); 589 (PO_4^{-3} ν_4), 959 (PO_4^{-3} ν_1; P-O symmetric stretch), and 1070 (CO_3^{-2} ν_1; C-O in plane stretch). There is a noticeable jump in the overall background intensity relative to the observed peaks, due to proteins, which fluoresce.

lighter gray level values (indicative of higher degrees of mineralization) throughout the sample at localized regions that run between channels where Haversian canals are located [24]. Calculations from Figure 2-3(a) yielded ~58 wt.% mineral content. The Raman spectrum in Figure 2-3(b) has peaks which denote bands characteristic of the mineral in bone [45]. Porosity and mineral content are within expected ranges [15].

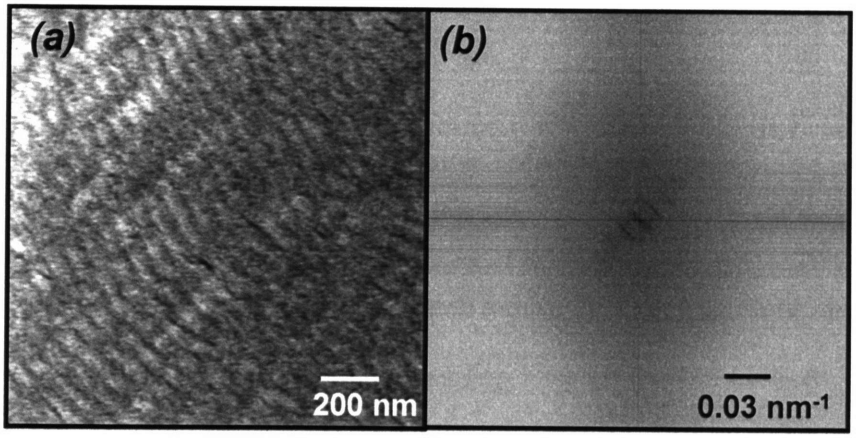

Figure 2-4. Characterization of an H_3PO_4-treated (~4% mineral) longitudinal section of adult bovine cortical bone; *(a)* Scanning electron microscopy (SEM) image, *(b)* 2D Fast Fourier Transform (FFT) of *(a)* which exhibits the known characteristic axial banding periodicity of 67 nm for type I collagen fibrils.

Figure 2-4(a) is an SEM micrograph of the bone sample which had been etched for 120 seconds in H_3PO_4 and shows a distinct layer of collagen fibrils on the surface, with a preferred orientation of the fibril axis in the plane of the sample, as well as the 65-70 nm characteristic banding periodicity (Figure 2-4(b)). Interlocking of fibrils was

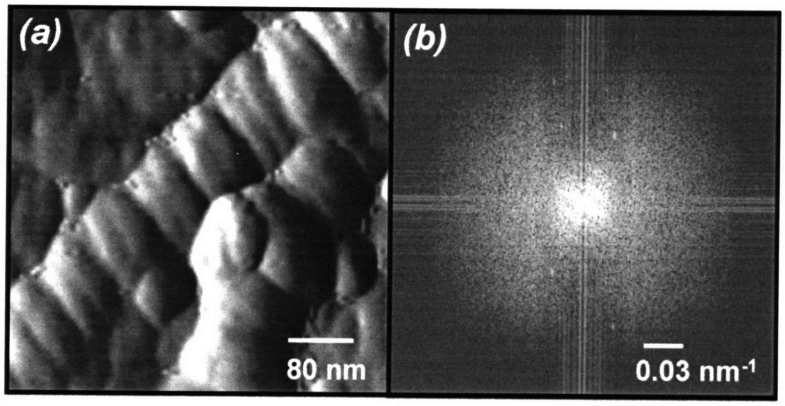

Figure 2-5. Characterization of an H_3PO_4-treated (~4% mineral) longitudinal section of adult bovine cortical bone; *(a)* higher resolution TMAFM amplitude image in air (taken with *DI Multimode AFM*), *(b)* 2DFFT of *(a)* which shows the expected 67 nm axial periodicity.

observed in TMAFM images as shown in Figure 2-5(a). The average fibril diameter was found to be 151.0 ± 16.9 nm with parallel banding lines oriented at an angle of ~10° to the collagen fibrillar axis. Uniformly distributed on top of the surface of the fibrils, there also appears to be softer (in many cases deformed by the probe tip during imaging) tiny globular structures (size ~10 nm) present that can be attributed to non-collagenous

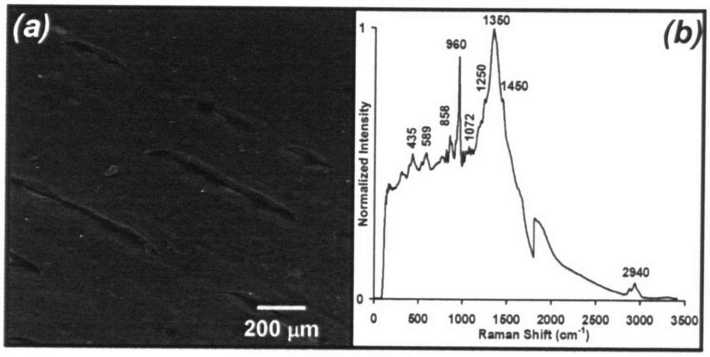

Figure 2-6. Characterization of an H_3PO_4-treated (~4% mineral) longitudinal section of adult bovine cortical bone; *(a)* low vacuum micron-scale (back-scattered electron) BSE image in water vapor, and *(b)* Raman spectrum. The peak at 1447 (CH_2 wag) cm^{-1} denotes a typical organic presence. The Raman spectrum shows a good deal of fluorescence due to a greater percentage of protein in the sample compared to the smaller "mineral" peaks.

proteins. A 2DFFT (Figure 2-5(b)) of Figure 2-5(a) agrees with the data in Figure 2-4(b). The relatively dark BSE gray levels shown in Figure 2-6(a) indicate that the mineral content (~4 wt.%) is significantly lower compared to the undemineralized bone sample Figure 2-6(b) confirms peaks which denote bands characteristic of the mineral in bone [45].

Figure 2-7 shows BSE images that exhibit the full range of mineralization from the phase pure HA (Figure 2-7(a)) to the completely demineralized bone (Figure 2-7(e)). The etched samples had mineral contents of ~37wt.% (1 second etch), 26wt/% (10 second etch), ~19wt.% (40 second etch), and ~wt.4% (120 second etch), which was determined by the etch time. All bone samples that subjected to the demineralization etch exhibited the same type of fibrillar banding structure found in the Figure 2-5(a) (Figure 2-7(f)) as observed by TMAFM.

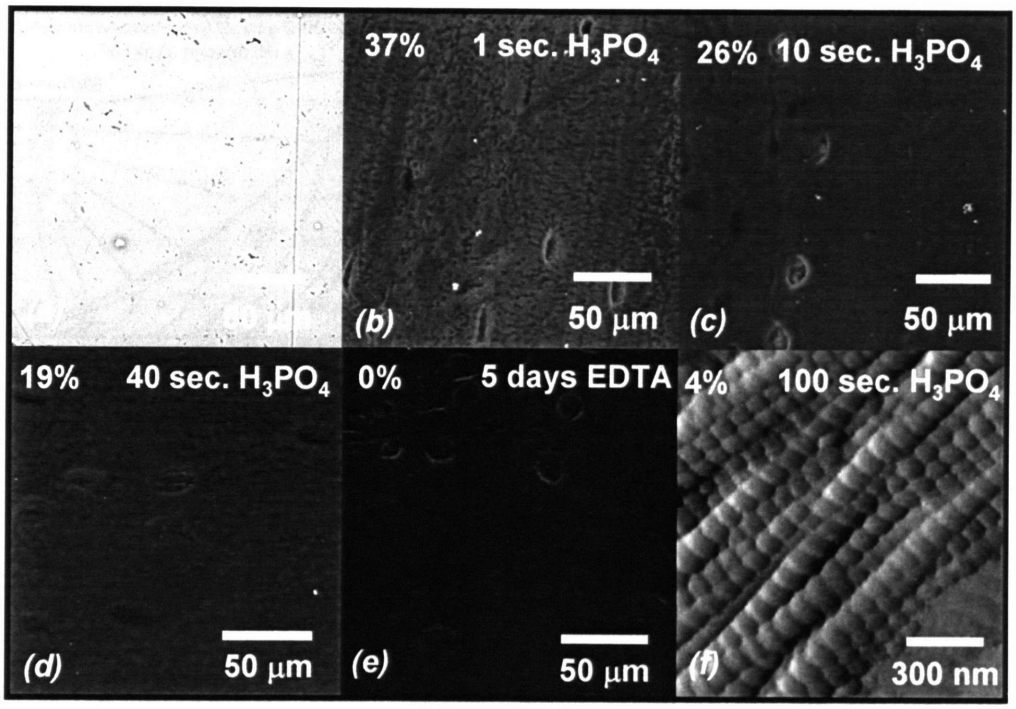

Figure 2-7. Characterization of longitudinal sections of adult bovine cortical bone with varying mineral content. Back-scattered electron (BSE) images; *(a)* phase-pure synthetic HA (100 weight(wt.)% mineral content), *(b)* 37 wt.% mineral, *(c)* 26 wt.% mineral, *(d)* 19 wt.% mineral, and *(e)* 0 wt.% mineral. *(f)* Typical type I collagen fibrillar banding structure observed under higher resolution TMAFM (amplitude image in air using *DI Multimode AFM*).

2.3.2 Nanoindentation and Elastic Contact Mechanical Analysis

Averaged nanoindentation curves on loading and unloading are shown in Figures 2-8 and 2-9 for the various samples up to maximum loads of ~1000 μN. All samples exhibited mechanical hysteresis at each load tested. The loading responses exhibit significant changes in mechanical behavior shown in the shape of the overall loading and unloading response as the mineral content was varied. Particularly, the initial unloading slope, dP/dh, of the unloading curve and the residual depth of impression vary markedly.

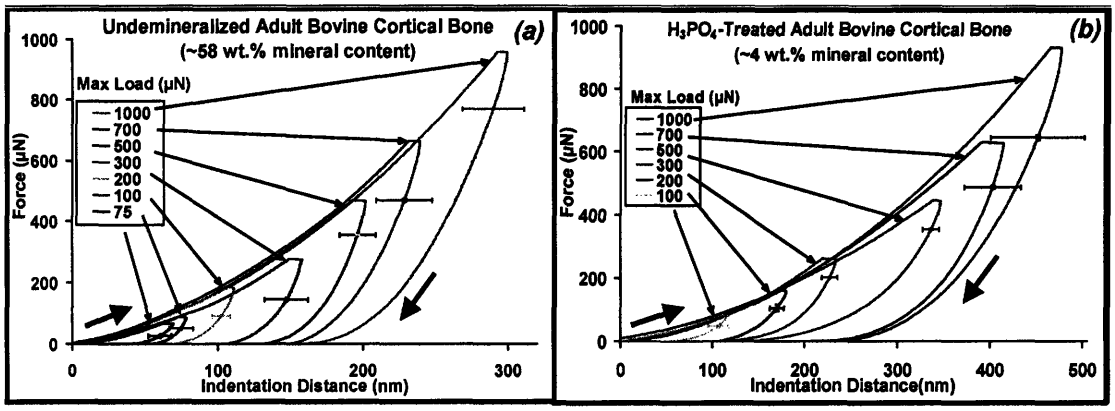

Figure 2-8. *(a)* Undemineralized and *(b)* Partially demineralized bone samples indentations at varying maximum loads

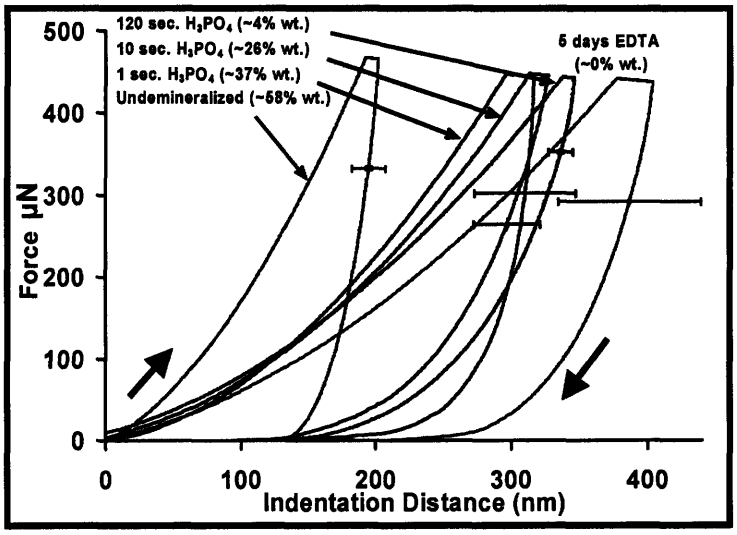

Figure 2-9. A comparison of the average force (μN) versus indentation distance (nm) curves for differently mineralized longitudinal sections of adult bovine cortical bone with the maximum load set to 500 μN and an indentation rate of 9.0 ±0.4 μN/sec.

The individual nanoindentation curves were relatively smooth with no discontinuities or distinct changes in slope apparent (*data not shown*). The O-P fits yielded average elastic moduli that ranged from 12.86 ± 2.9 (~58 wt.% mineral content) to 1.91 ± 0.12 GPa (~0 wt.% mineral content) (Figure 2-10(a), blue diamond symbols and Table 2-1). Figure 2-10(b) shows the relation of the energy dissipation as a function of the maximum force exerted by the indenter tip on the undemineralized and ~4wt. % mineral samples.

Comparing the two ratios, the undemineralized bone has less of an energy dissipation to maximum load ratio as the maximum force increases. For the maximum load of 900 □N, average values for the acid-treated bone compared with that of the undemineralized bone were statistically very different (>0.999 t-percentile).

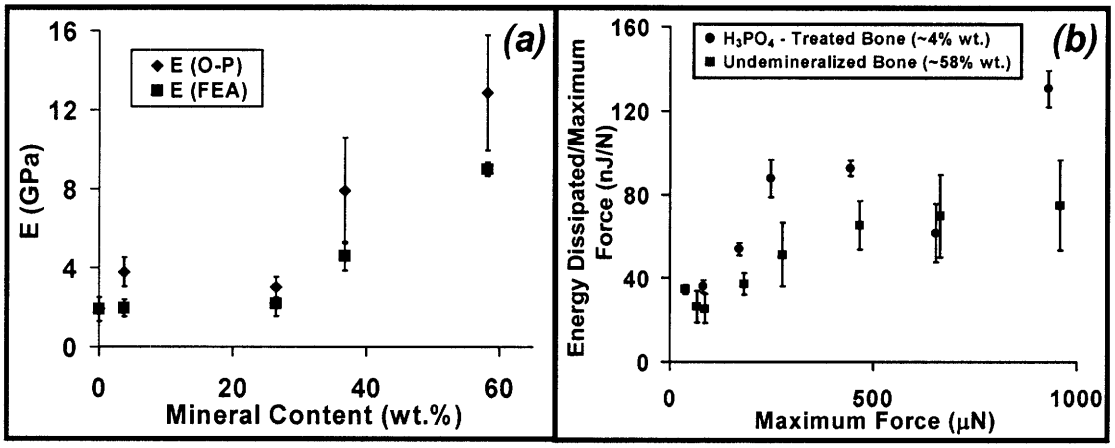

Figure 2-10. Plots of *(a)* elastic modulus values calculated from the fits to the Oliver-Pharr (O-P) method and finite element analysis (FEA) simulations, as a function of the weight(wt) % mineral content estimated from BSE which are also detailed in **Table 1**. Student t-tests revealed statistically significant differences in stiffness the undemineralized bone compared to the other samples. Wt% in the datasets label in the plot corresponds to the mineral content. *(b)* Normalized energy loss as a function of maximum load.

Wt.% Mineral Content	*E GPa (O-P)*	*E GPa (FEA)*	*σ_y GPa (FEA)*
58	12.9 ± 2.9	9.0 ± 0.35	0.24 ± 0.1
37	7.9 ± 2.7	4.6 ± 0.7	0.08 ± 0.04
26	3.0 ± 0.5	2.2 ± 0.6	0.16 ± 0.03
4	3.8 ± 0.7	2.0 ± 0.4	0.11 ± 0.08
0	1.9 ± 0.1	1.9 ± 0.6	0.07 ± 0.03

Table 2-1. Modulus and yield stress values as calculated by finite element analysis (FEA) and the Oliver-Pharr (O-P) method for samples of varying degree of mineralization.

2.3.3 AFM Imaging of Indented Regions

Figure 2-11(a) is a TMAFM image (*Q-scope*) of the indented region of the undemineralized bone sample. Residual deformation is clearly visible localized within the indent region with no apparent deformation of the material away from the indent region or any signs of brittle microcracks. The surface topographical features have been flattened within the indent region and there is an appreciable amount of feature consolidation and material pileup at the edges of the indent region. For the ~4 wt.% sample (Figure 2-11(b)) at 300 μN maximum load, collagen fibril banding was still clearly visible in areas within the indent regions, while at a higher maximum load of 700 μN (Figure 2-11(c)), much of the indented area had lost its characteristic banding (mechanical denaturation). For the lower maximum load of 300 μN, discontinuities and kinking along the axial fibril direction were visible within the indented region. For both maximum loads, a tortuous curved, path was visible along the tip apex lines which appeared to slice through the thickness of the collagen fibrils. At the higher maximum load of 700 μN (Figure 2-11(c)), a crack was observed to continue outside of the indented region in the same direction as the tip apex lines. Other similar cracks were observed outside the indented region and appeared to be due to failure of interfibril interfaces. Figures 2-12(a) and 2-12(b) are AFM images of the ~4% wt.% mineral content samples deformed to higher loads of 1000 and 7000 μN, respectively, taken 3 hours post-indent and show more extensive mechanical denaturation of collagen fibrils, in particular at the apex of the indent where the greatest pressure is applied. Figure 2-12(b) exhibits an interesting 3-lobed, amorphous, unbanded region which follows the probe tip apex lines.

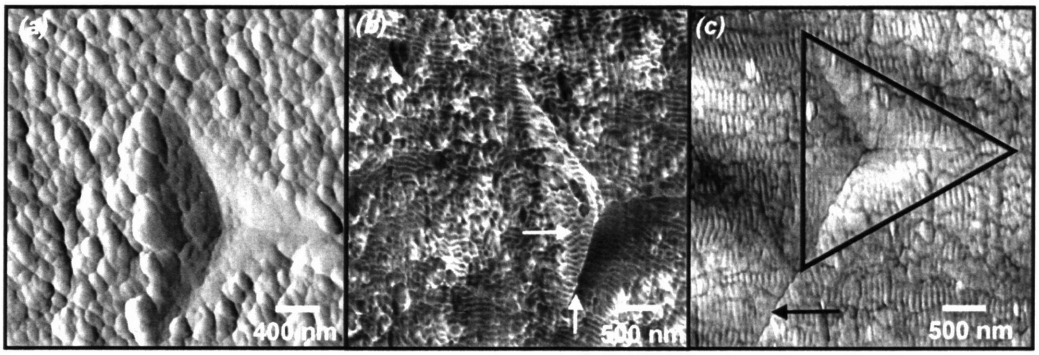

Figure 2-11. Tapping mode atomic force microscopy (TMAFM) amplitude images of residual indentation impressions (taken with a *Quesant* AFM attached to a *Hysitron* nanoindentor), *(a)* amplitude image of undemineralized longitudinal section of adult bovine cortical bone at a maximum load of 700 μN, *(b)* phase image of H_3PO_4-treated longitudinal section of adult bovine cortical bone at a maximum load of 300 μN. The arrow pointing vertically shows that along the apex lines, the kinked collagen fibrils maintain their banded structure. The arrow pointing hortizonally shows clearly that under slight pressure, although a bit distorted, the collagen fibrils preserve their banding configuration.

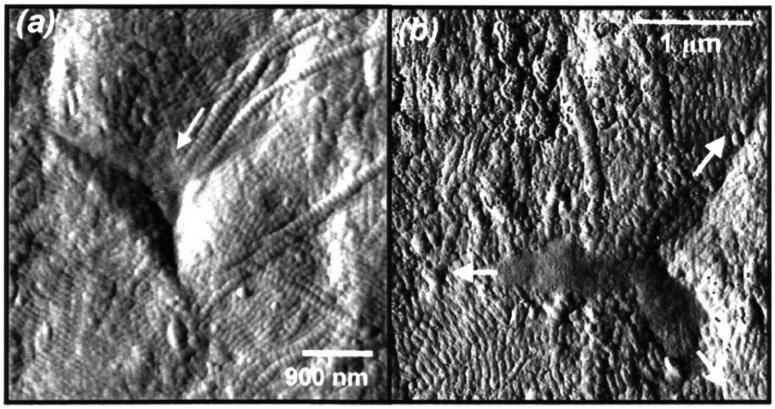

Figure 2-12. *(a)* The arrow shows the path of collagen fibrils that lose their supramolecular banding structure as the pressure nearing the apex impression increases. Along the outside, where the force is significantly lower, the fibrils merely flatten out from the sink-in deformation. The indent was made using ~1 mN maximum load. *(b) H*igh resolution tapping mode atomic force microscopy (TMAFM) amplitude image in air of indentation impressions 3 hours post-indent taken with *DI Multimode*. The middle indent region is shown where the arrows mark the apex lines of the indenter. The indent was made using a ~7 mN maximum load.

2.3.4 Elastic-Plastic FEA Simulations of Nanoindentation

The significant amount of residual deformation observed by AFM imaging (Figure 2-12) is likely due to a combination of viscoelastic and plastic deformation. Since it was observed by AFM imaging that the indentation impression did not disappear after a number of hours upon removal of the indentation load, there is a relatively long recovery time for viscoelastic deformation. In macroscopic uniaxial tension and compression tests of bone, the onset of plastic deformation is characterized as a distinct slope change in the stress-strain curve, i.e. the yield stress, σ_y, followed by a viscoplastic region typically with a small amount of strain hardening, depending on the type of bone [29, 46, 47]. The purpose of the numerical modeling portion of this paper is to use a simple constitutive model to characterize the nonlinear nano- to micro-mechanical behavior of bone and to approximate the local material properties such as the elastic modulus and yield strength. Hence, FEA simulations were conducted using a stress-strain relation in the form of an elasto-perfectly plastic model, which is intended to approximate the stress-strain behavior demonstrated in macroscopic mechanical tests [48]. Here, we refer to "plastic" as residual deformation due to a combination of permanent and viscoelastic deformation. One justification for using an elastic-plastic model to describe the nanomechanical behavior of these samples is the long recovery time observed for deformation. In addition, recent studies [49] have shown that the effect of time-dependence during typical nanoindentation in cortical tibial bone is minimal as evidenced by the fact that as the indentation rate was varied by 100x the energy dissipation due to plasticity varied by < 10%. In this previous work [49], it was also observed that when the time segment in between loading and unloading held at maximum load was increased by 100X, the energy dissipation varied by <10%. The elastic-plastic

model thus provides a simple constitutive model with minimal material parameters (two). Other constitutive models which incorporate large deformation viscoelastic or viscoplastic behavior require additional two or more material parameters, thus reducing confidence in the fits.

As the nanoindentation tests conducted in this paper contain ~ 30 collagen fibrils laterally and ~ 3 collagen fibrils vertically with the contact area, as a first approximation the sample was modeled as a homogeneous material. More refined FEA models which take into account the mechanical properties of the mineral and organic constituents, anisotropy due to local orientation of the collagen fibrils, viscoelasticity, and structural heterogeneity are currently under development. Figure 2-13 shows FEA fits to the averaged nanoindentation data for the undemineralized sample, ~4 wt.% mineral content sample, and the completely demineralized sample, respectively. In general, the elastic-plastic model captures both loading and unloading behavior reasonably well. The most important regions for fitting the two parameters were the initial unloading slope and the residual plastic indentation depth. Figure 2-10 shows the FEA fitted results (square symbols) for the moduli compared to the O-P method (diamond symbols) as a function of weight percent mineral content. The FEM simulations predict moduli values 21 - 48% lower than the O-P method, but display a similar trend with mineral content

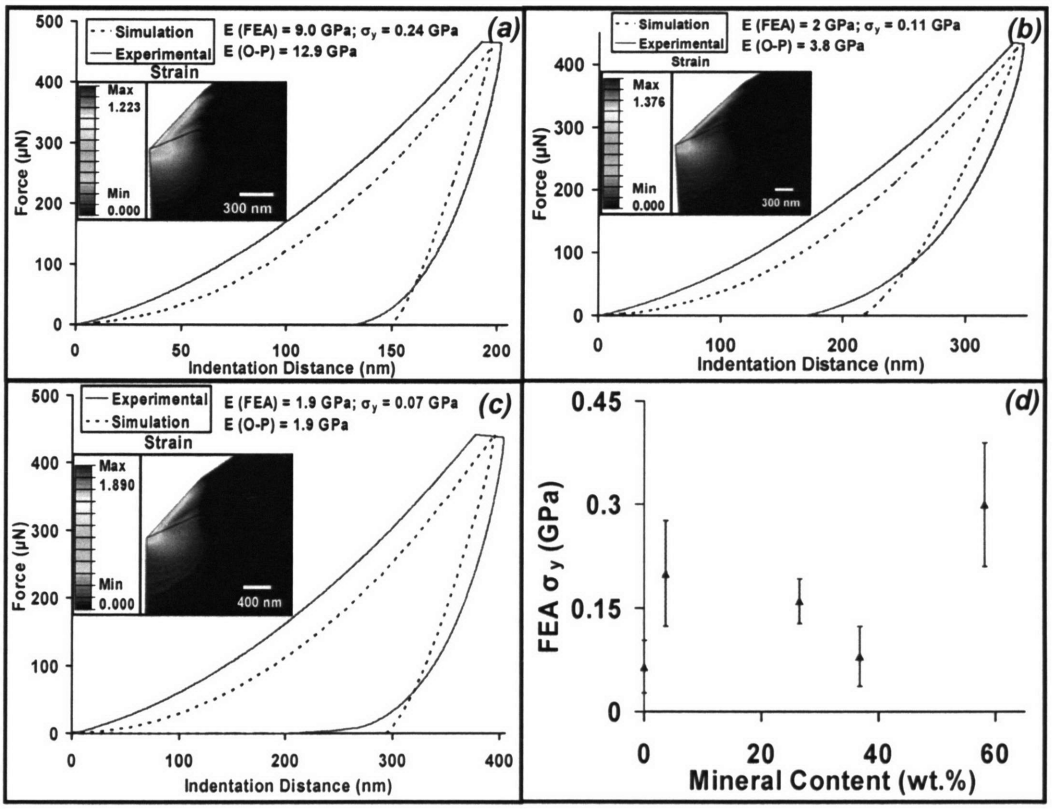

Figure 2-13. Plots which show a comparison between the experimental nanoindentation data and the finite element analysis (FEA) simulations for; *(a)* undemineralized bone, *(b)* partially demineralized bone (~4 wt.%), and *(c)* fully demineralized bone. Inset represents contour plots for the simulated plastic strain. *(d)* Finite element analysis (FEA) fits for the yield stress, as a function of weight(wt.)% mineral content.

(Table 2-1). From the evidence of pileup shown in Figure 2-11(a), the O-P prediction most likely underestimates the true contact area, resulting in an overestimation of the Young's modulus. T-test results revealed the difference between the ~0 wt.% and ~58 wt.% samples to be statistically significant (percentile > 0.995). Figure 2-13(d) shows the yield strengths predicted from the FEA simulations as a function of mineral content and give ~ 0.30 ± 0.09 GPa for undemineralized bone, and ~ 0.07 – 0.2 GPa for the partially demineralized samples. Student t-test shows a > 0.95 percentile statistical difference for comparisons between the completely demineralized and undemineralized

bone. Figure 2-14 shows the mesh that was formulated in the FEA to carry out the simulation.

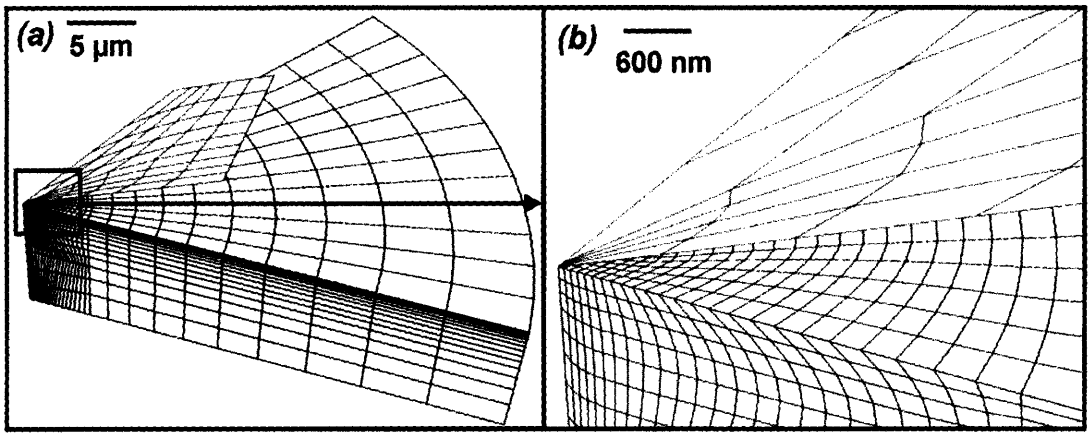

Figure 2-14. The one sixth homogeneous mesh plot for FEA simulation is shown in *(a)*. *(b)* A closer view of the finer mesh where the majority of strain occurs.

2.4 Discussion

Coarse positionally-specific nanoindentation experiments in conjunction with optical microscopy on human femoral and vertebral cortical bone in air at relatively large loads up to ~20 mN and ~1 μm depths have been reported in the literature and shown variations in nanomechanical properties for different types of bone (e.g. interstitial, osteonal, etc.) [50], with age [50], orientation [24], and location (e.g. distance from osteonal center) [17, 24]. In a related study, high maximum load indentations (~15 mN) were performed on articular calcified cartilage and subchondral bone of post mortem and osteoarthritic femoral heads at locations of varying degrees of mineralization [26]. Modulus values for cortical bone predicted from the O-P method in these studies ranged between ~15-25 GPa, similar to that reported for tensile macroscopic mechanical properties [51].

2.4.1 Moduli

Values for average moduli estimated by fits to both elastic and elastic-plastic models for the undemineralized bone (~12.9 GPa, ~7 GPa, respectively) are somewhat less than that experimentally reported by nanoindentation for the same direction for dehydrated and embedded human tibial cortical bone (16.6-17 GPa) [25]. Here, the authors apply a simple rule of mixtures correction to take into account osteonal, interstitial, and void volume fraction and assume a 15% artificial increase in modulus due to ethanol dehydration (used in the sample preparation process) yielding corrected moduli values of 14.4-14.9 GPa. These reported values may differ from those obtained in this study due to additional stiffening from ethanol dehydration, higher maximum loads up to 20 mN covering greater contact areas, faster loading rates of 1 mN/sec, and the different species of bone used [22-24, 50].

The average moduli value calculated from both elastic and elastic-plastic models for the undemineralized sample was found to exceed the other samples by up to ~ 6X which is consistent with the trend for macroscopic tensile modulus of cortical bone known increase with the mineral content [52]. XRD studies show that acid demineralization leads to both an averaged reduction in the mineral crystallite size as well as the lattice microstrain in bone [53]. Internal porosity is also likely. As in macroscopic mechanical property measurements, it should be stated that trends with mineral content observed here are likely to be complicated by other structural and chemical changes in the distribution and location of mineral, the organic-mineral interface, and the physiochemical properties of collagen.

2.4.2 Yield Strength

The yield strengths, $_y$, predicted from the FEA simulations are » $\frac{1}{8}$ to$\frac{1}{24}$ of the FEA-determined elastic moduli, E, which are higher than those obtained in macroscopic mechanical testing tests [29]. For example, a survey of 39 bones from 22 species found that s_y » $\frac{1}{120}E$ to$\frac{1}{140}E$ [29]. $_y$ obtained from fits to nanoindentation data have been observed to exceed those measured by macroscopic mechanical measurements for other types of other materials as well [54]. Possible reasons for this observation are a decreased number of defects as the volume of material deformed becomes small and/or pressure-induced hardening (increased yield strength) due to the increasing internal resistance for damage to develop as the pressure increases [55] (discussed further in the next section).

2.4.3 Nanoscale Mechanisms of Deformation and Energy Dissipation

As described in the Introduction section, yielding and the resulting high toughness of bone has been attributed to a variety of deformation mechanisms that take place at multiple length scales. Our high resolution AFM images of the partially demineralized bone (Figures 2-11(b) and 2-12) clearly show that during deformation collagen fibril lateral curvature and normal flattening can be achieved while still maintaining the collagen banding structure indicative of the native supramolecular structure. This finding is consistent with AFM studies on collagen fibrils in tendon [56] and supports the idea of an adaptable, compliant fluid-like fibril structure [57]. Since collagen fibril-fibril interfaces appear to remain in-tact during deformation, interlocking fibril adhesion appears to be particularly efficient and strong. At the resolution of our images, interfibril

shear mechanisms can not be conclusively discerned. Kinking along the axial direction observed here is also consistent with previous studies[56]. Interestingly, at the highest applied indentation loads, mechanical denaturation of collagen fibrils is observed (Figure 2-12) taking place close to the junction edge of the two faces of the indenter, which is the region found to have the highest plastic deformation as revealed by FEA simulations (Figure 2-13).

In the undemineralized bone samples (Figure 2-11(a)), a dramatic near complete elimination of surface topographical features is observed which could be indicative of the pressure induced structural transition of bone mineral previously mentioned[58]. While it was not possible to observe denaturation of collagen fibrils (since the collagen banding was not visible in the undeformed sample Figure 2-11(a)), it can not be ruled out as well. FEA simulations reveal that at an indentation depth of 280 nm (maximum load of 1000 □N) the highest pressure is about 520 MPa, which is close to the pressure required for phase transition in sintered synthetic dense HA [58]. In addition to the high pressure, the material is also subjected to high shear stress; the FEA simulation shows the highest equivalent shear stress to be about 140 MPa, which can initiate plastic deformation of HA plates, as well as expedite the phase transition due to increased lattice energy when the material is subjected to shear stress. Although displacement of individual mineral platelets could not be resolved, the occurrence of extensive mineral viscoplastic deformation and collagen denaturation suggests that this is likely. Analogously, micromechanics studies of a rubber filled thermoplastic composite system show that the plastic deformation of thermoplastic results in the displacement of particles after unloading [59, 60].

The yielding mechanism is also susceptible to retardation by pressure, which leads to an increased yield stress observed in nanoindentation. For instance, the slippage between collagen fibrils and themselves and/or mineral particles is expected to be retarded by the pressure because of increasing resistance to the relative motions. Microcracks, if they exist, also are subjected retardation because the applied pressure tends to close these cracks, requiring a higher stress to propagate the cracks resulting in a higher yield stress.

As shown in Figures 2-9 and 2-10(b), the partially demineralized bone exhibits the highest ductility and dissipates the most energy at all maximum forces tested. One explanation for this result, in particular when comparing to the undemineralized bone, is the possibility of underlying porosity and voiding, which would relieve triaxial stresses, and facilitate plastic deformation via for example, increased molecular mobility and mineral displacement mechanisms. Differences in the collagen supramolecular structure and water content (which are unknown) are also likely to have a significant impact on the energy dissipation.

2.4.4 Conclusions

In this paper, a multitechnique experimental and numerical modeling methodology was employed for studying the nanomechanical properties and detailed ultrastructural deformation mechanisms of bone. Bovine tibial cortical bone samples of known and varied mineral content (~58%, ~37%, ~26%, ~4%, and ~0 wt%) were prepared, characterized, tested by nanoindentation perpendicular to the osteonal axis, and analyzed *in-situ* and *post-mortem* by high resolution AFM imaging. Mineral content was

found to have a significant effect on both the nanoscale mechanisms of deformation and nanomechanical properties. A 2-6X increase in modulus was observed for the ~58 wt.% sample (~7-12 GPa) compared to the ~0 wt.% sample sample. Upon inspection, all samples exhibited similar values for work of plastic deformation. The yield strength predicted by FEA simulations was found to have a very slight dependence on the mineral content. For the partially demineralized samples, collagen fibrils were observed to be able to withstand forces up to 1 mN and indentation distances up to 400 nm without significant disruption of the banding structure or interfibril interfaces, suggesting a compliant, adaptable ultrastructure with highly effective adhesive interfaces. Plastic deformation was observed in these samples to take place via the nanoscale mechanism of mechanical denaturation of collagen fibrils at the highest loads tested of 7 mN corresponding to 800 nm indentation residual displacement. For the undemineralized ~ 58 wt.% sample, the near complete elimination of surface topographical features provided evidence for plastic deformation via the mechanism of a pressure induced structural transition of the mineral component observed at loads as low as 300 μN and displacements of 100 nm. The FEA elastic-plastic continuum model was able to predict the nanomechanical behavior of the differently mineralized samples reasonably well on loading and unloading suggesting applicability at the length scales probed in this study. While the O-P method yields immediate quick results in a simple and effective manner, it tended to overestimate the elastic moduli by 21 - 48% as compared to the FEA simulations at the nanoscale which still require better models for predictive accuracy.

Chapter 3

Nanogranular Origins of the Strength of Bone

This chapter was published as a paper in Nano Letters [61].

3.1 Introduction

The ultrastructural origins of the plasticity of bone and its complex relationship to damage accumulation and fracture risk are poorly understood. Recent studies [62-64] have primarily probed tensile modes of deformation, which are relevant, for example, to avulsion fractures at tendinous and ligamentous insertions and bending fractures in the diaphyseal regions of long bones [65]. In this study, the focus is on the nanoscale compressive strength of bone, which is a significant physiological loading condition [15] and a key requirement *in vivo*. While day-to-day deformation of bone generally takes place in the linear elastic regime [66], excessive injurious loads, fatigue, degradation of biomechanical properties due to age or disease can lead to microdamage [67], and fracture [68] *in vivo* at compressive locations such as metaphyseal areas, vertebral bodies, and the calcaneus [65]. Hence, a fundamental mechanistic understanding of how the structural design of bone is able to achieve optimal resistance to compressive yield is critically important for predicting tissue-level fracture, simulating remodeling processes, and developing clinical approaches to treat biomechanical degradation.

It is known that cortical bone exhibits a macroscopic yield strength in compression that is greater (~2×) than in tension or torsion [69], which is indicative of pressure sensitive plasticity. The strength of bone must begin at the ultrastructural level. At this length scale, plate-like carbonated apatite mineralites exist (~10s of nm in length

and width, 3-5 nm in thickness [12]) that permeate in and around type I collagen fibrils in an overlapping manner [70]. This chapter explores the possibility of nanogranular friction from mineral-mineral interparticle interactions as a contributing source of the compressive yield strength of bone. This hypothesis is based on a number of experimental observations. First, the inorganic component is known to be a critical determinant of the macroscopic compressive mechanical properties of bone; the yield stress [71], maximal stress [72], and failure strength [73] are all known to increase with increasing mineral content. Second, the fact that mineral content of human bone is typically above the percolation threshold of 50% packing density (corresponding to ~43% mineral content) [74, 75]. Lastly, previously reported data of the direct visualization of the ultrastructural plasticity of bone via nanoindentation combined with high resolution atomic force microscopy (AFM) imaging of residual impressions show the nanogranular structure of contacting mineralites flattened, but still visible, within the plastically deformed indented region (Figures 2-2(a) and 3-1) [8]. The appearance of the undeformed mineralites outside of the indent region compared to within suggest mineral displacement and the possibility of interparticle frictional interactions. These data are consistent with recent scanning electron microscopy images of collagen fibrils bridging a crack within a compressed trabeculae [76]. Given that many mineralized fibrils are in direct contact with each other, deformation away from their unstressed configurations must involve mineral-mineral displacement. Hence, it is hypothesized that the ultrastructure of bone is a cohesive-frictional material [77], following a Mohr-Coulomb pressure dependent strength criterion [78] (i.e. which arises from the pressure dependence of the density of interparticle contacts).

3.2 Methods

3.2.1 Sample Preparation

Adult compact bovine bone from between the tibial metaphysis and diaphysis was cut down to 1.5 mm thick specimens and polishing to a 0.05 μm finish. Samples were rinsed copiously with DI water followed by ultrasonicatation in DI water between polishing intervals. Samples were then immediately stored in 20°C PBS. Complete demineralization was accomplished by storage in 0.5 M ethylenediaminetetraacetic acid (EDTA) for a minimum of 7 days, where the solution was changed every day. Complete deorganification was accomplished by heating for 5 days at 400°C and measuring no eventual weight change. X-ray photoelectron spectroscopy (XPS) also demonstrated no evidence of residual protein (lack of nitrogen) on the surface of the sample (Appendix). X-ray diffraction showed minimal change in the degree of crystallinity of the deorganified bone sample compared with the undemineralized bone (Appendix)

3.2.2 Nanoindentation

Nanoindentation experiments were conducted in ambient conditions using the *Hysitron, Inc.* Triboindenter using the *Quesant* AFM for tapping mode imaging of residual impressions. Indentations were carried out perpendicular to the long bone axis. For dual geometry triaxial stresses, load-controlled nanoindentations were performed using both Berkovich (included angle 142.3°, half angle 65.3°) and Cube Corner (included angle 90°, half angle 54.6°) diamond probe tips. Experiments at 1000 and 7000 μN maximum load were done on different sample locations for each indent.

3.2.3 Incorporation of Mohr-Coulomb Criterion in Finite Element Analysis (FEA) of Nanoindentation

The nanoindentation of cortical bone was predicted using an elastic-plastic three-dimensional finite element analysis (FEA) model for two independent triaxial stress states [79] achieved with two different indenter geometries, Berkovich and Cube Corner, which incorporated the Mohr-Coloumb pressure dependent strength criterion. In this case, the strength domain in the principal stress space, $\sigma_I \geq \sigma_{II} \geq \sigma_{III}$, is defined by:

$$f(\sigma_{ij}) = \sigma_I(1+\sin\varphi) - \sigma_{III}(1-\sin\varphi) - 2c\cos\varphi \leq 0$$

where: c is the interparticle cohesion, which is the finite value of cohesive shear strength required to cause sliding when the normal stress is zero, and φ is the internal friction angle, which provides the failure envelope given by the relationship of the linear slope between shear and normal stress. This internal friction approaches the "dry" (zero cohesion) angle of repose, which is measured when a bulk quantity of particles is poured onto a horizontal surface and is defined as the angle formed by the inclined edge of the pile and the horizontal plane. The FEA model utilized large deformation theory and incorporated a rigid indenter with frictionless contacts between the tip and sample. A modulus of 18 GPa was fixed in the simulations and approximated from the unloading slope of the nanoindentation data using an isotropic, elastic continuum mechanical half-space formulation [2]. A Poisson's ratio of 0.3 was also fixed [80]. Two material properties were reduced from the experimental data; c and φ, which were free fitting parameters. The difference between the experimental indentation response and the theoretical predictions were minimized by the quadratic error for values that best fit both

indenter geometries. To reduce computational cost and due to symmetry, only 1/6 of the tip and the surface were modeled and the corresponding boundary conditions were applied to ensure the symmetry, i.e. the nodes on the sidewalls were fixed in the direction normal to the sidewall surface (the nodal displacement in this direction is set to be zero). The same method that was employed before [8] was used here in order to approximate the degree of wear for the Berkovich and Cube Corner diamond tips.

3.2.4 Angle of Repose Measurements

The deorganified bone was first ground up with a mortar and pestle and in order to ensure that the bone sample was completely devoid of organic, the particles were reheated for 5 days in 350°C. The particles were subsequently ultrasonicated in deionized water with a *Branson Ultrasonics* (Danbury, CT) Sonifier 450. The size of the particles were measured through dynamic light scattering with a *Brookhaven Instruments Corporation* (Holtsville, NY) 90Plus Particle Size Analyzer. The ambient angle of repose was directly recorded by pouring the mineral particles on a flat surface and then measuring the angle between the edge of the pile and the horizontal surface. The dry angle of repose was then recorded by placing the pile in a vacuum chamber. As cohesion through atmospheric hydration occurs between particles, once water vapor is removed from the surrounding environment, the pile spontaneously falls to a lower angle of repose.

3.3 Results

3.3.1 Residual Indentation Imaging of Nanogranular Morphology

AFM imaging of the residual indentation for both the Berkovich and Cube Corner geometries reveal a highly granular morphology on the surface of the sample. The difference between Berkovich and Cube Corner (sharper) geometry is evidenced in the image shown in Figure 3-1. The undeformed regions away from the residual indent area are composed of nanogranular topographical features in contact with each other which have a heterogeneous shape and size distribution (maximum lateral dimension = 51.0 ± 30.7 nm) which is consistent with the known dimensions of mineral particles, as measured by scanning electron microscopy [70], transmission electron microscopy [10], small angle X-ray scattering [81].

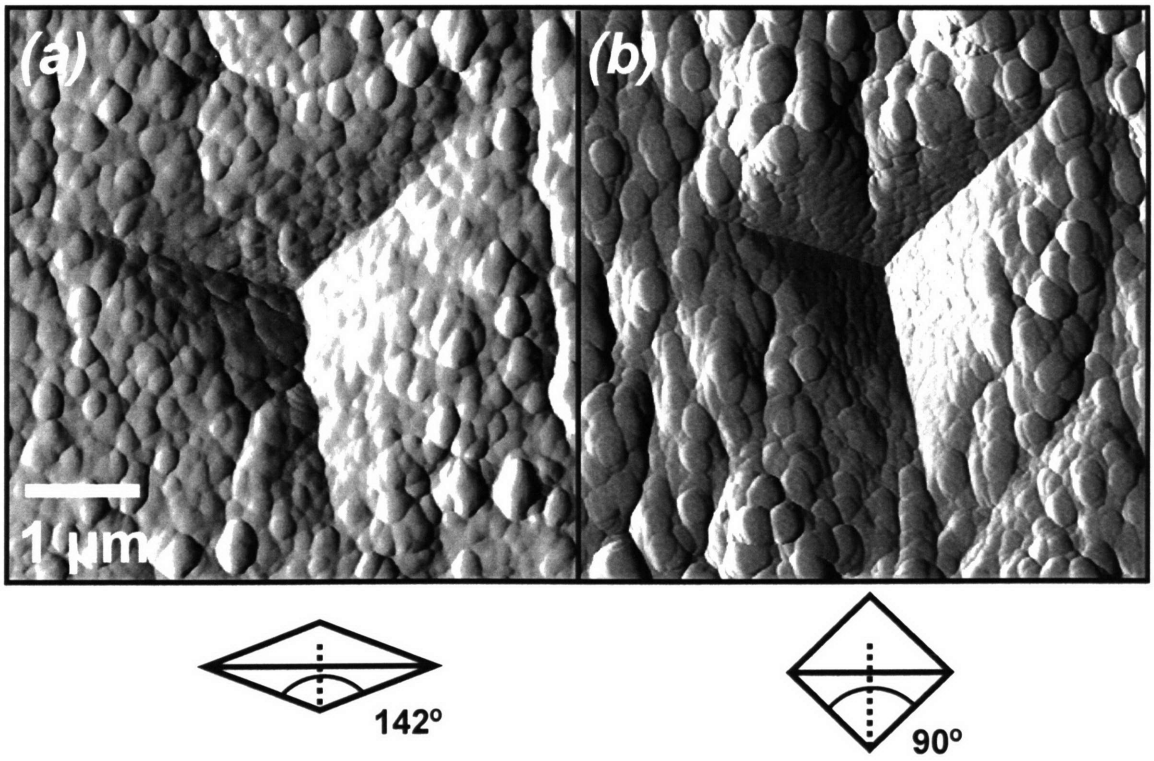

Figure 3-1. Tapping mode atomic force microscopy amplitude images (*Quesant*) of a residual nanoindentation impression in adult bovine cortical bone (~ 65 wt.% measured through back-scattered electron imaging, which probes a depth of ~1 μm) immediately after loading to 7000 μN followed by unloading (*Hysitron* Triboindenter, loading / unloading rate of 50 μN/second) using *(a)* Berkovich (~850 nm depth) and *(b)* Cube

Corner (~1.5 □m depth) geometry. Experiments were conducted with the loading direction perpendicular to the long bone axis in ambient conditions.

3.3.2 Dual Indentation Frictional Analysis

The predictions of the theoretical fits were compared to nanoindentation force versus indentation depth data taken on loading of adult bovine cortical bone perpendicular to the long bone axis for both the Berkovich and Cube Corner geometries (Figure 3-2). The best fit φ and c values for both indenter geometries was found to be 15° and 100 MPa, respectively ($R^2 = 0.99$). The indentation simulations on loading exhibited a small elastic region (indentation depths < ~10 nm) followed by yield (as assessed by monitoring the plastic equivalent strain of each element) due to local stress concentrations at the tip apex. The friction angle that best fits both indenter geometries translates into a uniaxial compressive strength – to – tensile strength ratio ($Y_c / Y_t = (1 + \sin \varphi)/ (1-\sin \varphi)$) of 1.7, which is remarkably close to the known macroscopic ratio ~2 [69]. Theoretical fits were also carried out on nanoindentation data taken on fully demineralized bone (treated for 5 days in 0.5 M EDTA). The modulus was fixed to that reduced from the unloading slope (~2.3 GPa) and Poisson's ratio was set to 0.3 as previously, yielding best fit φ and c values for both indenter geometries of 5° and 100 MPa, respectively (Figure 3-3) translating to a compressive strength – to – tensile strength ratio of 1.2. Figure 3-4 compares all four experimental nanoindentation datasets on a single plot and shows an increased force for a given depth (i.e. resistance to yield) for the intact compared to demineralized bone.

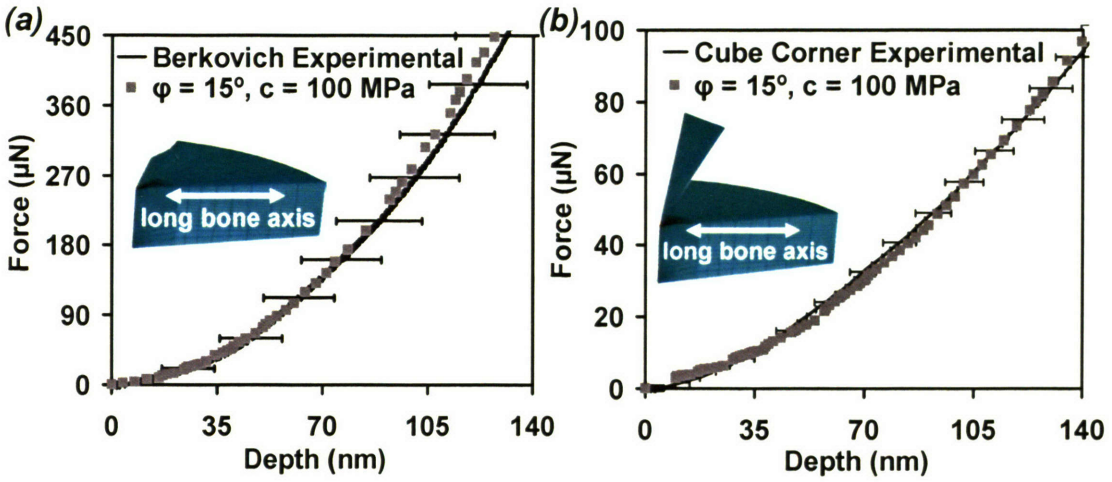

Figure 3-2. Comparison of the predictions of a three-dimensional elastic-perfectly plastic finite element analyses (FEA) model (ABAQUS) incorporating a Mohr-Coulomb cohesive-frictional yield strength criterion to averaged nanoindentation data on loading of intact adult bovine cortical bone in ambient conditions (*Hysitron* Triboindenter, loading rate ~ 50 □N/second) using; *(a)* Berkovich and *(b)* Cube Corner probe tips. The two fitting parameters used were the internal friction angle (φ) and cohesion (c). The best-fit parameters (R^2=0.99) produced the same value for the two different indenter geometries. *(a)* Berkovich and *(b)* Cube Corner FEA meshes are also shown. 8-node linear elastic brick hybrid elements (C3D8H) were used. The probe tip end radius and truncate height were approximated from control experiments on a fused quartz sample. Each averaged force versus depth curve represents 80 individual nanoindentation experiments; horizontal bars are one standard deviation.

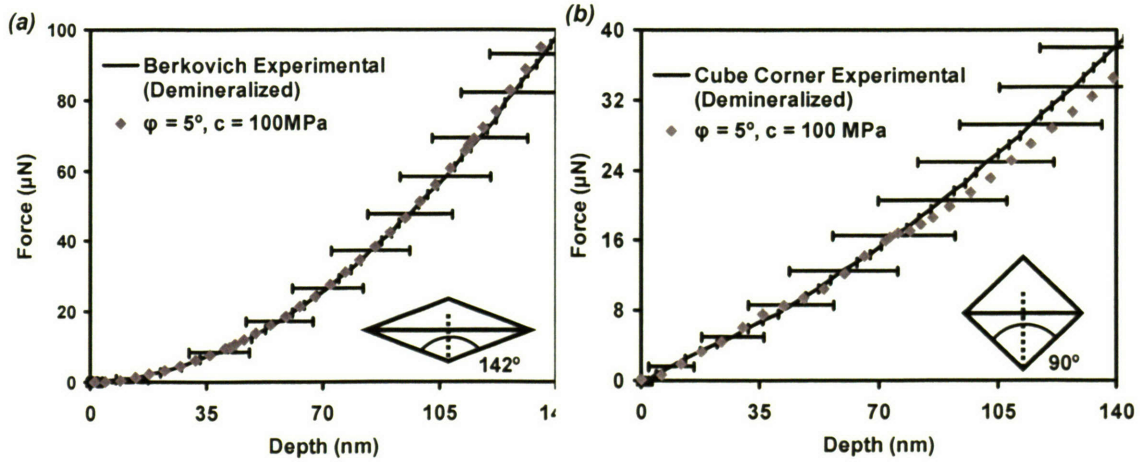

Figure 3-3. Adult bovine cortical bone was demineralized using 0.5 M ethylenediaminetetraacetic acid treatment for 5 days. Lack of mineral was verified through X-ray photoelectron spectroscopy (no evidence of Ca or P), heat treatment (400°C to show complete loss of material), and energy dispersive X-ray analysis (no Ca,

P). A three-dimensional elastic-perfectly plastic finite element analyses (FEA) model incorporating the Mohr-Coulomb cohesive-frictional strength criterion (described in Figure 2 caption) was fit to the averaged experimental nanoindentation force versus depth curve for demineralized bone tested perpendicular to the osteonal axis in ambient conditions for *(a)* Berkovich and *(b)* Cube Corner probe tips (R^2=0.99). Each averaged force versus depth curve represents 80 individual nanoindentation experiments

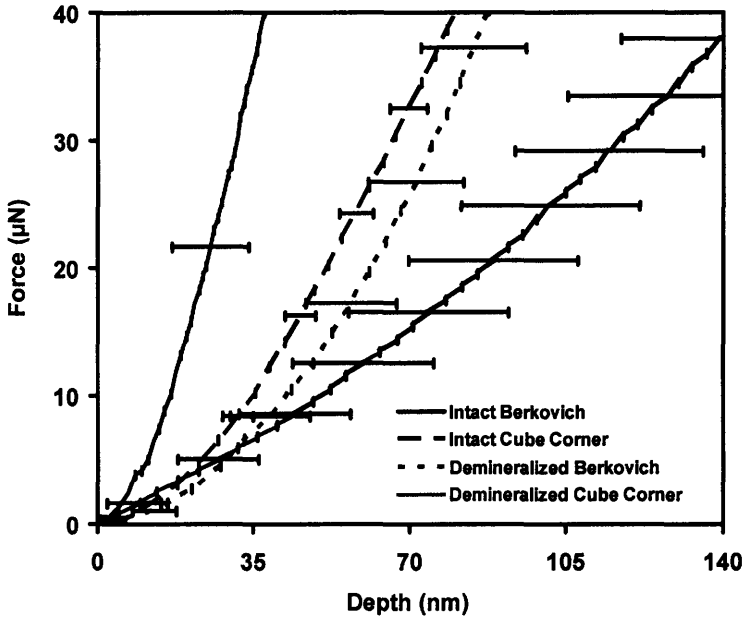

Figure 3-4. Plot comparing experimental nanoindentation data on loading in ambient conditions perpendicular to the long bone axis showing intact (data from Figure 2) and demineralized (data from Figure 3) bone indented with both Berkovich and Cube Corner probe tips. Each averaged force versus depth curve represents 80 individual nanoindentation experiments; horizontal bars are one standard deviation.

3.3.3 Verification of Friction Parameter Through Particle and Angle of Repose Measurements

The smallest particle size distribution obtained were 914 ± 44 nm (from dynamic light scattering) and the corresponding angles of repose were found to be $\varphi_{ambient}$ = 32.8 ± 3.1° and φ_{vacuum} = 18.2 ± 2.5° (number of measurements, n=4). Since $\varphi_{vacuum} < \varphi_{ambient}$, this suggests that the vacuum was effective in minimizing interparticle cohesion likely due to hydration layers. φ_{vacuum} was found to be statistically independent ($p<0.05$) of particle size up to 25 μm (Figure 3-6). It was observed that the internal friction angle

obtained from fitting nanoindentation data to the Mohr-Coloumb formulation in intact bone (~15°) was slightly lower than the measured angle of repose in vacuum φ_{vacuum} (~18.2°) for the deorganified bone. Hence, rather than introducing additional friction due to macromolecular shear (as might be expected since $\varphi = 5°$ for the demineralized bone), the interfacial organic has a slight lubricating effect, which is consistent with nanomechanical studies which show that certain interfacial organics, in particular polyelectrolyte macromolecules, can enhance lubrication [82]. This may be a trade-off effect, in order to counteract the reduction of tensile capacity compared to the cohesive shear strength (primarily carried by the organic component) due to frictional interactions.

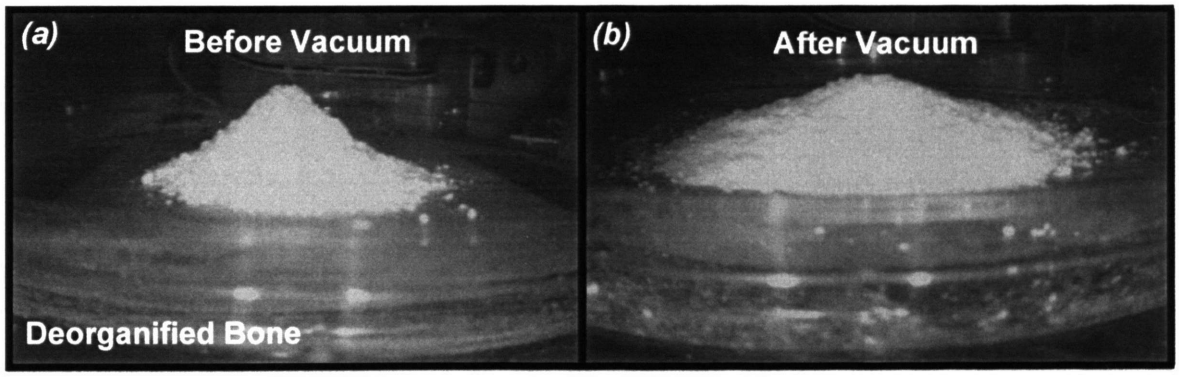

Figure 3-5. Angle of repose experiments performed in ambient environmental conditions and in vacuum. The deorganified bone (400°C heat treatment where no weight change after 5 days was recorded) powder is shown *(a)* before vacuum, ambient conditions and *(b)* after vacuum. Angles measured from deorganified bone were compared to one another and found to be ~33° in the ambient state and ~18° in vacuum.

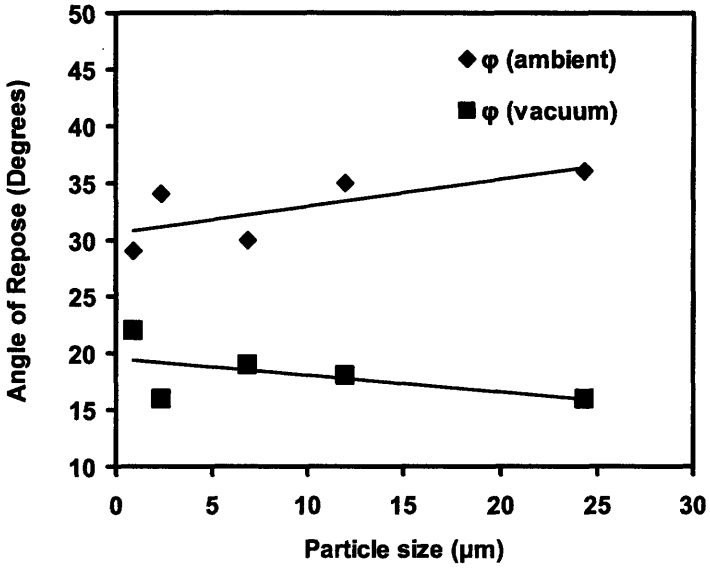

Figure 3-6. Angles measured from deorganified bone were compared to one another and found to be ~33° in the ambient state and ~18° in vacuum. The particle size was varied (~1-25 μm) and controlled by the degree of sonication (Branson, Sonifier 450) and measured by a Brookhaven 90Plus Particle Size Analyzer. The angle of repose did not change significantly for the range of particle sizes measured.

3.4 Discussion

It is interesting to note that c (intact bone) $\approx$ c (demineralized bone) which may well suggest that cohesion values quantified by nanoindentation are attributable to the organic itself, rather than to interfacial mineral-organic bonding [83]. Indeed, cohesion may arise from collagen crosslinking (which includes intermolecular pyridinoline and pyrrole linkages arising from linkages between lysine and hydroxylysine aldehyde residues [84, 85] or noncovalent "sacrificial" bonding in non-collagenous proteins (e.g. proteoglycans, osteopontin, bone sialoprotein [86, 87]).

Note in Figure 3-1 the absence of pileup and rather the presence of sink-in which is explained as follows. The ultrastructure of bone has been suggested to possess nanoscale porosity (~20 nm in size) [88] which is a characteristic of a nanogranular

material. Hence, when bone is compressed during nanoindentation, there is mostly likely a plastic contracting behaviour until the material reaches a state (called the critical state, a concept introduced for granular soils from which all Cam-Clay models derive [89]; at which it behaves like a cohesive-frictional material in the Mohr-Coulomb sense (i.e. the state which we model with FEA). In return, the plastic contracting behavior can explain why we observe sink-in rather than pile-up. This is observed in the AFM images (Figure 3-1): rather than being squeezed out, the particles in the imprint area are higher compacted than far away. Refined models, currently in development, aim at taking this contracting behaviour into account, by considering a critical-state Cam-clay type plasticity model for bone nanoindentation. This refined model, which considers nanoscale porosity, is expected to shed light on the observable contracting behaviour in nanoindentation, while it is not expected to change the overall result that bone's ultrastructure is a cohesive-frictional material. In order to further investigate the nanogranular friction in bone, angle of repose experiments were performed on ground and ultrasonicated powders of deorganified adult bovine cortical bone mineral (Figure 3-5) in a sealed chamber in ambient ($\varphi_{ambient}$) and vacuum environments (φ_{vacuum}).

The fact that φ (intact bone) > φ (demineralized bone) (Figures 3-2 and 3-3) and φ (intact bone) $\approx$ φ_{vacuum} (deorganified bone) (Figures 3-2 and 3-5) suggest that the ultrastructural origins of the friction angle arise primarily from mineral interparticle interactions and that organic frictional contribution (e.g. internal friction arising from, for example, molecular rotations, stick-slip sliding, and/or barrier-hop fluctuations [90]) is minimal. Potential interparticle frictional mechanisms cited in the literature that may be relevant include mechanical interlocking and deformation of surface nanoasperities,

which has been observed directly by scanning electron microscopy for adjacent aragonite-based nacre tablets (from the inner layer of a gastropod mollusk) [91]. In this paper [91], it was postulated that inter-tablet shear resistance was enhanced as nanoasperities were required to "climb" over one another in order for inter-tablet sliding. Another potential mechanism at even smaller length scales has been studied by atomistic molecular dynamics modeling and involves mechanical locking due to surface roughness between atoms, as well as dynamic friction characterized by translational kinetic energy that dissipates during sliding into internal energy motions [92]. Stick-slip and smooth sliding between atoms and the transition between the two at atomic length scales could be relevant to bone mineral interactions as well [93].

The addition of mineral and corresponding frictional interactions results in an increase in the resistance to plasticity (strength or elasticity domain) in compression at these small lengths (Figure 3-4), which is the dominating physiological stress state in bone, and correlates with the correct trend macroscopically [71]. Our interpretation is consistent with the known structure-function relationships of other mineralized tissues; for example, human tendon has little to no mineral volume and is loaded predominantly in tension [94] while ear or whale bones have a considerable amount of mineral (~90 wt.%) and are primarily loaded in compression [74]. Human (as well as bovine) bone (~60 wt.% mineral) seems to be an intermediate compromise, providing strength in compression for physiological loading plus some degree of protection for accidental shear/torsion/bending loading. Mineralization has also been shown to vary with anatomical site [95], leading to correlated inter-site variation in compressive stiffness [96] (reflective of mineral content) and yield strength [97].

The macroscopic experimental value of the compressive yield strength of these adult bovine cortical bone samples was measured perpendicular to the long bone axis as σ_y (compression) ~178 ± 47 MPa (Zwick Allround-Line Mechanical Tester, 0.01 mm/s load rate), which is 30% less than that calculated from the Mohr-Coloumb friction angle and cohesion reduced from nanoindentation data (~260 MPa). This comparison suggests that larger length scale structures serve to weaken, rather than strengthen bone, possibility due to heterogeneity, porosity, or other defects present.

A number of nanoscale deformation mechanisms have been proposed in the literature, based on various types of experimental data, including void and crack formation [98], extension of bridging noncollagenous proteins with sacrificial bonds during collagen fibril separation [62], and mineralized collagen fibril-matrix shear [63]. Several of these behaviors are expected to be pressure dependent, i.e. consistent with macroscopic yield. These mechanisms were all observed primarily in tensile modes of deformation. No distinct microcracking was observed in the direct imaging of the compressive deformation (Figure 3-1), but it should be noted that very small loads and lengths scale are being probed and hence, our results do not preclude this mechanism from taking place at larger deformations. No distinct jumps or discontinuities were observed in the individual force versus depth curves as well (data not shown) suggesting the absence of underlying microcracking [99] and a uniform continuum response. The mineralized collagen fibril - matrix shear mechanism in tension could in fact activate the mechanism proposed here, mineralite interparticle friction, as well as rupture of sacrificial bonds in the organic [62]. The results presented here suggest, however, that the

former is more dominant for this particular compressive experimental geometry studied and is an important factor in the pressure-dependent yield strength of bone.

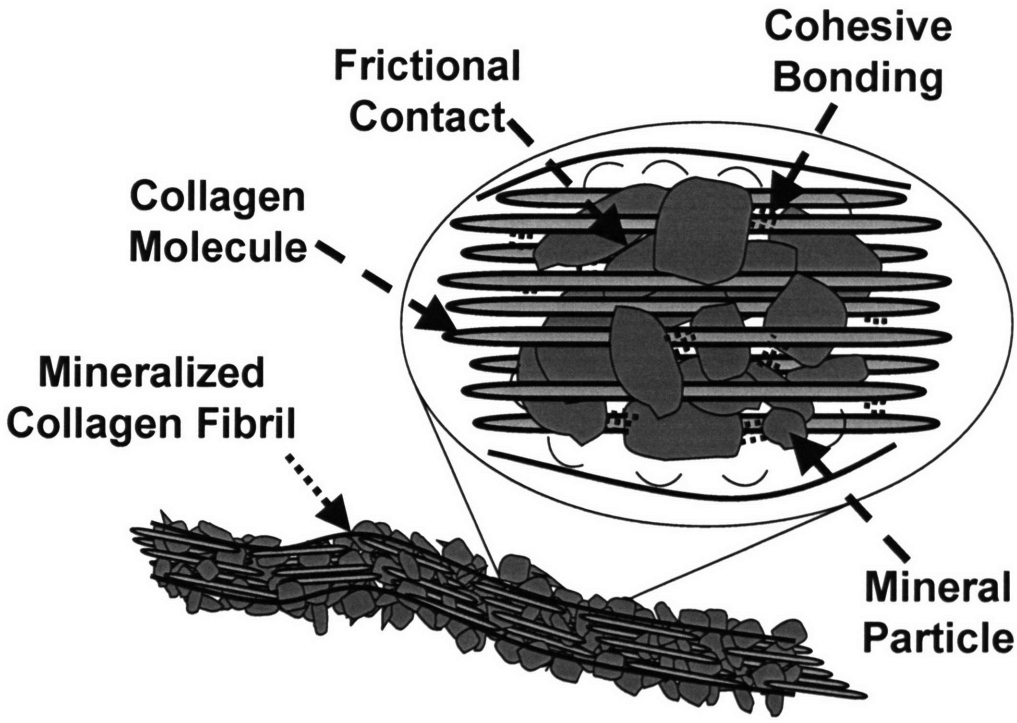

Figure 3-7. Visualized schematic description of mineral particles contacted with each other within and around a collagen fibril.

Chapter 4

Nanoscale Heterogeneity Promotes Energy Dissipation in Bone as Demonstrated Through Spatial Force Mapping Indentation Using Atomic Force Microscopy

Most of this chapter is in revision for publication.

4.1 Introduction

Bone, like many natural materials, is inherently structurally, and hence mechanically, heterogeneous due to spatial distributions in the shape, size, and composition of its constituent building blocks. Heterogeneity also arises from a multitude of different types of biomacromolecules, pores containing fluids of variable viscosities, and numerous interfaces (e.g. solid-solid, solid-fluid, damage-based) [12, 100]. As a consequence of the hierarchical nature of bone [9], mechanical heterogeneity is expected to exist at multiple length scales. Macroscopically, significant variations in mechanical properties have been observed for different anatomical locations [101], as well as regions within a particular anatomical location [102], and are thought to develop in response to distinct loading requirements [103]. At the microscopic level, nanoindentation has further identified differences in moduli and hardness for specific features such as trabeculae, interstitial lamellae, and thick and thin lamellae in osteons, which have been attributed to collagen fibril orientation and anisotropy, as well as variations in mineral content [24, 104]. Heterogeneity at this length scale is also expected to arise from the continual cellular remodelling processes resulting in a composite of "old" and "young" bone at any

given time. For example, osteonal bone typically undergoes substantial remodelling whereas older interstitial bone [105] has a higher degree of mineralization [50], leading to increased stiffness [104]. These studies have ignited speculation on the role of heterogeneity in strain concentration, fracture risk, adaptation, and damage accumulation [104, 106-110]. They also raise important issues as to whether heterogeneity is advantageous or disadvantageous to the mechanical function of bone [100]. Furthermore, detailed and quantitative studies of the *nanoscale* mechanical heterogeneity and its consequences on the structural integrity and proper function of the tissue are largely unknown.

This chapter shows how mechanical heterogeneity at nanometer length scales was quantified for the first time. Here, the mechanical response arises from an individual mineralized collagen fibril within the bone extracellular matrix, which is composed of plate-like carbonated apatite mineralites (~ tens of nm in length and width, and 3-5 nm in thickness [12]) that permeate in and around type I collagen in an overlapping manner [62], as well as a small concentration of ~200 different types of noncollageneous proteins (<10 wt.% of total protein) [12]. It has become increasingly evident that the unique nanoscale properties of bone play a key role in its macroscopic biomechanical function [61-63, 111], as this is where inelastic (including plastic) deformation and fracture must first initiate. Furthermore, since osteocytic processes have dimensions that are of the nanometer length scale [112], nanoscale heterogeneities in material properties of the surrounding extracellular matrix would be expected to modulate local stresses, thereby potentially influencing processes such as remodeling, migration, and adhesion.

4.2 Materials and Methods

4.2.1 Sample Preparation and Characterization

Adult compact bovine bone from between the tibial metaphysis and diaphysis was cut down to 1.5 mm thick specimens and polishing to a 0.05 μm finish as previously described [8]. Samples were rinsed copiously with DI water followed by ultrasonicatation in DI water between polishing intervals. Samples were then immediately stored in 20°C PBS. Sample preparation did not involve chemical treatment, dehydration, or embedding. The mineral content measured by back-scattered electron microscopy was found to be ~58 weight (wt.) %. Tapping mode (TM)AFM imaging in ambient temperature and humidity was employed using a Three-Dimensional Molecular Force Probe (MFP-3D, *Asylum Research, Inc.*, Santa Barbara, CA) on hydrated samples of osteonal bone using a silicon etched OMCL-AC160TS (*Olympus*, Tokyo, Japan) rectangular cantilever with a tetrahedral probe tip (cantilever spring constant, k ~ 56.2 N/m, probe tip end-radius ~ 15 nm, Fig. 1) at a z-piezo displacement rate of 1 μm/s in ambient conditions. The tip radius was measured by TMAFM imaging of a gold nanoparticle calibration standard [113].

4.2.2 AFM Probe Nanoindentation

In order to quantify nanoscale mechanical heterogeneity, nanoindentation using a spatially controlled atomic force microscope (AFM)-based instrument was carried out with a sharp tetrahedral probe tip (end-radius ~ 15 nm) in ambient conditions using the MFP-3D and the same probe tip as that used for TMAFM imaging. This instrument has a fully three-dimensional closed loop piezoelectric displacement system that ensures

positional accuracies in three-dimensions of < 1 nm. The inverse optical lever sensitivity and cantilever spring constant calibrations were carried out as previously reported [114]. Displacement-controlled nanoindentation was performed by loading at a rate of 1 μm/s up to a trigger force of 5 μN followed by unloading at the same rate. The loading/ unloading rate was varied from 0.05 - 10 μm/second and no statistically significant differences in calculated moduli were observed at loading rates between 0.5 - 5 μm/second, indicating that viscoelastic effects were minimized. The tip contact area function was calibrated using a sample of glycol methacrylate using a 6 GPa modulus from previous indentation data taken on a Hysitron Triboindentor. Values for elastic moduli were calculated from 95% - 20% of the initial unloading curve by fitting these data to contact mechanical theory for an isotropic, elastic half-space [2] for each individual curve. Due to the assumptions of this model [115] (e.g. isotropy), the modulus is more appropriately defined as "apparent" in that it reflects relative mechanical stiffness and does not produce absolute quantitative values. However, the relative spatial differences in stiffness can be compared.

Grids of indentations [116] over a 2 μm × 2 μm area were performed on adult bovine tibial cortical bone both perpendicular and parallel to the long bone axis, where the separation distance between each indent was 100 nm. Experimental histogram distributions of the modulus taken at a much larger interindent spacing of 1 μm showed statistically similar modulus distributions ($p<0.05$). Cyclic indentations carried out at the same position showed that the moduli values obtained were reproducible within ± 1 GPa. The maximum indentation depth was ~ 30 nm at a 5 μN maximum load corresponding to an elastic contact radius of ~ 60 nm (estimated by FEA). Since type I collagen fibrils in

bone have a typical diameter of ~ 150 nm[8], deformation induced by the indent was on the length scale of an individual fibril. Two-dimensional contour maps of local stiffness were constructed which enabled the direct visualization of nanomechanical spatial heterogeneity. These maps were compared with high resolution tapping mode AFM images of the bone ultrastructure taken of the same area prior to indentation.

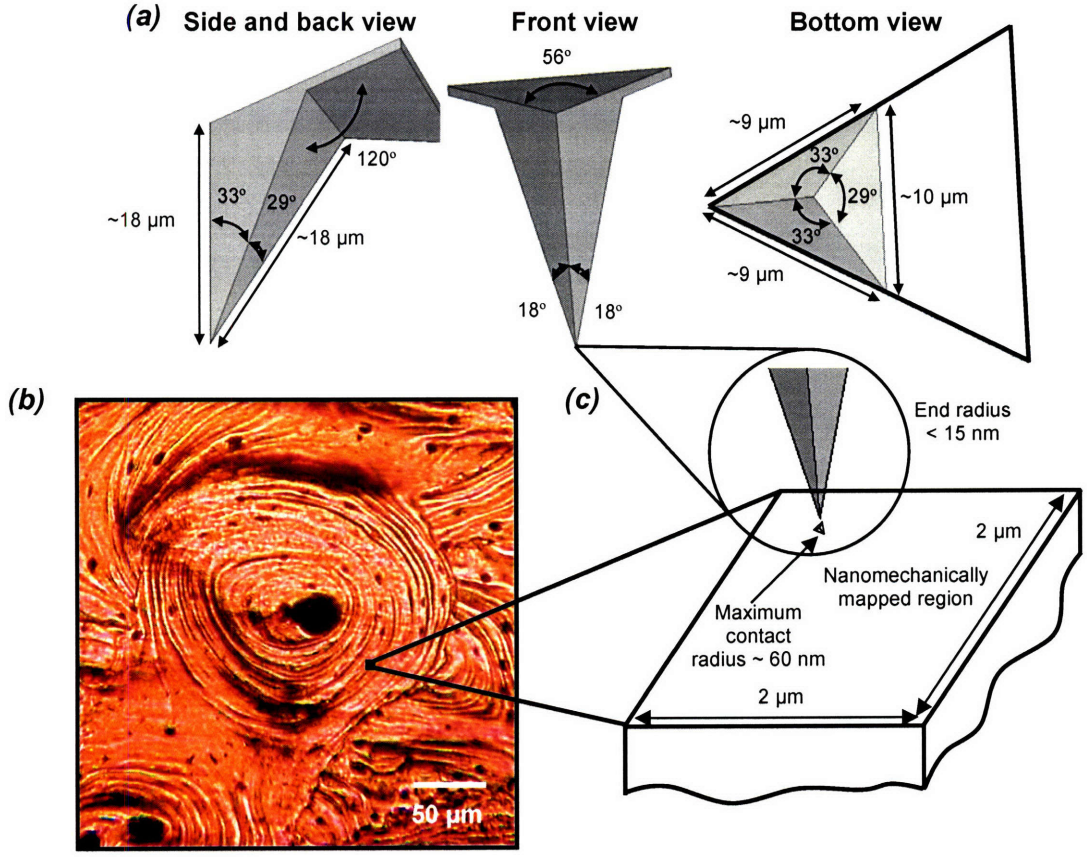

Figure 4-1. Schematic of experiment used to quantify nanomechanical heterogeneity in bone. *(a)* Three-dimensional schematics illustrating probe tip geometry and dimensions from side and back view (left), front view (middle) and bottom view (right) as determined by scanning electron microscopy. *(b)* Optical microscopy image of an individual osteon in adult bovine cortical bone showing Haversian canal, circumferential lamellae, and the lacuno-canalicular porosity. *(c)* Schematic of 2 µm × 2 µm region probed nanomechanically drawn to scale relative to osteon size; the size of the indented region is also drawn to scale.

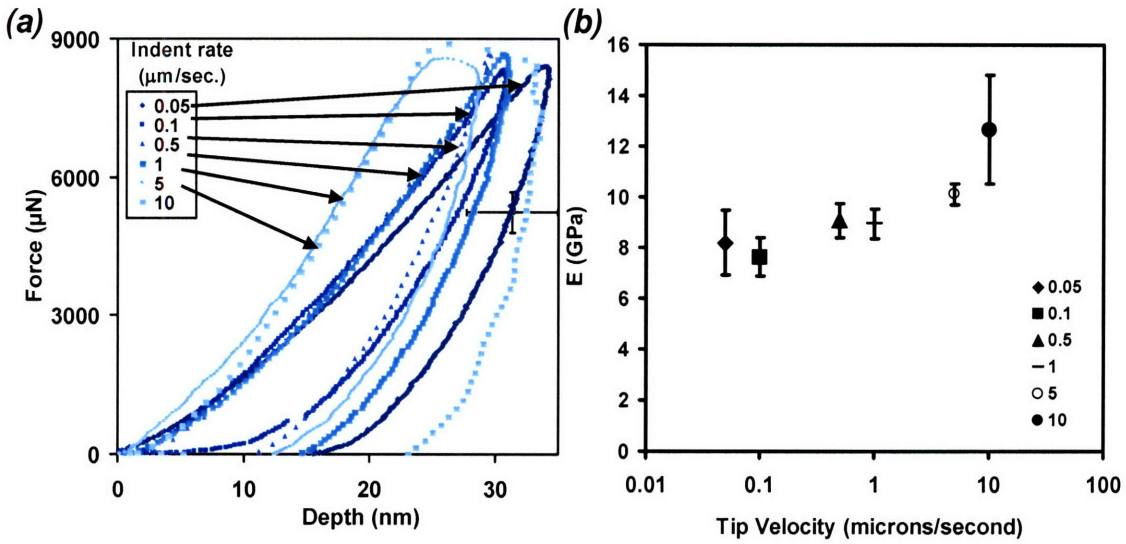

Figure 4-2. *(a)* Average indent curves of on undemineralized bone with varying rates from 0.05 – 10 μm/second. *(b)* Calculated modulus as a function of tip velocity

4.2.3 Wavelet Decomposition Analysis

Wavelet Transform (WT) allows localization of both space and frequency, achieved by dilating and translating a finite wavelet function to capture different frequency ranges and their spatial locations [117]. The discrete wavelet transform (DWT) represents a 1D sampled data with a limited number of decomposition levels (frequency scales). A set of low- and high-pass filters is used for decomposing the data into a coarse *approximation* and a residual *detail*. Wavelets also allow particular frequency sub bands to be isolated within an image, which are treated as 2D signals [1]. The diagram below (Figure 4-3) depicts a one-level decomposition of a 2D image. Filters are applied in the *x*-direction and the results are down-sampled by deleting every other column. This yields two images of approximately half the size of the original, one containing high-frequency components of the rows and the other containing low-frequency components. These two images are then each filtered down the columns using the corresponding filters and

down-sampling the results along the rows. This results in the smoothed approximation, the horizontal detail, the vertical detail, and the diagonal detail sub images. The process is repeated on the smoothed approximation sub image to obtain the next level of decomposition.

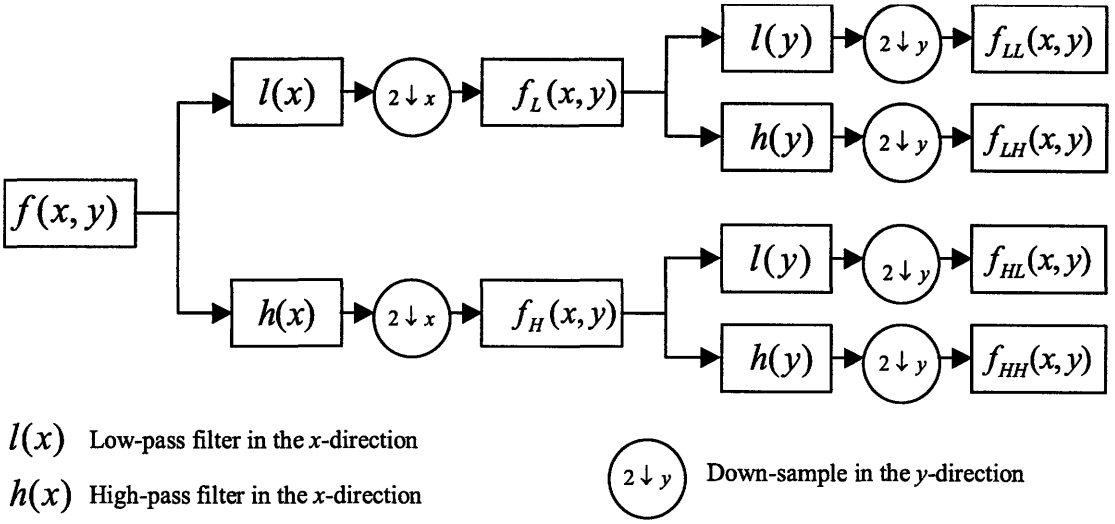

Figure 4-3. Wavelet decomposition of a 2D image [1]. F_{LL}, f_{LH}, f_{HL}, and f_{HH} represent the smoothed approximation, the horizontal detail, the vertical detail and the diagonal detail, respectively.

4.2.4 Finite Element Analysis

Two different virtual mechanical tests were built using the software package ABAQUS. One is a two-dimensional plane-strain 4-point bend model (40μm wide and 5μm high) (Figure 4-4) and the other is a two-dimensional plane-stress indentation test with a 90° included angle and a rounded off tip radius of 140 nm (Figure 4-5). The bending and indent tests are to illustrate typical load schemes that are predominantly tensile and compressive, respectively. The modulus maps were incorporated within the FEA model for both specimens with indents perpendicular and parallel to the long bone axis by assigning a specific material section to whichever elements spatially coincided

with each particular material region. An elastic limit strain-based von Mises plasticity constitutive law was used to model the energy dissipating inelastic deformation and to obtain a local yield stress value as described in the main manuscript text, The elements in the area immediately to the right and left of the 2 μm × 2 μm heterogeneous region were assigned the experimentally measured average homogeneous value of modulus and corresponding yield stress (based on the criterion discussed previously). The elements in the bottom portion were assigned only the purely elastic average homogeneous modulus value. The bending simulation was displacement controlled with the bottom two boundary conditions (spaced 20 μm apart) displaced 2.5 μm while the two fixed regions are at the end. 4-node bilinear plane strain quadrilateral elements (CPE4) were used in this study and the mesh was highly refined in the heterogeneous mapped region. There were 9424 elements in the 600 nm notched specimen; 3116 of those elements were within the heterogeneous region. The number of yielded elements was tracked through the equivalent inelastic strain and the reaction force in the vertical direction was measured at the fixed points. Energy dissipation was calculated by integrating the area between the loading and unloading force-displacement curves up to 2.5 μm displacement. The indent simulation was also displacement controlled, using 4-node bilinear plane stress quadrilateral elements (CPS4) with a highly refined heterogeneous region. The entire sample is 10 μm wide and 10 μm deep. There were 5200 elements in total and the indenter penetrated to ~900 μN maximum force. Energy dissipation was calculated by integrating the hysteresis area under the force-displacement curve. The number of yielded elements was tracked through the equivalent inelastic strain.

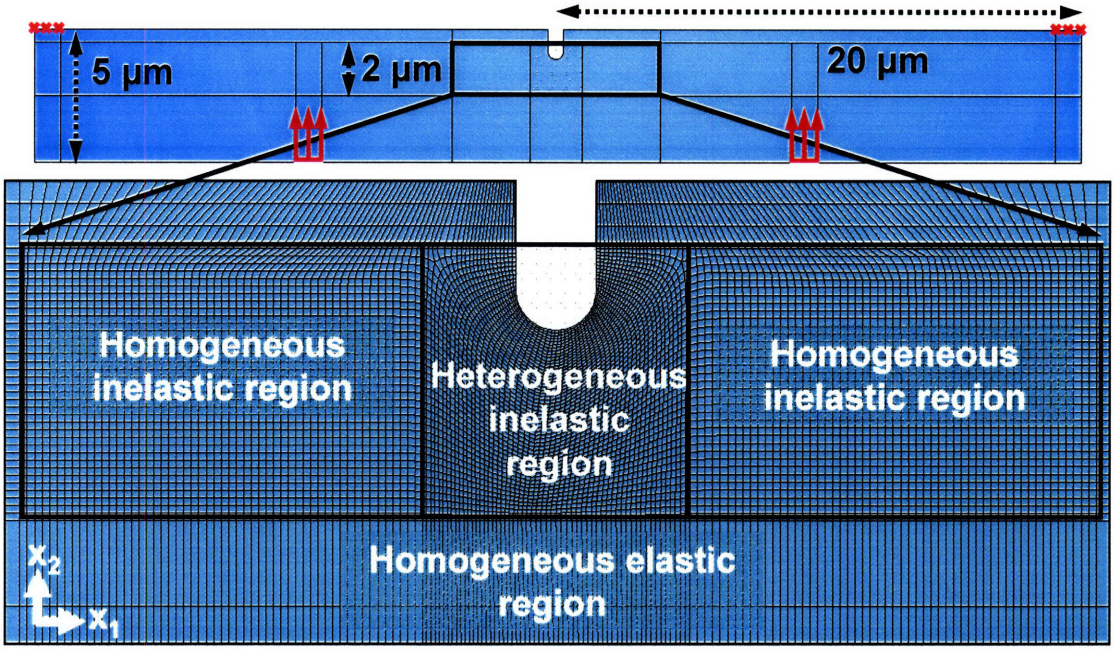

Figure 4-4. Two-dimensional notched four-point bend FEA model geometry showing dimensions and mesh. Modulus maps for adult bovine cortical bone were superimposed in a 2 µm × 2 µm heterogeneous region ahead of the notch.

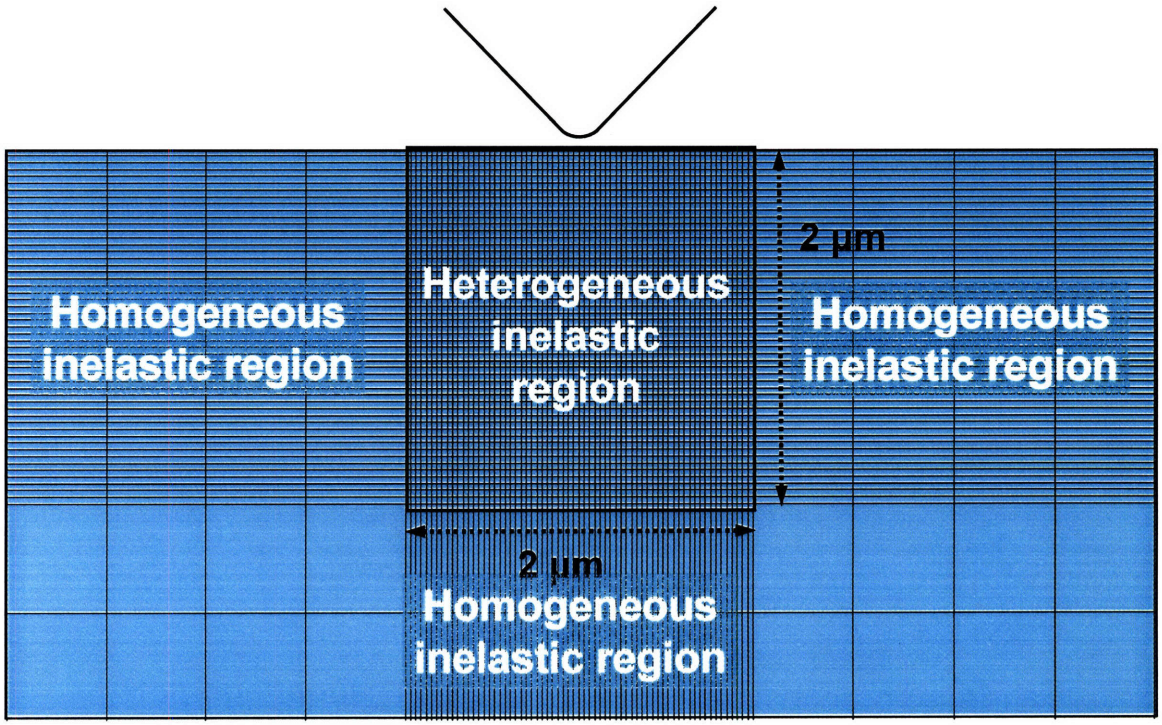

Figure 4-5. Two-dimensional compressive indent FEA model showing dimensions and mesh. Modulus maps for adult bovine cortical bone were superimposed in a 2 µm × 2 µm heterogeneous region ahead of the notch.

4.3 Results

4.3.1 Nanomechanical Property Contour Maps

The ultrastructure of osteonal bone viewed perpendicular to the long bone axis showed a nanogranular morphology of a dense array of mineralites (Figure 4-6(a)) with an average maximum lateral dimension ~ 56.0 ± 36.2 nm and a peak-to-valley height < 10 nm (measured from corresponding height images). Distinct type I collagen fibrils and their characteristic 67 nm periodicity were not observed due to the dense array of mineralites present. However, as reported previously [8], AFM imaging after partial demineralization, using a one second etch in ethylenediaminetetraacetic acid, reveals a packed surface of type I collagen fibrils with varying degrees of orientation within the sample plane, the correct 67 nm banding, and a mean diameter of ~ 151 ± 17 nm. The stiffness map (Figure 4-6(b)) corresponding to the area imaged in Figure 4-6(a) exhibits a distribution with values ranging from 26 GPa (appearing black) to 2 GPa (appearing white) with an averaged apparent modulus value of 8.55 ± 3.7 GPa and coefficient of variation (ratio of the standard deviation to the mean) of 0.43. A curved region of lower stiffness appears diagonally across the mapped region (length ~ 1.8 μm) while higher stiffness regions appear horizontally across the top of the mapped region. Smaller localized variations and gradients occur throughout the map as well. Multiple mapping experiments were carried out on different samples. While the fine details of the stiffness fluctuations of each map varied, the stiffness distribution and coefficient of variation were highly reproducible. Assuming a helicoidal collagen fibril arrangement [118] and transversely isotropic properties of individual collagen fibrils [119], variations in collagen fibril orientation are not expected to play a major role in the observed

heterogeneity since the loading axis is perpendicular to the collagen fibril axis. Other possible sources of observed heterogeneity include nano- to microscale organic–inorganic compositional variations, underlying porosity, and/or damage (e.g. cracking). Compositional fluctuations are known to exist down to ~ 1 μm, as revealed by microRaman spectroscopy [120]. Porosity at the length scales probed here include canalicular channels (diameters ranging from 80 to 710 nm) [112] and hypothesized collagen-apatite porosity associated with space between collagen fibrils and apatite mineralites (~ 20 nm) [88].

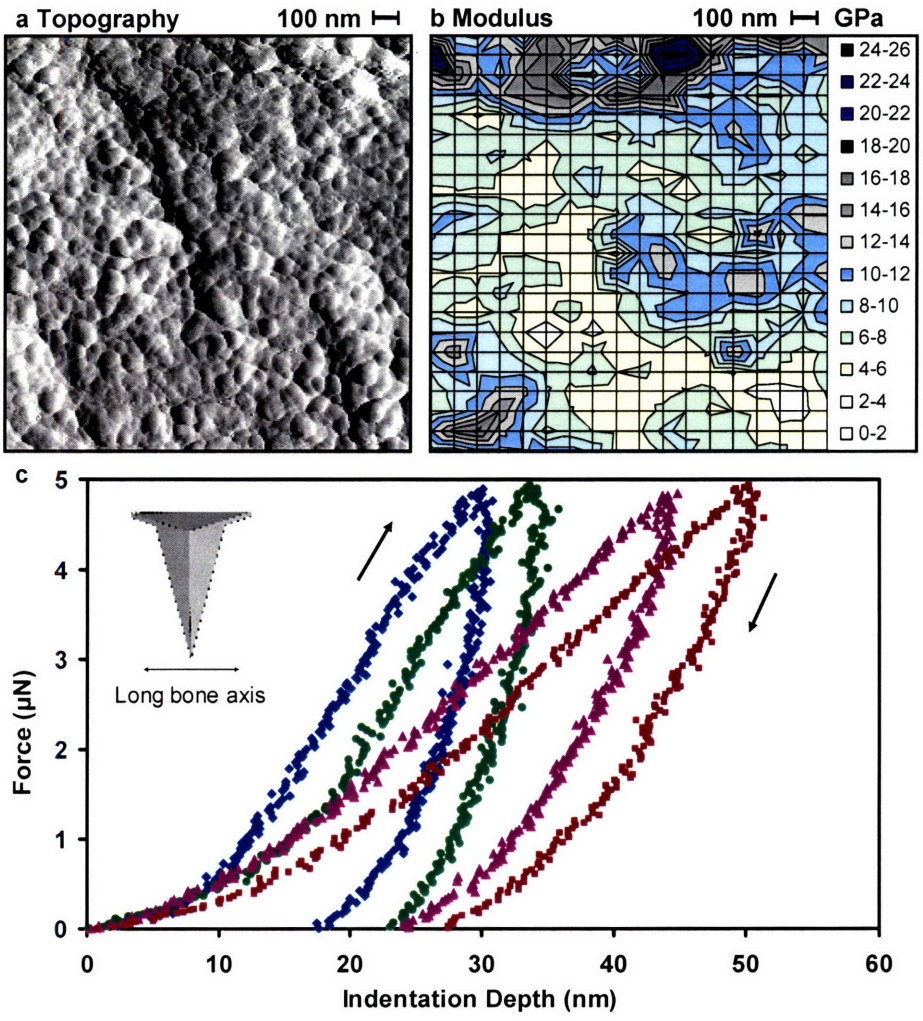

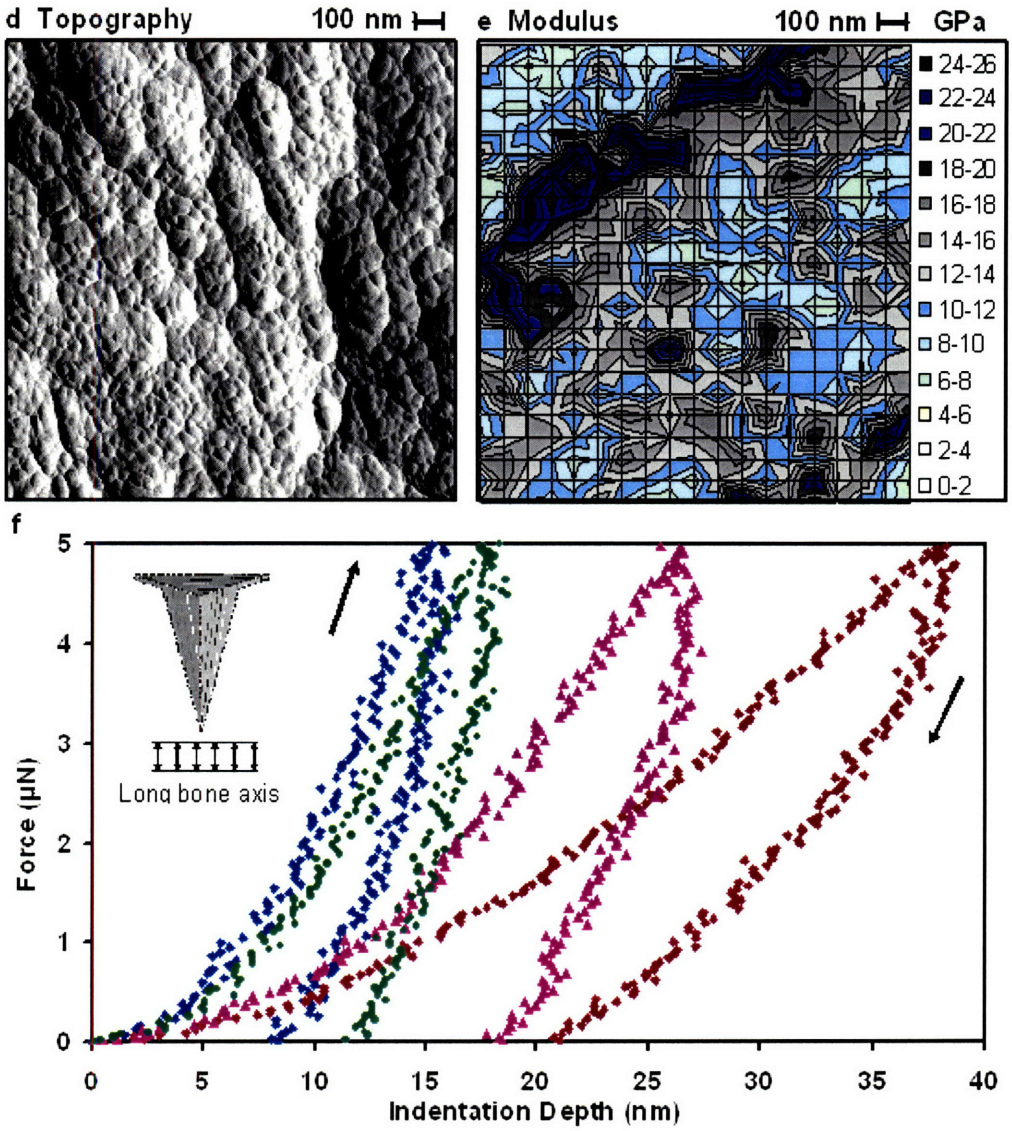

Figure 4-6 The ultrastructure and nanomechanical spatial heterogeneity of of bone stiffness. **a,** Tapping mode atomic force microscope (TMAFM) amplitude image perpendicular to the long bone axis. **b,** Two-dimensional contour map of modulus reduced from nanoindentation data [2] for the area shown in **a**. **c,** Individual nanoindentation curves at different locations within modulus map **b**; moduli (GPa) ♦ 12.5, ● 10.5, ▲ 5.4, ■ 4.2. **d,** TMAFM amplitude image parallel to the long bone axis. **e,** Two-dimensional contour map of modulus for the area shown in **d**. **f,** Individual nanoindentation curves at different locations within modulus map **e**; moduli (GPa) ♦ 24.2, ● 18.1, ▲ 15.8, ■ 5.7.

Apparent modulus data taken with the loading axis parallel to the long bone axis show less heterogeneity (coefficient of variation of 0.37) and increased mean stiffness

(~12.9 ± 4.8 GPa) (Figures. 4-6(d-f)) compared to the perpendicular orientation (by factor of ~ 1.5). This trend is consistent with macroscopic tissue level data [102] and collagen fibril anisotropy (increased stiffness along fibril axis compared to transverse directions) [119]. A large curved region is observed with increased stiffness (thickness ~ 250 nm) in the upper left hand side of the map, as well as the lower right hand side (distance between high stiffness regions ~1.5 μm). Figure 4-7 provides 3-D visualization of the nanoscale stiffness data with the vertical direction corresponding to the stiffness magnitude comparing the parallel and perpendicular orientation directions. While the coefficient of variation for the contour map perpendicular to the long bone axis is greater, the differences in peak-to-valley modulus values are more apparent for the map from indents taken parallel to the long bone axis in the 3-D visualizations. Assuming the spiral model for collagen fibril orientation [121], this occurrence may arise from off-axis loading of collagen fibrils, as opposed to in-plane loading in the perpendicular orientation. If the heterogeneity observed was solely due to collagen fibril orientation, a more-or-less continuous stiffness gradient would be observed, which does not appear to be the case here. Thick and thin lamellae have been measured to be approximately ~ 5-7 and 1 μm in width, respectively [122], with the thin lamellae being ~ 10% softer than the thick ones [104]. No distinct patterns were observed that could be conclusively associated with such features. Hence, the fluctuations observed must be partially originating from smaller length scale features.

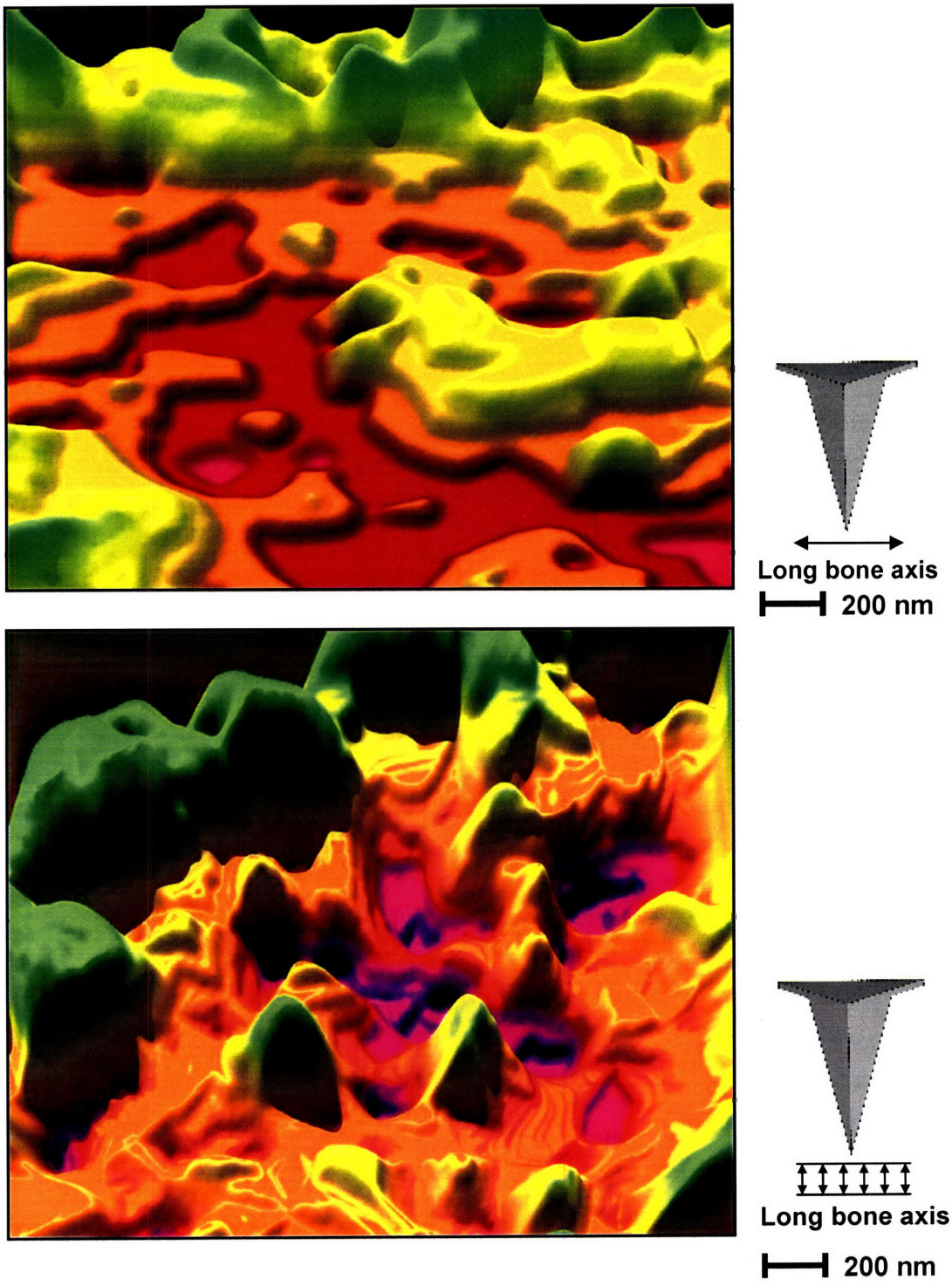

Figure 4-7 Three-dimensional graphic illustrations of modulus maps shown in Figure 2-6(b) (top) where loading was carried out perpendicular to the long bone axis and Figure 2-6(e) (bottom) where loading carried out parallel to the long bone axis. The vertical axis corresponds to stiffness where the highest vertical topography corresponds to the maximum value and lowest topography corresponds to minimum value.

The mechanical heterogeneity described above for the AFM-based nanoindentation experiments is much more pronounced compared to depth-sensing microindentation performed on the same specimens. The coefficients of variation for micro-scale indentations (Berkovich geometry at 500 μN maximum load, interindent spacing of 5 μm) both perpendicular and parallel to the long bone axis were 0.25 and 0.26, respectively. This is approximately a factor of two less than the nanoscale data presented here suggesting a scale-dependent homogenization effect. Other studies have reported microscale coefficients of variation values of 0.12 (bone perpendicular to the long axis)[7] and 0.15 (bone parallel to the long axis) [104].

4.3.2 Discrete Wavelet Transform Analysis

The modulus maps were analyzed quantitatively using the discrete wavelet transform [123] where decomposition of spatial frequencies creates a coarser approximation of the image. Details can be associated with a "pseudofrequency" that identifies the length scales of the patterns removed at spatially specific regions. Figures 4-8(a) and 4-8(b) depict the first level approximations of the original images corresponding to indents perpendicular and parallel to the long bone axis, respectively. The diagonal details for those corresponding maps were removed to obtain the coarser image (Figures 2-8(c) and 2-8(d)). The detail images show primarily the random features that prevail at the high spatial frequencies. However, they also capture specific patterns associated with the high modulus areas. One can observe high modulus peaks that coincide with the larger high modulus domains (more apparent with the image parallel to the bone axis, Figure 2-8(d). The first level of decomposition thus appears to remove the

local high modulus peaks leaving broader regions of stiffness. The characteristic length scale given by the pseudo(spatial)frequency analysis, identified as ~ 156 ± 28 nm, corresponds almost exactly to the experimentally measured mean diameter of an individual collagen fibril [8].

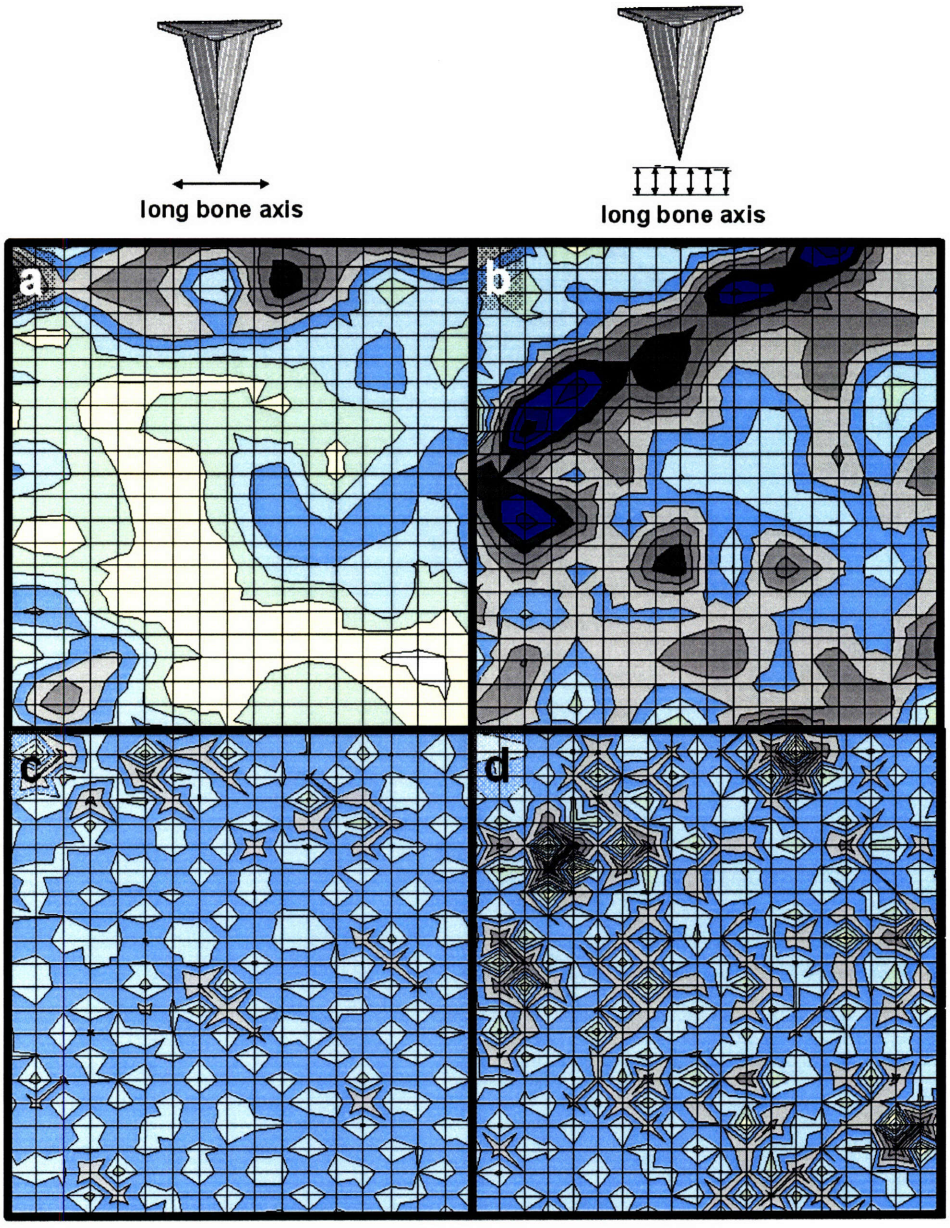

Figure 4-8. Quantitative analysis of nanomechanical property maps using discrete wavelet transform. a, Level 1 approximation for modulus map given in Figure 4-6(b) (loading axis perpendicular to the long bone axis). b, Level 1 approximation for modulus map given in Figure 4-6(e) (loading axis parallel to the long bone axis). c, diagonal details corresponding to a. d, diagonal details corresponding to b.

4.3.3 Finite Element Analysis: Tensile Predominance Via 4-Point Bend

In order to better understand how nanoscale mechanical heterogeneity influences larger length scale biomechanical properties, finite element simulations were performed using the experimentally determined fine-scale heterogeneity and local mechanical property variations extracted from AFM-based indentation experiments. The experimentally measured heterogeneous nanoscale stiffness maps were directly incorporated into a highly refined region of finite elements just ahead of a notched 4-point bend mesh (Figure 4-4), so as to capture the localization of strain in a region with nanoscale structural nonuniformity. Inelasticity was also incorporated into the 4-point bend mesh as follows. Inelastic deformation was first assessed during individual indentation experiments by constructing an axisymmetric 2D FEA simulation with an equivalent tip apex angle of 23.5°, i.e. the same indentation volume versus depth as for the AFM probe tip, that assumed a perfect Mises plasticity constitutive law, as well as a modulus evaluated from the unloading slope [2]. For each force vs. depth indentation curve, various trial yield stress (σ_Y) values were chosen to determine the optimal value at which the simulated data that fit the experimental curve. This best-fit value was then used to calculate the corresponding equivalent (elastic) limit strain at the yield point as given by; $\bar{\varepsilon}_Y = \frac{2(1+\nu)\sigma_Y}{3E}$. The $\bar{\varepsilon}_Y$ values were found to be ~ 0.04 ± 0.02 for specimens tested parallel to the long bone axis and ~ 0.044 ± 0.02 for specimens tested perpendicular to the long bone axis. These observations suggest that a constant elastic limit strain criterion is a reasonable first order approximation. Therefore, taking the above average value of

$\bar{\varepsilon}_Y$, the local yield stress value, σ_Y, can be obtained conversely using; $\sigma_Y = \frac{3E\bar{\varepsilon}_Y}{2(1+\nu)}$. The energy dissipative inelastic deformation is incorporated here since a finite residual depth is observed after unloading of the indentation curves (Figures 4-6(c) and 4-6(f)).

Figure 4-9 shows the progression of equivalent strain (defined as the time integral of $\sqrt{2/3}$ multiplied by the magnitude of the inelastic strain rate) during two virtual 4-point bend FEA simulations (displacement-controlled). The first (right column) incorporated the heterogeneously mapped data from Figure 4-6(b) (loading axis perpendicular to the long bone axis). The second (left column) was a control which was an elastic-perfectly plastic simulation with purely homogeneous mechanical properties (set to the volume averaged mean value of modulus measured experimentally in Figure 4-6(b) and the volume averaged mean value of yield stress obtained from the strain-based yield criterion). The measured inelastic strain in the vicinity of the notch is continuously greater for the heterogeneous case than the homogeneous from 1.5 - 2.5 μm displacement. The inelastic strain develops irregularly ahead of the notch and extends ~ 2 times further for the heterogeneous material compared to the homogeneous one at 2.5 μm displacement. Nonuniform notch opening and blunting took place in the heterogeneous case, as compared to a more uniform shape change for the homogeneous.

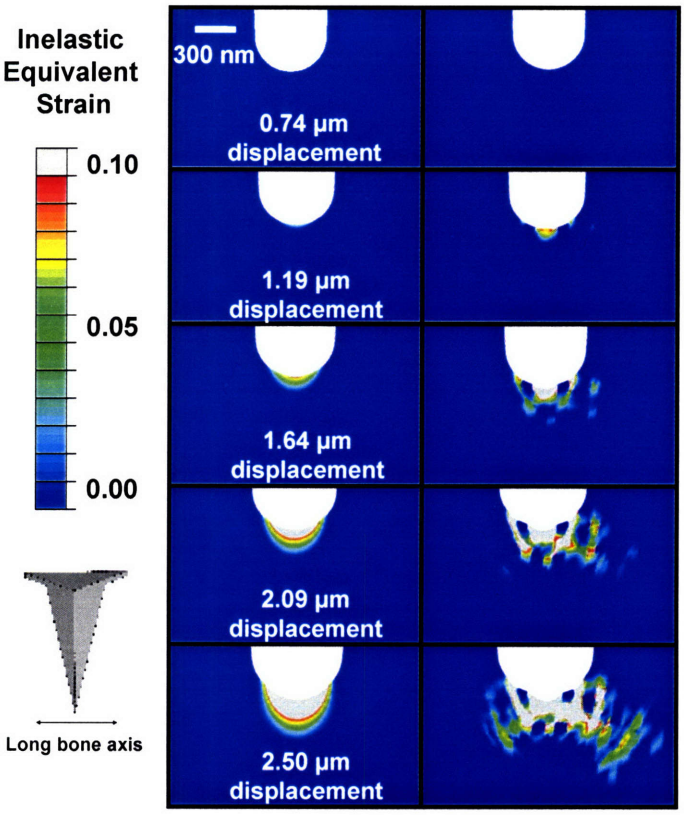

Figure 4-9. Snapshots of equivalent inelastic strain for the 4-point bend FEA virtual simulations comparing homogeneous to heterogeneous case for loading up to 2.5 µm. This particular dataset employed heterogeneous data with the loading axis perpendicular to the long bone axis (Figure 4-6(b)).

Figure 4-10 shows the equivalent plastic strain for the 4-pont bend FEA simulations at 2.5 µm displacement for the same nanoindentation data (Figure 4-6(b)) where the heterogeneous map ahead of the notch is rotated by 0°, 90°, 180°, and 270° in the plane defined by the long bone axis (in the plane of the paper). Figure 4-11 shows the same data except instead of being rotated, the modulus maps were shifted up and down 300 nm. While the fine details of the inelasticity pathways are different for different rotations, all simulations show heterogeneous diffuse deformation over a greater area compared to the homogeneous material. There is a less than 10% variation in plastic

strain in the entire deformed area for a complete rotation over 360° as well as the 300 nm displacement shift.

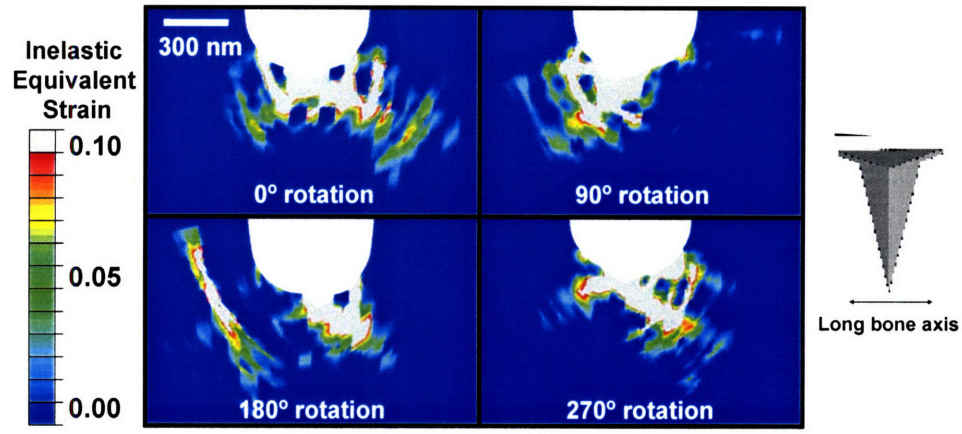

Figure 4-10. Equivalent inelastic strain for the 4-pont bend FEA virtual simulations which incorporated the heterogeneous nanoindentation data taken with the loading axis perpendicular to the long bone axis (Figure 4-6(b)) where the 2 μm x 2 μm mechanical property map is rotated in the plane of the long bone axis (the plane of the paper) by 0°, 90°, 180°, and 270°. There does not appear to be any difference in the overall inelastically strained area even though the distribution varies.

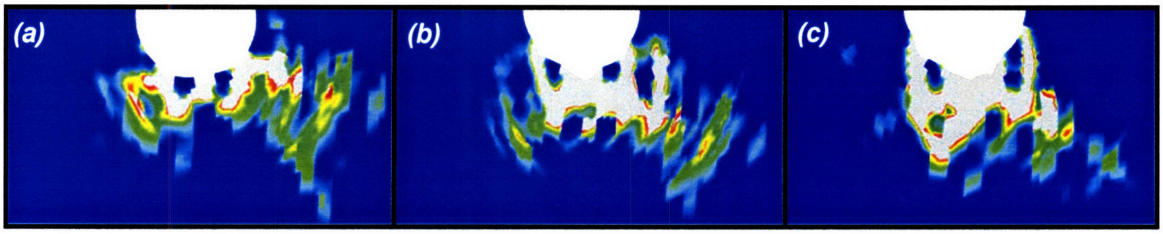

Figure 4-11. Equivalent inelastic strain for the 4-pont bend FEA virtual simulations which incorporated the heterogeneous nanoindentation data taken with the loading axis perpendicular to the long bone axis (Figure 4-6(b)) where the 2 μm x 2 μm mechanical property map is *(a)* shifted 300 nm down, *(b)* not shifted at all, and *(c)* shifted up 300 nm in the plane of the long bone axis (the plane of the paper). There does not appear to be any difference in the overall inelastically strained area even though the distribution varies.

The effect of varying the size of the notch was also explored. Figure 4-12 shows the results of incorporating notch sizes of 300 nm, 600 nm, and 1200 nm. Figure 4-13 gives the quantified inelastically strained area for these different cases. Even though in general, with greater notch size, there appears to be a greater inelastic area, the inelastic

area for the heterogeneous case is greater than for the homogeneous case no matter what the notch size is.

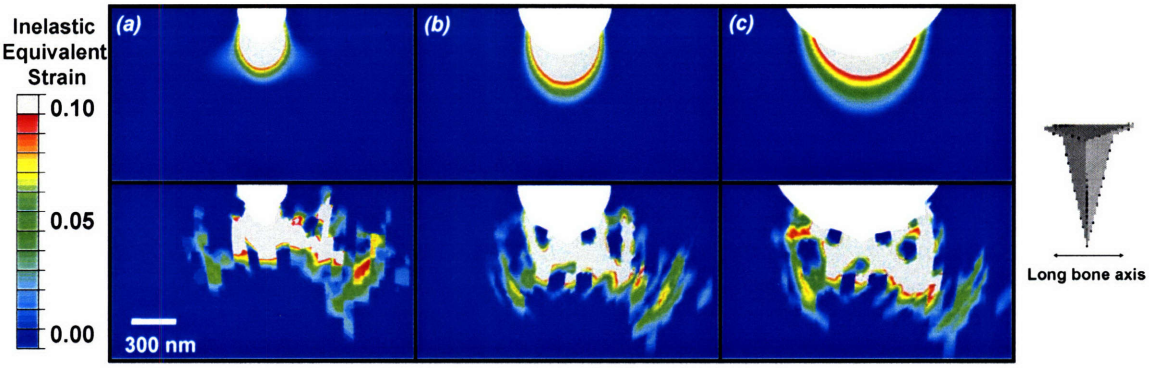

Figure 4-12. Equivalent inelastic strain for the 4-pont bend FEA virtual simulations which incorporated the heterogeneous nanoindentation data taken with the loading axis perpendicular to the long bone axis (Figure 4-6(b)) where the 2 μm x 2 μm mechanical property map is placed in close proximity to a *(a)* 300 nm notch, *(b)* a 600 nm notch (as presented thus far), and *(c)* a 1200 nm notch in the plane of the long bone axis (the plane of the paper). There appears to be greater inelastically strained area with greater notch size.

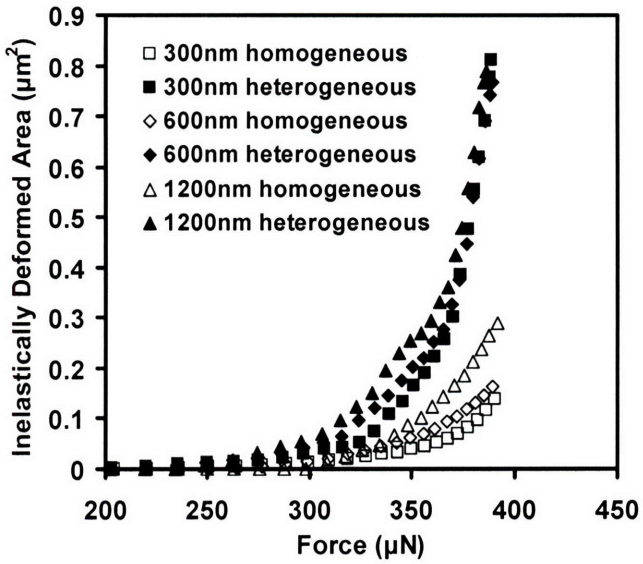

Figure 4-13. The inelastically strained area is plotted in this graph as a function of force for FEA virtual 4-point bend experiments incorporating the homogeneous and heterogeneous maps in the 2 μm x 2 μm region of interest for notch sizes of 300 nm, 600 nm, and 1200 nm.

Similar FEA simulations were carried out for mechanical property maps where indentations were performed parallel to the long bone axis. The inelastically strained area was less than that for indents taken perpendicular to the long bone axis, which is as expected because the plastic stiffness is greater in the parallel direction (Figure 4-14). In general, the overall behavior is similar to that already demonstrated for superimposed mechanical property maps that were rotated (Figure 4-15), shifted up and down 300 nm (Figure 4-16), and for different notch size specimens (Figure 4-17).

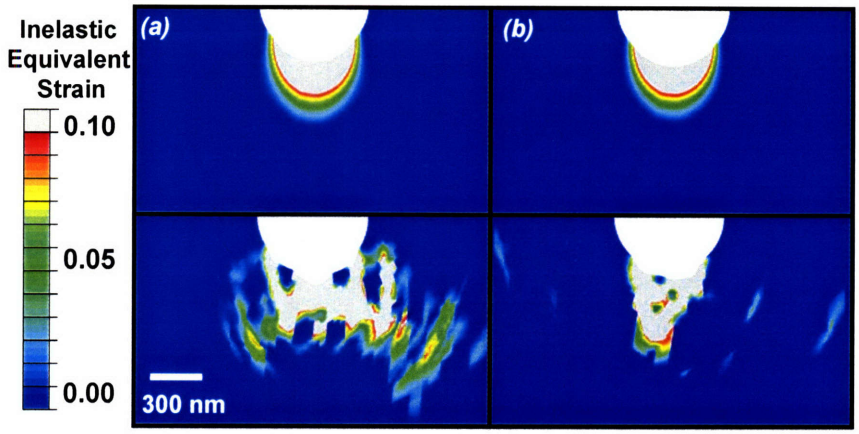

Figure 4-14. The equivalent inelastic strain is given here for 4-point bend FEA simulations where both the homogeneous and heterogeneous mechanical property maps are superimposed at the notched region for indents taken both *(a)* perpendicular and *(b)* parallel to the long bone axis. There appears to be a significantly greater inelastically strained area for the heterogeneous case where property values are recorded perpendicular to the long bone axis.

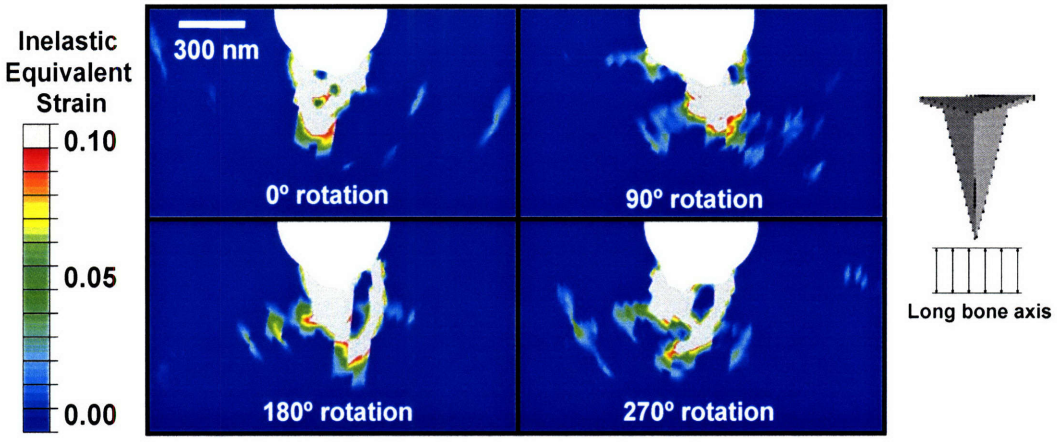

Figure 4-15. Equivalent inelastic strain for the 4-pont bend FEA virtual simulations which incorporated the heterogeneous nanoindentation data taken with the loading axis parallel to the long bone axis (Figure 4-6(e)) where the 2 μm x 2 μm mechanical property map is rotated in the plane of the long bone axis (the plane of the paper) by 0°, 90°, 180°, and 270°. There does not appear to be any difference in the overall inelastically strained area even though the distribution varies.

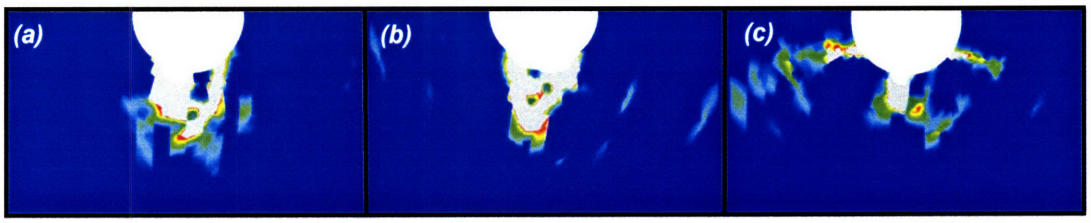

Figure 4-16. Equivalent inelastic strain for the 4-pont bend FEA virtual simulations which incorporated the heterogeneous nanoindentation data taken with the loading axis parallel to the long bone axis (Figure 4-6(b)) where the 2 μm x 2 μm mechanical property map is *(a)* shifted 300 nm down, *(b)* not shifted at all, and *(c)* shifted up 300 nm in the plane of the long bone axis (the plane of the paper). There does not appear to be any difference in the overall inelastically strained area even though the distribution varies.

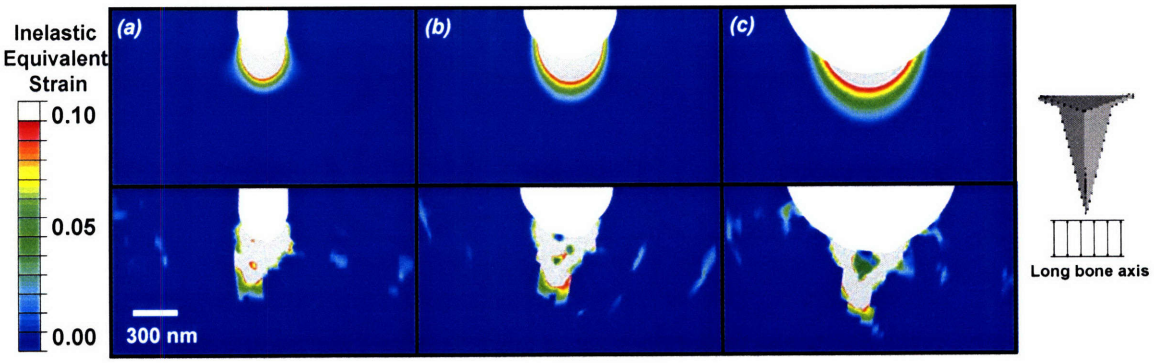

Figure 4-17. Equivalent inelastic strain for the 4-pont bend FEA virtual simulations which incorporated the heterogeneous nanoindentation data taken with the loading axis parallel to the long bone axis (Figure 4-6(b)) where the 2 μm x 2 μm mechanical property map is placed in close proximity to a *(a)* 300 nm notch, *(b)* a 600 nm notch (as presented thus far), and *(c)* a 1200 nm notch in the plane of the long bone axis (the plane of the paper). There appears to be greater inelastically strained area with greater notch size.

The deformed area as a function of applied force is given (Figure 4-18(a)) for cases both perpendicular and parallel to the long bone axis for both heterogeneous and homogeneous cases. For tests perpendicular to the long bone axis, the inelastically deformed area was ~ 3 times greater for the heterogeneous than the homogeneous case at 390 μN maximum force. For tests parallel to the osteonal axis, the inelastic deformation area was ~ 2 times greater for the heterogeneous case at 610 μN maximum force. In general, for a 2.5 μm displacement, the plastic strain region corresponded to an increased applied force for stiffer modulus values, on average. A comparison between maps taken with different loading orientations showed similar energy dissipation (Figure 4-18(b)), which was ~ 2× greater for the heterogeneous map compared to the homogeneous case. Also, as the notch diameter was increased, there was a slight increase (~10%) in the plastic strain region for heterogeneous and homogeneous cases in both orientations (data not shown).

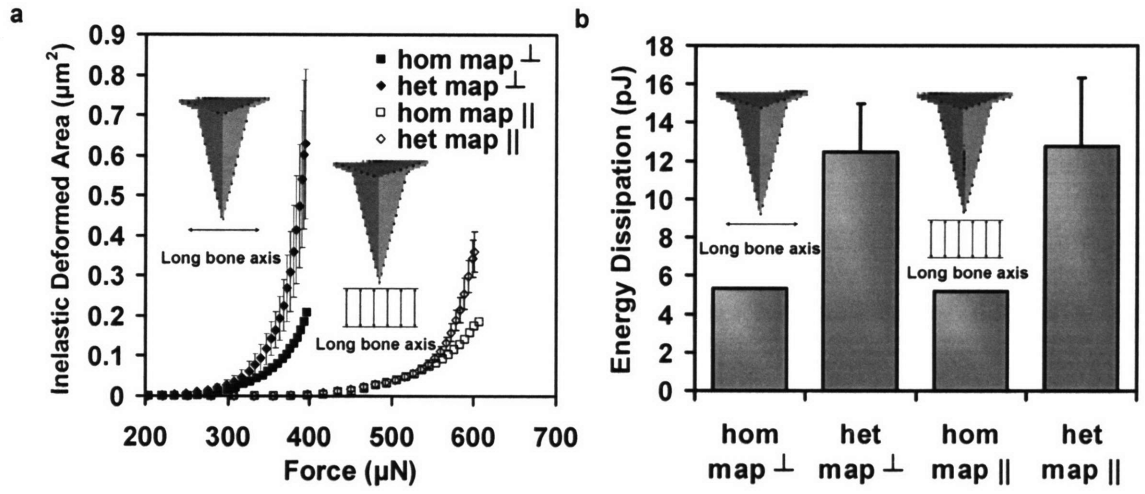

Figure 4-18. **a,** The inelastically deformed area is plotted as a function of force for each set of tests, both perpendicular and parallel to the long bone axis comparing the homogeneous and heterogeneous cases. The heterogeneous plots are averages of the rotated and shifted contour mapped regions, indicated by standard error bars. **b,** Energy dissipation bar plots for each set of simulations, both perpendicular and parallel to the long bone axis comparing the homogeneous and heterogeneous cases. The heterogeneous plots are averages of the rotated and shifted contour mapped regions, indicated by standard error bars. A unit thickness of 1 μm in the two-dimensional model is used to compute the energy dissipation.

4.3.4 Finite Element Analysis: Compressive Predominance Via Indent

A similar two-dimensional FEA nanoindentation model was also built with compression as the chief loading mechanism (Figure 4-19). Here, similar to the bending case, the modulus map was superimposed onto a fine mesh with a 90° included angle indentation geometry to demonstrate that the same trends are observed as with the 4-point bend simulations. Figure 4-20(a) shows that the simulated force versus indentation depth curves for the homogeneous stiffness map exhibit a smaller deformation for a given load compared to the heterogeneous material (Figure 4-6(b)) for loads larger than ~250 μN. The energy dissipation given by the curves were 114 pJ and 162 pJ for the homogeneous and heterogeneous cases, respectively (for 850 μN max load). The inelastically deformed

area for the heterogeneous case was markedly greater than the homogeneous (Figure 4-20(b)), consistent with the results obtained from the 4-point bending simulations. This result further suggests that even though heterogeneity at the micro- and macro-scale may have deleterious effects, leading to fracture and interfacial instabilities [124], inelastic heterogeneity at the nanoscale offers an advantageous mechanism for ductile energy dissipation.

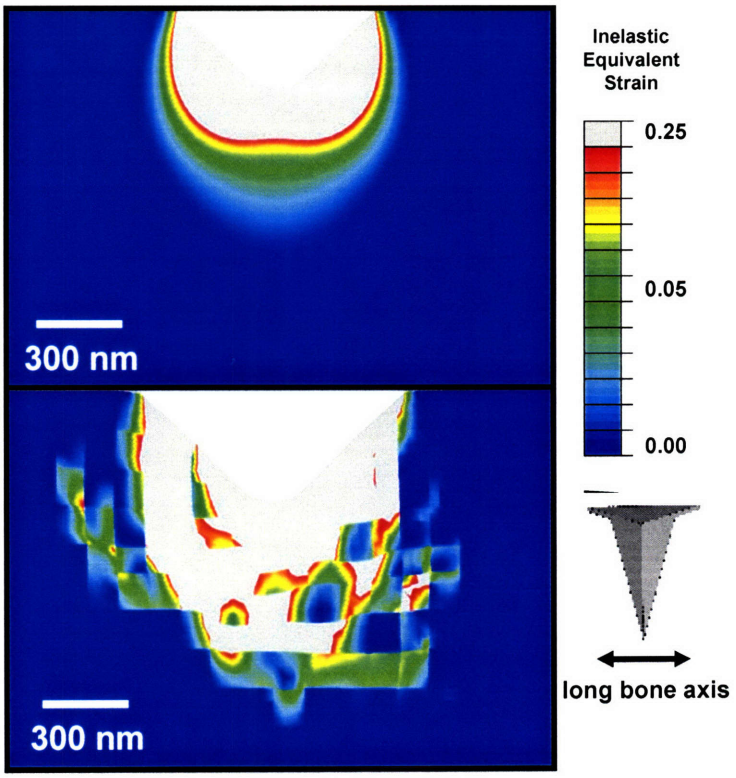

Figure 4-19. Finite element analysis (FEA) is shown of the effect of nanomechanical spatial heterogeneity on compressive loading. A Two-dimensional indentation FEA model shows snap shots of equivalent inelastic strain for an indentation virtual simulation comparing homogeneous to heterogeneous case for loading up to ~850 μN. This particular dataset employed heterogeneous data with the loading axis perpendicular to the long bone axis (Figure 4-6(b)). A unit thickness of 1 μm in the two-dimensional model is used to compute the energy dissipation.

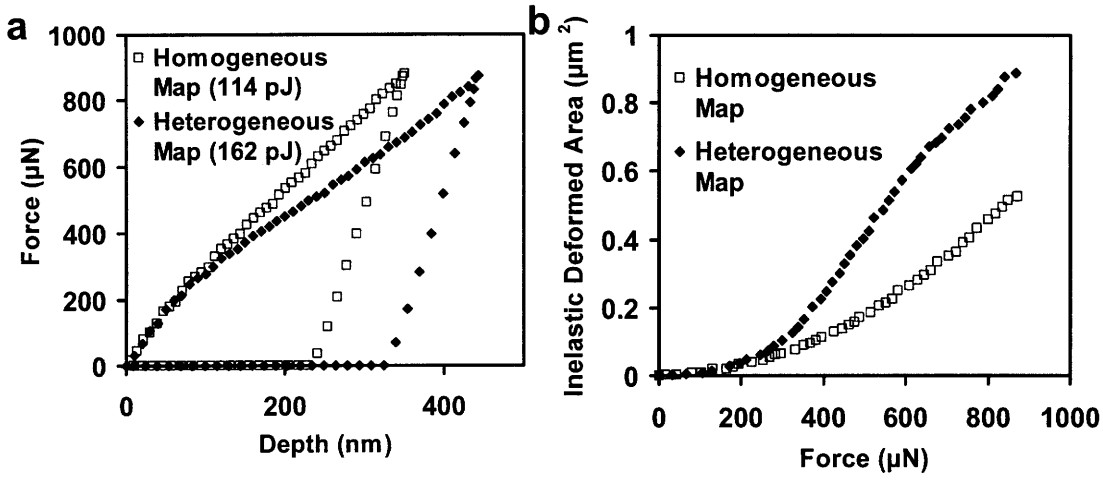

Figure 4-20. **a,** The force-depth curves are plotted for the homogeneous and heterogeneous cases. **b**, The inelastically deformed area is plotted as a function of force comparing the homogeneous and heterogeneous cases.

4.4 Discussion

One previous study reported finite element analysis of a perfectly elastic heterogeneous microstructure based on mean tissue-level experimental data. In that work, the apparent elastic modulus decreased nonlinearly with increasing coefficient of variation (artificially induced in the simulation). In addition, a marked increase in the number of failed elements (determined by an elastic limit strain criterion) was observed with increasing heterogeneity [125].

Strain-controlled micro- and macro-scale failure of bone has also been studied experimentally using four-point bend specimens with rounded notches [64]. As noted in that work the inelastic constitutive response of bone is presently not fully understood. In compression, nanogranular friction and intraorganic cohesion are thought to be major contributing factors to the inelastic resistance of bone initially [61]. Other mechanisms are likely come into play at higher strains due to the effects of collagen fibril shear [63]

and denaturation [8], crack initiation/propagation [64], and sacrificial bond rupture [62]. While bone is known to exhibit significant tension-compression asymmetry, plasticity models involving the von Mises yield criterion are typically employed to capture, at least approximately, the strain fields in bone undergoing inelastic deformation. In the spirit of developing detailed quantitative trends for relative assessments of the role of structural heterogeneity from the nano- to the micro-scale, invoked here as in earlier studies, is a plasticity analysis in our finite element model with the full realization that comprehensive constitutive models for inelastic deformation of bone have not yet been developed.

In summary, herein proposes a new energy dissipation mechanism for bone arising from nanomechanical heterogeneity by recourse to experimental results that provide high-resolution, spatially specific nanomechanical tests in conjunction with detailed computational simulations of locally inelastic deformation. These results provide compelling evidence for enhanced ductility and energy dissipation through nanoscale structural heterogeneity. They also suggest that hierarchical mechanical heterogeneity at multiple length scales provides redundant protection against catastrophic failure. This concept is generally applicable to a broad class of natural materials (e.g. nacre, dentin, ganoine) since nanomechanical and hierarchical heterogeneity is expected to be ubiquitously present. In addition, since osteocytes are continually sampling their mechanical environment [126], deformation spread out over greater spatial areas due to nanomechanical heterogeneity may facilitate damage detection in the extracellular matrix and improved remodeling responses. The heterogeneous nanomechanical patterns measured experimentally in turn would cause corresponding local heterogeneous strains when loaded macroscopically. Such strains are expected to be amplified by the softer

surrounding pericellular matrix of osteocytes [127], further affecting cellular processes. Lastly, heterogeneous local strains are also expected to influence interstitial fluid flow which has been shown to be critical to the proper maintenance of metabolic activity [128].

Chapter 5

Nanoindentation Based Bone Fiber Composite Model

5.1 Introduction

Finite element analysis (FEA) can be used to give structural-mechanical insight into the relative contribution of individual constituents found in bone. A previous study [80] incorporates nanoindentation data, AFM imaging, and FEA together in assessing nanoscale mechanical properties as well as mechanisms of deformation as a function of mineral content in adult bovine tibial cortical bone tested perpendicular to the long bone axis [8]. FEA was used primarily to estimate the elastic stiffness as well as yield stress of the sample approximated as a homogeneously isotropic material.

As first approximated, bone is not a homogeneously isotropic material. In fact, it is highly heterogeneous on virtually every length scale [107, 125]. Although it is micro- and macro-scopically orthotropic, it has been thought to be considered as a mineralized foam matrix whose individual constituents are inherently isotropic in nature[129]. The arrangement of these basic components (i.e. apatite, collagen, proteins) into microstructural features ultimately give rise to the highly anistropic mechanical behavior in bone [74, 130]. It is the goal of this study to use nanoindentation FEA to incorporate an intermediate level of structure between that of microscopic features and individual building blocks in bone into continuum modeling. High resolution TEM images show different structures indicative of fibrils that are surrounded by a highly mineralized matrix [131, 132]. There is a distinct extra-fibrillar matrix which is made up of

hydroxyapatite, non-collagenous proteins and water along with an intra-fibrillar matrix which is made up of the three mentioned materials plus type I collagen. High resolution SEM also gives evidence of mineralized fibrils align in a particular direction at the nanoscale[62].

In this chapter, the nanoindentation data gathered previously is used in conjunction with more complex finite element analysis (FEA) simulations, taking into account the orthotropic nature of bone as well as the mineralized fibril structural nature. Elastic and plastic potentials were incorporated in the material model for orthotropic indentation simulations. Inspired by high resolution TEM and SEM, a more complex FEA model was also built up integrating three different regions of interest. There is 1) an outer homogenous area with an inner fibrillar core that has two separate regions, 2) the intra-fibrillar and the 3) extra-fibrillar. Each of the three regions are assigned material elastic-perfectly plastic properties based on estimations of the relative proportions of mineral, organic, and water. These values are approximated primarily through wet tissue density and water content as a function of a large number of neutron diffraction studies performed on a wide range of mineralized tissues.

5.2 Methods

5.2.1 Orthotropic Elastic-Plastic Finite Element Analysis (FEA) of Nanoindentation

A three dimensional elastic-plastic model was built by FEA using the software package ABAQUS (Hibbitt, Karlsson & Sorensen, Inc.) and solved numerically using the elastic modulus and yield strength as the two fitting parameters. To reduce computational

cost and due to symmetry, 1/2 of the tip and the surface were modeled and the corresponding boundary conditions were applied to ensure the symmetry, i.e. the nodes on the sidewalls were fixed in the direction normal to the sidewall surface (the nodal displacement in this direction is set to be zero). The same The indenter was modeled as a rigid surface with Berkovich geometry (inclined face angle = 24.7°, apex angle 77.1°) having a tip radius of 180 nm and truncate height of 4 nm. The mesh, made up of 8-node linear C3D8H brick elements, was refined in the vicinity of the contact region where large gradients in stress and strain prevail. Several mesh densities were analyzed and an optimal mesh was finally chosen for use in all simulations which contained 25,392 nodes and 23,034 elements. The element size increased with increasing distance from the indentation axis and surface. Figure 5-1 shows the assembly that was formulated in the FEA to carry out the simulation. Large deformation theory and frictionless contact between the indenter and material were assumed throughout the analysis. Elastic constants were taken from ultrasonic velocity tests [133] and variations were made independently one at a time from 1-10 GPa in the indent and non-indent directions. When a variation was made in one of the directions, all of the other direction moduli were fixed. The elastic modulus values used from Rho, 1996 were as follows: E_1 = 11.7 GPa, E_2 = 12.2 GPa, E_3 = 20.7 GPa, ν_{13} = 0.237, ν_{23} = 0.231, ν_{12} = 0.42, G_{13} = 5.17 GPa, G_{23} = 5.7 GPa, and G_{12} = 4.1 GPa. In addition, orthotropic plasticity potentials were incorporated in the material model as well centered around 1 GPa. The simulations were displacement controlled down to 200 nm depth.

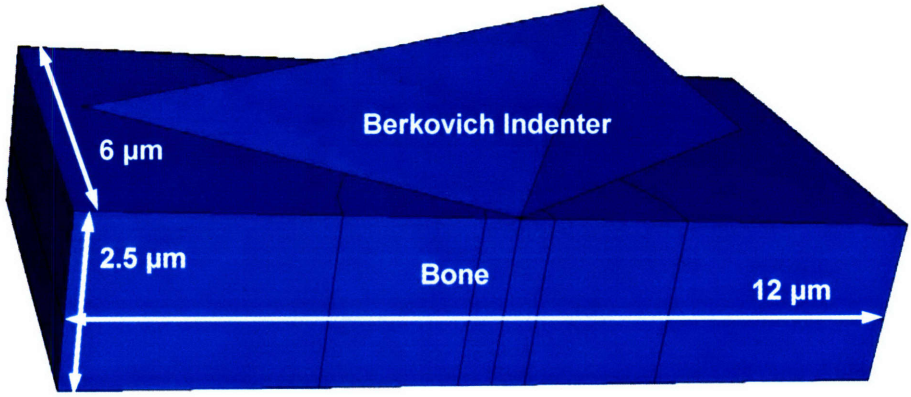

Figure 5-1. Symmetric half space finite element model mesh used for anisotropic nanoindentation simulations.

5.2.2 Fiber Composite Elastic-Plastic FEA of Nanoindentation: Three Different Approaches for Intact and Partially Demineralized Bone

A similar half space assumption was incorporated into another type of model, which takes into account structural variation within the bone extracellular matrix. The mesh was also made up of 8-node linear C3D8H brick elements, refined in the vicinity of the contact region. The mesh that was used in this case included 36,735 nodes and 33,936 elements. Using the high resolution TEM images previously shown as motivation, a fiber composite model was developed where fibrils are surrounded by a highly mineralized matrix. As the extrafibrillar matrix is made up of HA, non-collagenous proteins, and water, the fibrillar matrix is made up type I collagen in addition to these three constituents. There are three different regions of interest which are an outer homogenously isotropic volume that surrounds a biphasic inner fibrillar core that includes two separate regions, one that is fibrillar (each fibril is 150 nm in diameter) and another that is extrafibrillar. Each of these regions would have distinct material property values assigned to them based on the varying proportions of ultrastructural constituents. The major assumptions that comprised the model were based on of neutron diffraction experiments taken by Lees on a wide variety of mineralized tissues[134]. From these

data, as a function of the wet tissue density (1.9 g/mL), it is possible to estimate the relative volume proportions of non-collagenous protein matrix (~17%) grouped together with water, the intrafibrillar volume (~55%), and the volume of hydroxyapatite in the extrafibrillar space (~70%). Type I collagen was also considered to be 90% of the organic as well[7]. Figure 5-2 gives a diagram for the FEA model.

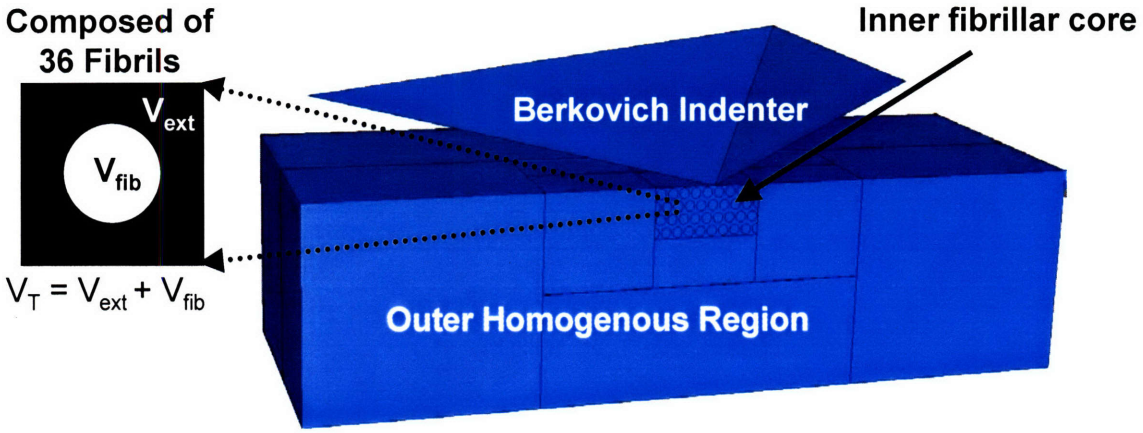

Figure 5-2. This fiber-composite model consists of an outer homogeneous region that surrounds a more refined inner fibrillar core which is comprised of a 55%/45% intrafibrillar/extrafibrillar volume. The three material properties are the outer homogeneous region, the intrafibrillar volume, and the extrafibrillar volume.

The modulus for the collagen is taken to be E_{col} = 2 GPa based on tensile property measurements taken previously [135, 136]. Nanoindentation measurements taken on type I collagen directly, which chiefly probes compressive stresses, gives a modulus value of 2.9 ± 0.6 GPa (Appendix D), which is reasonably close to the 2 GPa assumption. The modulus for hydroxyapatite was taken to be E_{HA} = 100 GPa [12], which is realistic for ceramic materials. The modulus for the non-collagenous protein matrix was taken to be E_{NCP} = 3.2 GPa, which is higher than expected, but there is little to no previous experimental measurement besides what is taken from hydrostatic experiments conducted on bone fluid[137]. This matrix is not a significant portion of bone as it makes up roughly ~10% of bone.

Three different models were taken into account in attempts to estimate the values in the different regions for modulus in the intrafibrillar, E_{fib}, and extrafibrillar, E_{ext}, space. Two of them were standard upper and lower bound approximations based on fiber reinforced composite structures. The upper bound calculation is as follows:

$$E_{fib} = E_{col}v_{col}^{fib} + E_{HA}v_{HA}^{fib} + E_{NCP}v_{NCP}^{fib}$$

$$E_{ext} = E_{HA}v_{HA}^{ext} + E_{NCP}v_{NCP}^{ext}$$

where v^{fib} and v^{ext} refer to the volume percentage in the intra- and extra-fibrillar space, respectively. Using these equations, E_{fib} = 8.4 GPa and E_{ext} = 70.2 GPa. The lower bound calculation uses an inverse method as follows:

$$\frac{1}{E_{fib}} = \frac{v_{col}^{fib}}{E_{col}} + \frac{v_{HA}^{fib}}{E_{HA}} + \frac{v_{NCP}^{fib}}{E_{NCP}}$$

$$\frac{1}{E_{ext}} = \frac{v_{HA}^{ext}}{E_{HA}} + \frac{v_{NCP}^{ext}}{E_{NCP}}$$

where E_{fib} = 2.2 GPa and E_{ext} = 10.0 GPa. The last method is using the Guth theory of filler reinforcement[138], where in a softer nanostructure that is packed with small rigid particles, the overall modulus can be estimated based on the volume fraction of rigid particles (hydroxyapatite) and the modulus of the solvent (organic):

$$E_{fib} = E_{col}\left[1 + 2.5v_{HA}^{fib} + 14.1\left(v_{HA}^{fib}\right)^2\right]$$

$$E_{col} = E_{NCP}\left[1 + 2.5v_{HA}^{ext} + 14.1\left(v_{HA}^{ext}\right)^2\right]$$

where E_{fib} = 2.4 GPa and E_{ext} = 30.9 GPa. Using these 3 different calculations, yield stress values for the intra- and extra-fibrillar regions can be fit to the experimental nanoindentation data shown before. The outer homogeneous isotropic region can be determined with the same method as previously described in the previous chapter.

Lastly, this model was also extended to the partially demineralized bone sample where mineral was leached out using H_3PO_4. From neutron diffraction spacing

experiments, it was shown that with decreasing mineral content, the spacing between tropocollagen molecules tends to increase, which ultimately results in an increase of fibril diameter [134, 139]. From these data, a 4% mineral fiber-composite model was built up with the intrafibrillar space taking up 96% of the total volume. The difference between the relative volume proportions for intact and partially demineralized bone are shown in Figure 5-3.

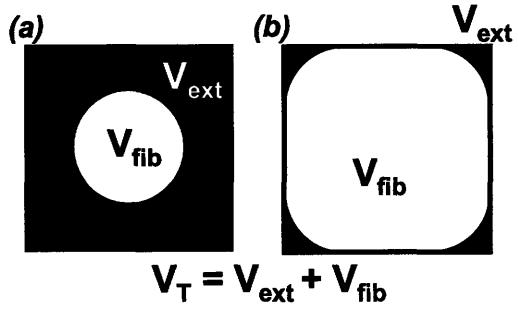

Figure 5-3. A comparison is made of the volume proportions for intrafibrillar and extrafibrillar space in *(a)* intact bone and *(b)* partially demineralized bone.

5.3 Results

5.3.1 Isotropic and Orthotropic Material Input

Results from incorporation of isotropic and an orthotropic material models are shown here in Figures 5-4 and 5-5, respectively. There is even stresses and residual plastic deformation for the isotropic case (Figure 5-4), which was used previously (Chapter 2). In the FEA that incorporated the orthotropic material model, the stress distribution of a typical simulation to 200 nm indentation depth is shown in Figure 5-5. Mises stresses were as high as 800 MPa at high deformation regions. The residual stresses and plastic deformation as shown from a top down view in Figures 5-5(b) and 5-5(d) are asymmetric, showing a greater degree of stress on two lobes of the indentation impression. The force-depth results reveal that changes in the non-indent directions only

begin to affect the results when adjustments of ~10 GPa were made (Figure 5-6). Yield strength was also found to play a large role in the overall indent behavior, similarly to that in the isotropic case. When fixing the non-indent direction parameters and fitting for E_3 and yield stress, results similar to that for the isotropic case were generated (Figure 5-7) as values for E_3 and yield stress were 10 GPa and 200 MPa, respectively.

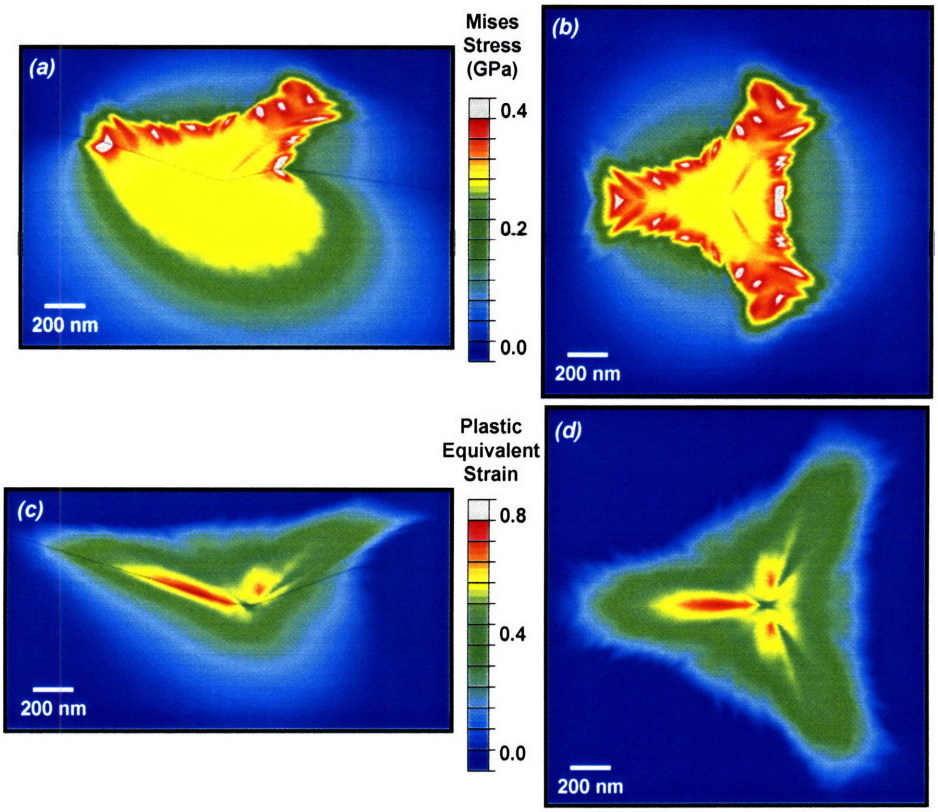

Figure 5-4. FEA indentation results incorporating isotropic elastic constants for the bone model are given here. The stress distribution is spread out evenly throughout the material as given from a *(a)* side and *(b)* top down view. The plastic equivalent strain is also relatively even in distribution shown in the *(a)* side and *(b)* top down views as well.

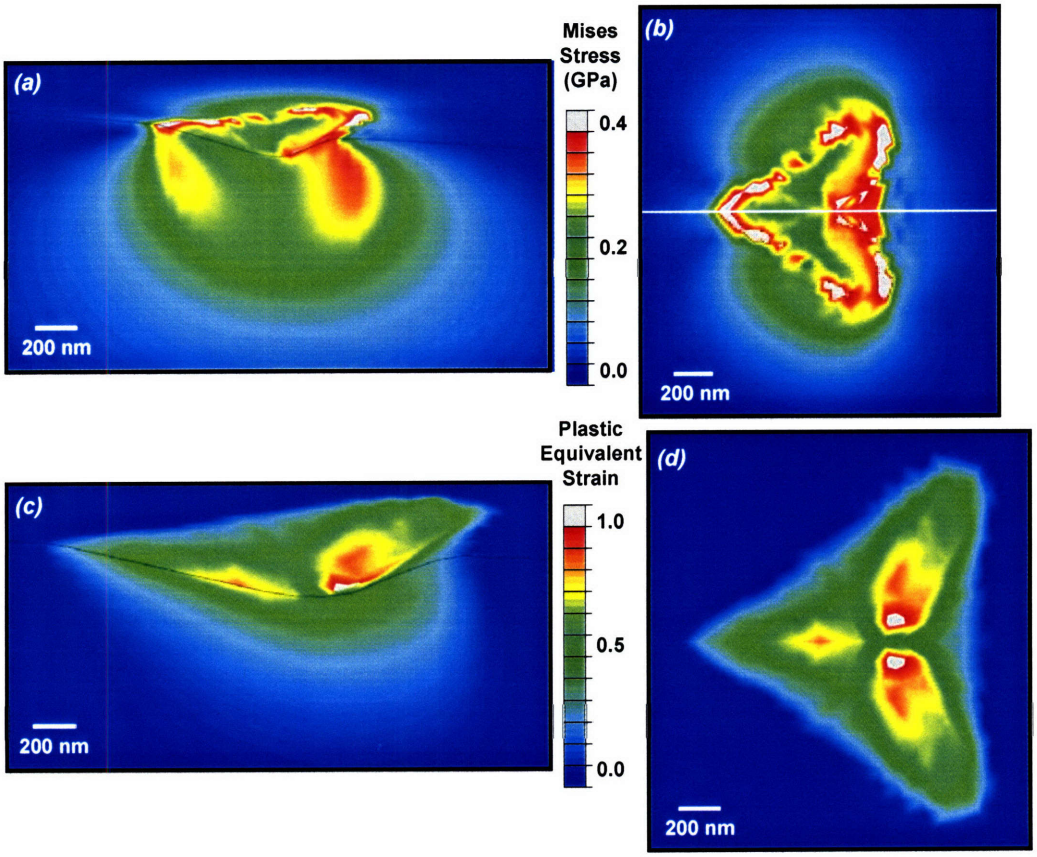

Figure 5-5. FEA indentation results incorporating orthotropic elastic constants for the bone model are given here. The stress distribution is spread out unevenly biased toward the right side of the material as shown in the *(a)* side and *(b)* top down views. The plastic equivalent strain is also relatively biased in distribution shown in the *(a)* side and *(b)* top down views as well.

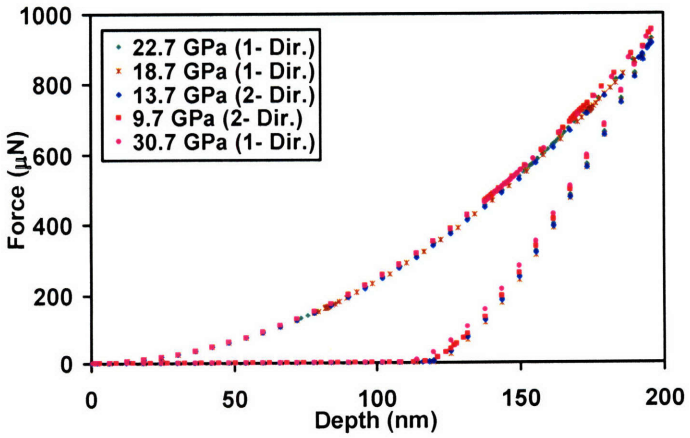

Figure 5-6. Indentation results using ultrasonic velocity measurements for all of the orthotropic elastic constants. When modulus values were varied in the non-indent directions ± 2 GPa, little change in the overall force-depth behavior occurred. Change only started to occur when a variation of 10 GPa was incorporated.

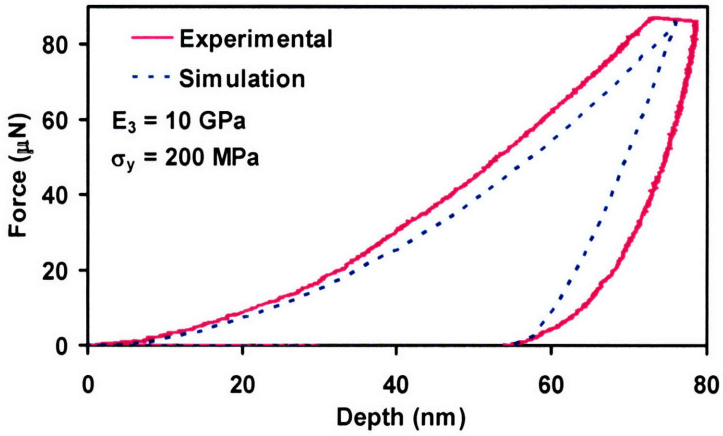

Figure 5-7. Indentation result matching the initial unloading slope and residual depth of deformation from experimental nanoindentation curves to the orthotropic FEA analysis. Given that values were fixed in the non-indent direction, behavior for the simulation was similar to that for the isotropic case.

5.3.2 Fiber-Composite Model: Undemineralized Bone

The inner fibrillar core for one of the fiber-composite FEA simulation results for undemineralized (intact) bone is shown in Figure 5-8. The stress distribution during indentation is shown in Figures 5-8(a) and 5-8(b). The ½ space symmetry is extended to the complete model where the view is top down in Figures 5-8(b) and 5-8(d). The plastic strain is shown in Figure 5-8(c) and 5-8(d). Upon inspection, indentation deformation is directly visualized as fibrils are pushed outward as stresses were built up near the indenter tip apex lines. At an indentation depth of 150 nm Mises stresses, were as high as 900 MPa. Even though much physical deformation occurred to the intrafibrillar regions, the stresses were distributed primarily to the extrafibrillar spaces surrounding the fibrils. The highest compressive pressures were also where tip apex lines are localized, which is where the greatest degree of deformation occurred as well. The top down visualization

shows a stratification of stresses and deformed strains that follows the periodic fibril spacing designed into the model. The soft underlying fibrillar structures are accentuated in the surface deformation behavior, easily visualized by the plastic strain. When the entire sample simulated was set to an isotropic homogeneous material model (similar to that presented in a previous chapter), the outer homogeneous region would be set to 9 GPa and 250 MPa for the modulus and yield stress, respectively.

For the upper bound approximation (Figure 5-9), as the moduli were previously determined, the yield stress yielding the best fit for the extrafibrillar and intrafibrillar regions were 190 MPa and 120 MPa, respectively. The initial unloading slope is noticeably greater for the FEA simulation and the residual depth is ~20 nm off from the experimental average. For the lower bound approximation (Figure 5-10), as the moduli were previously determined, the yield stress yielding the best fit for the extrafibrillar and intrafibrillar regions were 450 MPa and 120 MPa, respectively. The initial unloading slope is noticeably less for the FEA simulation and the residual depth is ~5 nm off from the experimental average. For the Guth model approximation (Figure 5-11), as the moduli were previously determined, the yield stress yielding the best fit for the extrafibrillar and intrafibrillar regions were 300 MPa and 100 MPa, respectively. The initial unloading slopes between the experimental average and the FEA simulation are similar and the residual depth is ~20 nm greater for the model. The initial power law slopes for both the Guth model and lower bound approximation match fairly well with a slight offset.

In addition, the direction orientation at which the indent occurred was varied in that the Berkovich indenter was also set to indent parallel to the fibrillar axis. The stresses and plastic strain were recorded and the distributions are shown for the ½ space

symmetry and full top down views in Figure 5-12. The stresses revealed in Figures 5-12(a) and 5-12(b) are dispersed in and around the fibrillar regions with concentrations that build up at the interfaces between intra-fibrillar and extra-fibrillar. Similar to the case where indentation is perpendicular to the fibrillar axis, the extra-fibrillar matrix takes up the bulk of the loading. Plastic strain deformation in Figures 5-12(c) and 5-12(d) are localized following the tip apex lines as well. The softer fibrillar locations are easily recognized in both types of 3-D plots.

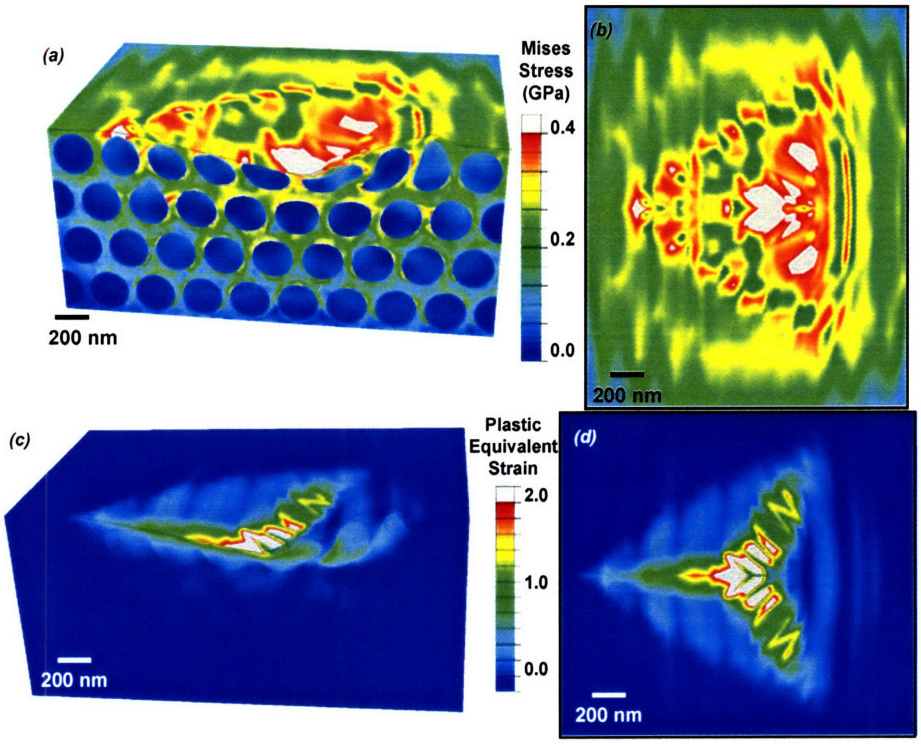

Figure 5-8. Stress visualization of the indentation result in the 3-direction on the inner fibrillar core using FEA is shown here for the intact bone. As the indenter moves forward into the material perpendicular to the long bone axis, fibrils are deformed and displaced outward. Stresses are concentrated particularly at contact points and interfacial regions throughout the matrix. Mises stress and plastic strain contour distributions are shown for *(a) (c)* side profile and *(b) (d)* top down views, respectively.

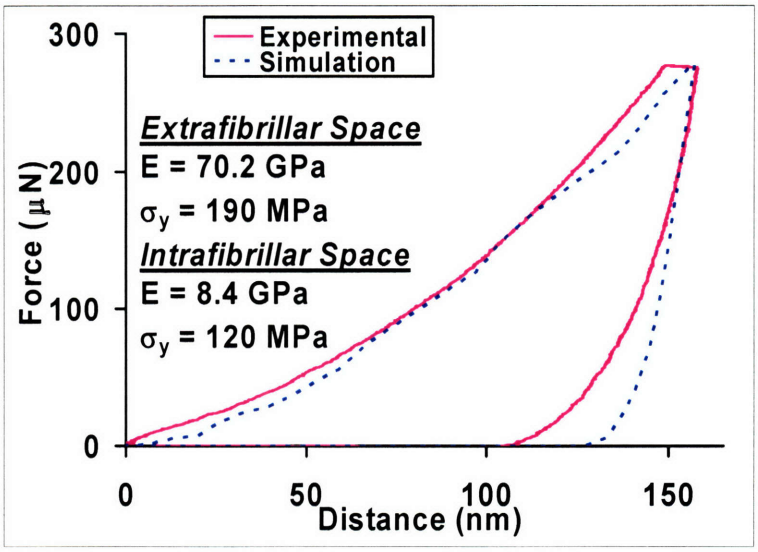

Figure 5-9. Upper bound approximation matching the experimental indentation average to the FEA simulation is shown here. Given the high moduli values for both the intra- and extra-fibrillar spaces, the initial unloading slope and residual depth were difficult to match sufficiently well.

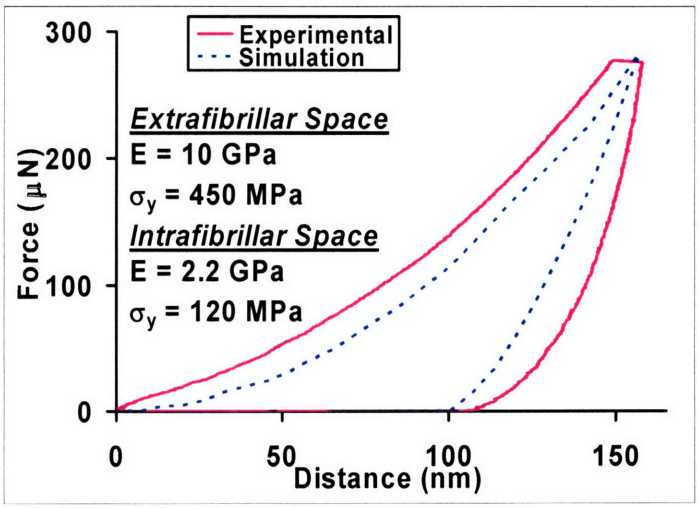

Figure 5-10. Lower bound approximation matching the experimental indentation average to the FEA simulation is given here. The lower moduli values for both the intra- and extra-fibrillar spaces gave rise to a more amenable fit compared to the upper bound solution for the initial unloading slope and residual depth. The initial unloading slope is noticeably less than for the experimental data. The power law relation upon loading is also quite satisfactory.

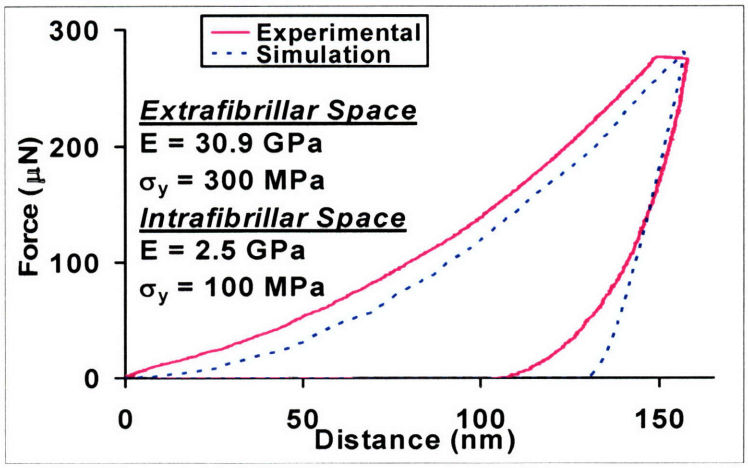

Figure 5-11. The Guth filler reinforcement approximation is shown here matching the experimental indentation average to the FEA simulation. The lower moduli values for both the intra- and extra-fibrillar spaces gave rise to reasonable modulus fit to the initial unloading slope in the experimental data. The residual depth is ~20 nm greater than the experimental data, which is expected. The power law relation upon loading is also quite satisfactory.

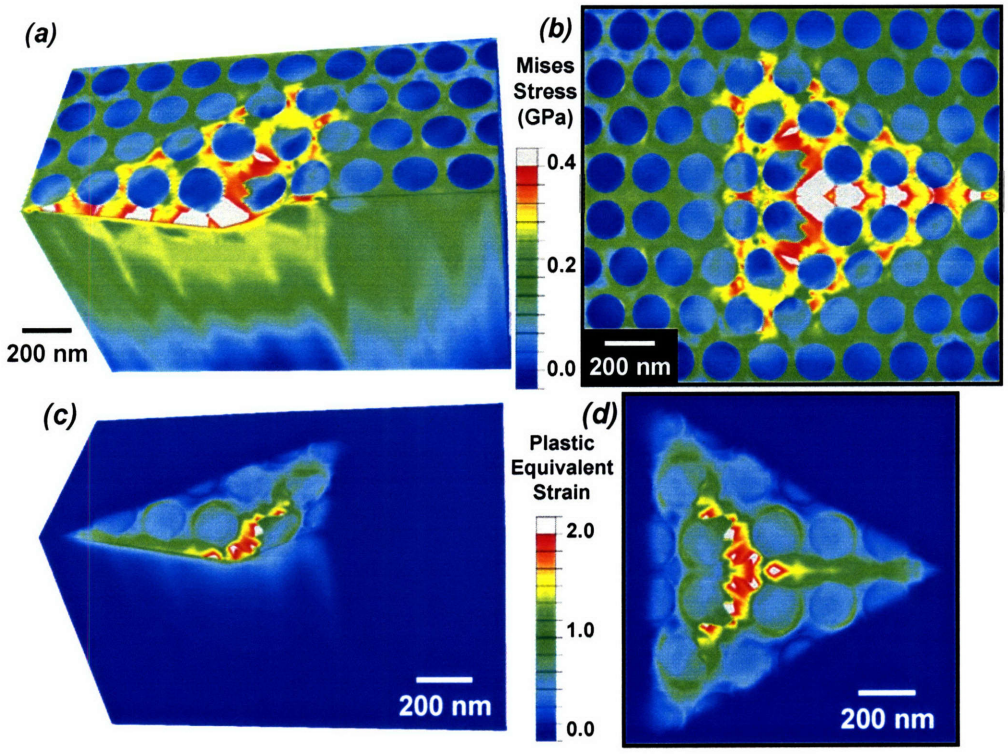

Figure 5-12. Visualization of the plastically deformed area when indented parallel to the long bone axis. Mises stress and plastic strain contour distributions are shown for *(a) (c)* side profile and *(b) (d)* top down views, respectively.

5.3.3 Fiber-Composite Model: Partially Demineralized Bone

The model was also extended into indentations of the partially demineralized bone as well. Stresses and plastic strains are given for the 96% fibrillar volume space in Figure 5-13. Stresses given in Figures 5-13(a) and 5-13(b) reach nearly 4 GPa, which is ~4x greater than that for the intact undemineralized case. Stresses are also concentrated in the extra-fibrillar regions which are sparsely divided throughout the matrix. The plastic strain given in Figures 5-13(a) and 5-13(b) also not only show increased deformation along tip contact points on the sample, but also a less degree of strain for stiffer extra-fibrillar regions that take up more stress. Intra-fibrillar regions in this case, displace much more readily than the extra-fibrillar.

Only the Guth model approximation was performed in this case, the results shown in Figure 5-14. As the moduli were previously determined, the yield stress yielding the best fit for the extrafibrillar and intrafibrillar regions were 300 MPa and 120 MPa, respectively. Similar to the previous model, the initial unloading slopes between the experimental average and the FEA simulation are similar and the residual depth is ~20 nm greater for the model. The initial power law slopes for both the Guth model and lower bound approximation also match fairly well with a slight offset.

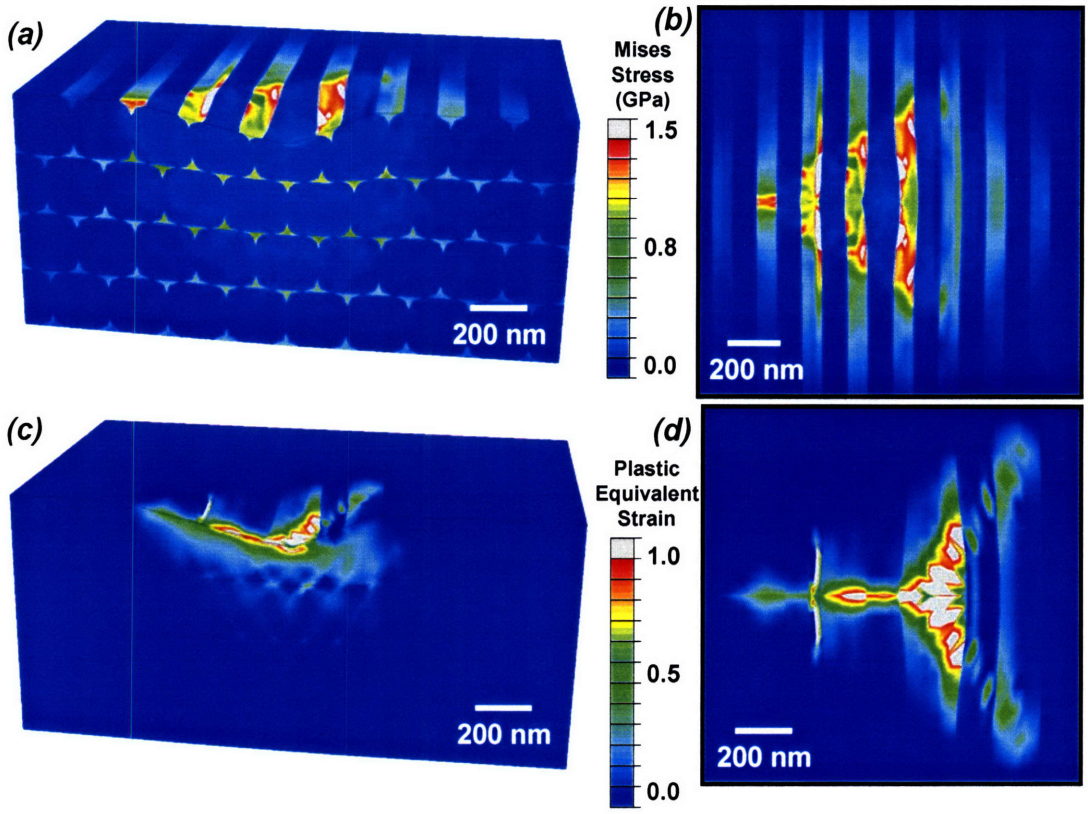

Figure 5-13. Stress visualization of the indentation result in the 3-direction on the inner fibrillar core using FEA is shown here for the partially demineralized bone. As the indenter moves forward into the material, fibrils are deformed further into the sample. The extrafibrillar matrix takes up much of the stress. Mises stress and plastic strain contour distributions are shown for *(a) (c)* side profile and *(b) (d)* top down views, respectively.

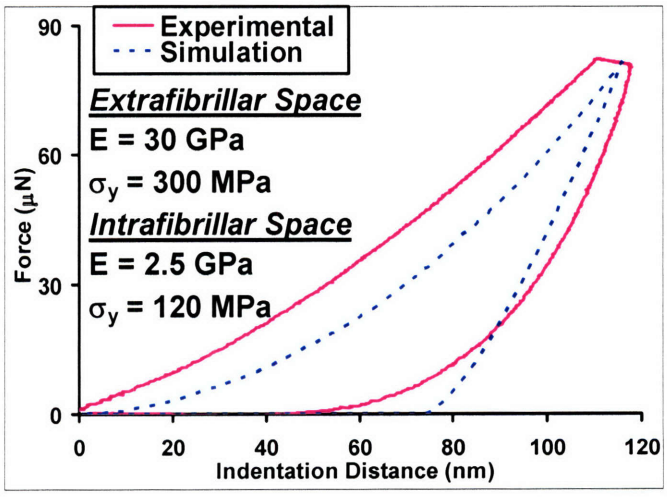

Figure 5-14. The Guth filler reinforcement approximation is shown here matching the experimental indentation average to the FEA simulation. The lower moduli values for both the intra- and extra-fibrillar spaces gave rise to reasonable modulus fit to the initial

unloading slope in the experimental data. The residual depth is ~20 nm greater than the experimental data, which is comparable to the intact bone data. The values for yield stress are similar to that for the intact bone.

5.4 Discussion

Micro- and macro-scopically, bone is an orthotropic material, but as the ultrastructural units are considered, it becomes more and more challenging to break down the components that lead to structural variation at the nanoscale. The extrafibrillar matrix, in general, is considered to behave isotropically[74], yet the manner in which tropocollagen molecules are oriented in collagen fibrils naturally gives rise to anisotropic structural features. The triple helical twist made up of a repeating tri-peptide pattern makes up a nano-staggered formation which ultimately forms a structure that is physically stronger in one direction than its amorphous gelatin counterpart. There is still much room for fundamental understanding of the contributions of separate nanoscale constituents to structure-function and mechanical properties. The following is a discussion of the results and their implications for furher insight into this highly complex composite material.

5.4.1 Orthotropic Material Modeling

Modeling bone as an orthotropic material is a natural first step in understanding its compressive deformation behavior. Values of modulus were used from ultrasonic velocity tests [133] and applied to the nanoindentation experimental and simulation model used here. The results in this study demonstrate that variation of up to 10 GPa in the non-indent directions minimally affect the nanodeformation behavior. It is variation of properties chiefly in the direction of indentation that ultimately have the most

significant affect on the force-depth response. In this model, the yield strength was modeled as an anisotropic material, but with plastic potentials applied throughout the structure. In this respect, if the stiffness is greater in a particular direction, then the yield strength would also be greater in proportion to that stiffness. The relative potentials between directions were not modified, but as the base yield stress was changed, the force-depth behavior would differ significantly as well. Because the principal is similar to that for the isotropic case, overall yield strength naturally plays a large role in the overall indent behavior. In order to explore the role of yield stress through adjustment of plastic potentials, further study would be required.

5.4.2 Fiber-Composite Structural Modeling: Anisotropy Refinement

This is the first time that a fiber-composite FEA model was developed to gain insight into the structural peculiarities of the nanoindentation behavior of bone as the simulations were inspired from TEM imaging of bone and other commonly found mineralized tissues such as mineralized turkey tendon and dentin [131, 132, 139]. While there are still several aspects of bone that have yet to be taken into account (i.e. ultrastructural heterogeneity, orientation of individual constituents, frictional behavior and rate/time dependence) the results demonstrate a further need for study and understanding of bone at the nano- to micro-scale level.

Visualization of the simulated indentation of the intact bone perpendicular to the collagen axes (Figure 5-8) reveals definite anisotropic behavior both in the overall stress and plastic strain contours in contrast to the completely isotropic model where stress and plastic strain are symmetrically observed in each of the three indentation lobes (Figure 5-4). Similar to the orthotropic model (Figure 5-5), stresses are concentrated over to one

side of the indent and are generally striated in the direction of the fibrillar space. Although the orthotropic model does not specifically show the heterogeneous stress behavior, the overall result is consistent in that there is preferential stresses flow in the direction of the fibrils. A related effect occurs when comparing the visualized plastic strain deformation for the 55% fibrillar volume simulation perpendicular to the long bone axis to the orthotropic model. The orthotropic model only captures the general directional behavior of plasticity whereas while collagen fibrils are sure to run through the bone matrix, the intact bone model shows a higher likelihood for fibril deformation beneath the surface.

5.4.3 Fiber-Composite Structural Modeling: Exploring Orientation

The direction of indentation is also a useful way to further explore mechanical structure-function relationships. Results from the simulations are highly variable depending on whether or not indentation is conducted perpendicular (Figure 5-8) or parallel (Figure 5-12) to the long bone axis. The layered stress and plastic strain distributions are evident from both sets of visualizations showing that even though ordered behavior can be captured through these independent test directions, different aspects of the overall structure are revealed. Plots of the force-depth curves for FEA simulations of both indentations for the exact material properties are given in Figure 5-15 showing that the overall force-depth deformation behavior is the same. This surprising result, considering that there is anisotropy at length scales below and above this particular one, suggests the need for higher degrees of sophistication to be added to the model. Although the visualization of stresses and plastic strains serve to provide further insight

into mechanical behavior at the nano- to micro-scale, it is expected that the indentation direction parallel to the fibrillar (long bone) axis would yield a stiffer and stronger result. This could be due to the fact that althoughthe extrafibrillar matrix is, for the most part, homogeneously isotropic at this length scale, the intrafibrillar matrix is expected to still exhibit a high degree of anisotropy. The simple fact that coiled molecules are aligned along the fibrillar axis such that higher mechanical integrity would occur in that direction indicates that such behavior should be incorporated into the model. The simplest way for this implementation would be to use an orthotropic material model, similarly used before except for the entire material, for the fibrillar region only. Another way would be to incorporate a new constitutive material model or include higher order degrees of structural complexity into the model (coils of mineralized collagen fibrils within the intrafibrillar space), which is advised to be taken into account further into the future.

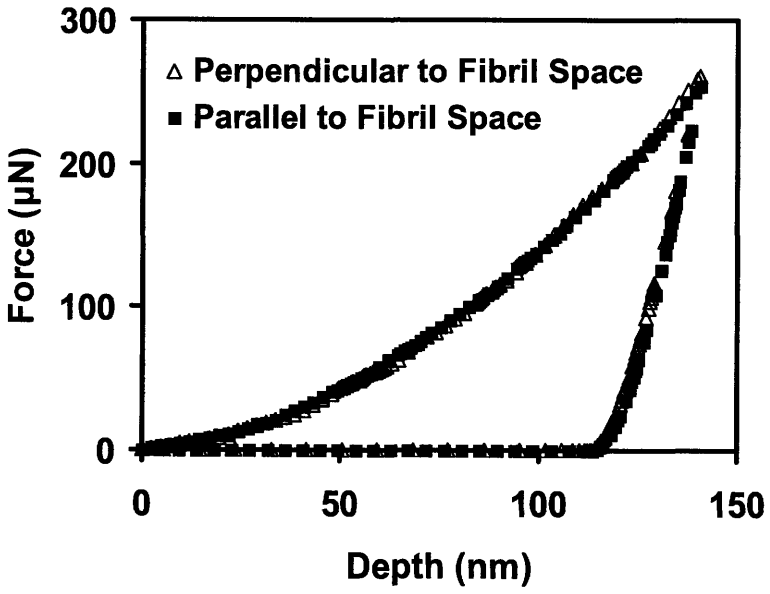

Figure 5-15. Force-depth plots comparing the FEA indentation simulations of the fiber-composite model for testing both perpendicular and parallel to the fibrillar axis.

5.4.4 Fiber-Composite Structural Modeling: Demineralized Bone

A comparison was also made to the structure-mechanical behavior of intact and partially demineralized bone (Figure 5-13) with a slight amount of mineralized extra-fibrillar matrix scattered throughout the matrix. In this case, because the extrafibrillar space is only 4% of the volume, it is reasonable that only a small portion of indented material will retain most of the stresses. In general, the behavior is quite similar to that for the intact bone indentation. The intrafibrillar region does not take up much of the stresses, yet deform much more readily compared to the extrafibrillar space. In this case, the fibrillar space is in immediate contact with the indenter rather than simply dwelling in the underlying material. As a result, the deformation occurs almost exclusively in the intrafibrillar zone.

It is interesting to see that using the same set of material parameters using the Guth model approximation for the modulus values, for both the intact and partially demineralized bone, yields the closest possible fit to the experimental average curve. This result serves to support both the model and experimentation (especially sample preparation) because it shows that the intrafibrillar and extrafibrillar space delineations are, in fact, a viable natural design option for bone as well as giving evidence that the manner in which mineral is leached from the material (methods given in Chapter 2) do not significantly alter the mechanical properties of the matrix.

5.4.5 Further Direction in Structural Modeling in Bone

The work presented in this chapter complements that presented on nanoscale heterogeneity in Chapter 4 in helping to proceed on to the next level of structural complexity in bone. The link between nanoscale and microscale mechanical deformation is at an interface that is still largely unexplored. Understanding the lack of knowledge in this particular field, there is a wide array of possibilities available in structure-function research in bone. A possible next step would be to incorporate the heterogeneity found from AFM probe indentation into the larger scale FEA model (isotropic and fiber-composite) in order to see whether or not the overall behavior is captured reasonably well. Since bone is a viscoelastic material, incorporation of time dependent behavior such as creep and relaxation studies would be beneficial [140]. Lastly, fracture and crack-propagation modeling are also important areas that naturally follow from existing experimental work [64].

Chapter 6

Effect of Mineral Content on Nanoscale Interactions of Adult Bovine Tibial Cortical Bone Using High Resolution Force Spectroscopy

6.1 Introduction

The intermolecular forces (i.e. electrostatics, van der Waals, hydrogen bonding, etc.) that exist in bone are expected to play a significant role in determining its morphology, structural integrity, interaction with bone fluid and its constituent biomolecular species as well as synthetic bone implant materials [12]. There has been little progress made in understanding the interface between HA and collagen as the interfacial strength between organic and inorganic has yet to be measured [63]. The collagen framework is thought to directly or indirectly orient and control crystal growth, suggesting that it could be a perfect interface (chemically and structurally) [12]. Much of the interfacial bonding between the mineral and organic phases of bone are due to the strong adsorption affinity of HA for organic material involving electrostatic interactions between the cationic sites of the mineral (calcium) and the anionic domains of proteins (carboxyl groups) at the interface from electrical double layer effects [141]. Anionic and cationic chemisorption also occurs through direct bond formation between adsorbing species and the mineral apatite surface [141]. Other types of interactions between mineral and organic such as van der Waals, hydrogen bonding, and hydrophobic binding may

occur as well. Noncollagenous proteins, which play a vital role in bone resorption and formation although being 10% of the organic [142], are generally anionic [143] and have a high affinity for the calcium binding site mineral [141]. Phosphate and flouride ions significantly affect adhesion between mineral and organic which is further suggestive that electrostatics play a large role in function as well as mechanical properties [141, 144-146]. Pulsed fluid flow through the lacuno-canalicular network is also a significant source for electrical potential generation [147, 148]. Indeed the dynamics of surface charge distribution is an area of considerable interest in bone restorative therapies as application of electrical currents/fields is a possible route to manipulate the surface energy in bone such that mediated growth could occur [149].

Understanding of the macromolecular mechanisms of biomineralization in bone is an area of significant interest that is widely applicable to a wide range of materials applications, both biological in origin and synthetic. Type I collagen soaked in supersaturated simulated body fluid has been observed to nucleate hydroxyapatite (HA) crystals, particularly in highly carboxylated regions [150]. In biological systems, it is thought that Ca-P granules are extruded out of cellular vesicles originating from mitochondria into the extracellular space which then selectively (i.e. through space, charge, electrochemical configurations) become lodged in collagen fibril hole zone regions [151].

Although the macromolecular organization of type I collagen is considered to be a major factor in facilitating bone mineralization [152, 153], a considerable amount of evidence points to noncollagenous proteins (NCPs) having a significant role in regulation of bone remodeling. The fact that type I collagen is present in many connective tissues

that do not mineralize, suggests that NCPs may play a role in bone mineralization regulation [153]. One study in particular details the discovery and characterization of osteonectin which has been shown, through radioactive labeling and immunological assays, to selectively bind to type I collagen, apatite crystals, and free Ca^{+2} ions in solution [154]. The collagen-osteonectin-HA complex also has been observed to nucleate mineral deposition from metastable balanced salt solution (0.1 M NaCl, 0.05 M Tris-HCl, 2-3 nM Ca^{+2}/nM osteonectin). The study hypothesizes that after osteonectin is bound to collagen fibrils, mineralization proceeds primarily through ion binding followed by mineral nuclei formation, phase transitions, crystal formation, and epitaxial growth. Further study through circular dichroism has shown that osteonectin has an irregular structure lacking significant □-helical content which may serve to hold Ca^{+2} ions in a specific configuration such that nucleation may occur in the presence of free ions or collagen [155]. The presence of osteocalcin has often been observed in normally and pathologically mineralizing bone, implicating its role in tissue maintenance [154, 156]. When Ca^{+2} ions are bound to osteocalcin, a major conformational change occurs as it adopts a highly □-helical conformation (30% increase from the unbound state) [156]. Osteocalcin has several periodically spaced has □-carboxyglutamic acid residues, which have a high affinity for hydroxyapatite [156, 157]. Bone sialoprotein is a highly anionic phosphorylated glycoprotein which is a readily nucleates HA formation particularly due to two α-helical polyglutamic acid regions that instigate a hydroxylation, tyrosine sulfation, and serine/threonine phosphorylation [158, 159]. Electrostatic effects in bone sialoprotein is also believed to be significant, particularly in long range interactions which have a stabilizing effect for the formation of short range low affinity complexes

[159]. In teeth, which is highly similar in composition to bone, phosphophoryn has been shown to bind both specifically and reversibly, to collagen monomers and fibrils, enhancing uptake of Ca^{+2} onto fiber surfaces. This, in turn, localizes Ca^{+2} binding which leads to the growth of collagen oriented calcified HA crystals [160]. In general, a substantial amount of evidence points to phosphoprotein involvement in the regulation of calcification along with extracellular fluid, pressure gradients, and collagen macromolecules which lead to crystallites of Ca-P that are highly organized, parallel to the long axes of the collagen fibrils [151].

Until recently, the majority of surface charge values have been performed through zeta potential measurement, which is performed by electrophoresis on dilute colloidal suspensions [161], and has been shown to vary with several environmental factors. Change in zeta potential magnitude has been found to be directly related to periods of bone growth or turnover from heightened activity such as ion exchange and development of fluid pressure gradients leading to stress generated electrical potentials [162, 163]. Net surface charge measured through zeta potential have also shown strong correlation between positive ionic forces and tissue adherence [164]. Zeta potential is defined as the electrical potential of the double layer at the boundary which separates the stationary fluid layer (also called the Stern surface, slip plane, and hydrodynamic shear plane) made up of rigidly bound counter-ions that are tightly bound to the solid from the diffusive layer of fluid that is highly mobile relative to the surface. The Stern surface is typically a few molecular diameters from the surface. When a particle moves in a liquid under electrophoretic influence, the mobility that is measured is directly related to the zeta potential. Although zeta potential experiments are the predominant methodology for

surface charge measurement, the physical grinding of bone into particles inherently affects the natural electrochemical properties of bone by reducing the diffusion boundaries into fragments that expose portions of the matrix that previously may have been compartmentalized into custom-designed localities [165]. In general, zeta potential measurements are averaged bulk measurements highly variable depending on pH [166], steeping time [167], solution concentration [168], chemical cross-linking [168], composition [166, 169, 170], and particulate geometry [163, 165]. If the surface charge is directly measured as in the technique presented here, zeta potential can be calculated from the nonlinear PB equation. Another measure of electrical charge found to be directly proportional to zeta potential is through streaming potentials [167], which is the pressure gradient generated from fluid flow past fluid filled walls [147, 168].

In general, the magnitude of surface charge calculated at 0.01 M IS is consistent with zeta potential measurements which are found in other reports to vary from -5 to –75 mV [148, 163, 171-173]. Because zeta potential measurements vary with such a wide variety of parameters, it is difficult to make direct comparisons in magnitude of surface charge to zeta potential calculations. For this reason, when performing zeta potential experiments, it is important to make relative comparisons instead of absolute.

With the development of novel methodology, further progress in achieving a fundamental understanding of the nanoscale intermolecular interactions of the organic and inorganic components in bone can now occur. High resolution force spectroscopy (HRFS) allows for direct measurement of forces between a nanosized probe tip functionalized with SAMs which are molecules of uniform structure, charge, and chemistry as a function of separation distance from the sample in fluid. This data on

approach can be compared to electrostatic double layer theory, and the surface charge density (□) can be estimated numerically. Here we measure, for the first time, normal electrostatic double layer forces between a SAM functionalized probe tip and bone of varying mineral content. Here, we particularly focus on the realm of electrostatics, where surface charge densities and London Dispersion forces are recorded as a function of bone mineral content.

The results presented here will be discussed in the light of zeta potential measurements and synthetic bone implant materials. The extent to which bonding between mineral and organic constituent phases in bone (whether due to chemical or mechanical linkages) relates to interfacial rupture/crack initiation is thought to be essential for understanding the mechanistic origin of bone disease such as osteoporosis [174, 175]. In orthopedic implants that trigger apatite precipitation, it is thought that bone deposition is instigated by enhanced bioactivity on the surface of the biomaterial which is brought about by a variety of factors including electrostatics, interfacial bonding, protein adsorption, peptide sequence recognition, cell adhesion, and other physiochemical mechanisms.

6.2 Materials and Methods

6.2.1 Sample Preparation

Samples of adult compact bovine bone were taken from the proximal tibial metaphysis and cut down to 1.5 mm thick specimens using a diamond-impregnated annular wafering saw (ISOMET 5000; *Buehler*, Lake Bluff, IL) running at 400-600 rpm with constant phosphate buffered saline (PBS, IS=0.15M, pH7.4) irrigation. Longitudinal

sections (cut parallel to the long bone axis) were polished down in 2-3 minute intervals using a metallographic polishing wheel (MODEL 920, *South Bay Technology,* San Clemente, CA) at ~100 rpm and adhesive papers with successively smaller Al_2O_3 particle grit sizes; 9 μm, 3 μm, 1 μm, 0.3 μm, 0.1 μm, and 0.05 μm (*South Bay Technology*). Samples were rinsed copiously with DI water followed by ultrasonication in DI water between polishing intervals. Samples were then immediately stored in 20°C PBS. Demineralization etches were performed using 40% H_3PO_4/60% DI water for 0, 1, 10, 40, and 120 seconds, followed by at least 48 hours of rehydration time in PBS during which time the collagen fibrils were allowed to refibrillate [28, 31].

6.2.2 Sample Characterization: AFM, SEM, GSE, BSE, Contact Angle Measurement

Tapping mode (TM)AFM imaging in ambient temperature and humidity was employed using a 3-Dimensional Molecular Force Probe (MFP-3D, *Asylum Research,* Santa Barbara, CA) on hydrated samples using a silicon etched *OMCL-AC160TS* rectangular cantilever with a tetrahedral probe tip (cantilever spring constant ~56.2 N/m, probe tip end-radius ~15 nm, resonance frequency □ ~ 300 kHz, front angle = 34°, side angle = 30°) in ambient conditions. For imaging, the cantilever was driven just below ω using a scan rate of 2 Hz and maximum sampling size of 512 x 512 pixels. The images reported gave information regarding sample height, amplitude, and phase. The height image is the surface topography tracked by the piezo. Amplitude consists of cantilever frequency variation which is reflective of surface topography where light areas are regions of high topography and darker areas of regions of lower topography. Phase imaging is cantilever oscillation phase lag from the signal at which the cantilever is

driven. This information is generally used to measure properties of different materials based on which is reflective of viscoelasticity, adhesion, and friction. Light areas are regions of high phase lag and darker areas of regions of lower phase lag.

An environmental SEM (ESEM, *Philips/FEI* XL30 FEG-SEM, Netherlands) was employed for sample characterization in a water vapor environment for uncoated bone samples. Fully demineralized bone [176], dense, phase-pure hydroxyapatite [177], undemineralized bone, and partially demineralized bone using various etch times were mounted on the same metal base. Electron acceleration was set to 20 kV with a 184 μA operating current. The working distance was set to 9.6 mm and the water vapor was at 0.4 Torr. Contrast and brightness levels were adjusted and held so that electron images would appear optimally for all samples, allowing for feasible gray level calibration using BSE detection. A gaseous secondary electron (GSE) detector was also placed in the chamber so that regular secondary electron emissions could be detected to form images of the samples as well. Mineral content for the different samples were estimated using mean gray level BSE images [36, 37, 178-181].

Advancing contact angles were also measured for each of the samples to measure the relative degree of hydrophobicity. At least 3 different droplet angles were recorded for each sample.

6.2.3 HRFS: Cantilever Probe Tip Functionalization

HRFS experiments were performed with Si_3N_4 cantilever probe tips that were Au-coated[182] and chemically functionalized with alkanethiol SAMs terminated with a COO^- end group (11-mercaptoundecanoic acid, $HS\text{-}(CH_2)_{10}\text{-}COOH$, *Aldrich*).

The Au-coated cantilever probe tip was cleaned in O_2 plasma for 10 seconds right before placing it in 1 mM SAM solutions in ethanol solvent. A planar silicon substrate that was Au-coated and cleaned with Piranha solution (3:1 ratio of H_2SO_4 and H_2O_2) was also placed in the solution for control experiments to be run. After 20 hours the cantilever and planar substrate were both rinsed with 100% ethanol and stored in deionized water.

6.2.4 HRFS: Probe Tip End-Radius Measurements

Scanning electron microscopy (SEM, *JEOL JSM-6060*, Peabody, MA) was employed after all HRFS experiments were finished in order to measure the cantilever probe tip end-radius. A magnification of 75,000x was used and the tip radius was determined by drawing a circle on the SEM image inside the rounded tip point and comparing the radius to the image scale bar. The radius was measured to be 85 nm.

6.2.5 HRFS: Force Measurements on Approach and Retract

HRFS experiments were conducted using the MFP-3D, to measure force, F (nN), vs. tip-sample separation distance, D (nm), on approach and retract (F-D curves) with V-shaped, "D" cantilever (*Thermomicroscopes,* Sunnyvale, CA*)*. The instrument is placed on an anti-vibration table (Hertzan) and housed in an environmental isolation chamber so as to minimize instabilities due to the ambient background noise. In order to obtain the F and D quantities, the two values that need to be measured are the deflection of the cantilever, and the position of the chip. The deflection of the cantilever is recorded by a photodiode that tracks the position of the laser spot off the

backside of the reflective cantilever surface. The piezoelectric position of the chip is recorded by a linear variable differential transducer (LVDT). The deflection multiplied by the spring constant of the cantilever gives "force" and the difference between the LVDT and the deflection gives "distance". In order to calibrate the spring constant of the cantilever an inverse optical lever sensitivity (InvOLS) can be calculated by performing a force pull over a 1 μm approach and retract distance on a very hard surface in order for the instrument to determine the relation between cantilever deflection and voltage signal. The hard surface was freshly cleaved mica and the InvOLS measured was 28.3 nm/V. The spring constant was determined through a fit to thermal vibrations at the highest resonance frequency peak to be 0.042 N/m. HRFS experiments were carried out in aqueous electrolyte solutions having ISs of 0.001, 0.01, 0.1, and 3 M NaCl at pH 6. A 20 minute equilibration time was allowed between changes in solution with the order of experiments going from low to high IS so as to avoid salt contamination. Control HRFS experiments were performed on Au-coated silicon substrates [182] functionalized with the same COO^- terminated SAM to determine surface charge per unit area of the SAM for subsequent HRFS probing of bone samples. Approximately 20 individual HRFS probes were performed and averaged at each of three random locations on each sample of interest.

6.2.6 Electrostatic double layer theory

Force curves on approach were fit to the Derjaguin-Landau-Verwey-Overbeek (DLVO) theory involving an iterative numerical process of finding the best solution to the full nonlinear electrostatic double layer theory based on a Poisson-Boltzmann

formulation of a surface of constant charge per unit area [183]. The Poisson-Boltzmann equation gives an expression for the electrical potential, □(V), between two charged planar surfaces in an electrolyte solution. For a monovalent 1:1 electrolyte, the solution takes the form:

$$\nabla^2\Phi = \frac{2FC_0}{\varepsilon_w}\sinh\left(\frac{F\Phi}{RT}\right)$$

Where F is the Faraday constant (96,500 C/mol), C_0 is the bulk concentration of ions (mol/m^3), □$_w$ is the dielectric permittivity of water (6.9x10^{-10} C/N m^2), R is the universal gas constant (8.314 J/mol K), and T is the absolute temperature (K). Constant charge boundary conditions were used such that the electric field at the substrate and probe tip surfaces were related to the surface charge per unit area, i.e. $\nabla\square|_{substrate} = \square_{substrate}/\square_w$ and $\nabla\square|_{tip} = -\square_{tip}/\square_w$. Constant charge boundary conditions on both bounding surfaces are employed because in the experiments, neither the probe tip nor the substrate is electrically connected to any source that would cause them to maintain a constant potential. The Newton numerical method on finite differences was used to solve the full nonlinear Poisson-Boltzmann equation by minimizing the residual error difference of the two nonlinear terms given a reasonable initial guess. To calculate the surface charge of the COO^- terminated SAM probe tip, HRFS experiments were conducted using the COO^- terminated SAM probe tip vs. the COO^- terminated SAM planar substrate that was incubated in the same conditions. The data were compared to the electrostatic theory assuming that the two surfaces had the same surface charge density and □$_{COO^-}$ was estimated to be -0.02 C/m^2 where the fixed parameters in the analysis were R_{TIP} and the IS. The probe tip of known □ was then used to test the bone samples in varied IS solutions

and this experimental data were fit to the theoretical solution using the bone surface charge as the only free fitting variable.

The van der Waals force upon approach was accounted for in the form of a Hamaker constant given by:

$$F_{VDW}(D) = -\frac{AR}{6D^2}$$

where A is the Hamaker constant, R is R_{TIP}, and D is the tip-sample separation. At 3 M IS, where electrostatics are effectively screened out, it is appropriate to assume that in a chemically non-reactive surface, the major component of the force on approach will be from London Dispersion effects. From the above relation, the averaged approach curve for each type of sample was fit and the Hamaker constant was iteratively calculated.

For 0.001-0.1 M IS, HRFS data on "approach" (i.e. probe tip advancing towards surface) for the bone surface showed a nonlinearly increasing net repulsive force for D > ~5 nm and infrequent jump-to-contacts for D < ~5 nm. Jump-to-contact distances for individual force curves and power law fits at high salt concentrations (3M), where electrostatic forces are largely screened out, were both used to determine the Hamaker constant.

6.2.7 Position Sensitive HRFS

Force curves upon approach were also recorded at pre-determined locations on the sample surface. The same COO^- SAM cantilever that was used for spectroscopy was also used to image immediately beforehand using both contact and TMAFM in 0.01 M aqueous IS solution. For optimal imaging using TMAFM, the drive frequency was offset 7% from the second resonance peak (~28 kHz). TMAFM and contact mode imaging

were employed for two different positional length scales (1.5 and 5 μm scan sizes) respectively. Nine locations were specifically chosen for force pulls to be taken corresponding to chosen points on each of the images.

6.2.8 Retraction pull-offs

Adhesion forces and distances upon retract from the surface were also recorded and plotted as a function of IS. The adhesion force is considered to be the difference between the forces at different pull-off peak events. The adhesion distance was recorded from the distance at which a pull-off event occurred. The adhesion force was normalized by the tip radius so that an overall energy density value can be obtained for the sake of comparison to other HRFS experiments.

6.3 Results

6.3.1 TMAFM Imaging

The surface morphologies of the undemineralized bone as well as one of the partially demineralized samples are represented from TMAFM images (Figure 6-1). The granular type roughness (Figure 6-1(a)) is fairly evident for the 57 wt.% sample without any evidence of the characteristic collagen fibril banding structure. An amplitude images of the 32 wt.% sample (Figure 6-1(b)) reveals well formed fibrillar structures typical of type I collagen (~67 nm axial periodicity and ~180 nm fibril width) on the surface. TMAFM images for the other 3 partially demineralized samples had similar morphologies to that of the 32 wt.% sample. The deorganified sample exhibits a similar

morphology (Figure 6-1(c)) to that of the undemineralized sample without any evidence of the characteristic collagen fibril banding structure

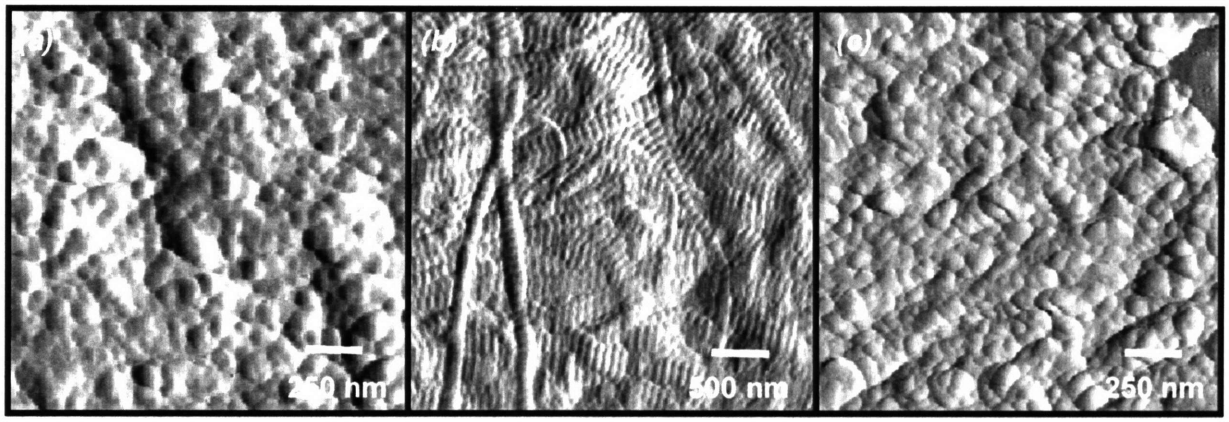

Figure 6-1. Tapping mode(TM) AFM amplitude images perpendicular to the long bone axis taken in ambient conditions of adult bovine tibial cortical bone. Samples imaged were of *(a)* undemineralized (57 wt.% mineral content) bone (maximum lateral dimension 56.0 ± 36.2 nm and a peak-to-valley height 9.7 ± 2.8 nm), *(b)* partially demineralized (32 wt.% mineral content) bone (fibril diameter 176 ± 46 nm), and *(c)* heat treated deorganified (100 wt.% mineral content) bone (maximum lateral dimension 49.3 ± 32.0 nm and a peak-to-valley height 10.7 ± 3.5 nm).

6.3.2 HRFS on Approach

Typical individual F-D curves are given at each mineral content at 0.01 M IS in (Figure 6-2) which all show repulsive nonlinear forces on approach of the probe tip to the bone surface. The repulsion observed at higher IS solutions are considerably less in magnitude and range than lower IS solutions. There is a small attractive "jump-to-contact" observed for ~15% of the samples. An individual curve for which there was a jump to contact observed is also shown (Figure 6-2). For the different types of samples, with any given individual force curve, the repulsion starts from 5-15 nm away. Normalized Force/Radius values on the right y-axis allow for energy comparisons to be made with tips of varying radius.

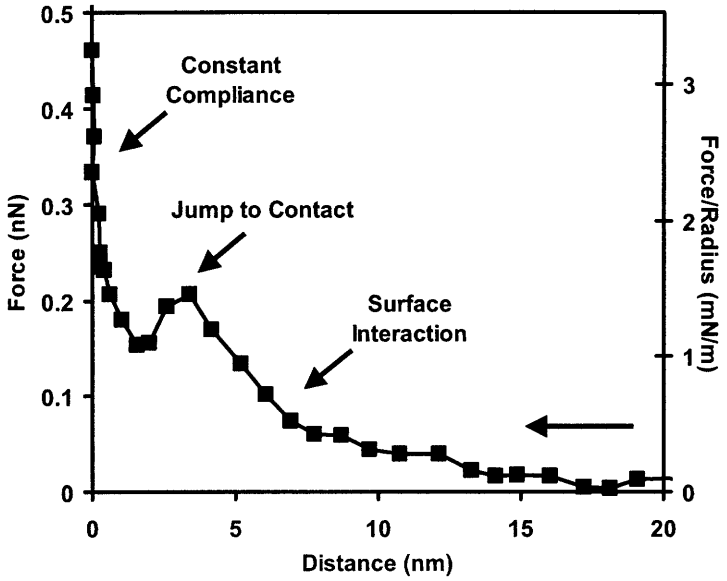

Figure 6-2. Typical individual high resolution force spectroscopy curves upon approach for adult bovine cortical tibial bone perpendicular to long bone axis with 57 wt.% mineral content in 0.01 M aqueous NaCl solution, pH = 6.5. The probe tip was functionalized with a COO^--SAM (surface charge per unit area, $\sigma_{COO^-} \sim -0.02$ C/m^2).

Force curves averaged for the 57 wt.% undemineralized sample are shown for 0.001 M, 0.01 M, 0.1 M, and 3 M IS (Figure 6-3). At 3 M IS, the overall force becomes attractive, presumably due to electrostatics being screened out from the high aqueous salt concentration. The trend for variation of mineral content at 0.01 M IS is also shown (Figure 6-4). In general, the repulsion starts at 10 nm for each sample and there does not appear to be large statistical differences between the average curves.

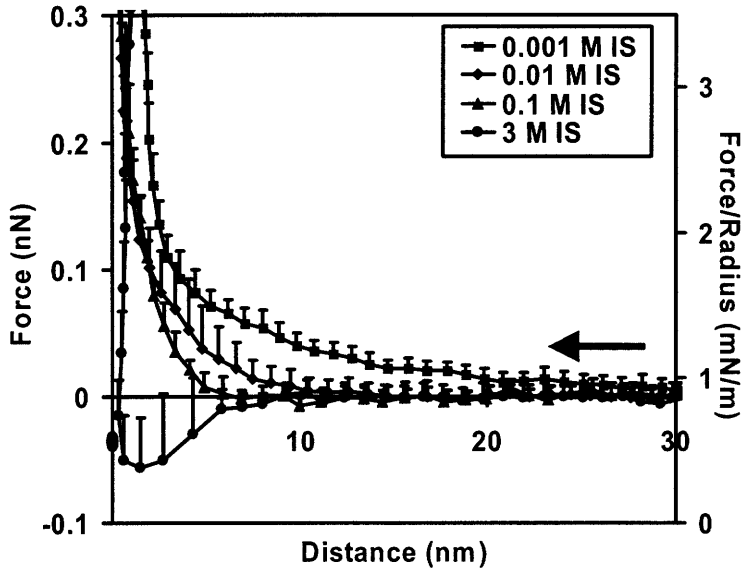

Figure 6-3. Averaged high resolution force spectroscopy data on undermineralized ~57 wt.% adult bovine cortical tibial bone perpendicular to long bone axis upon approach at 0.001M, 0.01M, 0.1M, and 3M NaCl ionic strength and pH 6.5. The probe tip was functionalized with a COO^--SAM (surface charge per unit area, $\sigma_{COO^-} \sim -0.02$ C/m^2). At each ionic strength condition, a total of n=20 experiments were carried out at 3 different sample locations and hi-lo bars represent one standard deviation.

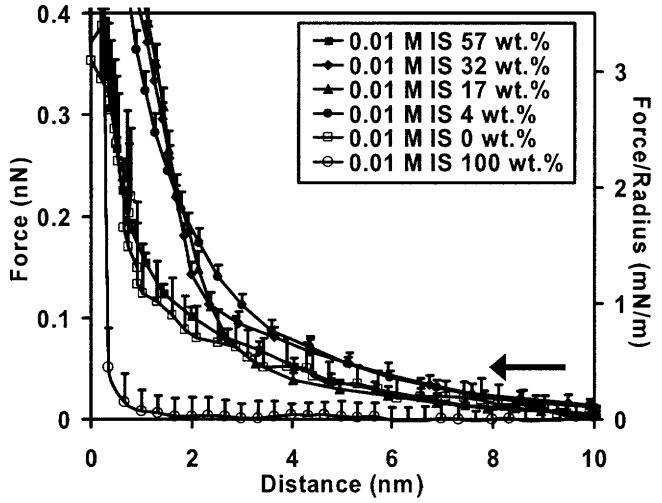

Figure 6-4. Averaged high resolution force spectroscopy data upon approach for adult bovine cortical tibial bone perpendicular to long bone axis at 0.01M and pH 6.5 for samples of 100%, 57%, 32%, 17%, and 4% wt. % mineral content. The tip was functionalized with a COO^--SAM (surface charge per unit area, $\sigma_{COO^-} \sim -0.02$ C/m^2). For each mineral content, a total of n=20 experiments were carried out at 3 different sample locations and hi-lo bars represent one standard deviation.

Contact angle measurements (Figure 6-5) indicate a slight increase in hydrophilicity as the mineral content decreases. The values that were calculated for Hamaker constant on average are $A_{0wt.\%} = 135$ zJ $A_{4wt.\%} = 181$ zJ, $A_{17wt.\%} = 181$ zJ, $A_{32wt.\%} = 109$ zJ, $A_{57wt.\%} = 153$ zJ, and $A_{100wt.\%} = 41$ zJ. A plot of the calculated Hamaker constant as a function of mineral content is also given (Figure 6-6). The trend appears to steadily decrease as mineral content increases. Typical individual F-D curves are also given at each mineral content at 3 M IS (Figure 6-7) along with the "Derjaguin approximation" fit for the Hamaker constant. Although there is no expectation for the force to be repulsive, the fits coincide very well with the experimental data from 3-10 nm.

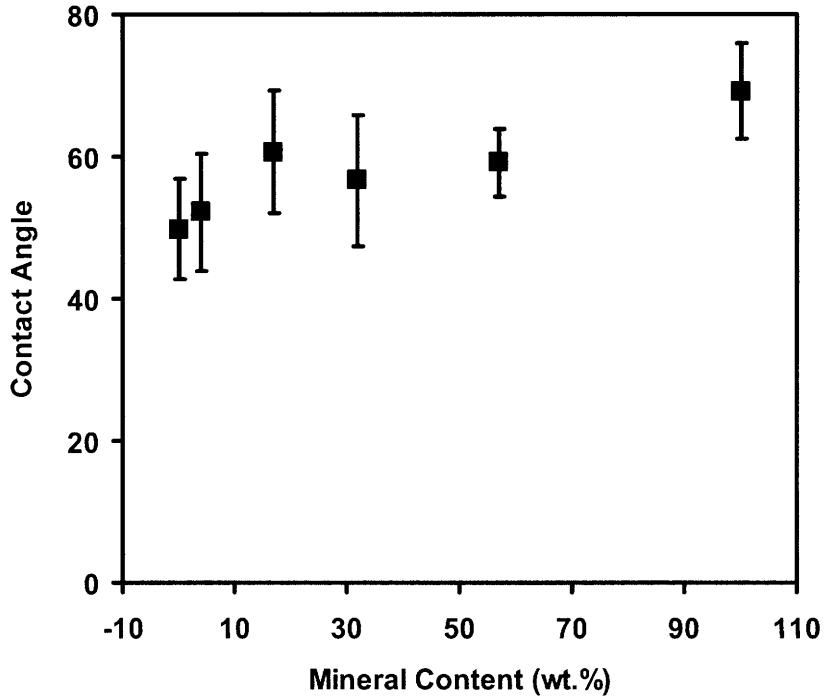

Figure 6-5. Plot of the advancing contact angle measurements using deionized water versus weight % mineral content of adult bovine cortical tibial bone perpendicular to long bone axis are shown here. There is a slight linear correlation of contact angle with mineral content as evidenced by the statistical difference between the mineral content data points at 0% and 100% mineral ($p < 0.01$).

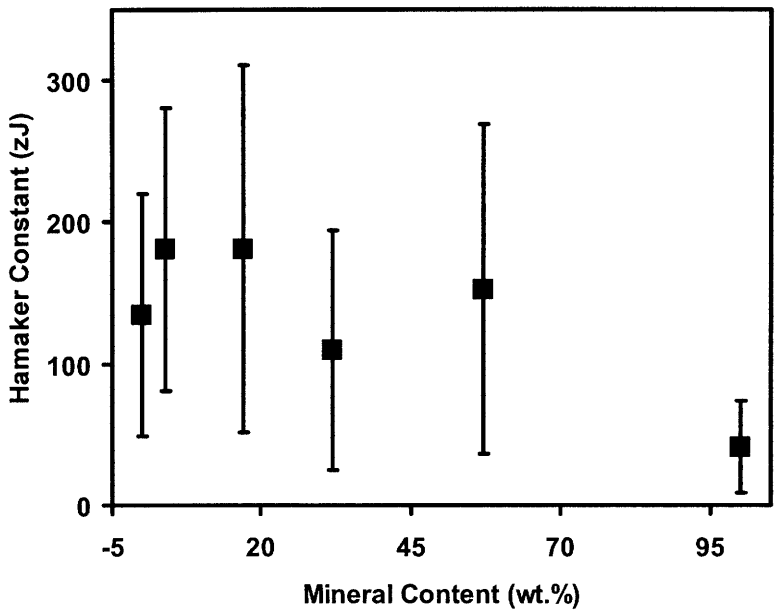

Figure 6-6. Hamaker constants versus % mineral content of adult bovine cortical tibial bone perpendicular to long bone axis calculated from jump-to-contact distances in nanomechanical data measured at 3M ionic strength and pH = 6.5 using a COO^--SAM functionalized probe tip (surface charge per unit area, $\sigma_{COO^-} \sim -0.02$ C/m^2). There were no statistically significant differences observed besides that for the deorganified sample ($p < 0.05$).

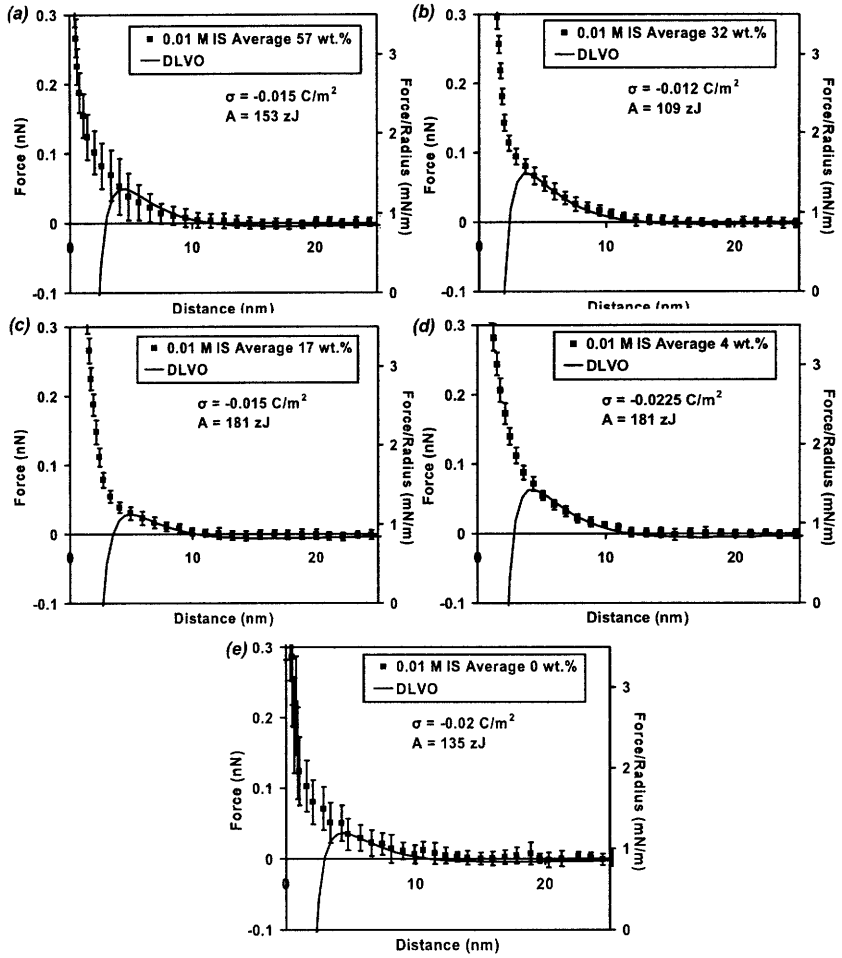

Figure 6-7. Averaged high resolution force spectroscopy data on approach (the number of experiments, n~20 at 3 different sample locations for each curve) was for adult bovine cortical tibial bone perpendicular to long bone axis for different mineral contents at 0.01M and pH = 6.5 using a COO^--SAM functionalized probe tip (surface charge per unit area, σ_{COO^-} ~ -0.02 C/m^2) compared to Derjaguin-Landau-Verwey-Overbeek predictions. The Hamaker constants were fixed to the average values calculated from the jump-to-contact distances at 3M. The tip radius and surface charge per unit area were also fixed parameters. The surface charge per unit area of the surface was left as the only free fitting parameter.

Numerical estimations of surface charge from DLVO theory are given (Figure 6-8). The corresponding Hamaker constant was incorporated in the numerical fit (performed in MATLAB) and for each type of sample, the theoretical fit matched up very well given the standard deviation bars at a range greater than 3 nm. The surface charge density values were numerically fit to become $\sigma_{0wt.\%}$ = -0.02 C/m^2, $\sigma_{4wt.\%}$ = -0.026 C/m^2,

$\sigma_{17wt.\%}$ = -0.015 C/m^2, $\sigma_{32wt.\%}$ = -0.012 C/m^2, $\sigma_{57wt.\%}$ = -0.015 C/m^2. These values were plotted as a function of mineral content at 0.01 M IS (Figure 6-8). There was no surface charge calculated for the deorganified sample because of numerical inaccuracies at separation distances <3 nm.

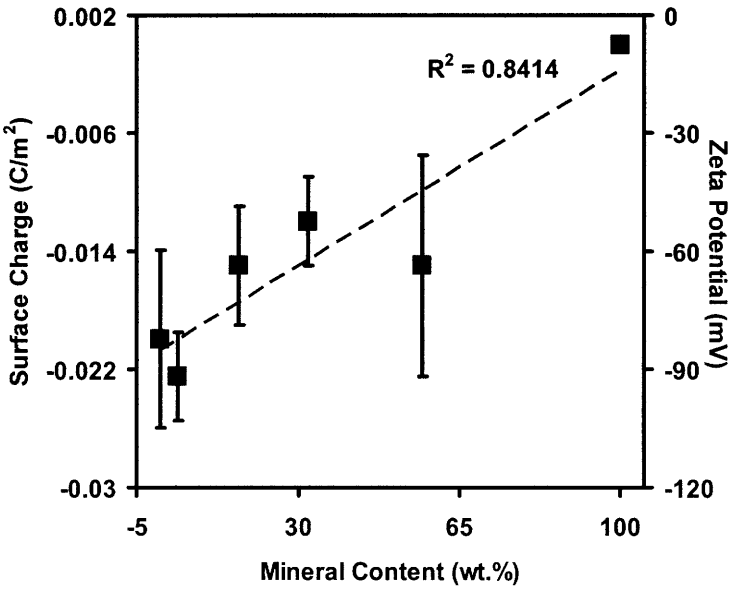

Figure 6-8. Surface charge per unit area plotted versus % mineral content for adult bovine cortical tibial bone perpendicular to long bone axis at 0.01M and pH = 6.5 from fits to Derjaguin-Landau-Verwey-Overbeek theory to nanomechanical data. .There is a statistically significant difference in the 4 wt.% sample with all of the other samples ($p < 0.01$). The 0 wt.% sample also shows statistical differences with the more mineralized samples as well ($p < 0.05$). The fits were performed with average, high, and low values (n=3) for each sample from approach curves for surface charge. The hi-lo bars represent one standard deviation for these three fits.

Position sensitive data was also recorded as images were taken in both tapping and contact mode AFM shown (Figure 6-9) for the two different positional length scales. The TMAFM images given (Figure 6-9(a)) were used for a small 1.5 μm scan size. Contact mode images for a larger 5 μm scan size are also shown (Figure 6-9(b)). The positions that force pulls were taken at are given by targets which are the amplitude and deflection images respectively. The images taken in aqueous ionic solution appear to

have similar surface morphologies compared to that of the same undemineralized bone taken in air. Averaged force-distance curves for each of the 9 positions plotted on top of one another upon approach are all shown for both sets of images (Figure 6-10). The surface charge behavior appears to be similar for both positional length scales. On a log y-axis, the repulsion begins at approximately ~5 Debye lengths away from the surface, indicating significant electrostatic repulsion in the system.

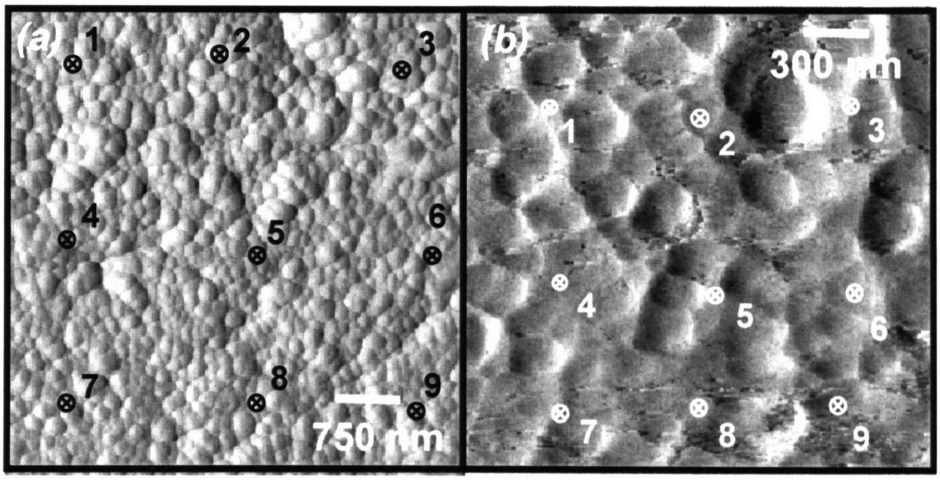

Figure 6-9. Contact mode AFM *(a)* deflection image of undemineralized (57 wt.% mineral content) adult bovine tibial cortical bone perpendicular to the long bone axis taken in 0.01 M IS aqueous solution at pH 6.5 using a probe tip that was functionalized with a COO^-SAM shown with the positions of the force spectroscopy experiments located in the deflection image given by the 9 black numbered targets. Tapping mode AFM *(b)* amplitude image of the same sample where the positions of the force spectroscopy experiments are located in the amplitude image signified by the 9 white numbered targets displayed.

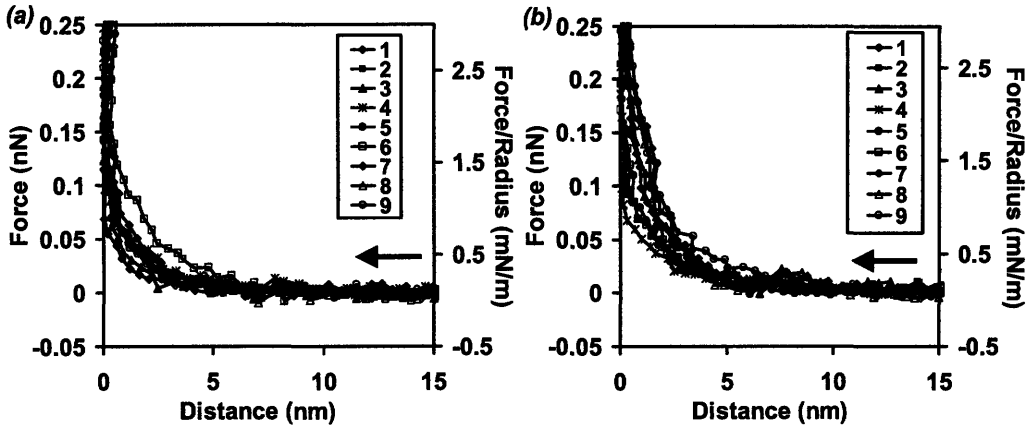

Figure 6-10. High resolution force spectroscopy data upon approach to undemineralized (57 wt.% mineral content) adult bovine tibial cortical bone perpendicular to the long bone axis taken in 0.01 M IS aqueous solution pH 6.5 using the same cantilever probe tip functionalized with COO^- SAM that was used to image (Fig. 9), at each location specified for the *(a)* 5 μm (1.5 □m spacing between sets of 20 experiments at each location) and *(b)* 1.5 μm (500 nm spacing between sets of 20 experiments at each location) scan sizes.

6.3.3 Adhesion

Upon retract (probe tip moving away from the surface), long-range, nonlinear attractive events were frequently observed for the partially demineralized bone but rarely for the undemineralized sample. Typical F-D curves upon retract are shown (Figure 6-11). There are what appear to be larger scale pull-off events with smaller "saw-toothed" behavior littered throughout the retraction. The larger scale regions appear to be localized around 100 and 150 nm from the surface. Plots of the radius normalized adhesion force and pull-off distance show that there is little variability with IS in adhesion. Corresponding frequency histograms of the adhesion force and pull-off distance are given (Figure 6-12). The distribution of retraction events appear to be fairly regular with a minimal degree of bimodality in (Figures 6-12(a) and 6-12(f)).

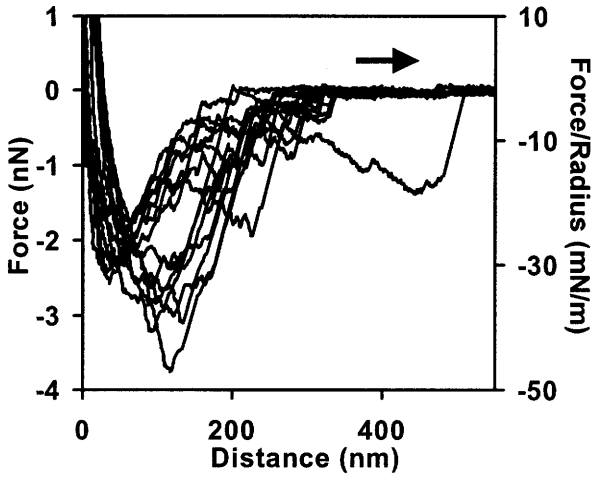

Figure 6-11. Typical nanomechanical data upon retract from the surface of adult bovine cortical tibial bone perpendicular to the long bone axis (4 wt.% mineral) at 0.01 IS and pH. The adhesive events are localized around two general regions about ~100 nm and ~150 nm from the surface.

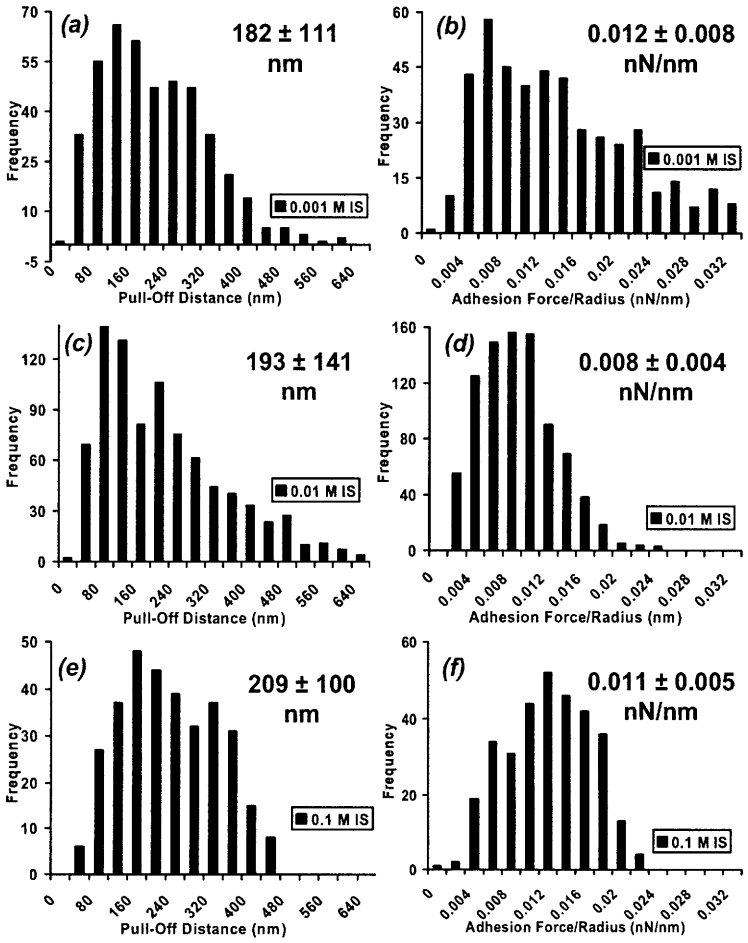

Figure 6-12. The frequency histograms are plotted at 0.001 M (n = 445), 0.01 M (n = 869), and 0.1 M (n = 326) ionic strengths for pull-off distance *(a)*, *(c)*, *(e)* and normalized adhesion force *(b)*, *(d)*, *(f)* on the 4wt.% mineral content bone sample. There appears to be a regular distribution for these values around the averaged values shown in the insets.

For ~4wt.%, the average maximum attractive Force/R_{TIP} was ~12.4 ± 7.7 mN/m, ~7.7 ± 4.1 mN/m, and ~11.0 ± 4.6 mN/m for 0.001 – 0.1 M IS, respectively. The results were minimally statistically different ($p < 0.01$). Detachment distances were ~182 ± 111 nm, ~194 ± 141 nm , and ~209 ± 100 nm. These values were statistically insignificant for 0.001-0.01M IS comparisons, $p > 0.1$, and were on the order of the contour length of individual collagen molecules. Pull-off events were rarely observed (<5%) for undemineralized bone (57 wt.%) but were very frequent (~90%) for the 4 wt.% sample.

Mineral Content (wt.%)	Contact Angle	Hamaker Constant (zJ)	Surface Charge (-C/m²)	Calculated Zeta Potential (-mV)
100	69.2 ± 6.7	41 ± 33	n/a	n/a
57	59.2 ± 4.7	153 ± 116	0.015 ± 0.0075	62
32	56.7 ± 9.2	109 ± 85	0.012 ± 0.003	52
17	60.7 ± 8.7	181 ± 130	0.015 ± 0.004	62
4	52.2 ± 8.2	181 ± 100	0.026 ± 0.003	92
0	49.8 ± 7.1	135 ± 85	0.02 ± 0.01	77

Table 6-1. Calculated values for Hamaker constant, surface charge, and its corresponding zeta potential estimated by chemically specific high resolution force spectroscopy for adult bovine cortical tibial bone perpendicular to long bone axis at 0.01M and pH = 6.5 for various mineral contents.

6.4 Discussion

In this paper, recently optimized nanomechanical techniques were used to measure inter-molecular forces with extremely sensitive precision. Nanosized cantilever tips of known chemistry and geometry were used to probe different samples of bone with

varying mineral contents. This study presents a controlled way of assessing surface potential and charge, which can also be carried out as a function of nanoscale position. Although not likely to largely influence electrical potentials, mineral content, however, is known to play a significant role in the nanoindentation (inelastic and cohesive-frictional) behavior of bone at these length scales [178], thus revealing the dual nature at the nanoscale of the two major components in bone. The exact function of surface charge and van der Waals forces in bone function is still an open question as related to the biological processes in cell activity and orthopedic implant stability.

6.4.1 Approach

The HRFS experimental data reveals that much of the intersurface interaction is dominated by electrostatic double layer forces as the net repulsion typically begins at distances that are ~5 Debye lengths away from the surface. At 0.01 M IS where the Debye length is 2.96 nm and most of the electrostatic fits performed (and presented), this check is confirmed as repulsion begins at distances >10 nm. At high IS (3 M), on the other hand, the net force is purely attractive, which is expected due to the large number of counter-ionic charge screening. Hamaker models fit very well to the experimental data between 3 to 6 nm where attractive forces were shown to be dominant with charge screening. At distances less than 3 nm, in general, contact between the probe tip and surface would ensue giving rise to infinitely large repulsion forces. At distances greater than 10 nm, van der Waals forces were not sensed between the two surfaces. The trend of Hamaker constants 41 and 181 zJ at varying mineral contents exhibited definite statistical significance between the 100 wt.% specimen and the rest of the samples ($p<0.005$). But

when comparing the rest of the samples with each other, there were only slight statistical differences using the paired t-test between the different values ($p<0.05$). This result suggests that much of the van der Waals forces are tied directly to the organic phase in bone tissues. It is possible that there is an optimal degree of mineralization in conjunction with organic material that gives rise to greater surface attraction due to spatial positioning and ordering between consituents. A more detailed and controlled study would be required in order to probe these surface heterogeneities. Typical Hamaker constant values are 69 and 52 zJ for COO^- and SO_3^- monolayers respectively [182, 184], implying that bone has a more diverse surface structure as opposed to the different SAM surfaces where hydrophobic carbon layers attract one another when polar components are charge shielded. HRFS using a COO^- SAM on glass/Ti/Au/C16OH/HOH/C16OH/Au/Ti/ Si3N4 [184] was measured to be 34 zJ, which is 4.5x less than that measured for the undemineralized bone sample surface.

All of the different bone samples with varying mineral contents exhibited a net negative surface charge per unit area ranging from -0.012 to -0.026 C/m^2. The DLVO model fit the experimental data extremely well for distance greater than 3 nm and would increasingly differ from the data with decreasing tip sample separation distances less than 3 nm. This deviation is presumed to be due to the increasing nature of non-uniform permittivity and the ions taking up more space at smaller separation distances. Overall, the trends using the paired t-test for each of the difference values at various mineral contents exhibited slight statistical significances ($p>0.01$) but there was no direct correlation of surface charge to mineral content. This finding indicates that the surface charge does not largely vary with mineral content. This gives rise to the possibility that

the organic phase, rather than the mineral component, dominates the nanoscale interactions in these samples. Zeta potential measurements, which will be discussed in more detail later on confirms the overall net negative surface charge found in bone. While the actual origin for the overall negative charge in bone is still an area of investigation, there are several reasons why nature could have designed bone to be negatively charged. One possibility for why bone is negatively charged is because the surface glycocalyx of most cells found in nature are negatively charged due to the large number of polypeptides that migrate through the fluidic predominantly lipid membrane. Several of these proteins are used for recognition so it is possible that even though bone does not serve the same purpose as typical cells found throughout the body, it is a material that cells readily will attach to, migrate along, and proliferate on. It is thought that electrostatic charge is a vital element to cell-cell and cell-surface detection and so bone naturally will display these characteristics. Surfaces that are shown to exhibit blood compatibility are also negatively charged [185, 186] which is a category under which bone would obviously lie. HA formation is thought to occur more readily on negatively charged surfaces in simulated body fluid (SBF) as well, attracting positive Ca+2 ions to the surface initiating apatite precipitation [185, 187, 188]. If the electrostatic potential is governed by the organic, then the negative charge implies that the amino acid side chains have a tendency to have low pKa values.

As more and more mineral was removed, there appeared to be minimal change in the surface charge. This result implies that the mineral has little influence on the surface charge of bone. Changes due to the mineral removal such as creation of underlying voiding or pore-structural alterations could also contribute to surface charge

measurements. Where before, there was little methodology developed for directly measuring surface charge [185], here we present an approach that allows for further study (e.g. dynamically monitoring surface charge, species specific measurements, precipitation observations) to be done.

The question then becomes where this highly negative charge originates from. The chief molecular constituents found in bone include tropocollagen polypeptides, hydroxylation through hydroxyl-hydroxylysine linkages, noncollagenous protein (NCP) organic, and hydroxyapatite mineral. The triple helical intertwining of tropocollagen makes up ~88 wt.% of the organic material in bone with ~75% of the groups being neutral (predominantly glycine and hydroxyproline) at pH 6.5 [189]. Similarly, ~12.6% are positive and 12.1% are negatively charged, making collagen predominantly neutral. Hydroxylation bonds are covalent in nature, which are neutrally charged as well [190]. The mineral hydroxyapatite ($Ca_{10}(PO_4)_6(OH)_2$), which is composed of calcium phosphate, calcium carbonate, calcium fluoride, calcium hydroxide and citrate is likely to be neutral at pH 6.5 as well [152]. In contrast, noncollagenous proteins are highly negatively charged in nature [143], making them to be the most likely source for electrostatic behavior in bone. The data presented here not only gives further evidence that NCPS are negatively charged, but also supports evidence that NCPs play a large role in bone metabolic function [142].

6.4.2 Comparison to zeta potential

Even though it is inferred that the surface charge does not depend on mineral content, the surface charge measured for phase pure HA using the same technique came

out to range from -0.0037 to -0.072 [188], which is similar to that of overall bone albeit slightly greater in magnitude. This result could be due to inherent differences in processing and ion ordering between synthetic HA and naturally occurring HA. Another caveat to the comparisons is that PB theory does not include a potential drop in the immobilized liquid layer flush against the surface which actually moves with the particle in zeta potential electrophoresis. The surface charge model used in this paper would appear to represent more accurately the electrostatic interaction of a biological macromolecule or cell approaching a surface as the effective charge at the slip plane is what the mobile species usually feels inside the more diffused double layer.

Several studies have indicated that the electrokinetic behavior of bone tissue is dominated by the ultrastructure found in the organic phase leading to an overall negative charge at physiological conditions [165-167, 191, 192]. It was also found that the more negative the zeta potential is in magnitude, the greater the induction of bone growth is in correlation [149]. This negative charge is thought to arise from poverty in hydroxyl and phosphate groups at the surface [193]. As a result the electromechanical behavior of bone can be traced back to the interrelationship between collagen fibrils and the mineral particularly as the channel vasculature in bone varies functionally from region to region [191]. Furthermore, interactions between particular ions in solution have been found to have profound effects on the electrical potentials in bone [165, 168, 169, 173]. Separate phosphate and fluoride ion exposure after detergent treatment was shown to reduce the mechanical properties of intact but not demineralized samples while NaCl would not mechanically alter either one. The reason for this phosphate and fluoride ion occurrence is when the surrounding vasculature has been removed (from the detergent), due to a

competition with the negative organic domains for calcium binding sites, a partial debonding results between mineral and organic constituents, affecting the mechanical behavior [145]. Fluoride ions are found to exchange irreversibly with the surface hydroxyl ions as they become a part of the crystal HA, but phosphate ions exchange reversibly as organic constituents are found to reestablish linkages with the mineral phase immediately [146]. IR spectra studies reveal that the mineral phase is unaffected by either phosphate and fluoride treatment [146]. Conversely, the excellent bonding of hydroxyapatite to bone is thought to be due to native calcium phosphates that cyclically precipitate and grow epitaxially on the bone surface, allowing for a collagen incorporated granular bonding layer between the two surfaces [163, 173, 194].

6.4.3 Position sensitive HRFS

The spatially dependent experimental results shown previously (Figures 6-9 and 6-10) indicate a relative uniformity along the surface at length scales less than 5 μm wide with force pulls at distances 1.5 μm and 500 nm apart. With such complex structure in bone, it would be expected to see intermolecular force heterogeneity throughout the material. At the distances probed, it is surprising to see an overall homogeneous nature to the force-distance behavior. This result suggests a consistent distribution of charge throughout the length scale that was probed. It would be worthwhile to probe length scales significantly larger in order to capture charge allotments throughout the hierarchical complexity. Some regions in particular that would benefit from such analyses would be along and through microcracks, osteocyte lacunae, circumferential lamellae, and osteonal and interstitial bone.

6.4.4 Retract adhesion

Upon retract, there were a significant amount of pull-off forces from the samples with exposed collagen fibrillar structures. There was no statistical difference between adhesion forces or pull-off distances at 0.1 to 0.001 M IS ($p<0.005$). The maximum adhesive force normalized with radius is 0.0375 nN/nm. This value is typical of non-covalent interactions (e.g. hydrophobicity, London Dispersion forces, ionic, or hydrogen bonding). The average normalized adhesive force is 10.4 nN/nm. A previous study that compared the adhesion of the most abundant protein found in humans, human serum albumin (HSA) to an Au as well as CH_3 and COO^- SAM surfaces gave values of 21, 26, and 1.9 nN/nm respectively [184]. HSA was measured to exhibit a surface charge of -0.0064 C/m^2, which is comparable to our bone surface charge. The CH_3 and COO^- SAM surfaces are opposite in terms of polarity and it appears that the bone surface adheres nonspecifically somewhere in between that of nonpolar and polar behavior. The averaged pull-off distance of 195 nm is on the order that of the length of tropocollagen molecules (~300 nm), which is an expected result as the major protein component in the partially demineralized samples is collagen.

6.4.5 Summary and Conclusions

From directly measuring the intermolecular forces available in bone using precise nanomechanical methodology, the surface charge does not appear to vary significantly across a range of mineral contents. This result highlights the dual nature of the organic and inorganic components found in bone. Where mineral content significantly affects mechanical behavior, the electrostatic potential is minimally influenced. This is a

surprising result when held in comparison to synthetic phase pure HA, which is shown to exhibit a surface charge comparable to that measured here. It would be worthwhile to further examine the intermolecular and morphological differences between natural and synthetically produced HA. From numerous pull-off instances indicative of collagen fibrils being extracted from the surface, a more precise study concerning the interaction between mineral and collagen would also be beneficial.

Chapter 7

Structural and Nanoindentation Studies of Stem Cell-Based Tissue Engineered Bone in an Ectopic System Construct and a Non-Union Fracture Repair

Part of this chapter was published as a paper in Journal of Biomechanics in 2006 [195].

7.1 Introduction

Treatment of massive bone defects presents a major challenge in orthopaedic medicine as current methods through prostheses or transplantation do not provide long term stability and function. Current methods of treating massive bone loss mainly depend on artificial prostheses, which fail in the long term and often result in the loss of function and morbidity. Gene therapy offers a promising avenue to an efficient biological therapy for regenerating massive bone defects. In particular, Mesenchymal Stem Cell (MSC)-based tissue engineering has been reported to be an innovative and efficient approach for regenerating bone tissue in vivo [196-208]. The expression of an osteogenic growth factor from the BMP family like BMP-2, BMP-6 and BMP-9 by MSCs exerts a paracrine effect on the host MSCs and an autocrine effect on the engineered MSCs [198, 209]. Thus, enhanced bone formation is achieved by both the host MSCs and the engrafted engineered MSCs. The implantation of genetically engineered MSCs overexpressing the BMP-2 osteogenic gene in vivo has led to bone regeneration and fracture healing in various models including radius and calvaria non-unions, and spinal fusion. In spite of

the extensive research performed on genetically engineered stem cell-based bone tissue engineering during the last decade, no knowledge of the intrinsic structural and nanomechanical properties of such bone tissue exists. In order for this approach to be optimized for clinical settings, a thorough multiscale analysis of the chemical and physical properties needs to be systematically carried out.

New nanoscale methodologies, applied in particular to bone, such as atomic force microscopy imaging [8, 19, 70, 210, 211] high resolution force spectroscopy [21, 62, 212], and nanoindentation [8, 16, 17, 21, 26] enable a window into the fine details of structure and mechanical behavior at extremely small length scales. In some cases, micro- and macroscopic assays, which yield averaged quantities over larger length scales, may not be sensitive enough to identify the underlying differences between two different sample populations and hence, nanoscale studies are desirable. In addition, nanoscale methodologies are useful when the volume of material available is too small for larger scale analyses, for example with tissue-engineered bone formation in critical sized defects and mouse models. The accuracy of biomechanical properties reduced using traditional engineering beam theory applied to whole bone bending tests on mouse bone has also been questioned [213]. Nanoindentation studies, in particular, have focused on differences between cortical and trabecular bone [23], variations as a function of distance from the osteonal center [17] and through the femoral cortex [214], anisotropy [25], viscoelasticity and time-dependent plasticity [49], and variations due to mineral content [8, 26]. More clinically relevant studies are starting to appear including nanoindentation properties of aged bones [50, 215, 216] the senescence-accelerated mouse as a model for senile osteoporosis [213, 217], and rat osteopetrotic mutations [110].

Here, for the first time, a report is given of the comparison of the nanoindentation properties and nanoscale deformation mechanisms of tissue-engineered bone derived from genetically engineered MSCs that were implanted ectopically in mice in vivo to native femoral bone adjacent to the transplantation site. Nanomechanical analysis was also performed on an orthotopic site, a non-union fracture in the radius bone, which was repaired using genetically engineered MSCs overexpressing the BMP-2 gene. Other supplementary techniques were employed to further interpret the nanoscale data including; back-scattered electron (BSE) microscopy to estimate mineral content, Raman spectroscopy to identify chemical bonds, energy dispersive X-ray (EDX) analyses for elemental analysis, histology and micro-computerized tomography (μCT) scans for morphology and quantitative analysis. Such multitechnique investigations that combine new nanotechnological methodologies with traditional characterization tools will be crucial for the advancement of gene therapy and tissue engineering platforms towards the clinical settings.

7.2 Materials and Methods

7.2.1 Genetically engineered MSCs expressing BMP2

The genetic engineering of MSCs to express inducible rhBMP-2 has been described in detail previously [200]. Briefly, Cells from the C3H10T1/2 MSC line were transfected with a ptTATop-BMP2 plasmid vector that encodes for both a tetracycline transactivator and rhBMP-2. The inducible human BMP-2 expression vector, ptTATop-BMP2, has a bidirectional promoter (TATA sequence) and consists of six tetracycline operators flanked by two transcriptional units with opposite orientations. In this vector,

the level of the transactivator, which activates the bidirectional promoter, as well as the expression of hBMP-2 can be regulated by doxycycline, a derivative of tetracycline, yielding higher levels of gene expression as well as a greater frequency of inducible clones. The engineered MSCs were grown in DMEM supplemented with 2mM L-glutamine, 100units/ml penicillin, 100units/ml streptomycin, and 10% FCS (*Biological Industries*, Kibbutz Beit Haemek, Israel). Doxycycline was supplemented to the culture media in order to prevent cell differentiation before implantation.

7.2.2 In vivo ectopic bone formation

For transplantations in vivo the BMP2 expressing MSCs were transplanted in the following manner: After trypsinization, aliquots of approximately 3×10^6 cells were seeded on pre-cut, biodegradable fiber mats (3×3 mm) fabricated by the process of electrospinning[209]. Briefly, the solution of poly(lactide-co-glycolide) (PLAGA, 50:50) in a mixture of DMF and THF (35 wt.%) was loaded into a glass syringe with a capillary nozzle. The polymer solution was then electrospun at an electric potential of 30 kV and at a working distance of 30cm under ambient conditions to develop fibers having diameters in the range of 4-8μm. Prior to transplantation, C3H/HeN female mice age 6-8 weeks (n=10) were anesthetized using ketamine-xylazine mixture, injected intra-peritoneal, and the skin of the thigh muscle was swabbed with isopropyl alcohol (70%), and chlorhexidine gluconate (0.5%). The skin and muscle were cut and the cell-seeded scaffolds were transplanted. Ectopic bone formation was monitored using in vivo fluoroscopy (*Premier Encore Fluoroscan*, Hologic, MA, USA) once in two weeks. Doxycycline was not supplemented to the mice drinking water in order to induce BMP-2

expression, which would lead to bone formation. Four weeks post transplantation, when the formation of substantial bone tissue was verified by fluoroscopy, the mice were sacrificed.

7.2.3 In vivo orthotopic bone formation

After trypsinization, aliquots of approximately 2×10^6 cells were seeded on pre-cut, collagen I biodegradable scaffords and transplanted in vivo in 2.5 mm radial defects in immunocompetent mice. Prior to transplantation, C3H/HeN female mice age 6-8 weeks (n=10) were anesthetized using ketamine-xylazine mixture, injected intra-peritoneal, and the skin of the thigh muscle was swabbed with isopropyl alcohol (70%), and chlorhexidine gluconate (0.5%). The skin and muscle were cut and the cell-seeded scaffolds were transplanted. Orthotopic bone formation was monitored using in vivo fluoroscopy (*Premier Encore Fluoroscan*, Hologic, MA, USA) once in two weeks. Doxycycline was not supplemented to the mice drinking water in order to induce BMP-2 expression, which would lead to bone formation. Eight weeks post transplantation, when the formation of substantial bone tissue was verified by fluoroscopy, the mice were sacrificed.

7.2.4 Micro-Computerized Tomography (μCT)

A quantitative morphometric analysis of the bone formation, in intramuscular transplants, was undertaken using μCT scanning (*micro-CT40*, Scanco, Switzerland). Mice were sacrificed and the transplanted leg was dissected and subjected to micro-CT scan in vitro at a resolution of 20 μm. The bone tissue was segmented from marrow and

soft tissue using a global thresholding procedure. In addition to the visual assessment of structural images, morphometric indices were determined from the microtomographic datasets using direct 3D morphometry [218, 219]. The ectopic bone volume was computed by contouring the ectopic bone image and the bone density was calculated according to the ratio of bone volume to total tissue volume.

7.2.5 Bone sample preparation

Following ex vivo μCT scanning, bone samples were dissected from the sacrificed animals, rinsed with PBS, and embedded in glycol methacrylate using a JB-4 embedding kit (*Electron Microscopy Sciences*, PA, USA) in vacuum, according to the manufacturer protocol. Samples were prepared without chemical fixation, demineralization etches, or alcohol dehydration and stored in aqueous solution to ensure maximum hydration and as close to physiological conditions as possible. Blocks were cut with a diamond impregnated saw (*Buehler*) and then polished on Al_2O_3 paper (*South Bay Technologies*) from 9-0.05 μm grit size. For histology, the bones were fixed in 4% buffered formalin for 24 hours and decalcified in 0.5M ethylenediamine tetraacetic acid for three weeks. Samples were then passed through ethanol grade and embedded in paraffin. Paraffin blocks were sectioned into 5□m thick sections using an automated microtome (*Leica RM2165*, Germany) and stained using hematoxilin-eosin (H&E) and Masson's Trichrome stains.

7.2.6 BSE, Raman Spectroscopy, and EDX

A low vacuum electron detection ESEM (*Philips/FEI* XL30 FEG-SEM, Hillsboro, Oregon, USA) was employed in back-scattered mode a water vapor environment to image uncoated samples (electron acceleration =15 kV, operating current =180 μA, working distance =10.0 mm, water vapor =0.3 Torr, depth resolution ~3 μm, spatial resolution ~10 μm). Mineral contents were calculated directly from grayscale pixel values which directly correlate with average atomic number and mineral content (Skedros et al., 1993). Raman spectroscopy (*Kaiser Hololab 5000R*, Ann Arbor, Michigan, USA, depth resolution ~1μm, spatial resolution ~50 μm) was carried out at 785 nm utilizing coherent CW Argon/Ion and Ti/S Lasers using a 100 μm diameter optical fiber to maximize throughput. Elemental composition analysis was obtained via energy dispersive X-ray analysis (EDX) through a sapphire EDX detector (EDAX, Mahwah, New Jersey, USA, depth resolution ~3 μm, spatial resolution ~10 μm) with LEAP+ crystals for optimal light element performance.

7.2.7 Nanoindentation

Load-controlled nanoindentation experiments were conducted in ambient conditions using a *Hysitron, Inc.* (Minneapolis, Minnesota USA) Triboindenter and a Berkovich (trigonal pyramid) diamond probe tip following a protocol previously reported[8]. Each experiment involved a four segment load function; a 3 second hold at zero load, a constant loading rate of 50 μN/sec until the maximum set peak load was reached, a hold of 20sec,[1] and finally a constant unloading rate of 50 μN/second. Values for elastic

[1] To ensure that creep effects were kept at a minimum, the variation in elastic modulus was calculated (Oliver and Pharr, 1992) for three different experiments; *1)* the hold period was varied between 10 to 90 sec., *2)* after the hold period, the sample was unloaded to 20% of the maximum force and reloaded back to

moduli were calculated from 95-20% of the initial unloading curve by fitting these data to contact mechanical theory for an isotropic, elastic half-space (O-P method[2]).[2] Hardness (H=maximum load/area at maximum load) values were calculated from both the O-P contact area at maximum load and from contact areas measured by AFM imaging of residual indents immediately after indentation.[3] A 3-way ANOVA statistical analysis as performed on 2500 indents using *SYSTAT* software package (Point Richmond, CA, USA) which takes into account the different types of bone (femoral and engineered), animal (6 different animals), and maximum loading (500, 1000, and 7000 μN). Residual indents were imaged within a 20 minute time period after indentation using a *Quesant* Q-Scope 350 and Si_3N_4 Wavemode NSC16 cantilevers in tapping mode as previously reported[8]. There were 6 pairs tested with ~50 indents per sample at each maximum load, where the indents were spaced 7 μm apart creating a grid 60×60 μm in size (~40% of the total femur cross-section~150□m). Tests were conducted parallel to the cortical long bone axis for the femoral bone and in the cortical-like surface region for the engineered bone.

---

the maximum force for several cycles, and *3)* the loading/unloading rate was varied by 2 orders of magnitude (the limit of the instrument). All three series of experiments found that the variation in elastic moduli was < 10%.

[2] It is important to note that indentation moduli reported here as estimated by the O-P method should be regarded as "apparent" or "effective" since this model neglects plasticity, viscoelasticity, pileup, and anisotropy (Oliver and Pharr, 2004) and the fact that they are known to vary with length scale (Malzbender, 2005). Recently, more advanced theoretical approaches have started to be developed which are continuum mechanical in nature such as anisotropic elastic and elastic- perfectly plastic finite element analysis (Fan et al., 2004; Tai et al., 2005), poro-micromechanical models (Hellmich and Ulm, 2005), and two-phase composite formulations (Oyen and Ko, 2005). These models will be explored in future studies but for the purposes of this paper, i.e. to compare an experimental model and a control, the O-P method is sufficient (Tai et al., 2005) and also has the advantage of enabling the analysis of a larger amount of data (>2500 indentation curves) to get a more accurate statistical distribution in a reasonable period of time.

[3] The hardness calculated by the O-P method represents resistance to total deformation (elastic, viscoelastic, plastic) while the AFM calculated hardness represents resistance to plasticity. The O-P hardness has a tendency to underestimate the contact area, hence overestimate the hardness (Oliver and Pharr, 2004).

7.3 Results

7.3.1 μCT Analysis of Ectopic and Orthotopic Bone at Implant Sites

μCT scans shown in Figure 7-1 indicate significant growth of ectopic bone in between the femur and tibia at the transplantation site. Quantitative analysis performed on the scanned engineered bone tissue indicated that the average bone volume reached 21.84±2.61 SE mm^3 (n=6). The bone density (bone volume normalized by the total tissue volume) was calculated to be 0.19±0.0051 SE (n=6). 2D images demonstrate that the new bone tissue is composed of distinct compact (Figure 7-1(c)) and trabecular regions (Figure 7-1(d)), as indicated by the degree of porosity on the outer rim and the inner region, respectively. The outer and inner surfaces of the cortical –like region can be visualized using 3D reconstruction images (Figure 7-1(a) – outer aspect; Figure 7-1(b) – mid section showing inner aspect). All implants formed an oval-shaped structure following the initial 3D structure of the scaffold on which the cells had been seeded prior to implantation. These images highlight the powerful osteogenic potential of genetically engineered MSCs, which can induce robust bone formation within a short period of time. μCT scans of orthotopic bone shown in Figure 7-2 indicate substantial growth of engineered bone indicative of fracture healing at the transplantation site. Quantitative analysis performed on the scanned engineered bone tissue indicated that the average bone volume reached X SE mm^3(n=6). The bone density (bone volume normalized by the total tissue volume) was calculated to be X (n=6). These images highlight the powerful osteogenic potential of genetically engineered MSCs, which can induce robust bone formation within a short period of time.

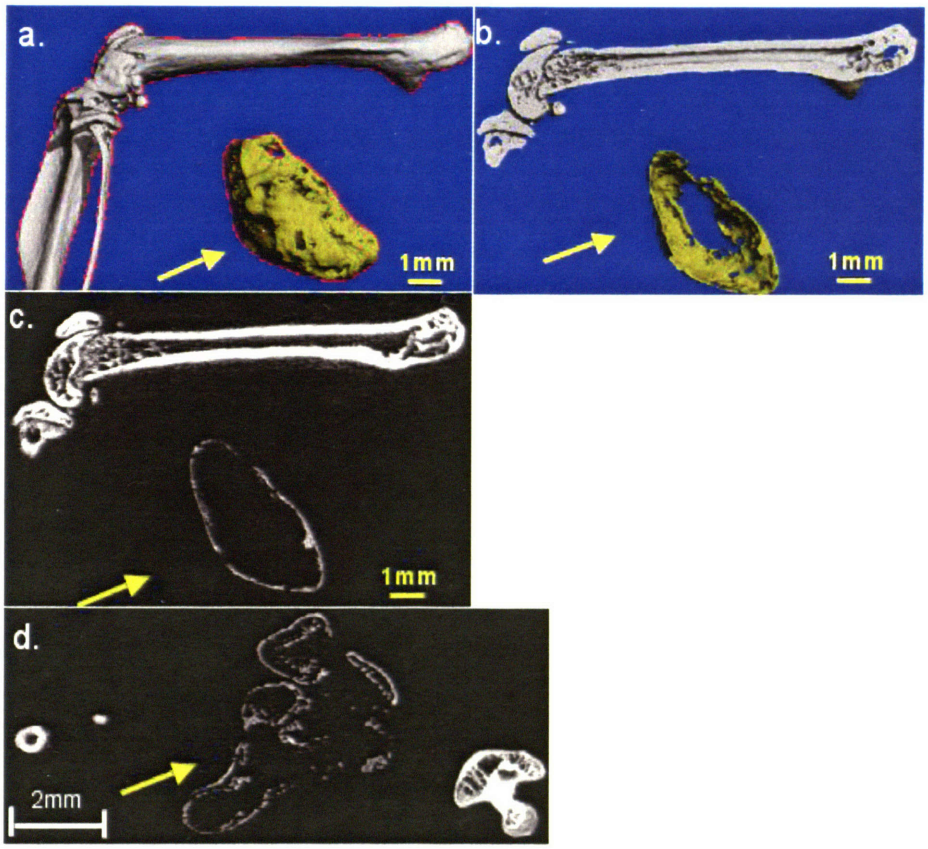

Figure 7-1. 3D *(a and b)* and 2D *(c and d)* μCT images of femoral and genetically engineered bone (the latter indicated by arrows). 3×10^6 BMP2 expressing MSCs were implanted in the thigh muscle of C3H/HeN mice. Four weeks post implantation the mice were sacrificed and the legs were subjected to μCT scans at 20μm resolution. Images obtained by μCT demonstrated the formation of new bone tissue within the implantation site. The new tissue had an outer cortical-like surface *(c)* and an inner compartment showing cancellous-like features (*d* Engineered bone was formed as an oval-shaped structure following the initial shape of the polymeric scaffold on which the cells were seeded. The outer *(a)* and inner *(b – mid section)* surface of the cortical-like region can be visualized using a 3D reconstruction of the μCT scans.

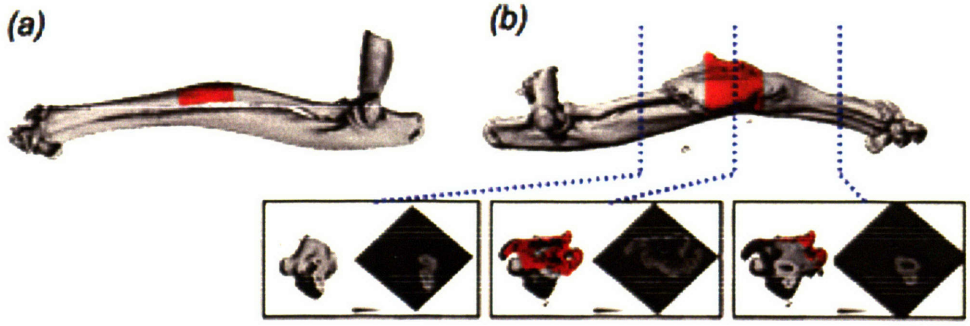

Figure 7-2. 3D μCT images of *(a)* native radial and *(b)* a radial defect filled with genetically engineered bone. 3×10^6 BMP2 expressing MSCs were implanted in a 2.5 mm radial defect of C3H/HeN mice. Eight weeks post implantation the mice were sacrificed and the areas of interest were subjected to μCT scans at 20μm resolution. Images obtained by μCT demonstrated the formation of new bone tissue within the implantation site.

7.3.2 Histological Analysis

H&E staining of 5μm sections of the newly formed engineered bone four weeks post implantation validated the results obtained by μCT scans (Figure 7-3). A dense region of bone was seen at the outer aspect of the implant resembling compact bone. In the inner compartment of the implants more sparse bone trabecules were evident (Figures 7-3(b-d)) surrounded by bone marrow. Thus, the inner compartment showed resemblance to native trabecular bone tissue. The presence of collagen within the new engineered bone trabecules was further demonstrated by a positive Masson's Trichrome staining (Figures 3(e) and 3(f)).

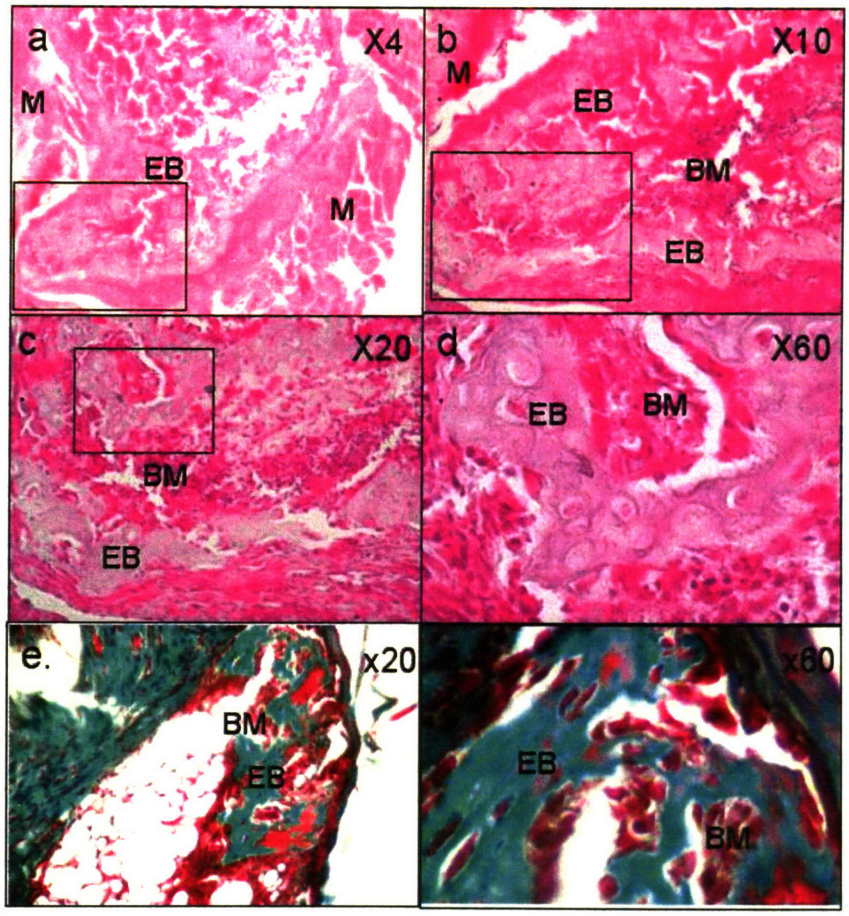

Figure 7-3. Histological evaluation of genetically engineered bone. Following μCT scans; bone samples were fixed in formalin and processed for histology. Hematoxilin-Eosin staining of 5μm paraffin sections demonstrated the formation of an outer region of dense bone tissue, surrounding an inner compartment containing a cancellous-like inner portion (*a*). Higher magnifications showed the presence of bone marrow within in the new bone (*b, c, d*). Masson's Trichrome staining indicated that the engineered bone was composed of collagen fibers stained with green color *(e, f)*. EB=engineered bone; M=muscle; BM=bone marrow. *(b* is a 10× magnification of the inlet in *a; c* is the magnification of the inlet in *b; d* is the magnification of the inlet in *c).*

7.3.3 Surface Morphology and Topography of Ectopic and Orthotopic Bone

A BSE image of the femoral cortical bone (view down the long axis, Figure 7-4(a)) shows a relatively uniformly mineralized structure (as reflected by the image grey scale) over ~1/10 of the entire femoral cross-section with uniformly shaped and oriented

lacunae and canaliculi. The genetically engineered bone (Figure 7-4(b)) shows a similar degree and uniformity of mineralization as the femoral bone, but with larger lacunae that are more nonuniform in orientation and shape. Canaliculi were also observed. The femoral bone and engineered bone samples were found to exhibit ~5% and ~10% porosity, respectively, as calculated from the lacunae visible in the BSE images. The distributions of weight percent mineral content (Figure 7-5) measured from BSE image analysis were found to be statistically similar ($p<0.001$) for genetically engineered (61.2±3.3wt.%) and femoral bone (64.6±2.0wt.%). Smaller scan size BSE images (Figure 7-6) reveal that the smaller length scale nanostructure for both the femoral and engineered bone are similar as well.

BSE microscopy for orthotopic samples indicate that the relative mineral content proportions in both types of bone to be similar (~50-60 weight %). Scanning electron microscopy images show lacunae from the engineered bone similar in size, shape, and orientation to that of the surrounding native bone. A BSE image of the native radial cortical bone (view perpendicular to the long axis, Figure 7-7(a)) shows a mineralized structure (as reflected by the image grey scale) randomly distributed lacunae and canaliculi. The genetically engineered bone (Figure 7-8(b)) shows a similar degree and uniformity of mineralization as the radial bone as well lacunae and canaliculi in orientation and shape. The femoral bone and engineered bone samples were found to exhibit ~5% and ~10% porosity, respectively, as calculated from the lacunae visible in the BSE images. After a 1 second demineralization etch in 40vol.% H3PO4), banded fibrillar structures were visible via TMAFM in both types of bone (Figure 7-8).

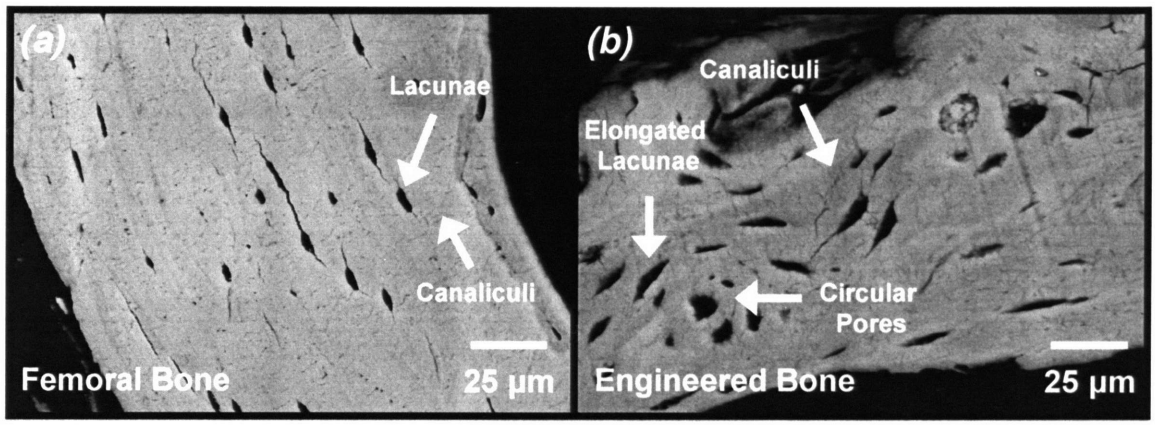

Figure 7-4. Environmental back-scattered scanning electron microscope images at 500x magnification of *(a)* femoral and *(b)* genetically engineered bone. The femoral view orientation is along the long bone axis and the genetically engineered bone is the outer cortical-like surface. Elongated pores are visible with an average aspect ratio of 3.4±1.0 and average maximum dimension of 9 ± 2µm that correspond well with the typical size of osteocyte lacunae (Currey, 2002). The maximum dimension of these pores is highly oriented within the section circumferentially. Closer inspection reveals the presence of channels emanating from the lacunae (a), which are presumably canaliculi. Osteons are not observed since mouse cortical bone does not undergo Haversian remodeling in the same manner as larger animals (e.g. bovine, human, etc.) (Bianco and Robey, 2000). BSE images of the cortical-like outer shell of the genetically engineered bone (b) shows a similar degree and uniformity of mineralization as the femoral bone, but with larger pores that are more nonuniform in orientation and shape with an average aspect ratio of 2.4±1.0 and average maximum dimension of 13±5µm where both of these parameters were statistically different from the femoral bone ($p<0.01$). It this section, we observe two larger, more circular pores surrounded circumferentially by elongated pores in the central portion of the section, and elongated pores with their long axes aligned parallel to the outer edge of the section. Canaliculi were also observed.

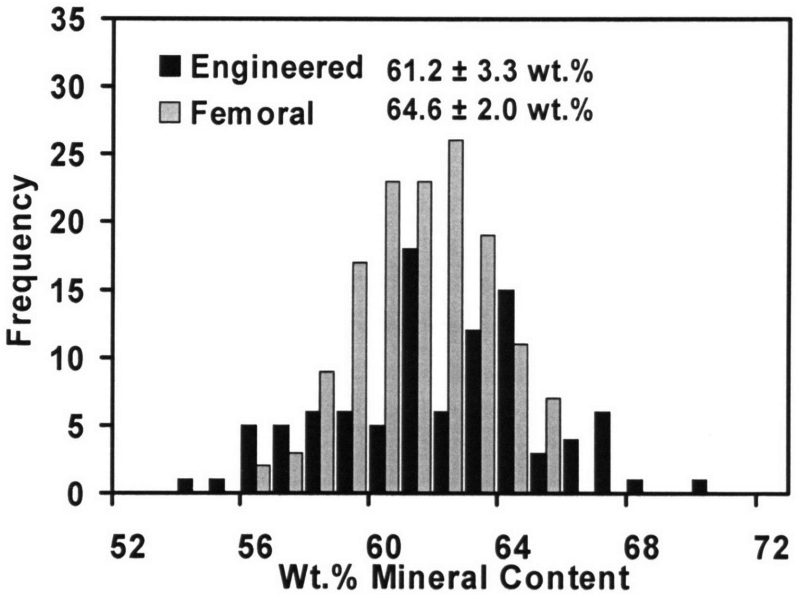

Figure 7-5. The distributions of weight percent mineral content measured from BSE image analysis of 4×4 μm square regions separated by 7 μm each (total analysis size 40×40 μm) for the genetically engineered and femoral bone.

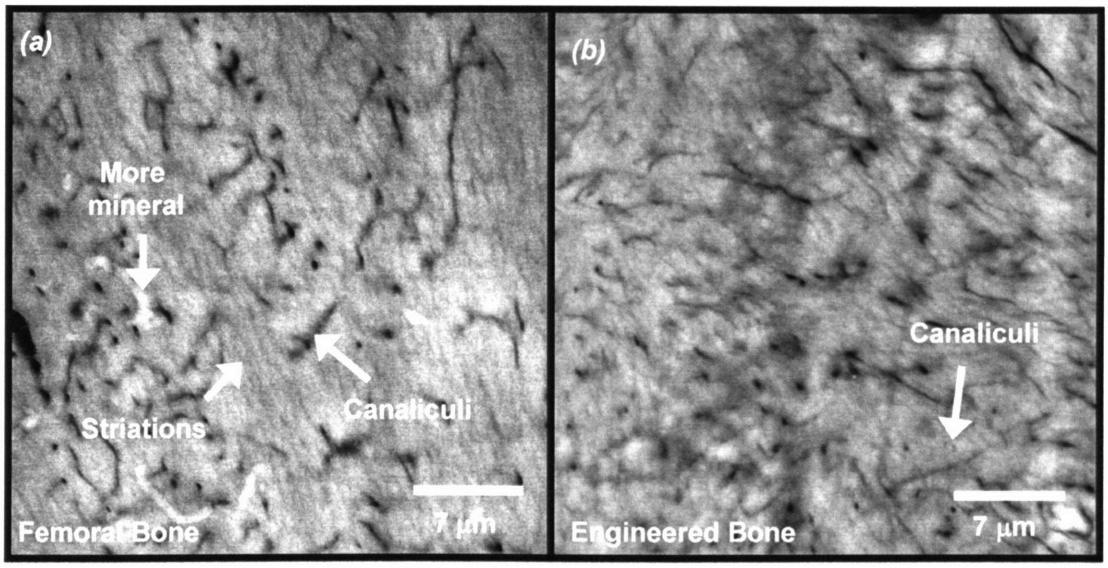

Figure 7-6. Environmental back-scattered scanning electron microscope images at 2000x magnification of *(a)* femoral and *(b)* genetically engineered bone. The femoral view orientation is parallel to the long bone axis. Heterogeneities in mineral content are visible and darker streaks throughout, whose dimensions are consistent with canaliculi. The femoral bone appears to have small localized regions of high mineral content and oriented striations running throughout the entirety of the image. While some regions appeared anisotropic, completely oriented striations were not observed in the engineered bone.

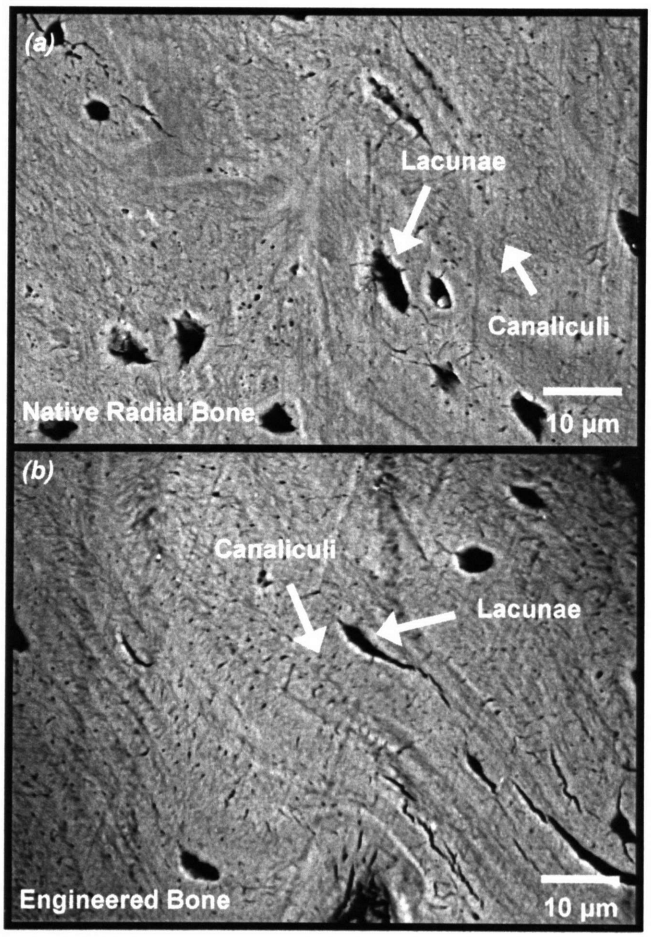

Figure 7-7. Environmental back-scattered scanning electron microscope images at 500x magnification of *(a)* native radial and *(b)* genetically engineered bone. The view orientations were perpendicular to the long bone axis for both types of bone. Elongated pores are visible with an average aspect ratio of 2.5 ± 1.0 and average maximum dimension of 9 ± 2µm that correspond well with the typical size of osteocyte lacunae[3]. Closer inspection reveals the presence of channels emanating from the lacunae, which are presumably canaliculi. Osteons are not observed since mouse cortical bone does not undergo Haversian remodeling in the same manner as larger animals (e.g. bovine, human, etc.)[4].

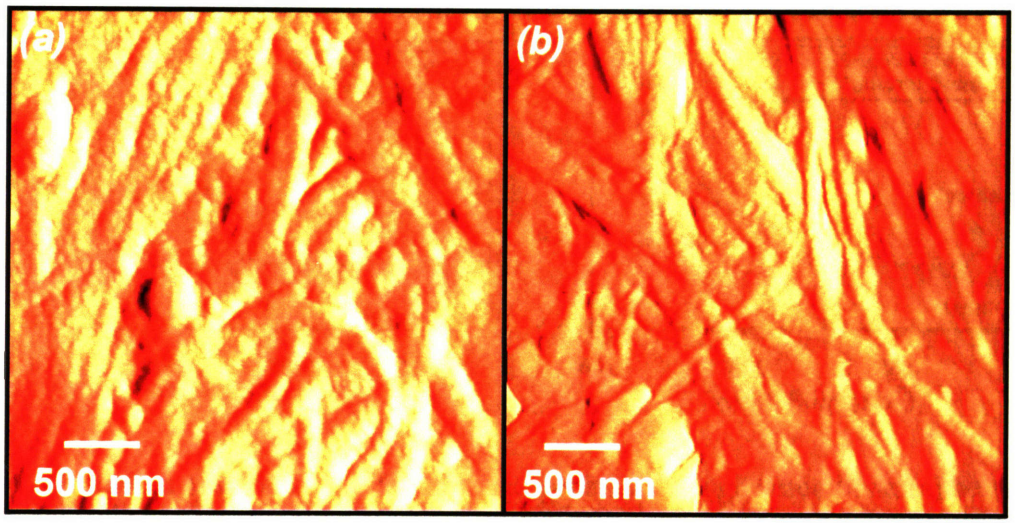

Figure 7-8. Upon a 1 second demineralization etch using 40vol.% H3PO4, AFM images of the *(a)* native radial and *(b)* genetically engineered surfaces show the presence of fibrillar structures suggestive of collagen.

7.3.4 Chemical Analysis

Raman spectra for the cortical and cortical-like regions of the femoral and engineered bone, respectively, showed similar structural compositions (Figure 7-9) and peaks characteristic of the mineral and organic phases. The increase in intensity for the amide I band in the engineered bone has been suggested to be due to an increase in non-reducible pyridinoline cross-link content in collagen (Nalla et al., 2005). An EDX analysis comparison indicates elemental composition and relative mineral content proportions in both types of bone to be similar as well (Figure 7-10). The Ca/P ratio for the femoral and engineered bone were found to be 0.77 and 0.70, respectively.

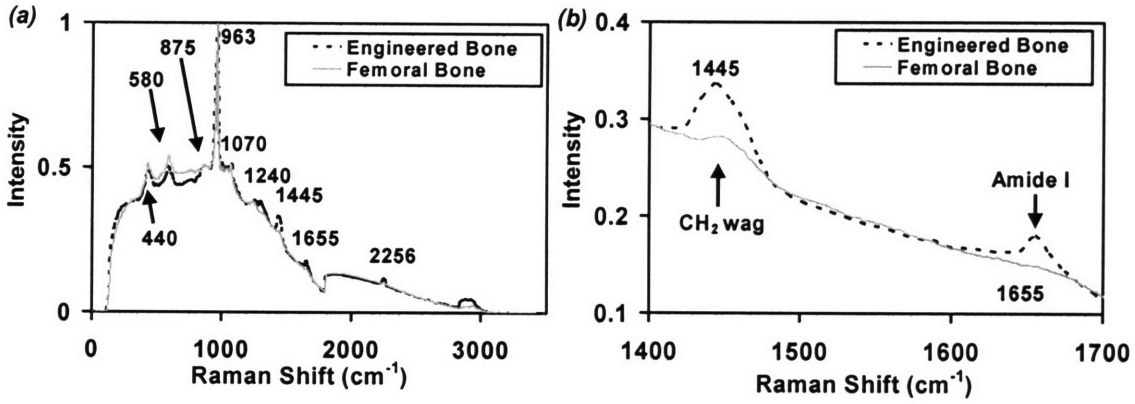

Figure 7-9. Raman spectra for the femoral and genetically engineered bone (a) between 0 and 3500 cm^{-1} and (b) expanded region between 1400 and 1700 cm^{-1}. The notable peaks at 1080, 960, 595, and 435 cm^{-1} correspond to typical phosphate and carbonate bonding (Carden et al., 2003; Tarnowski et al., 2002) from the mineral phase. The most prominent peak at 960 cm^{-1} which corresponds to the phosphate ion P-O υ_1 symmetric stretch, is observed in both bone materials. (b) Peaks at 1445 and 1655 cm^{-1} specify the presence of a CH_2 wag and amide I bond, respectively, from the organic phase.

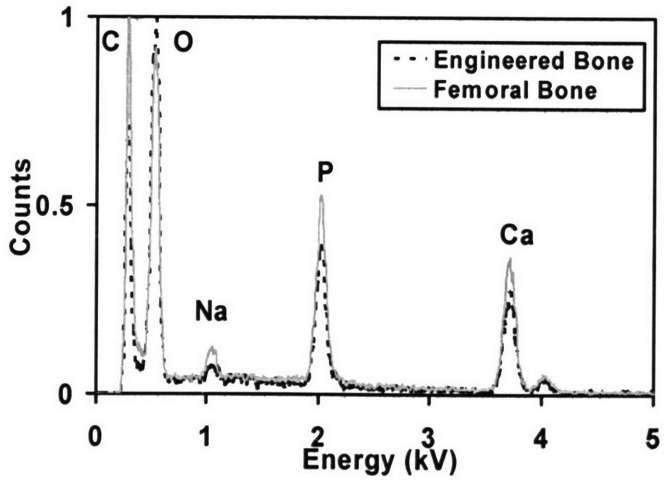

Figure 7-10. Energy-dispersive X-ray spectra for both femoral and genetically engineered bone.

7.3.5 Nanoindentation

Force vs. indentation depth data for one pair of femoral and genetically engineered bone were averaged and plotted together (Figure 7-11). The genetically engineered bone

(E~19.8±5.6GPa, H~0.9±0.4GPa) was statistically less stiff and had a lower average hardness than the femoral bone (E~27.3±10.5GPa, H~1.0±0.7GPa) (n=2449, $p<0.0005$, Figure 7-12), as calculated from the O-P method. Statistical differences between animals as well as maximum loads were observed for both modulus and hardness values ($p<0.0005$). The modulus and hardness values were found to increase with decreasing maximum load. The distribution of calculated modulus and hardness values (Figure 7-13) for both types of bone appear multimodal at lower maximum loads and homogenize and narrow at higher maximum loads. The engineered bone exhibited a broader distribution in elastic moduli. Hardness values calculated via AFM imaging of residual indents (n=6) were 0.7±0.2 and 0.8±0.3, for the femoral and engineered bone respectively (not statistically different, $p>0.01$ which is likely due to the small number of datapoints available). Force vs. indentation depth data for one pair of femoral and genetically engineered bone in the non-union defect model were averaged and plotted together (Figure 7-14). When the data between native radial and engineered bone is compared altogether, the genetically engineered bone (E~18.5±4.5GPa, H~0.8±0.2GPa) is statistically less stiff and has a lower average hardness than the radial bone (E~19.6±4.0GPa, H~0.9±0.2GPa) (n=1850, $p<0.001$) by ~6%, as calculated from the O-P method. Although the pooled data shows an overall difference, when comparisons are made between individual pairs of bone within each mouse, there is considerable variance in the statistics (Figure 7-15). For modulus tests at 1000 μN maximum load, the only pair that exhibited a significant difference is for animal 6. Subsequent modulus tests at 7000 μN showed statistical pair differences in mice 1, 5, and 6 ($p<0.001$). For hardness tests, the only two pairs that showed statistical similarity were for tests at 1000 μN maximum

load in mice 1 and 2 ($p<0.001$). In general, the modulus and hardness values were found to increase with decreasing maximum load. The distribution of calculated modulus and hardness values (Figure 7-16) for both types of bone appear to have a wider distribution at 1000 μN maximum loads as compared to 7000 μN loading. Stiffness values exhibited a more bimodal distribution in the engineered bone as compared with the native radial bone.

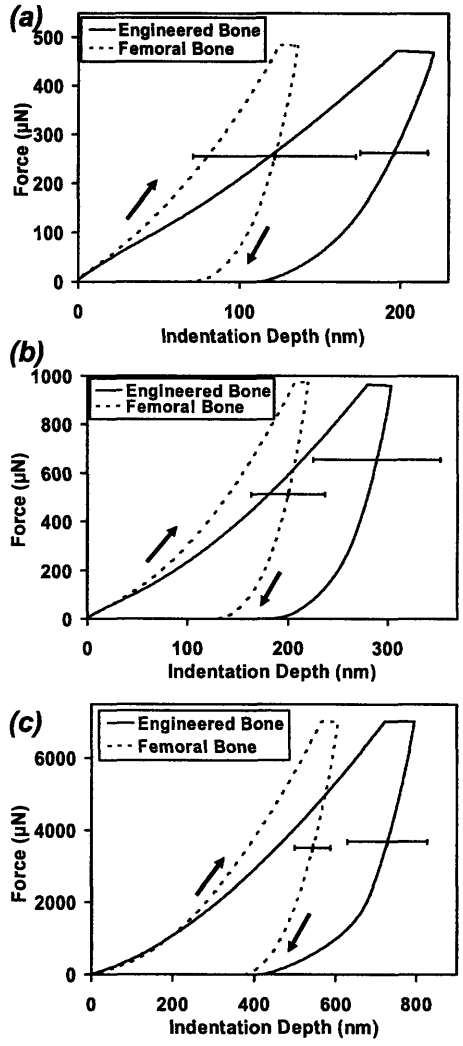

Figure 7-11. Typical nanoindentaion data on loading and unloading using a Berkovich probe tip comparing femoral and genetically engineered bone from one particular mouse

at maximum loads of *(a)* 500, *(b)* 1000, and *(c)* 7000 μN at a loading rate of 50 μN/sec. There were >50 indents for each averaged curve where each indent was spaced 10 μm apart. The horizontal error bars represent ± standard deviation and are typical for the entire loading curve (i.e. vary by < 5% with load). The femoral view orientation is parallel to the long bone axis and the genetically engineered bone is the outer cortical-like surface.

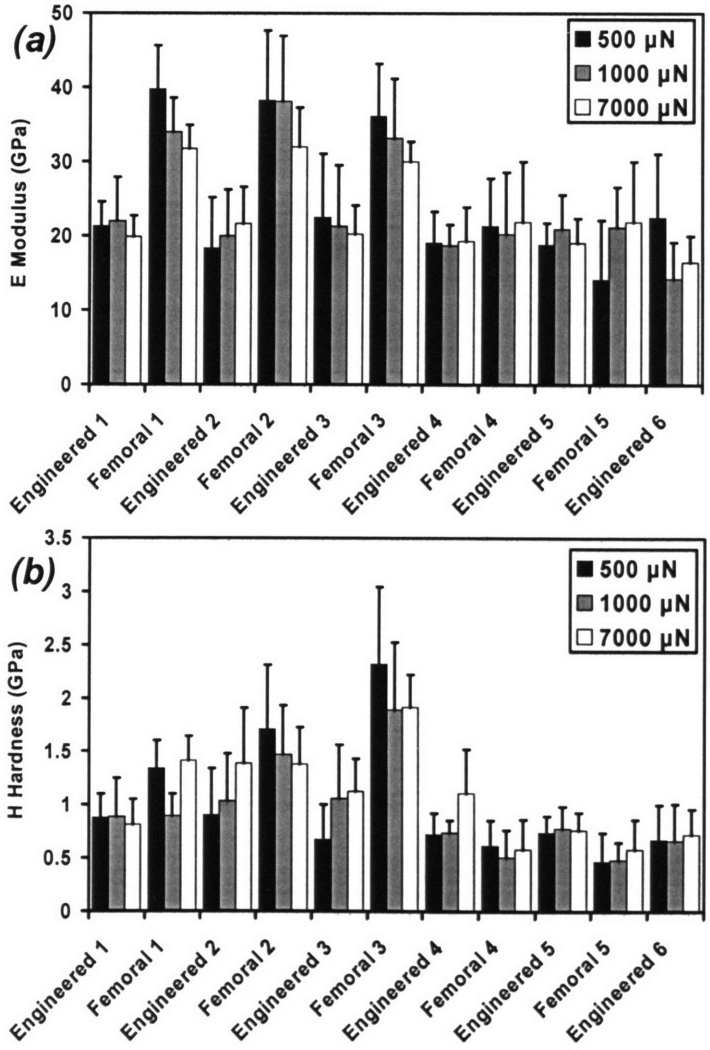

Figure 7-12. Apparent *(a)* moduli and *(b)* hardnesses reduced from nanoindentation data via the Oliver-Pharr method (Oliver and Pharr, 1992) for 6 different bone sample pairs (i.e. 6 difference mice) with >50 indents for each set of data.. The femoral view orientation is parallel to the long bone axis and the genetically engineered bone is the outer cortical-like surface. Hi-lo bars represent one standard deviation.

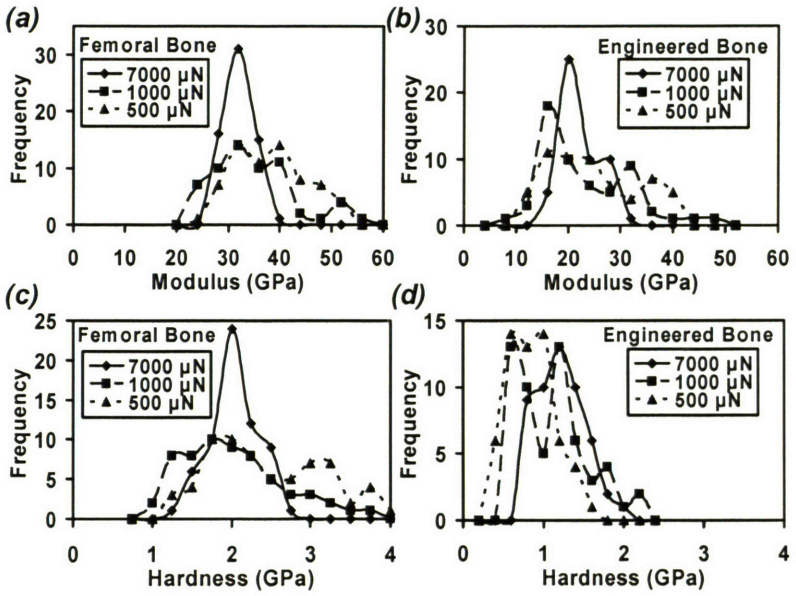

Figure 7-13. Histograms of calculated modulus and hardness values for femoral and engineered bone in animal 3 at the three different maximum loadings.

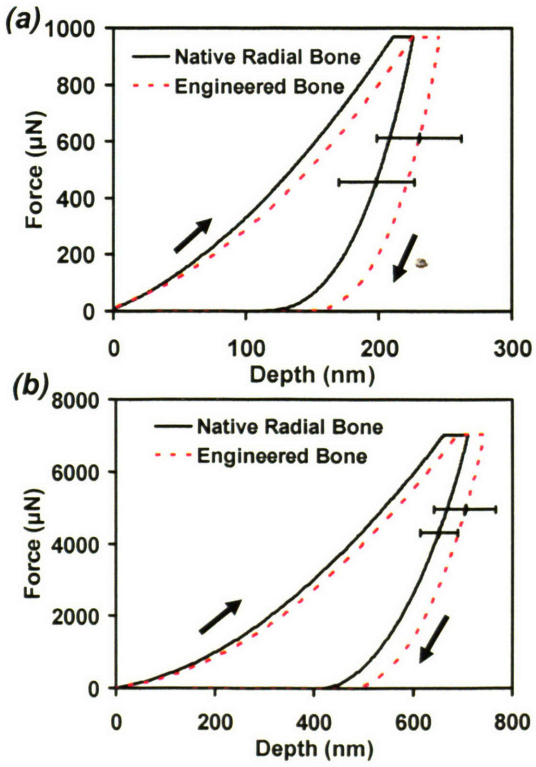

Figure 7-14. Typical nanoindentaion data on loading and unloading using a Berkovich probe tip comparing native radial and genetically engineered bone from one particular mouse at maximum loads of *(a)* 1000 and *(b)* 7000 µN at a loading rate of 50 µN/sec. There were >50 indents for each averaged curve where each indent was spaced 10 µm apart. The horizontal error bars represent ± standard deviation and are typical for the

entire loading curve (i.e. vary by < 5% with load). The orientation is perpendicular to the long bone axis.

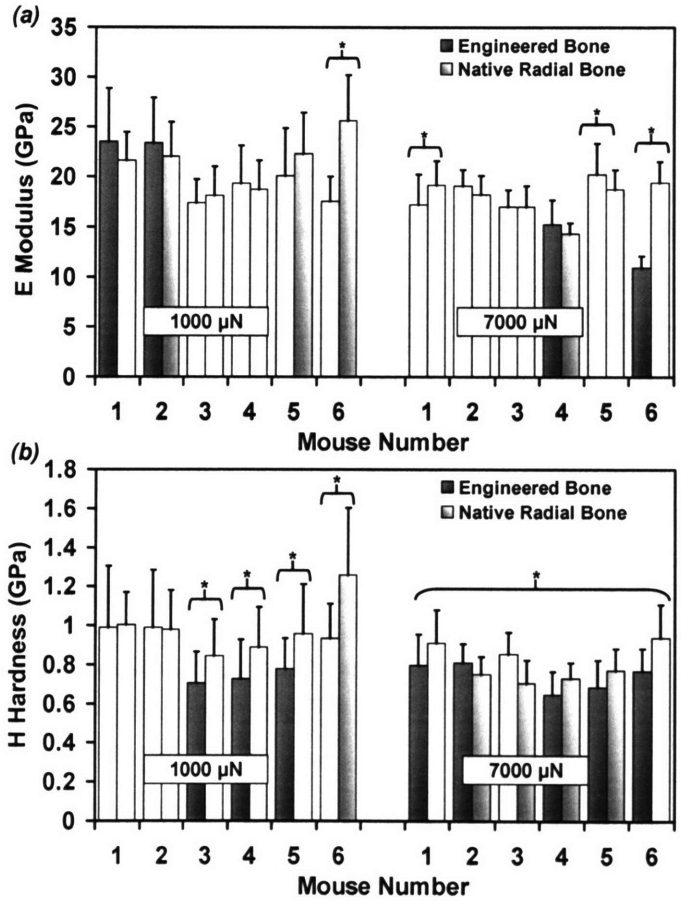

Figure 7-15. Histograms of calculated *(a and b)* modulus and *(c and d)* hardness values for femoral and engineered bone in animal 4 at the two different maximum loading.

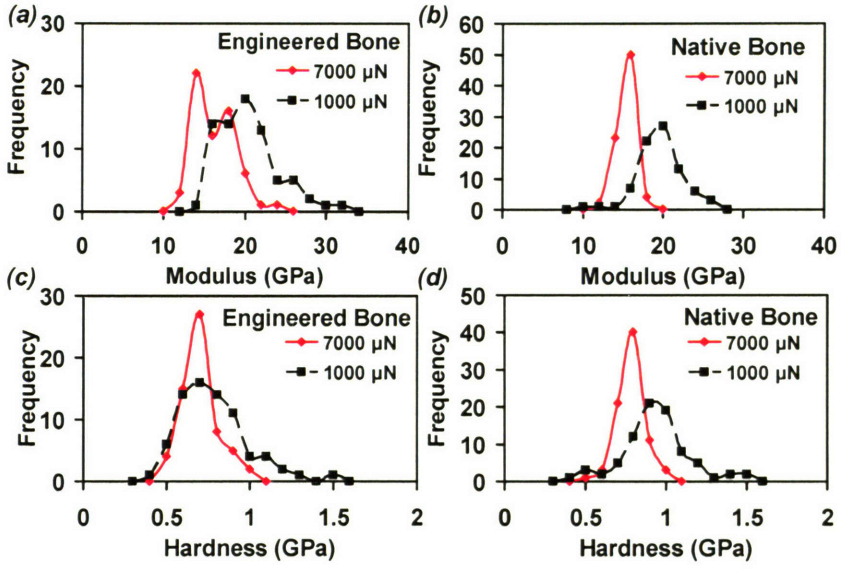

Figure 7-16. Apparent *(a)* moduli and *(b)* hardnesses reduced from nanoindentation data via the Oliver-Pharr method (Oliver and Pharr, 1992) for 6 different bone sample pairs (i.e. 6 difference mice) with >50 indents for each set of data.. The test orientation is perpendicular to the long bone axis for both types of bone. Hi-lo bars represent one standard deviation. Data was paired up and analyzed with to the student t test according to the comparison between native radial and engineered bone within the same mouse. The "*" pairs indicate a statistical difference with $p<0.001$.

7.3.6 TMAFM Imaging of Residual Indents

TMAFM images (Figure 7-17) show clear residual viscoelastic plastic deformation localized within the indent regions and a granular morphology away from the indent region for both samples. Flattening of these surface topographical features was observed within the indent region for both samples. The femoral bone exhibited pileup along the edges of the indent (~100nm in height) while the genetically engineered bone did not (Figure 7-17(b) and 7-17(d)). Along the edge of the engineered bone indent impression, microcracks were observed that were not apparent in the femoral bone (Figure 7-17(e) and 7-17(f)). The average maximum lateral dimension of the topographical features away from the deformed region for the femoral and engineered bone were 158 ± 80 and

145±60nm, respectively which were found to be statistically different (Figure 7-18, $p<0.05$). The peak-to-valley height values, for the femoral and engineered bone, were measured to be 34 ± 13 and 34 ± 15 nm, respectively which were not statistically different ($p<0.001$). The appearance and dimensions of these features are slightly greater than that of previous studies of mineral particles in bone as determined by TMAFM [18], SAXS [220] and X-ray diffraction [10, 13, 14, 81]. This observation is likely due to assemblies of crystallites adhering together to form larger surface morphological features as individual platelets were not isolated from each other by chemical means. TMAFM images of radial defect model are similar to that for the ectopic system in Figure 7-17, showing clear residual inelastic deformation localized within the indent regions and a granular morphology away from the indent region for both samples (Figure 7-19). Topographical features were observed to have maximum dimensions of ~204 ± 48nm and ~196 ± 65nm, for the engineered and native bone respectively.

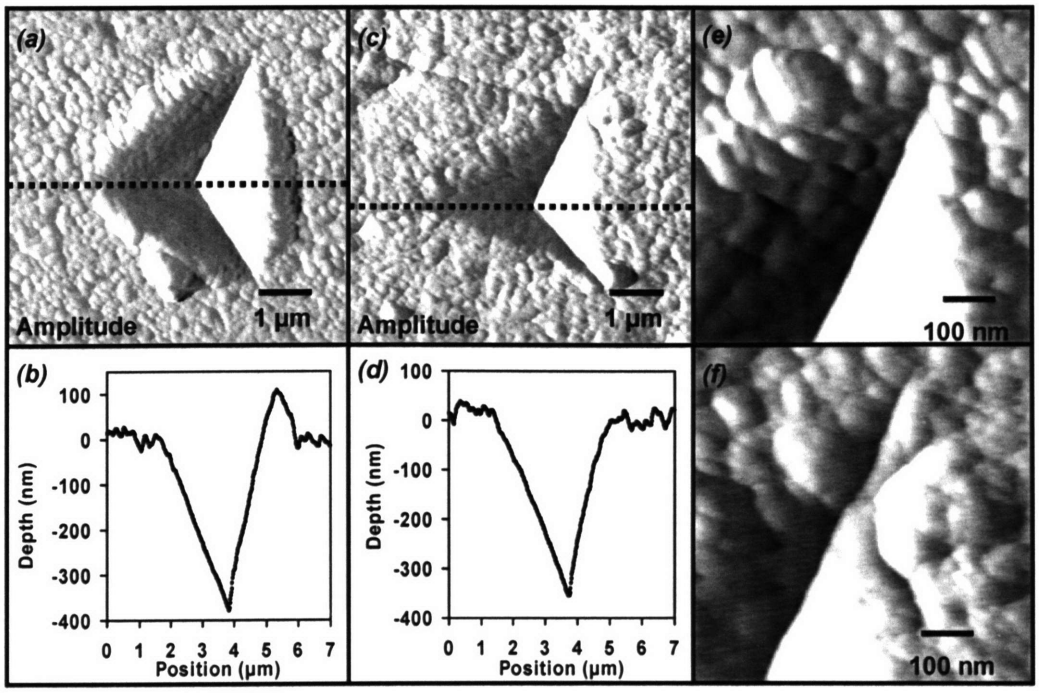

Figure 7-17. TMAFM amplitude images and section profiles are given of the residual impressions after loading and unloading to 7000 μN using a Berkovich probe tip at a loading rate of 50 μN/sec. The *(a)* femoral view orientation is parallel to the long bone axis and *(b)* the genetically engineered bone is the outer cortical-like surface. Amplitude images are reflective of abrupt surface topographical changes. Sectioned line scans through corresponding height images (*not shown*) show significant pileup for the *(c)* femoral bone, but a negligible amount for the *(d)* engineered bone. Signs of crack formation is not evident for the *(e)* femoral bone but is suggestive for the *(f)* engineered bone along the edge of the indent impression.

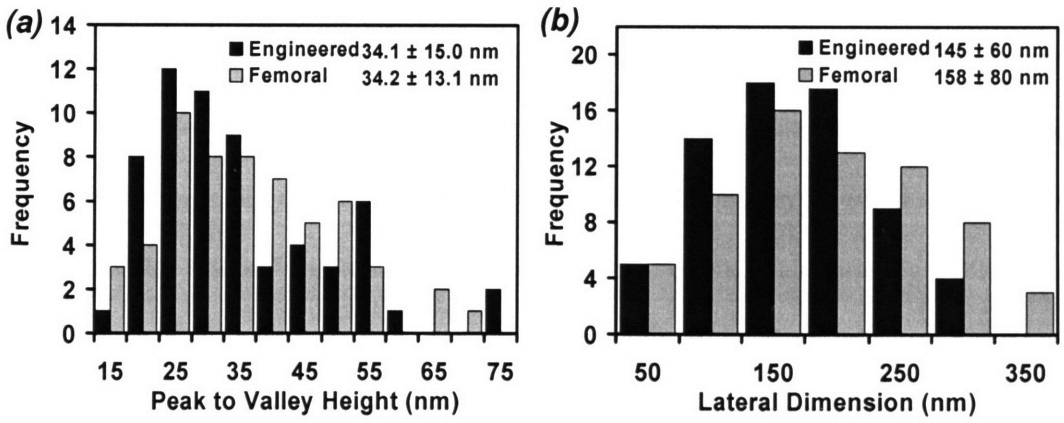

Figure 7-18. Histograms of the *(a)* peak to valley height and *(b)* lateral dimensions of nanoscale topographical features as measured from line scan profiles of AFM height data obtained for 4 different sample images (number of datapoints for each type of bone , n~50). The femoral view orientation is parallel to the long bone axis and the genetically engineered bone is the outer cortical-like surface. Hi-lo bars represent one standard deviation, insets are mean ± one standard deviation.

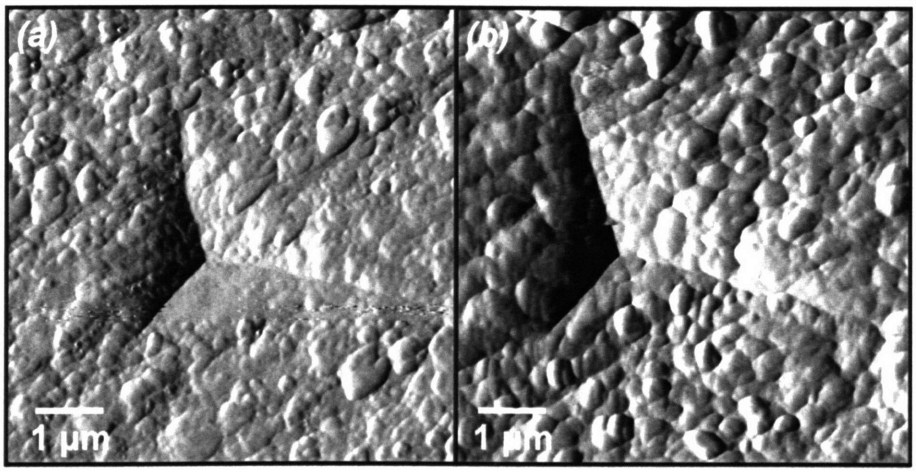

Figure 7-19. TMAFM amplitude images are given of the residual impressions after loading and unloading to 7000 μN using a Berkovich probe tip at a loading rate of 50 μN/sec. The *(a)* native radial and *(b)* genetically engineered bone view orientations are perpendicular to the long bone axis. Amplitude images are reflective of abrupt surface topographical changes. A rough granular surface topology is indicated for both types of samples as well as a relatively flattened in region within the indented portion.

7.4 Discussion

Nanoindentation has shown to be a viable technique for quantifying the bio(nano)mechanical properties of small volumes of tissue engineered bone produced in vivo. Table 7-1 compares structural and nanomechanical data obtained from mice femoral and genetically engineered ectopic bone. While the two types of bone were found to have similar mineral contents, overall porous microstructures showing lacunae and canaliculi, chemical compositions, and nanoscale topographical morphologies, apparent elastic moduli reduced from nanoindentation data were found to be statistically different with the femoral bone (indented parallel to the bone long axis) being ~1.4× stiffer than the engineered bone. The average value obtained for the femoral bone (~27 GPa) is slightly lower than that reported in the literature for femoral mouse cortical bone loaded in the same direction using nanoindentation which was found to be ~31 GPa [213] and 43.5 - 35.2 GPa [216] and may be due to the effects of alcohol and/or dehydration used in these studies [214]. O-P calculations showed that the femoral bone was ~1.1× harder than the engineered bone, and hence exhibited a greater resistance to total deformation (the sum of elastic, viscoelastic, and plastic). Since mineral content and nanoscale morphology were statistically similar for both types of bone, these parameters can not be responsible for these material property trends.

This study is also carried one step further in assessing a system that mimics a massive non-union bone defect in a weight-bearing site. Mineral content, chemical structure, and elemental composition were found to be similar for the genetically grown bone compared to its corresponding native control. In contrast to before, nanoindentation data showed that the native bone had more statistical similarities to that of the engineered bone. The apparent elastic moduli of the radial bone reduced from nanoindentation data were found to be ~6% statistically stiffer (indented perpendicular to the bone long axis) than the engineered bone. O-P calculations showed that the radial bone was ~12% harder than the engineered bone, and hence exhibited a greater resistance to total deformation (the sum of elastic, viscoelastic, and plastic). It was mentioned before that since mineral content and nanoscale morphology were statistically similar for both types of bone, these parameters are not expected to be responsible for these material property trends. It is quite possible that differences could arise from; *1)* variations in the overall organization and interactions between the organic and mineral constituents and/or *2)* variation in the composition and/or supramolecular structure of the organic component. One recurrent possibility of variation could result from differences in age (i.e. the radial bone is 14 - 16 weeks old and the ectopic is 8 weeks old). A likely source affecting the similarity in mechanical properties is the difference in loading condition. Even though the radius is not as weight-bearing as the neighboring ulna, the engineered bone would most certainly receive some load, stimulating cell migration and subsequent orientational bone growth. Ongoing nanotechnological studies provide a promising pathway to further investigate both of the above hypotheses, including; high resolution tapping mode AFM imaging as a function of acid demineralization [8] and chemically and spatially specific high

resolution force spectroscopy[221]. Lastly, the engineered bone also exhibited a more heterogeneous distribution of material properties likely because the overall structure seems to exhibit a lesser degree of regularity than the radial bone.

	Femoral	**Engineered**	**p**
Mineral Content (BSE, wt%)	64.6 ± 2.0	61.2 ± 3.2	>0.01
Lacunae aspect ratio (BSE)	3.4 ± 1.0	2.4 ± 1.0	<0.01**
Lacunae maximum dimension (BSE, □m)	9 ± 2	13 ± 5	<0.01**
Porosity (BSE, %)	5	10	-
Ca/P Ratio (EDX)	0.77	0.70	-
Maximum dimension of topographical features (AFM, nm)	158 ± 80	145 ± 60	>0.01
Peak-to-valley height of topographical features (AFM, nm)	34 ± 13	34 ± 15	>0.01
Apparent nanoindentation moduli, E (GPa)*	27.3 ± 10.5	19.8 ± 5.6	<0.0005**
Hardness, H, measured by nanoindentation (GPa)*	1.0 ± 0.7	0.9 ± 0.4	<0.0005**
Hardness calculated from AFM residual indent (GPa)	0.7 ± 0.2	0.8 ± 0.3	>0.01

Table 7-1. Summary comparison of the structural and nanomechanical properties of femoral and genetically engineered bone. For O-P estimated elastic moduli and hardness values, a 3-way ANOVA statistical analysis as performed on 2500 which takes into account the different types of bone (femoral and engineered), animal (6 different animals), and maximum loading (500, 1000, and 7000 μN). All other statistical tests were unpaired student t-tests carried out on pooled datasets (**indicates calculated by O-P method, **indicates statistical difference between femoral and engineered bone samples*).

The Raman-suggested increase in collagen crosslink density for the engineered bone relative to the femoral would be expected to result in an increase in modulus, and hence can not be responsible as well. Hence, other origins could be; *1)* variations in the overall organization and interactions between the organic and mineral constituents and/or *2)* variation in the composition and/or supramolecular structure of the organic component. Such variations could result from differences in age (i.e. the femoral bone is 10-12 weeks old and the ectopic is 4 weeks old) and/or loading conditions (i.e. the femoral bone is weight bearing while the ectopic is non-weight bearing). Ongoing

nanotechnological studies provide a promising pathway to further investigate both of the above hypotheses, including; high resolution tapping mode AFM imaging as a function of acid demineralization [8] and chemically and spatially specific high resolution force spectroscopy[222]. Lastly, the engineered bone also exhibited a more heterogeneous distribution of material properties likely because the overall structure seems to exhibit a lesser degree of regularity than the femoral bone.

Direct visualization of the nanoscale mechanisms of deformation via in-situ high resolution tapping mode AFM imaging was achieved. Generally, both samples exhibited similar viscoelastic plastic deformation at the length scales studied in this paper. However, fine differences in the residual indent area (smaller for the engineered bone), pile up (smaller for the engineered bone), and fracture mechanisms (microcracks for the engineered bone) were observed with the genetically engineered bone behaving more brittle than the femoral control. Viscoelastic / plastic deformation at this length scale may arise from a variety of mechanisms including; mineral particle displacement, underlying porosity and voiding which would relieve triaxial stresses, collagen fibril slippage, collagen denaturation, debonding of mineral-organic interfaces, crosslink scission, crack formation and propagation, deformation and structural phase transformation, viscous stretching of the organic component, and rupture of self-healing sacrificial bonds. Again, further nanomechanical studies will be able to shed insight into which deformation mechanisms may be dominant.

Coupled with the appropriate chemical analyses, the nanomechanical methods presented here have been shown to probe and measure the fine nanoscale details not accessible by traditional biomechanical techniques and have great potential for evaluation

of optimization of site-specific bone formation and healing for the treatment of fracture and disease induced defects. Future studies in this area include nanoindentation of the trabecular-like regions in the engineered bone, the rate dependence of nanoscale properties, the temporal evolution of bone remodeling, and the effects of mechanical loading of bone formation and adaptation, and at different implantation sites including critical-size bone defects in flat and long bones. The long term goal is to employ such nanomechanical methodologies as an optimization tool in the field of bone tissue engineering in general, for example via implanted cell number, transgene duration of expression, and scaffold design and composition. Such an optimization process will be crucial to the advancement of the tissue engineering strategy, described in this study, towards human clinical trials.

Chapter 8

Nanomechanics of Bone Defect Repair using Chitosan Glutamate Paste

8.1 Introduction

It is important for synthetic bone graft materials to be osteoconductive in order to function properly. Plaster of Paris (POP) and chitosan glutamate have been shown to be both biocompatible and osteoconductive. In order to be effective, synthetic bone graft materials also must contain agents that exhibit osteoinductive properties. Processed bone tissues (e.g. demineralized bone matrix, DBM), bone cells, and bone morphogenic proteins (BMP) are frequently used as osteoinductive agents. The material used in this study delivers bone cells grown form bone marrow as the osteoinducive agent. The same paste material can also be used to deliver other osteoinductive agents such as BMP, DBM, morcellized cancellous bone, and other biomolecules to aid in bone growth. The paste can be delivered through arthroscopic devices after combining with the patient's own cells. Currently, a number of products are being marketed as a synthetic bone graft material where the majority of them use processed bone tissues or DBM derived from bone tissues or collagen. Inorganic fillers include HA, tricalcium phosphate, carbonate apatite, and calcium sulphate. The paste can also be used to deliver other therapeutic drugs including cancer drugs to the affected site.

8.2 Materials and Methods

The animal models were based on the previous work studying the healing of bone defects in mice [223, 224]. Four rats were studied by filling the 4 mm gap with a paste of CH-G (0.125 g) and POP (0.5 g) mixed with 1 ml of media containing osteoblasts grown from bone marrow (about 10^6/ml). The other three rats had the control paste of CH-G with hydroxyapatite (HA) of the same composition as the CH-G and POP that also contained 1 ml of osteoblasts cell suspensions. Small metal plates stabilized the fracture. Sacrifice points were made at three, six, and nine months. There were three different groups, the operated control (plate only and no paste), the experimental group (plate and paste), and the unoperated control (no plate). Undecalcified histological sections were stained by modified Goldner's Trichrome and decalcified sections were stained by Hematoxylin and Eosin (H&E). Nanoindentation and microCT (as described previously in chapter 7) were also performed on the samples after their respective experimental time periods.

8.3 Results

8.3.1 Histology and microCT Imaging

Images from the histology of the different systems are shown in Figure 8-1. In general, when comparing the plated and unoperated control systems, the bone growth did not reach a point where it was comparable to that of the unoperated control. However, when comparing both of the plated system with and without the paste inserted, there appeared to be significantly more bone growth in the system where the paste was applied. This data is corroborated in Figures 8-2 and 8-3, which show microCT images of the same plated samples. In general, the bone growth of plated samples did not reach the

point of that of the unoperated control, yet there was more bone growth visible in the plated system with paste than without.

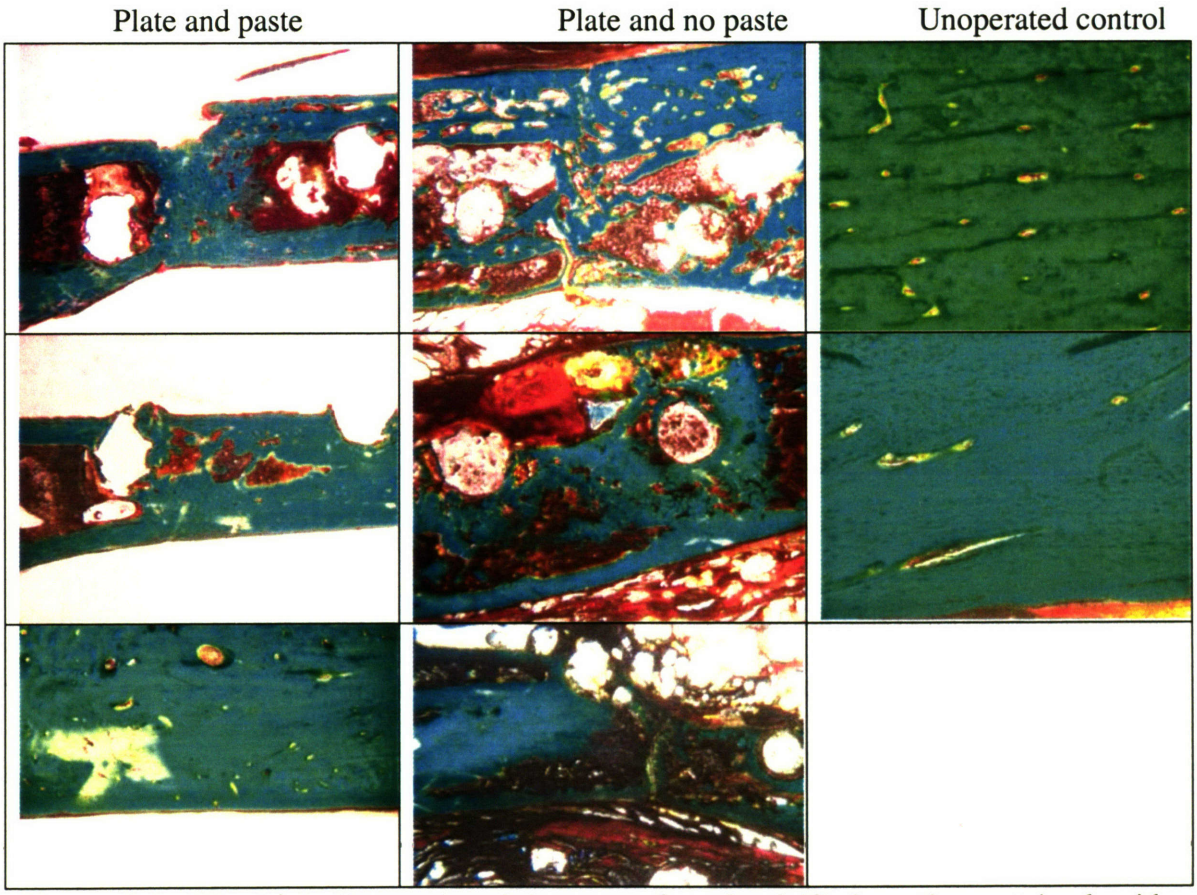

Figure 8-1. Histologically sectioned images of undecalcified sections stained with Goldner's trichrome stain are given after a 3 month study showing the results from the 3 different types of experiments; implanting plate with paste, a plate without paste, and an unoperated control.

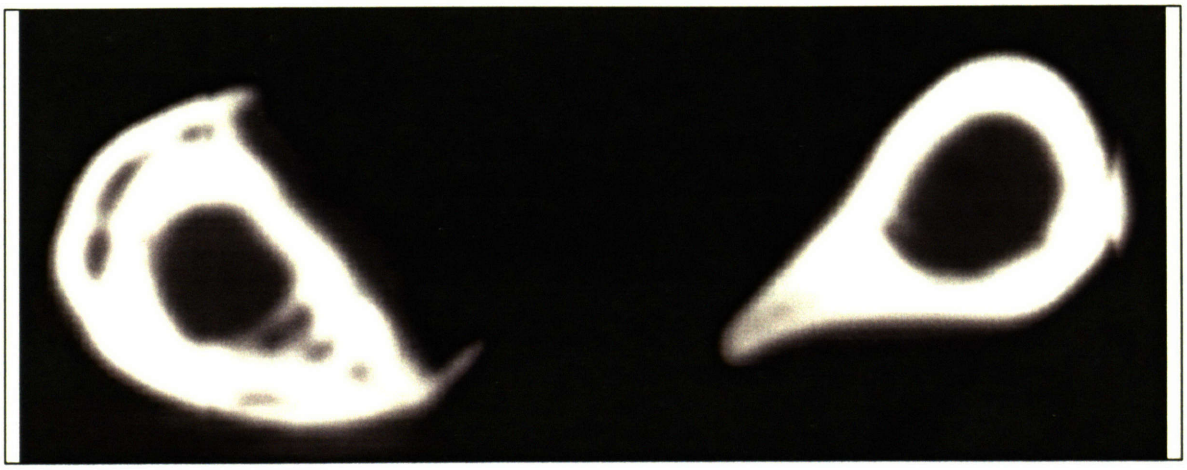

Figure 8-2. The microCT image here is of a 3 month study where there was plate and paste inserted into the defect region, showing significant bone density growth.

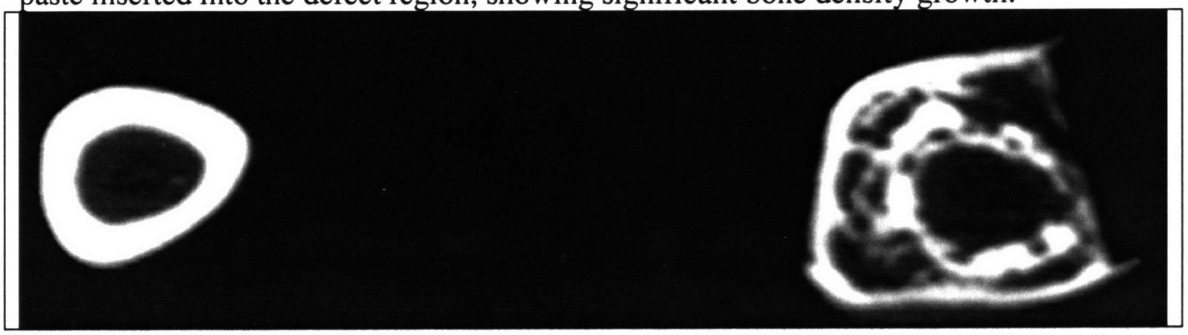

Figure 8-3. The microCT image here is of a 3 month study where there was plate and no paste inserted into the defect region, showing significantly bone growth compared to the image previously.

8.3.2 Nanoindentation

The force vs. indentation depth data for three pairs of unoperated and plated (with paste) systems were averaged and plotted together (Figure 8-4). The data for the systems yield statistically similar modulus and hardness values as calculated from the O-P method ($n \sim 1000$, $p < 0.05$). For the first set of data, for 7 mN maximum load, the unoperated control gave property values E ~17.3 ± 0.98 and H ~0.86 ± 0.08 GPa and the plate/paste system gave property values E ~20.3 ± 2.3 and H ~0.76 ± 0.12 GPa. For 1 mN maximum load, the unoperated control gave property values E ~22.0 ± 2.2 and H ~0.97 ± 0.15 GPa and the plate/paste system gave property values E ~23.6 ± 4.3 and H ~0.73 ± 0.15 GPa. For the second set of data, for 7 mN maximum load, the unoperated control gave property values E ~21.7 ± 1.9 and H ~0.88 ± 0.11 GPa and the plate/paste system gave property values E ~19.2 ± 1.8 and H ~0.81 ± 0.08 GPa. For 1 mN maximum load, the unoperated control gave property values E ~26.1 ± 3.4 and H ~1.15 ± 0.20 GPa and the plate/paste system gave property values E ~22.7 ± 3.1 and H ~0.94 ± 0.17 GPa. For the third set of data, for 7 mN maximum load, the unoperated control gave property values E ~20.4 ± 1.3 and H ~0.92 ± 0.07 GPa and the plate/paste system gave property values E ~20.8 ± 1.9

and H ~0.83 ± 0.11 GPa. For 1 mN maximum load, the unoperated control gave property values E ~23.5 ± 2.8 and H ~1.1 ± 0.17 GPa and the plate/paste system gave property values E ~21.5 ± 3.4 and H ~0.88 ± 0.19 GPa.

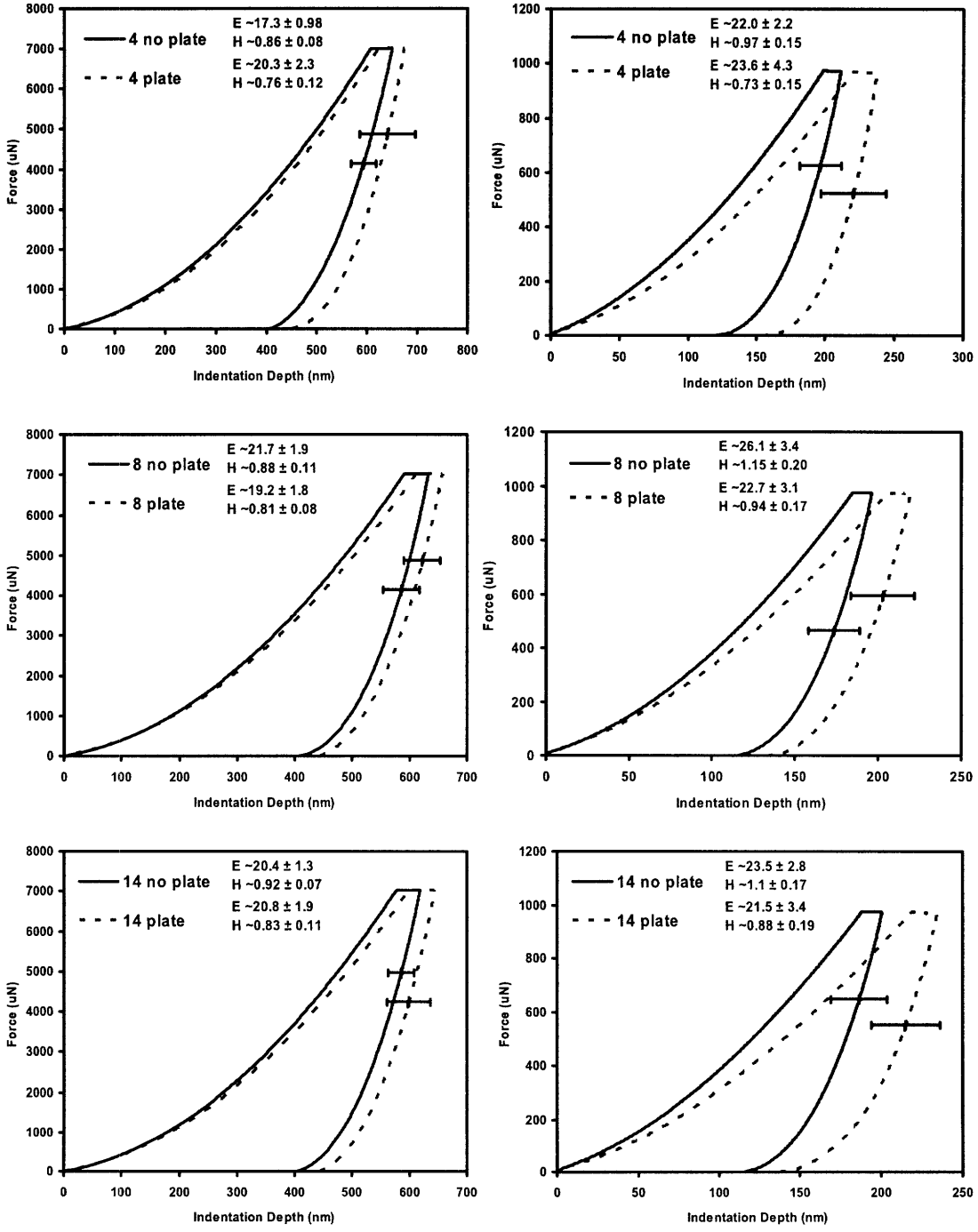

Figure 8-4. Nanonindentation curves at 7 and 1 mN maximum load for 3 different sets of data comparing the unoperated control to the plated system with paste.

8.4 Discussion

In general, the results of this study show that bone growth appeared to be greater for the defect system where paste was implanted with the plate as opposed to having no paste implanted at all. This is illustrated through the histology and microCT images of the systems showing the relative amount of bone growth for each. The extent of bone healing for the plated system with paste did not equal that of the unoperated controls. Nanoindentation data, on the other hand, showed promising results in that the intrinsic mechanical properties extracted from probing the local surface experimentally were similar comparing the unoperated control to that of the plated system with the paste. There is a strinkingly similar behavior of POP compared to that of HA, which has proven to be a very desirable osteoconductive material. The paste of POP and CH-G also appears to be a better paste from general handling considerations. The concept of delivery of cells cultured from patient's own bone marrow is inherently more appealing than other processed bone tissues (e.g. demineralized bone matrix or bone morphogenic proteins) because bone cells may be more potent than the processed bone tissues. Although the paste system presented here looks to be promising for orthopaedic regenerative therapies, it must be kept in mind that the data presented here are only preliminary experiments to illustrate a proof of concept. More rigorous studies that include more statistically significant mechanical tests and animal models should be performed in the future.

Appendix A

Macroscopic Mechanical Testing and Visualization

Macroscopic compressive tests were carried out in directions parallel and perpendicular to the long bone axis and the results are presented here. The specimens were rectangular parallelpiped in shape with the cross sectional area ~2 mm x ~2 mm and the length ~5 mm. Modulus was computed from the stress-strain curve as the slope of the initial linear regime. The yield stress and yield strain were calculated from the stress-strain curve as the point of stress and strain at which plasticity was incipient. Stress-strain curves are shown in Figures A-1 and A-2. Values of modulus, yield stress, and yield strain were 8.7 ± 2.5 GPa, 178.0 ± 46.6 MPa, and 0.035 ± 0.0077, respectively for tests perpendicular and to the long bone axis. For tests parallel to the long bone axis, values of modulus, yield stress, and yield strain were 15.4 ± 4.3 GPa, 254.6 ± 13.0 MPa, and 0.025 ± 0.0048, respectively. SEM images of the compressed samples were also taken, showing microscopic fibrillar deformation (Figure A-3).

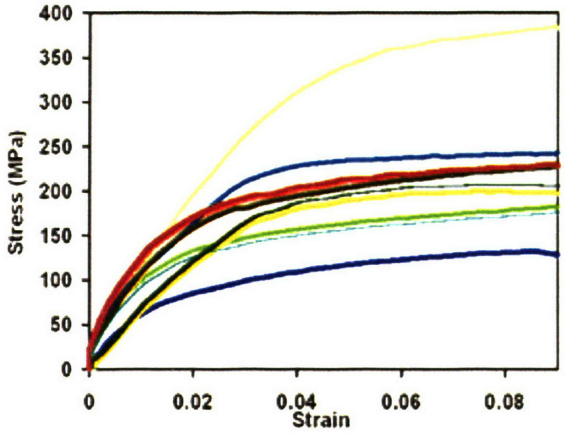

Figure A-1. Stress strain curve of bone compressed perpendicular to the long bone axis.

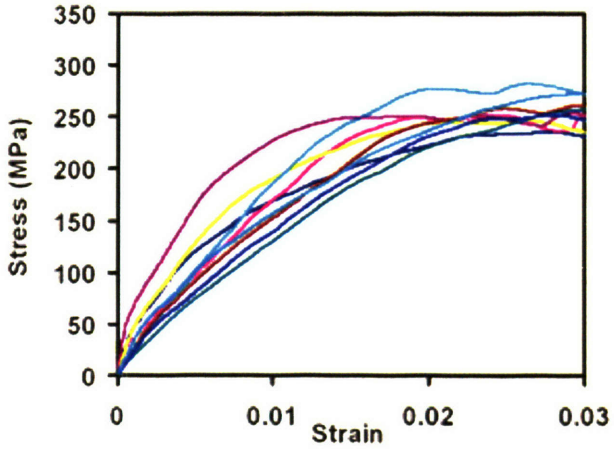

Figure A2. Stress strain curve of bone compressed parallel to the long bone axis.

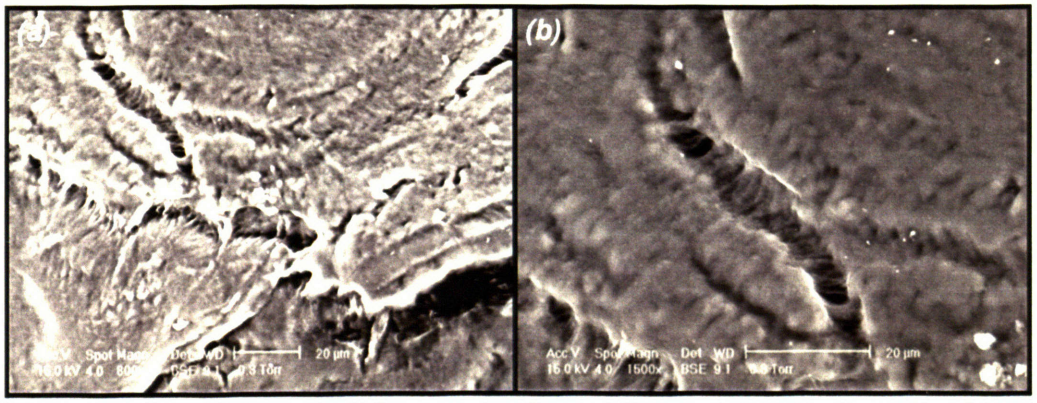

Figure A3. SEM image of fracture surfaces of a partially demineralized bone surface under compressive loading. Adhesive fibril bridging is evident between lamellar layers.

Appendix B

Supplementary Characterization: X-ray Diffraction (XRD), X-ray Photoelectron Spectroscopy (XPS), Energy Dispersive X-ray Analysis (EDX)

Bone samples were further analyzed through standard materials characterization techniques. XRD involves measurement of the pattern that arises from diffracted X-rays through the lattice of atoms in the hydroxyapatite material, which is useful for examining the crystallinity of the mineral phase in bone (Figure B-1). The diffraction pattern of a phase pure HA sample shows distinct mineral peaks showing a high degree of crystallinity. Regular undemineralized bone, on the other hand, has a relatively poor crystallinity. The deorganified (from heat treatment) bone sample shows a similar degree of crystal structure to that of the regular bone, suggesting that preparation did not alter the chemical structure in any significant way.

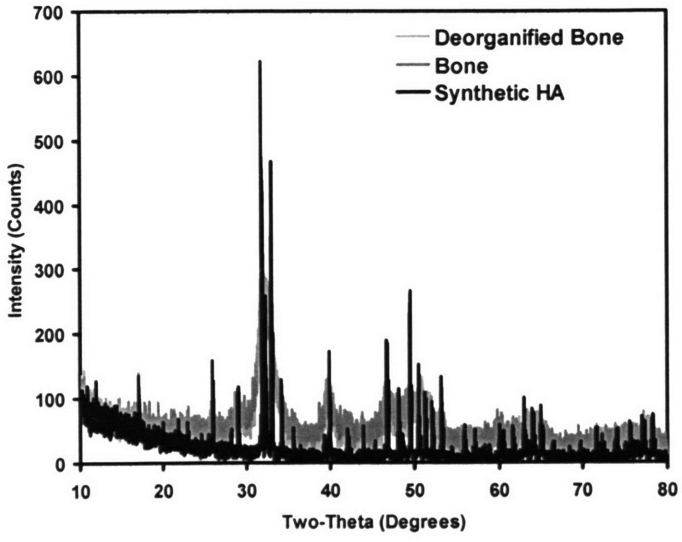

Figure B-1. X-ray diffraction patterns of phase pure HA, undemineralized bone, and deorganified bone samples.

XPS is based on the photoelectric effect where the ejection of excited photonelectrons from the solid surface is recorded, giving information on the materials surface composition. This technique is useful for studying chiefly the organic phase of the bone (Figure B-2). The deorganified bone sample shows no nitrogen content on the surface, indicating that the heat treatment successfully removed all traces of protein organic from the material. Undemineralized and demineralized bone, on the other hand, show strong nitrogen peaks, as expected.

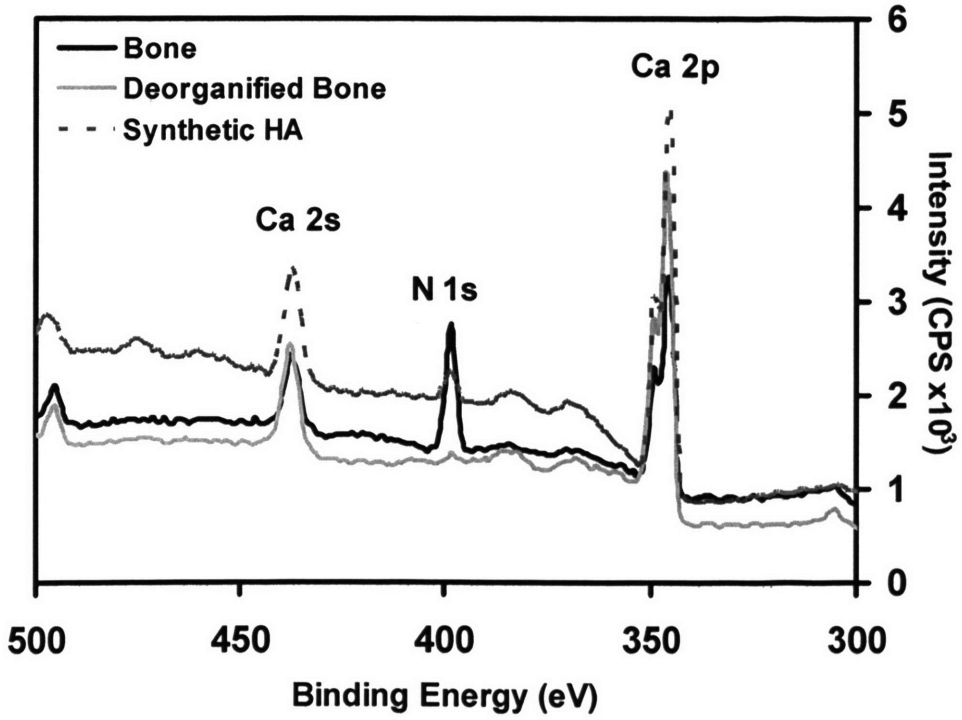

Figure B-2. X-ray photoelectron spectra of undemineralized bone, partially demineralized, and deorganified bone samples.

EDX involves an electron beam striking the atoms of the sample surface causing X-rays to be emitted with varying energies depending on the material composition. This method is useful for determining the relative elemental composition on the sample surface, especially higher elemental numbers (Figure B-3). No aluminum or silicon was recorded on the sample, indicating that polishing particles were not left on the surface of the bone. The undemineralized bone had strong calcium and phosphorus peaks and the partially demineralized sample had weak calcium and phosphorus peaks, both as expected.

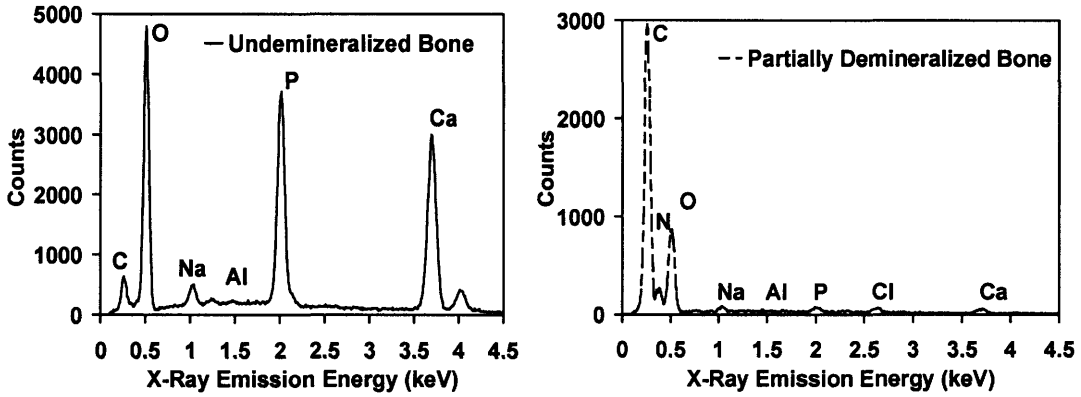

Figure B-3. Energy dispersive X-ray analyses of undemineralized bone, partially demineralized, and deorganified bone samples.

Appendix C

Collagen Fibril Deformation

Deformation characteristics were also experimentally observed for pure type I collagen derived from rat tail tendon. A wire stripper was used to pull collagen fibrils out of a rat tail and stored in PBS. In order to remove proteoglycan debris, fibrils were subsequently digrested in ~% trypsin at 37°C for 24 hours. Afterwards, fibrils were placed on a freshly cleaved mica surface, ready for analysis. Images of the residual impression indented with the Hysitron nanoindenter are shown in Figure C-1. Force-depth curves are shown in Figure C-2. Partially demineralized bone samples were indented using a stiff AFM cantilever probe tip followed by imaging with the same probe tip in tapping mode (Figure C-3).

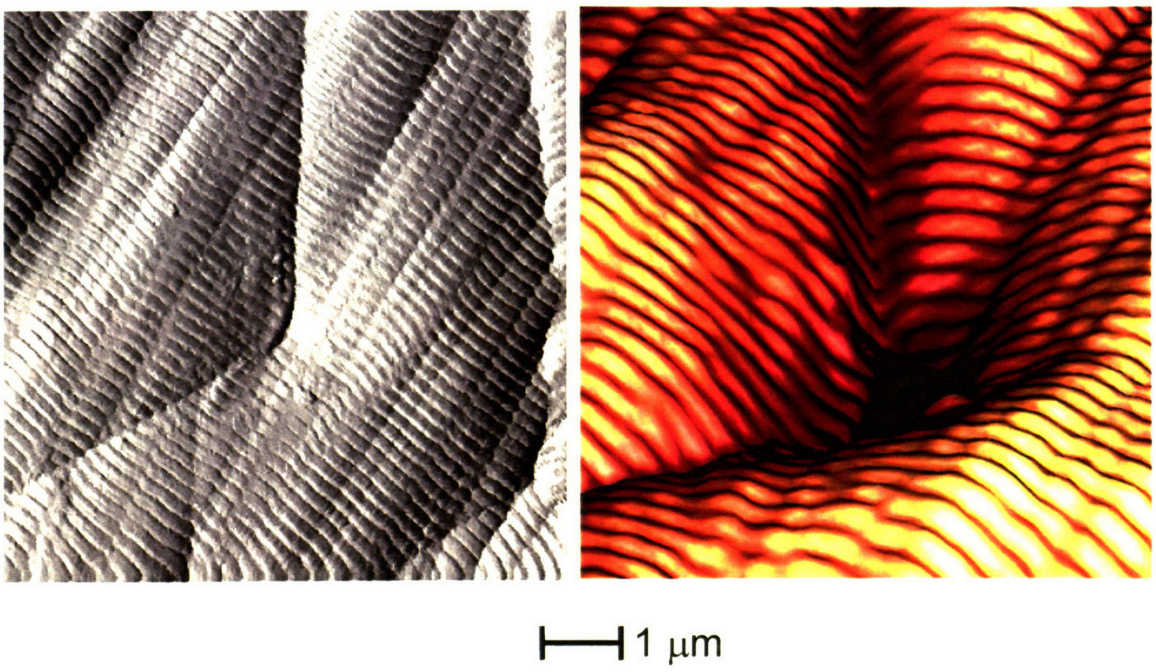

Figure C-1. AFM image of residual impression from collagen fibril indent.

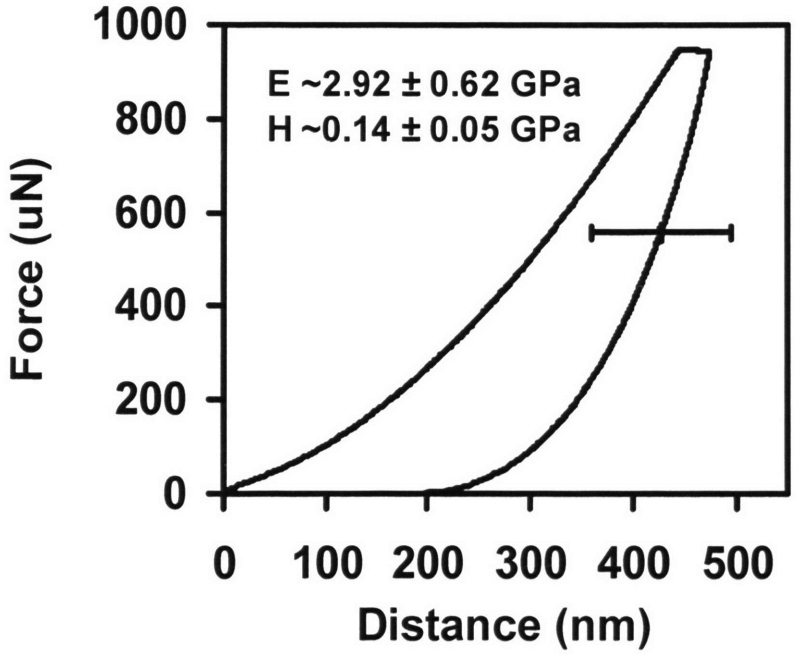

Figure C-2. Force-depth curves corresponding to collagen fibril indentation.

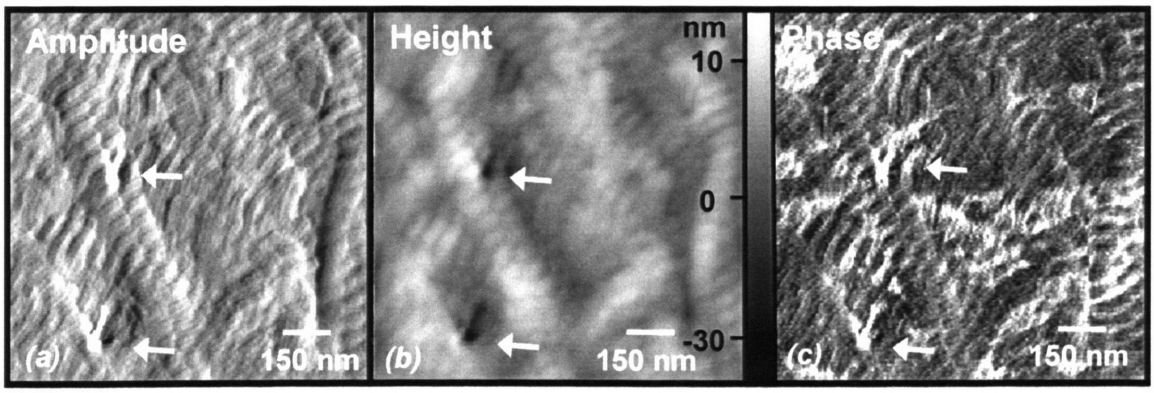

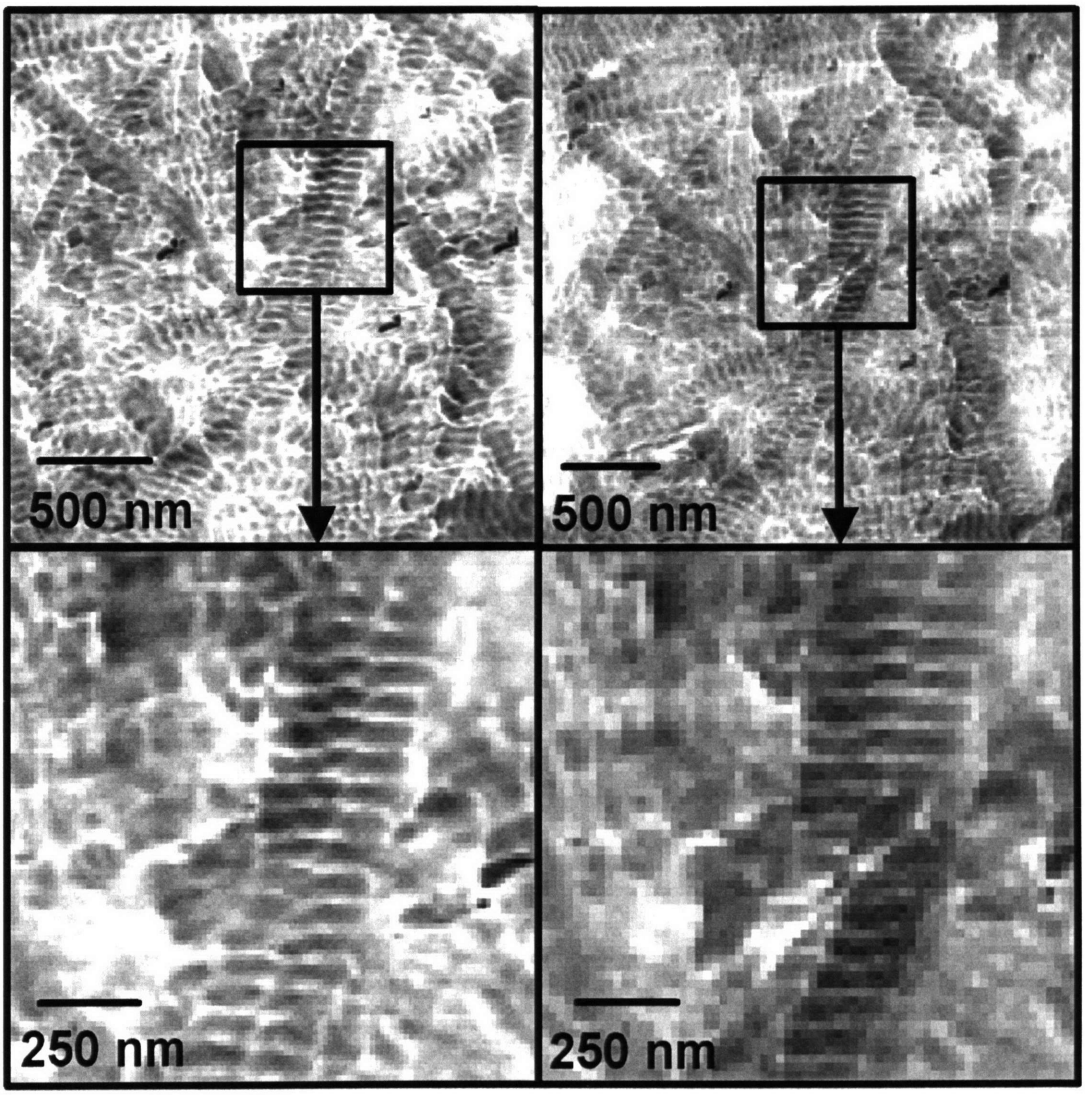

Figure C-3. AFM images of residual impressions from single collagen fibril indentation using a sharp AFM probe tip.

Appendix D

The Effect of Various Chemical Treatments on Bone

A thorough literature search was conducted, investigating the effect of common chemical treatments on bone. In addition, SEM images were also taken of ethanol treated bone. Ethanol is commonly used to dehydrate biological samples, which may, in fact, have a more deleterious effect on the bone material.

D.1 Demineralization

Phosphoric acid appears to disrupt intermolecular bonds of the collagen fibril, but exposure to water for periods greater than 24 h promotes re-assembly of the collagen molecules.

Reference	Treatment	Sample	Experimental Method	Result
Breschi, et al. 2003[225]	35% H3PO4 15, 30, 60 sec.	dentin	immunogold labeling/antibody binding	<15s similar antigenicity >15s reduction in antigenicity, 15s - collagen fibrils visible without causing structural modifications that inhibit antibody binding
Ritter, et al. 2001[226]	37% H3PO4 60 s	dentin	Amino acid composition (strong cation exchange column on HPLC) Cross-link (deoxypyridinoline and pyridinoline detection through fluorescence and radioactivity)	no significant change in aa and crosslink composition
Tai, et al, 2005[8]	37% H3PO4 10-120s, 48 hrs rehydration	cortical bone	AFM, SEM	correct banding structure

Feninat, et al. 1998[28]	17% H3PO4	Caries-free human molar dentin	AFM	correct banding structure
Eliades, et al 1997[227]	10% citric acid, 10% maleic acid	dentin	AFM, FTIR	collagen denaturation, smear layer removed, intertubular roughness increased, decrease in amide I carbonyls, irreversibly adsorbed thickeners
Oyarzun et al., 2000[228]	35% H3PO4	Human dentin	Immunohistochemistry; ultrastructural histochemistry	GAGs and peritubular proteoglycans were preserved; Loss of GAG and proteoglycan anionic sites.
Lewandrowski, et al., 1996 [229]	1.875, 3.65, 7.3% HCl	Human tibia diaphysis	Diffusion mass transfer modeling to predict demineralization rates	Planar and cylindrical geometries applicable based on differing geometries
Natsir et al., 1999 [230]	1, 3, 5, 10% tannic acid	Dentin	Woessner's assay determines the dissolved hydroxyproline in dentine powders, SEM	Collagen fiber structures still intact
Okamoto et al., 1991 [231]	0.5 M EDTA, 7 M H3PO4 and 1% tannic acid	Dentin collagen	Trypsin digestion, hydroxyproline assay	Dentin collagen treated with tannic acid less susceptible to trypsin solubilization, more susceptible to enzymatic degradation without tannic
Feninat et al., 2001 [232]	37% H3PO4 15 sec.	Dentin	TMAFM	Collagen banding observable
Perdigao et al., 1996 [233]	37% H3PO4 15 sec., glutaraldehyde	Dentin	SEM	Different demineralized regions observed, regions of denatured and intact collagen fibrils
Marshall et al., 1997 [234]	1.76M 0.025M, 0.0001M H3PO4 and up to 30 min.	Dentin	AFM, etching rates measured from depth change	Etching rate much faster for lower pH (higher concentrations)
Lewandrowski et al., 1997 [235]	0.5 M HCl and laser perforation	Rat bone grafts	Bone densitometry and histology	Bone growth was enhanced through partial demineralization and laser perforation
Farid et al., 1978 [236]	0.8 N HCl	1000 year old whale rib	Carbon-dating	Statistical uncertainty in dating
Urist and Strates, 1970 [237]	0.006 – 0.6 N HCl, 6 hours, 15 days	Rabbit compact tibial bone	Histology, ash weight	Morphogenetic structure survives degradation in HCl, dissolution depends on concentration of acid
Lewandrowski et al., 1995 [238]	0.5 N HCl	Human fibulae	Flexural rigidity mechanical tests	Rigidity dependent on reduction of cortical thicknesses by

				demineralization depths.
Schajowicz and Cabrini, 1954 [239]	7.5% HCl and HNO3	Articular cartilage, endochondral ossified tissue	Histochemical staining	HNO3 and HCl, rapid loss of cartilage metachromasia, destruction of cartilage tissue
Vandersteenhoven and Spector, 1983 [240]	0.6 N HCl	Diaphyseal cortical rat bone	Histology of implanted site	Calcification occurred in the cartilage and osteoid and within implanted matrix
Danilchenko et al., 2004 [53]	0.1 N HCl	Bovine femoral bone	XRD	More imperfections in the crystallite surface due to mineral dissolving in acid

Table D-1. Effect of acids on bone.

Reference	Treatment	Sample	Experimental Method	Result
Dickson and Jande, 1980 [241]				maintains molecular integrity
Carvalho et al., 2000 [242]	6days 0.5 M EDTA and storage for 48 months	Human molar dentin	Tensile testing and TEM	No significant changes in UTS or E after storage; Intact fibrillar structure
Sasaki et al., 2002 [243]	0.5 M EDTA	Bovine mid-diaphyseal femora	AFM	Well formed collagen fibrils
Fois et al., 2001 [244]	0.5M EDTA	Human mid-diaphyseal femoral bone	Thermally stimulated creep spectra (apply torque to sample at a given temperature, quench to lower temp to freeze orientation and remove stress, linearly increase temp and measure anelastic deformation recovery)	Viscoelastic response comes from organic
Olsson, 2000 [245]	EDTA	Whale rib	Radiocarbon dating	EDTA treatment can yield reliable ages given the proper sample treatment
Lewandrowski, et al., 1997 [235]	0.5 N HCl	Rat tibial cortical bone	SEM	Visualized diffusion kinetics of "shrinking core" from advancing demineralizatoin
Makarewicz, et al., 1980 [246]	2 N HCl	Cortical bone	Diffusion studies	"shrinking core" reaction model applies well to demineralization.
Wang et al, 2002 [247]	0.5 M EDTA, then 70C	Human demineralized bone	HPLC, Tensile test	Collagen denatured showed least stiffness, No significant changes in hydroxylysylpyridinoline and lysylpyridinoline crosslinks.

Catanese et al., 1999 [248]	0.5 M EDTA	Human and bovine cortical bone	Tensile test	E and UTS of demineralized bone are heterogeneous among different sites
Farid et al., 1978 [236]	EDTA	Tusk	Carbon dating	As long as EDTA is completely removed, EDTA treatment yielded reliable dating results.
Kumagai et al., 1989 [249]	0.1 M EDTA	Spinal cord and dorsal root ganglia	Immunohistochemistry for peptide antigen	Immunoreactivity the same as when bone tissue removed mechanically
Kiviranta et al., 1980 [250]	15, 8, 4% EDTA in 1, 3, 5 days	Rabbit bone	Atomic absorption spectrophotometry	Concentration of EDTA correlates with rate of calcium extraction
Nikiforuk and Sreebny, 1953 [251]	34% EDTA	Rat bones	x-raying specimens at different intervals, radio=opacity measurements	$1/7^{th}$ the velocity of demineralization of acid solutions, useful for histochemical, chemical and histologic studies, protein not destroyed easily and no #)2 bubbles developed
Charman and Reid, 1972 [252]	15% EDTA, 8 N formic acid	Adult rat head	Staining with Alcian blue, haematoxylin and eosin	The epithelial lining of the nasal cavities, glands overlying cartilage and turbinates, nuclear chromatin, basophilia, and acidophilia had good staining, tissue remained intact., bone cellular detail preserved

Table D-2. Effect of EDTA on bone

Progressive demineralization etches with phosphoric acid have also shown that re-fibrillization occurs when placed in water for >1 day using AFM studies to observe collagen banding structure. (Feninat) Storage in PBS for up to 48 months of EDTA treated samples (0.5 M) did not cause any significant alterations of mechanical properties or structure of collagen fibrils as measured through tensile testing and TEM.

D.2 Deproteination

Reference	Treatment	Sample	Experimental Method	Result
Daumer et al., 2000 [253]	H2O2, HOCl/OCl	Collagen type I (human bone) and II (Human articular cartilage)	UV Absorbance and Fluorescence, Gas Chromatography, Mass Spectrometry	Oxidation of amine groups and decrease in pyridinoline crosslinks
Saboia et al., 2002 [254]	36% H3PO4 15 sec. and 10% NaOCl 60 sec.	Human non-carious molars	Marginal microleakage measurement from tracer agent after surrounding specimen with restoration.	Reduced microleakage
Broz et al., 1997 [255]	5.25% NaOCl	Bovine cortical bone from mid-diaphyseal region	Instron three-point flexure mechanical tests	NaOCl treated specimen cracked and spalled along outermost surface; Structural framework of HA crystallites compromised
Toledano et al., 1999 [256]	35% H3PO4 15 s, 5% NaOCl 2 min.	Cary-free human molar dentin	Contact angle measurement, roughness profilometry	Increase in surface roughness and wettability
Carter et al., 2002 [257]	5% NaOCl	Human cortical bone	Immunostaining, TEM	Structural changes to rhomboidal plates. The inorganic phase changes in morphology and immunohistochemistry.

Table D-3. Effect of hypochlorite on bone.

5.25% NaOCl, pH balanced to 7.0 with HCl was used to deproteinate cortical bone samples which were then kept frozen until testing. The treatment produced discrete regions of mineralized and chemically altered tissues as observed through optical microscopy. Mechanical behavior and material properties of the mineralized cores of the NaOCl-treated samples were also significantly altered. Three-point flexure measurements indicated that elastic stress decreased with immersion times. The anorganic layer thickness would also increase with the structure becoming increasingly brittle. The micro-hardness in anorganic bone regions from NaOCl treatment would drop. From either reaction kinetics or fluid flow NaOCl was shown to weaken the HA interactions, destroying the crystallite support framework and leading to micro-cracking within

cortical bone. 4-5% Hypochlorite was also found to disrupt pyridinoline cross-links and oxidize amine groups in collagen type I and II shown by UV absorbance and fluorescence assay. Hypochlorite also rapidly reacts with chlorinate pyridinium compounds. In general, NaOCl does not leave the overall structural and material properties of the mineralized and anorganic tissues completely intact.

Reference	Treatment	Sample	Experimental Method	Result
Raspanti et al., 1994 [258]	300, 500, 700, 900, 1200 C NaOCl?	Bovine cortical bone from femoral diaphyses	TEM and colorimetric hydroxyproline assay	700-1200 C had major structural change, solid state reorganization into tightly packed crystals. Negative hydroxyproline assay. 300-500 C samples kept structure, even had cross-banded mineral arrangements
Guizzardi et al., 1995 [259]		Bovine cortical bone from femoral diaphyses	Implanted in bone defects created in rat tibiae and inspected through histology	Demonstrated appreciable osteoconductivity and biocompatibility
Holden et al., 1995 [260]	200, 400, 600, 800, 1000, 1200, 1400 C	Midshaft transverse human femoral bone	XRD	Main mineral poorly crystalline phase persisted until 600 C and then recrystallized into larger crystals. Partial decomposition about 1000C occurred to calcium oxide, beta-TCP, alpha-TCP
Mayer et al., 1997 [261]	400, 700, 1000 C	HA precipitated at pH 7 and 9 with and without carbonate	XRD, FTIR spectra, SEM	Decomposition of apatite at 1000C. Transform to beta TCP at 700C
Catanese et al., 1998 [248]	50, 300, 350, 400, 700 C	Bovine cortical bone	Tension and compression tests, FTIR, XRD	Crystallographic changes occur above 600C; 350C and intact bone show similar diffraction and FTIR patterns

Table D-4. Effect of heat treatment on bone

Cortical bone samples were heated to temperatures ranging from 300 to 1200C. Temperatures exceeding 500C (700-1200C) were found to cause complete disruption of the tissue architecture and solid state reorganization of the mineral phase into tightly packed dense crystals several microns wide as observed through SEM and TEM. Recrystallization of apatite crystals to larger crystals changing from rod-shapes to tabular or equidimensional shapes was observed at temperatures larger than 600C. The XRD pattern shows a reordering of crystallite to a purer more improved crystalline form, indicated by shaper peaks. At 1000C, decomposition of the hydroxyapatite occurs to beta-tricalcium phosphate, alpha –tricalcium phosphate, calcium oxide phosphate, and loss of carbonate. This heat treatment was also correlated with age. At temperatures less than 500C the structure and distribution of mineral were left intact maintaining a reciprocal position, showing a mould of cross-banded fibril inner structure. A hydroxyproline assay performed through acidic hydrolysis and colorimetry showed negative results, indicative of complete collagen removal. A 400C heat treatment for in vivo implantation into a rodent tibial artificial defect showed tight adherence, osteointegration (penetration by host connective tissue, cells, and vessles), and biocompatibility (lack of antigenic response). Collagen removal reduces microleakage. Dissolution of collagen by deproteinization produces greater bonding efficacy between resin and dentin interface. Where the Raspanti study showed complete organic removal at 300C, Catanese would heat to 350C until there was no weight change and then heat to 700C to remove remaining organic which was an additional 15%. Heating to 350C shows similarities in ultrastructure and mechanical behavior with tensile and compressive behavior not changing significantly. The collagen network was tested through

denaturation heating ranging from 37-200C. The fracture strength of bone decreases as denatured collagen increases. Elastic modulus of bone stays the same regardless of the denatured collagen.

To conclude, I would say that H3PO4 and EDTA are fine because the fibrillar morphology and collagen mechanical behavior do not seem to be significantly altered. The NaOCl, I would suggest to stay away from because they chemically alter the amino acid and cross-link composition. The heat treatment does not alter the hydroxyapatite as long as the temperature is 500C and below. There are conflicting references regarding how much protein was removed. Raspanti says that at 300C all protein is removed. Catanese says that at 350C, at least 85% of the protein was removed. All references seem to assent to a more heterogeneously mineralized material based on type of treatment and time. For protein removal, the outside is more mineralized. For demineralization, the core is more mineralized. Because we are interested in surface charge/properties, it seems safe to say that at 350C for long enough periods of time that no weight change is exhibited, the surface at the very least is devoid of protein.

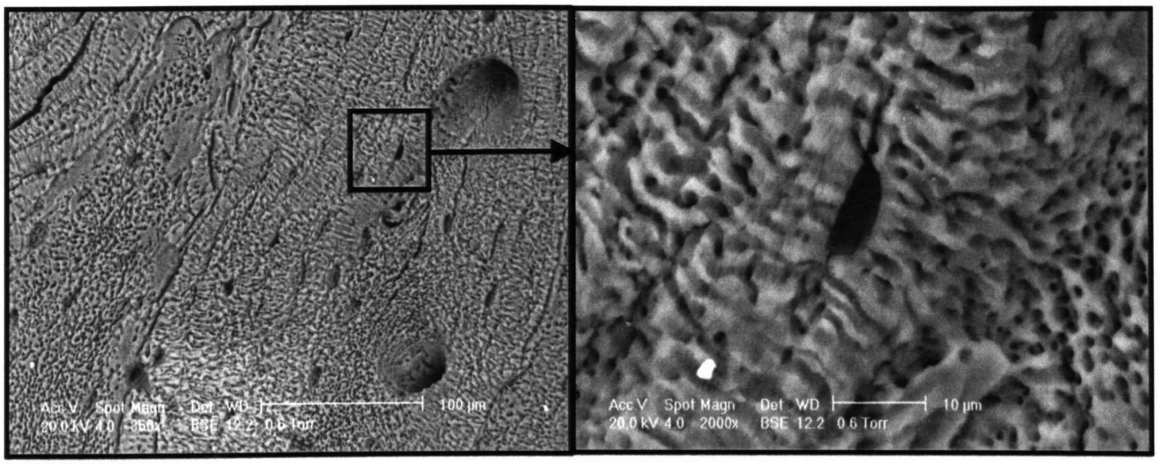

Figure D-1. SEM image of ethanol treated bone sample surface.

Appendix E

AFM Nanoindentation, Tip Calibration, and Rate Considerations

Tip area calibration is vital to accurate indentation results. The methods in this body of work for calibration of nanoindentation and AFM probe tips are shown here. Considerations will be given here regarding how inter-indent spacings have been properly chosen such that groups of indents yield the highest resolution mapping while not affecting their neighbors. A series of control studies on known samples were also performed in order to show that the contour mechanical property map results given in Chapter 4 are not a result of instrumental error.

E.1 Summary of AC160 Contact Area Indentation Calculations

Whether or not indentations laterally affect one another depends on how deep the probe penetrates into the surface and how much the residual plasticity affects the elastic and plastic zones. For Berkovich/Vickers probe geometry (semi-angle ~142°), approximately 3x the indent depth is a conservative estimate for the inter-indent spacing (Sneddon, Proc. Cambridge Phil. Soc., 1948). In this case, the AC160 silicon probe tip (semi-angle ~47°) has a much smaller lateral plasticity region. This study is to determine whether or not 100nm is a sufficient spacing between indents so that there is minimal effect between residual impressions between indents. The probe tip geometry was assessed (Figure E-1) through SEM and gold nanoparticle imaging [113]. It was found that the tip geometry was tetrahedral with a 17° bisected angle and a 30° side angle. If the

end of tip can be approximated by a spherical shape, the radius ~15 nm. Given these parameters, the approximate contact area was calculated through geometric analysis. The average penetration depth for the indent experiments ~25-30 nm. For indent depths of ~30 and ~50 nm, the contact area is estimated to be ~3000 and ~6000 nm^2. For the average ~30 nm depth, the inter-indent spacing is well within reason for no overlap. On the other hand, the ~50 nm depth is a borderline case for indent overlap. A 2-D axisymmetric finite element analysis (FEA) model shows the elastic and plastic zones (Figure E-2) for ~50 nm penetration depth. For a conservative strain estimate of 1% tolerance, the plastic zones go out to ~45 nm. For 100 MPa residual stress, the stress zone goes out to ~64 nm. Both of these cases are borderline for overlap. For these two cases, given that not every indent goes to ~50nm indentation depth, the 100nm spacing is within reason. Attempts were also made at imaging the surface of the region of interest both pre- and post-indent. At higher maximum loads (~20 μN) and with samples that are demineralized, images of residual impressions are visible. At ~5 μN maximum load and with undemineralized samples, the plastic deformation was below the resolution of the AFM tip that was used to image. This lack of visibility could also be attributed to visco-elastic recovery whose time scale is faster than that of AFM imaging. Whatever the case, the ability to detect surface features with resolution <5nm was not possible, this being perhaps, the strongest argument for sufficiency in inter-indent spacing. The greatest plasticity is found at the surface and if the surface deformation is not detectable, then below the surface is even more "undetectable". If indeed, the residual plasticity of one indent affected the subsequent mechanics of the next indent, then there would likely be a gradual increase in the average stiffness of the indent curves. There is no such pattern

observed from this type of behavior, hence, if there were any sort of mechanical rebound effect, the significance is minimal.

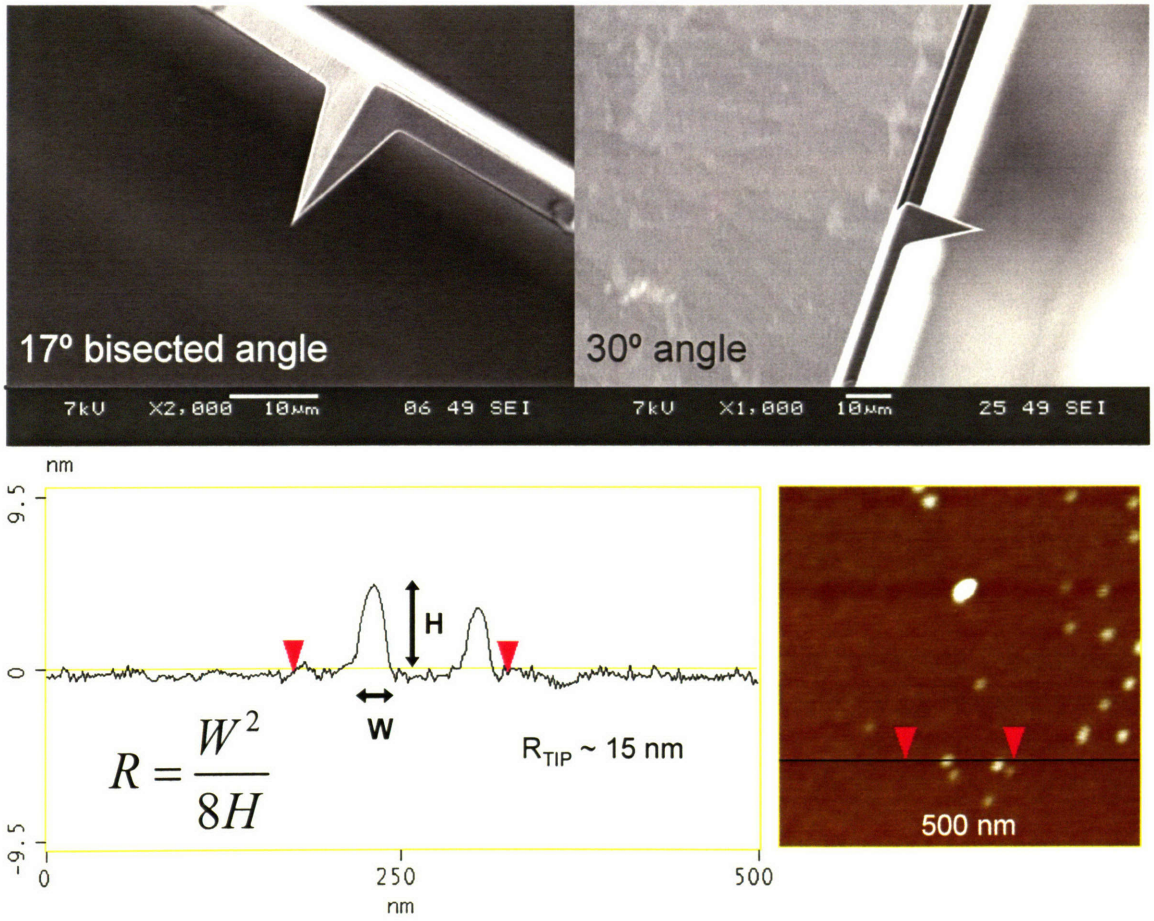

Figure E-1. The geometry of the probe tip was imaged through SEM and shown to have measured bisected and side view angles of 17° and 30° respectively. Based on height imaging of gold nanoparticles, the tip radius can be approximated (~15nm) given the width and height measured.

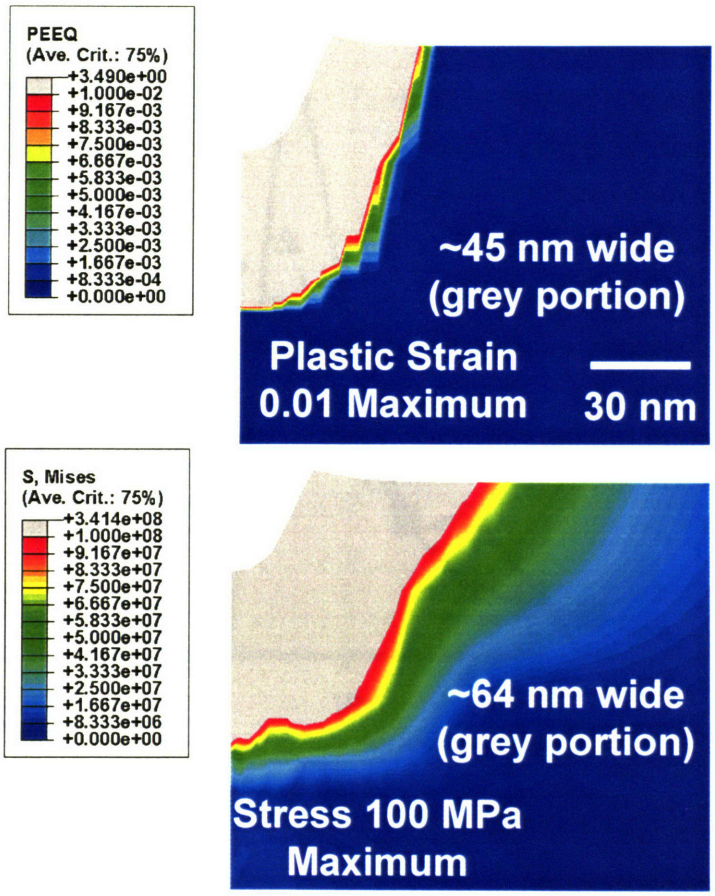

Figure E-2. Finite element back analysis shows that for the maximum indent shown, given an elastic-plastic model. For a threshold strain of 0.01 (shown by the grey portion), the maximum lateral width reaches to ~45-64nm.

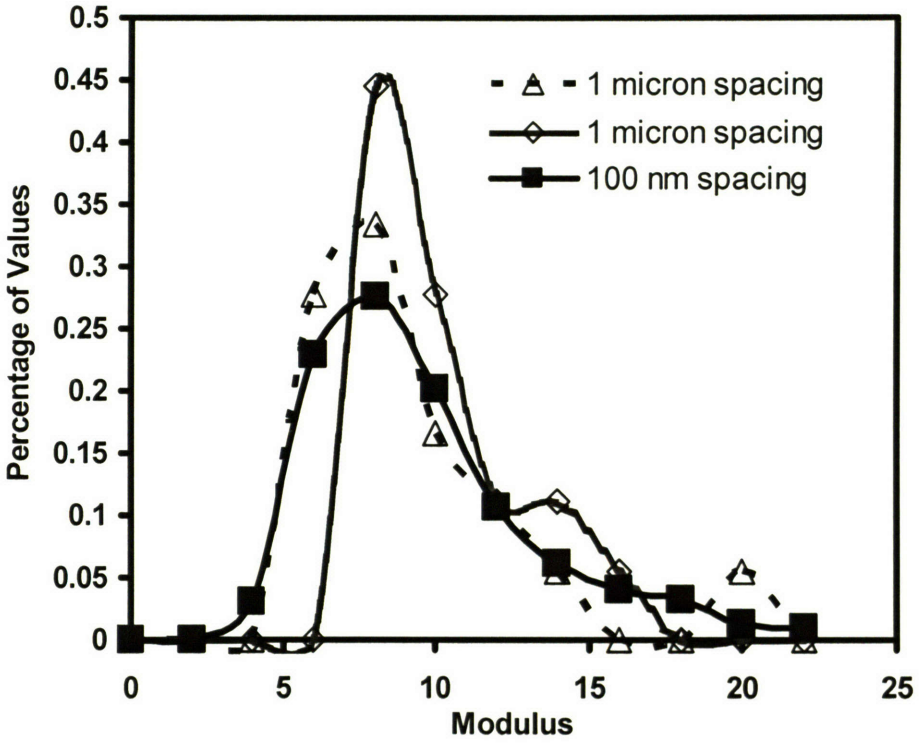

Figure E-3. Histogram distributions of 5μN indents spaced at 1 micron and 100 nm. The moduli values calculated were statistically similar ($p > 0.05$).

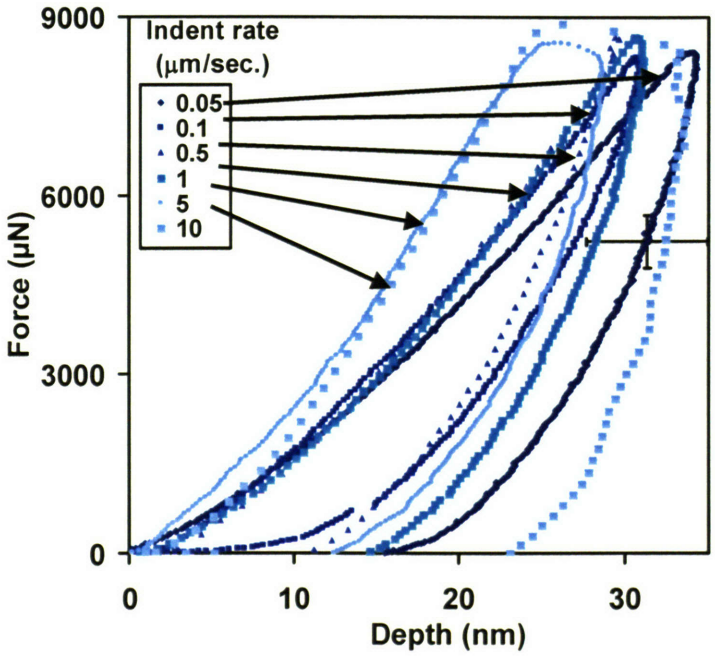

Figure E-4. Averaged AFM indentation curves on undemineralized bone with varying indent rates from 0.05 to 10 μm/sec.

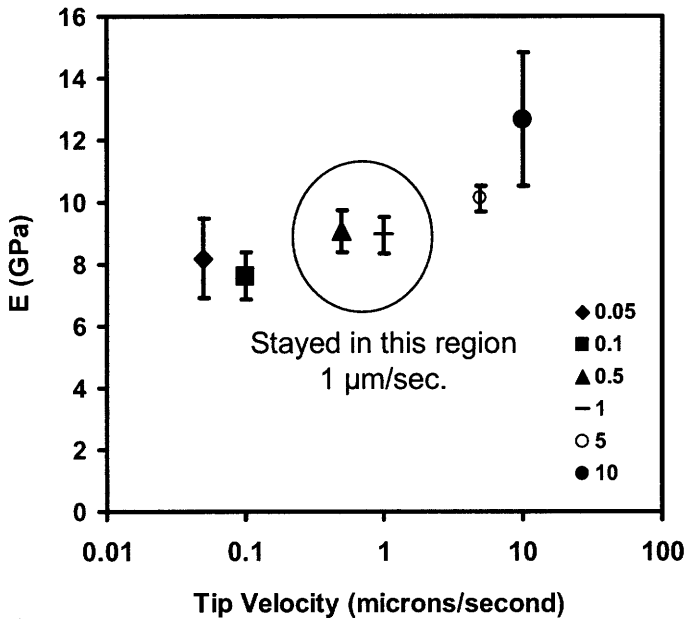

Figure E-5. Averaged modulus values from AFM indentation curves on undemineralized at varying indent rates from 0.05 to 10 μm/sec.

E.2 Validation Controls for AFM-Based Mapping Nanoindentation

A wide variety of control samples were used in order to show that the range and heterogeneity observed from the indentation mapping experiments were not a result of instrumental error. The contour property maps given previously (Chapter 4) have a range from 0-26 GPa. The samples that were tested as controls were carbon fiber (Figure E-6), polycarbonate (Figure E-7), nylon (Figure E-8), high-impact polystyrene (HIPS) (Figure E-9), nylon kevlar (Figure E-10), and epoxy (Figure E-11). The carbon fibers were 5-10 μm in diameter and held together by a more compliant epoxy matrix. A definite transition in material is evident from the AFM image, with corresponding changes in mechanical behavior as well. The apparent modulus values extracted for the carbon fiber and epoxy

across an interface were 33 ± 14 and 7.2 ± 2.7 GPa, respectively. The mechanical properties recorded for the polycarbonate, nylon, HIPS, nylon kevlar, and epoxy were 5.0 ± 1.2, 5.0 ± 0.5, 2.1 ± 0.5, 5.6 ± 1.1, and 2.9 ± 0.7 GPa, respectively. The range of apparent moduli values recorded for these samples did not span the 0-26 GPa scope that was found in bone, supporting that the mechanical behavior experiments recorded are not a result of instrumental error.

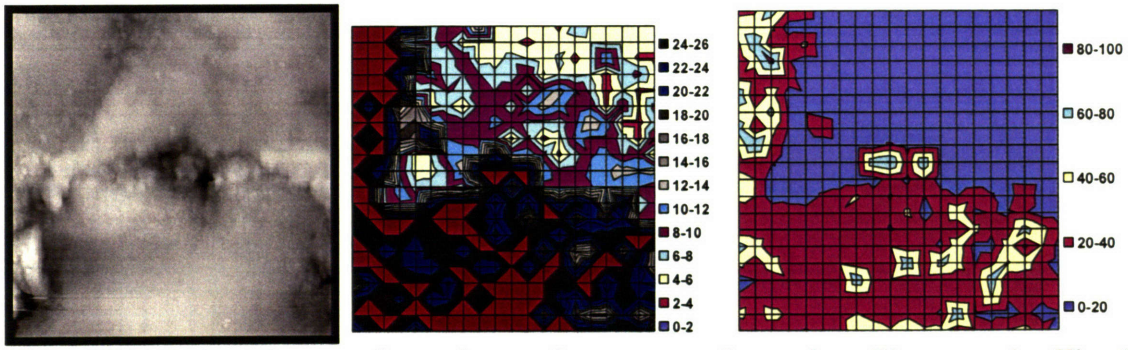

Figure E-6. Indentations performed on a 5 μm scan of a carbon fiber sample. The *(a)* AFM image shows the carbon fiber embedded within the surrounding epoxy material. The mechanical property map is shown for a range of *(b)* 0-26 GPa and *(c)* 0-100 GPa.

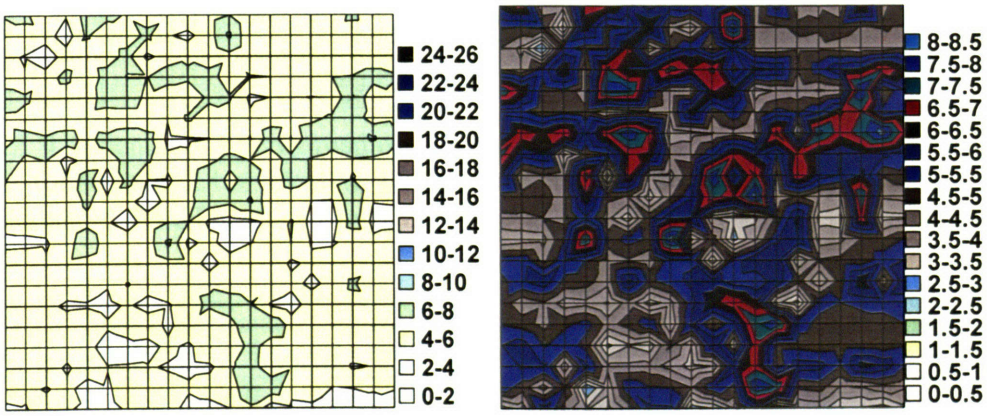

Figure E-7. Indentations performed on a 2 μm scan of a polycarbonate sample which is found to be 5.0 ± 1.2 GPa. The mechanical property map is shown for a range of 0-26 GPa and 0-8.5 GPa.

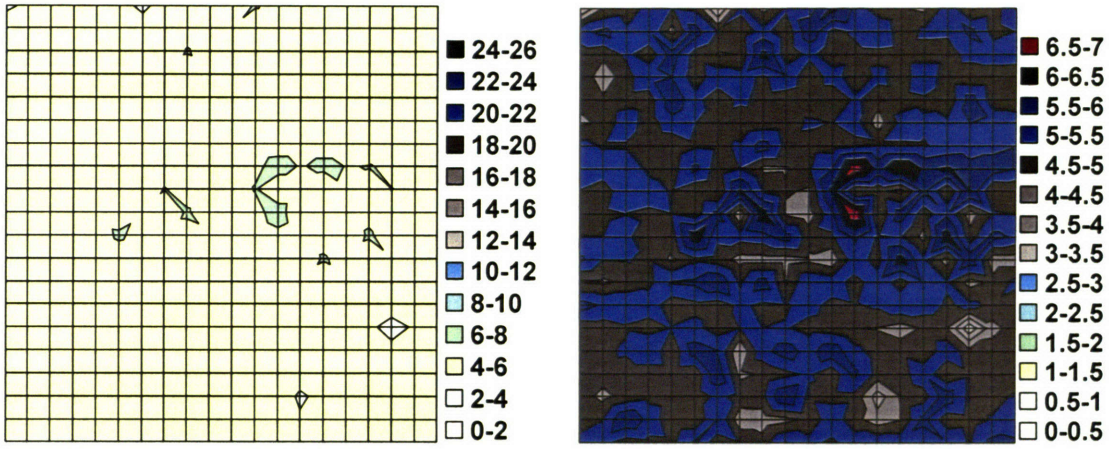

Figure E-8. Indentations performed on a 2 μm scan of a nylon sample which is found to be 5.0 ± 0.5 GPa. The mechanical property map is shown for a range of 0-26 GPa and 0-7 GPa.

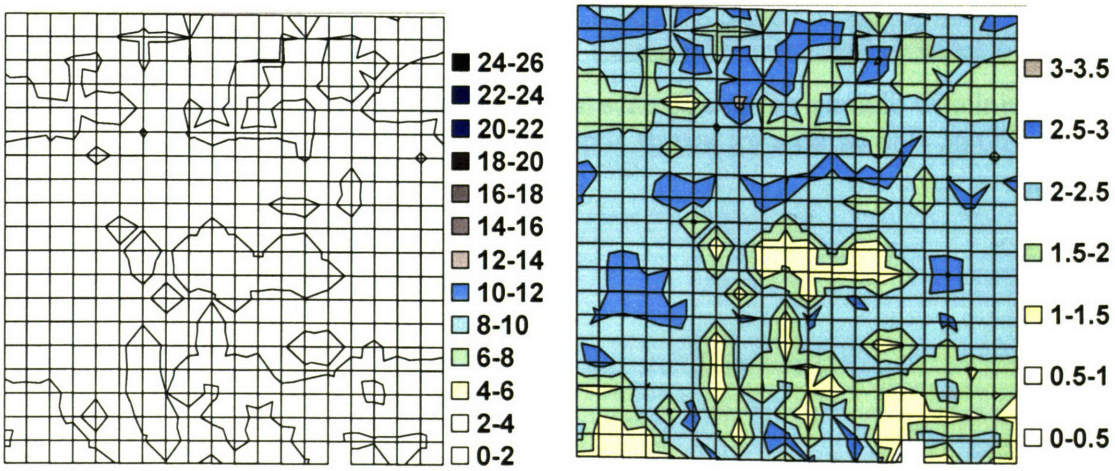

Figure E-9. Indentations performed on a 2 μm scan of a high-impact polystyrene sample which is found to be 2.1 ± 0.5 GPa. The mechanical property map is shown for a range of 0-26 GPa and 0-3.5 GPa.

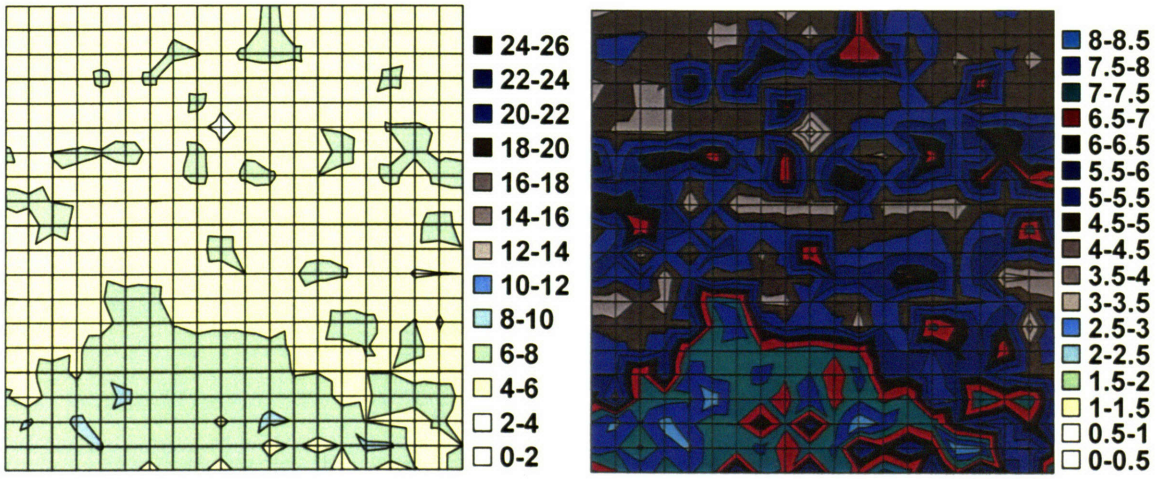

Figure E-10. Indentations performed on a 2 μm scan of a nylon Kevlar sample which is found to be 5.6 ± 1.1 GPa. The mechanical property map is shown for a range of 0-26 GPa and 0-8.5 GPa.

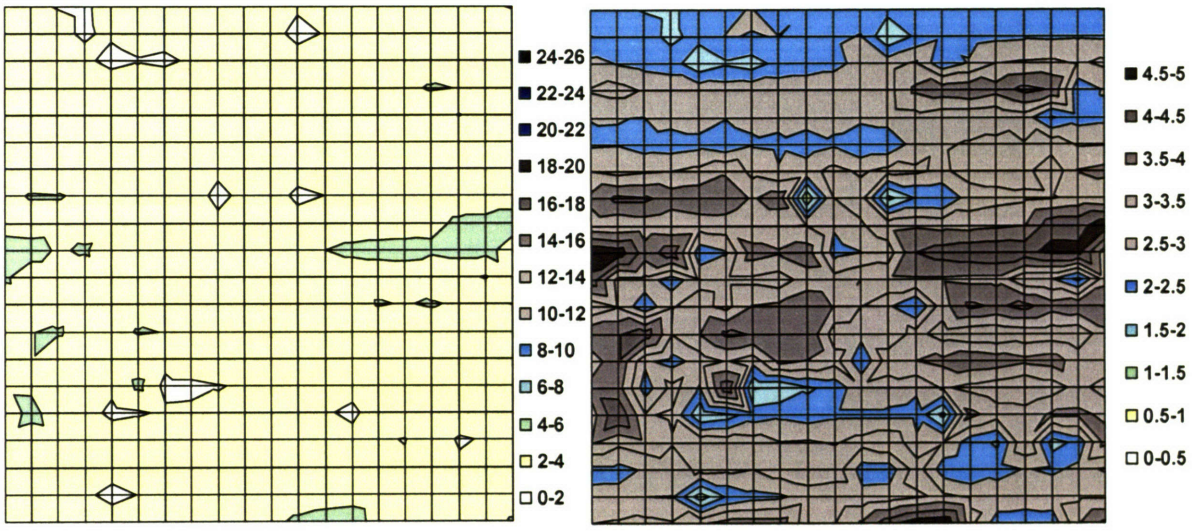

Figure E-11. Indentations performed on a 2 μm scan of a epoxy sample which is found to be 2.9 ± 0.7 GPa. The mechanical property map is shown for a range of 0-26 GPa and 0-5 GPa.

Appendix F

Additional FEA Information

F.1 Effect of Surface Roughness on AFM-Based Nanoindentation

FEA analysis was used to examine the effect of surface roughness on the indentation. A 2-D elastic-perfectly plastic FEA model was constructed in order to further study the effect of surface roughness. A topographical lateral dimension of 50 nm and peak-to-valley height of 10 nm were employed which were the experimentally measured average values from the corresponding AFM height images. The indenter had an apex angle of 34° and a tip radius of 15 nm (measured by SEM). 4-node bilinear plane stress quadrilateral (CPS4) elements were used. Two different cases were studied, one being where the indenter comes into contact with the top of a topographical feature and one where the indenter is exactly in between valleys of the topographical features. The results are shown in Figure F-1 and F-2. A 3.6% difference in modulus and 6.4% difference in yield stress were observed between these two models.

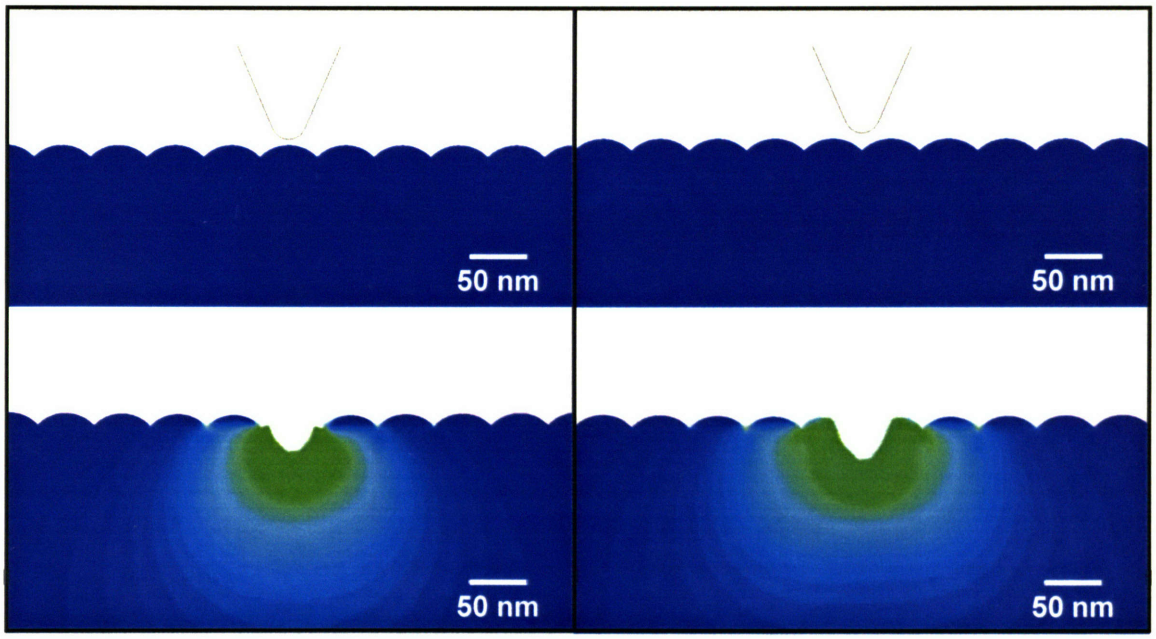

Figure F-1. 2D FEA model incorporating surface roughness features 50 nm in width and 10 nm in height. Left simulation is for tip on top of a nanoasperity and right simulation is for tip in valley between nanoasperities.

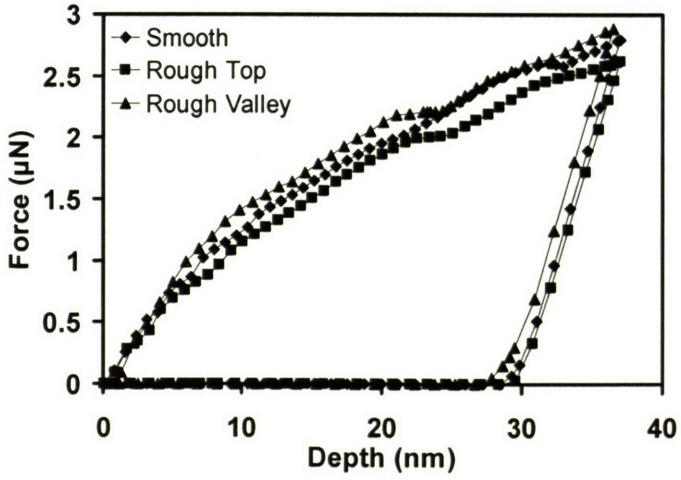

Figure F-2. Force-depth indentation curves resulting from the FEA simulations on a rough surface.

F.2 Effect of Surface Slope on AFM-Based Nanoindentation

The effect of sample slope was studied in this section through a 2-D FEA indentation using a rounded off rigid probe with a 34° included angle. It was shown that

there is no noticeable change in force-depth behavior upon indentation until there was a ~26° tilt in the sample surface (Figures F-1 and F-2).

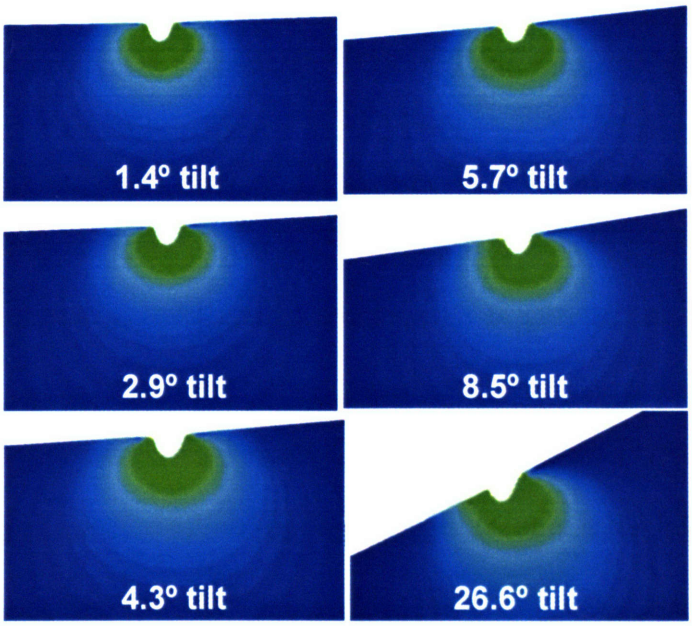

Figure F-3. The stress distribution for a 2-D FEA indentation model for tilt angles of 1.4°, 2.9°, 4.3°, 5.7°, 8.5°, and 26.6°.

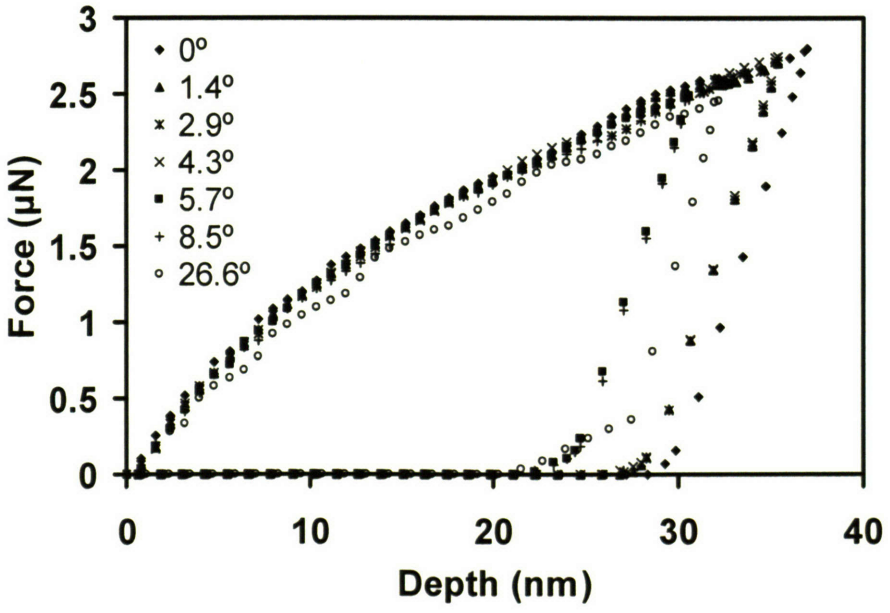

Figure F-4. Indentation plots are given for a 2-D FEA indentation model for tilt angles of 1.4°, 2.9°, 4.3°, 5.7°, 8.5°, and 26.6°.

Appendix G

Identification of Image Features of Bone Samples

The main tapping mode (TM)AFM images of untreated bone (polished) given in the thesis are given in Figures G-1 and G-2. Histograms recording the lateral dimensions of the clusters shown are overlayed in Figure G-3. In general, images taken with the Molecular Force Probe 3-D (MFP3D) are higher resolution than those from the Quesant due to a number of optimization parameters built in to the system. These features include a superluminescent diode (860 nm wavelength) which eliminates interference artifacts, closed loop operation utilizing a linear variable differential transducer to simultaneously track position while imaging, sensor noise <0.6 nm in average deviation laterally and <0.06 nm vertical deviation, and also vibration dampening systems (table and hood) which enable minimal outside interference. The Quesant, on the other hand, does not incorporate the same degree of imaging scrutiny.

Figure G-4 gives TMAFM (Kindt et al., 2005) and SEM (Thurner et al., 2006) images taken of trabecular bone (dried) that had been fractured in buffered solution (unpolished, 150 mM NaCl, 10 mM Hepes, pH 7.0), showing similar surface clustered mineral morphologies as those in Figure G-1. Histograms comparing Figure G-1 and G-4 are overlayed in Figure G-5, giving comparable overall dimensions. Figure G-6 gives images from Weiner and Price, 1986 as well as Eppell et al., 2001 that also give similar size distributions as those given here. Table G-1 also shows a comprehensive literature search of the particle sizes of hydroxyapatite clusters from various treatments observed

through different materials techniques (e.g. AFM, TEM, SEM, FTIR, SAXS, XRD). In general, the morphologies and range of sizes found are consistent with those presented here.

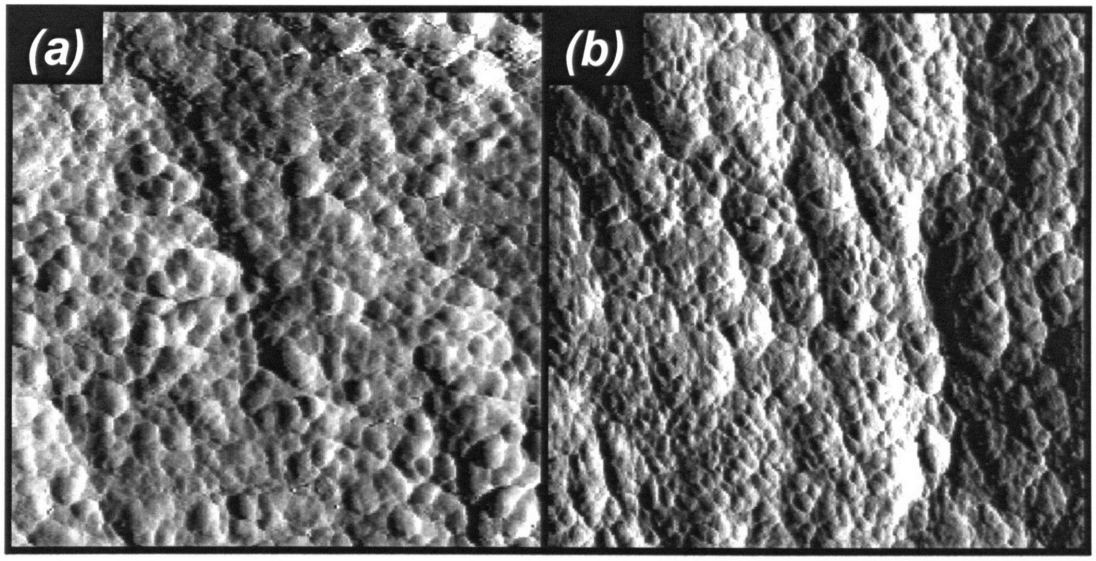

Figure G-1. Tapping mode AFM images (submitted) taken with the MFP3D (2 micron scan) with cluster sizes of *(a)* 71 ± 26 nm (n=69) and *(b)* 58 ± 25 nm (n=69).

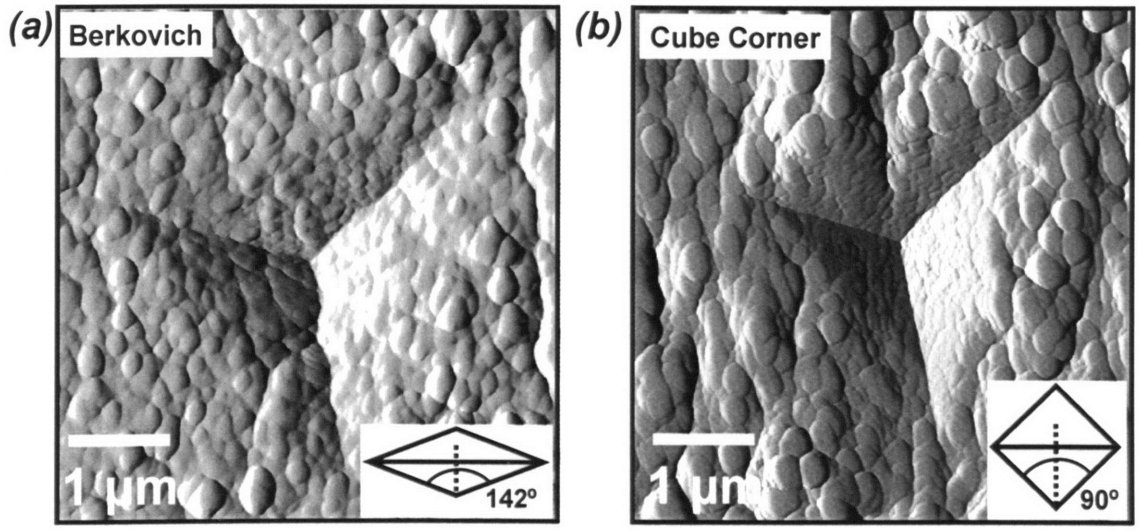

Figure G-2. Tapping mode AFM images (submitted) taken with the Quesant (5 micron scan) recording cluster sizes of *(a)* 108 ± 40 nm (n=69)with a Berkovich indent impression and *(b)* 184 ± 31 nm (n=69) with a Cube Corner indent.

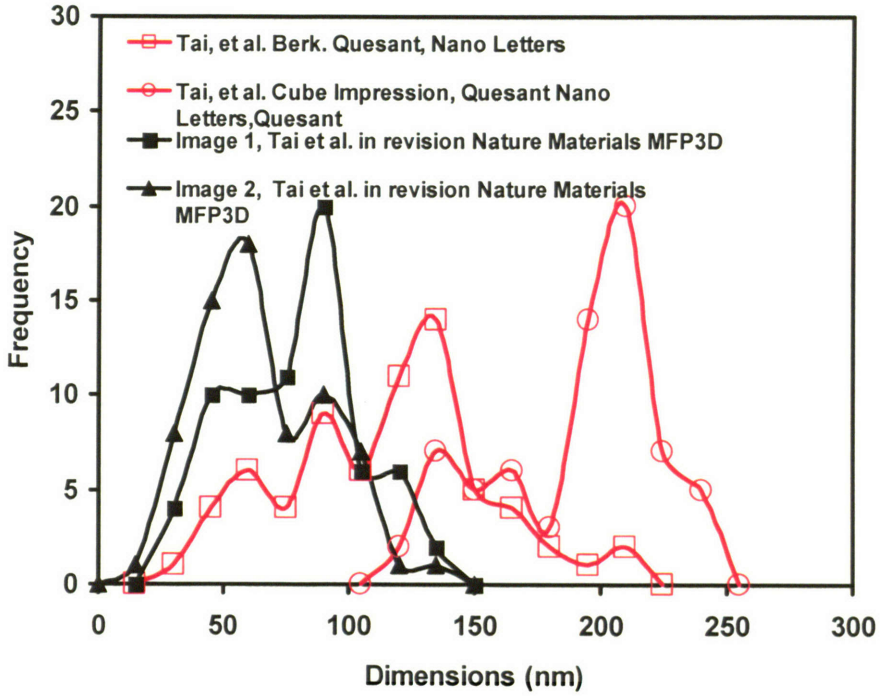

Figure G-3. Histograms showing the distribution of lateral dimension given for the images shown above. In general, images taken with the Quesant microscope are of lesser resolution than those taken with the MFP3D.

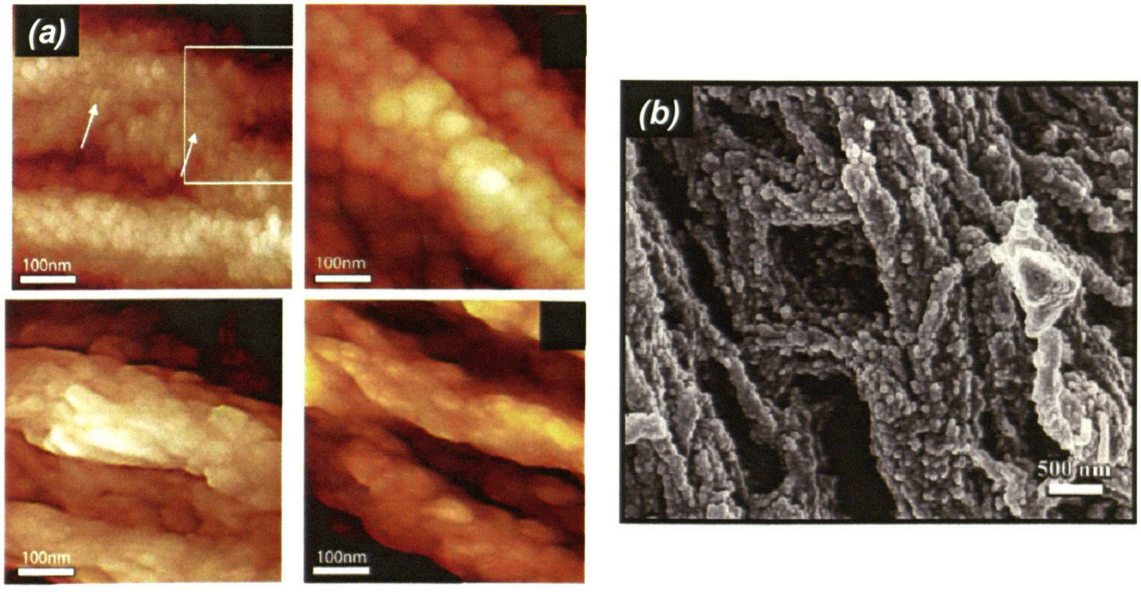

Figure G-4. *(a)* TMAFM images of bovine bone showing average cluster sizes of 42 ± 19 nm (n=69). *(b)* SEM images of bovine bone with average cluster sizes of 72 ± 17 nm (n=34).

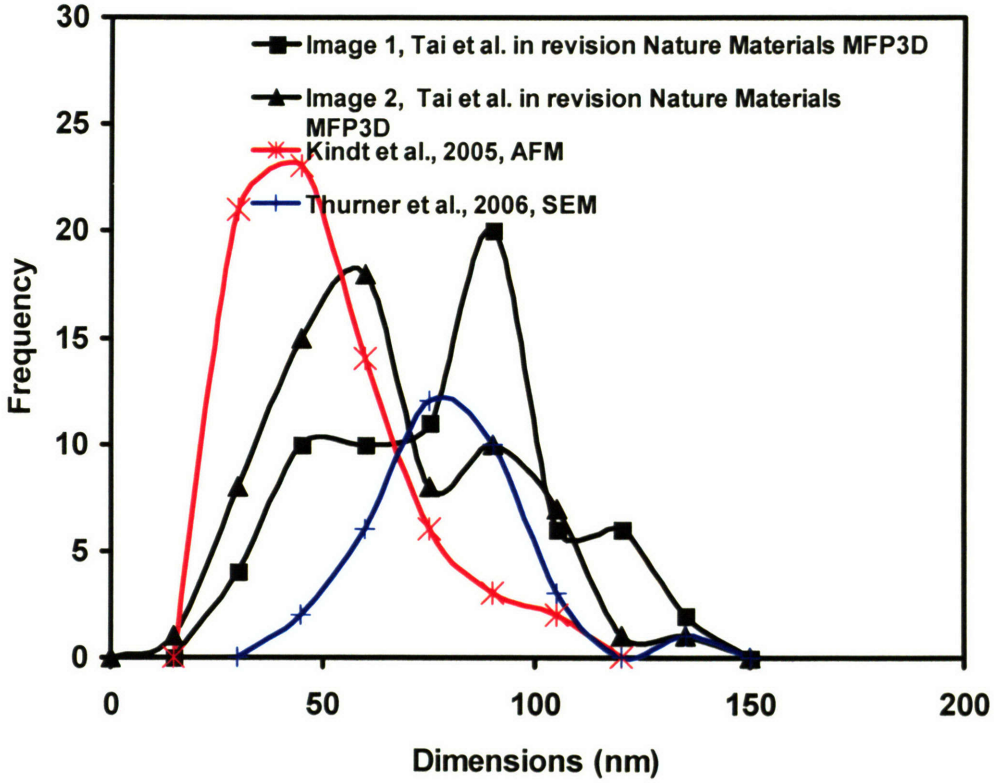

Figure G-5. Histograms showing comparable distributions of lateral dimension given for the images in figures 1 and 4, given previously.

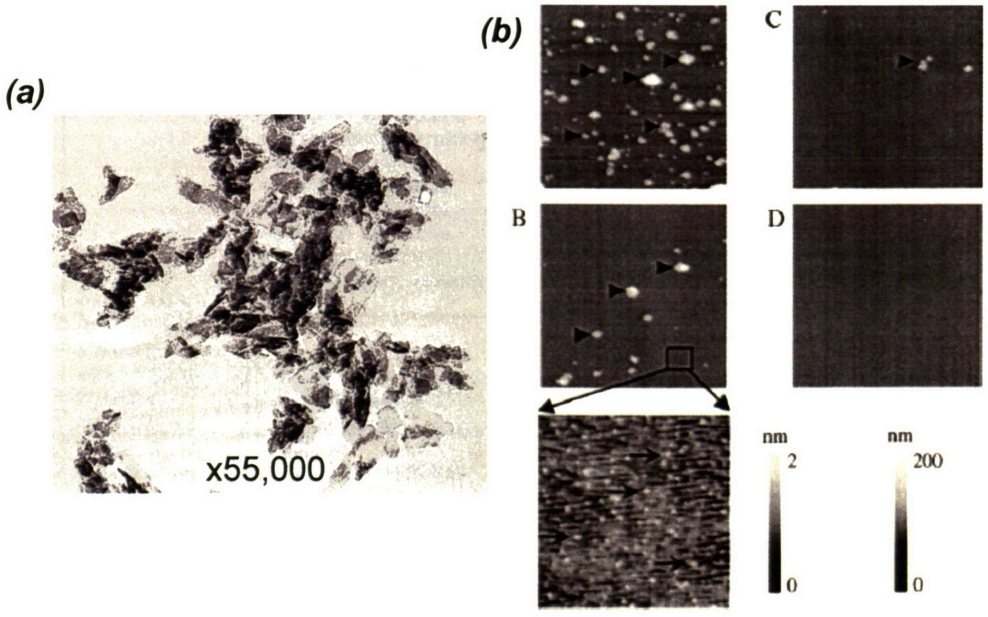

Figure G-6. *(a)* SEM images of bone crystallites showing average cluster sizes ranging from 45 – 60 nm. *(b)* TMAFM images of bone crystallites showing large and small crystallites ~90 and ~14 nm, respectively.

Reference	Sample Type	Preparation	Measurement	Crystal Size/Dimension
Ascenzi et al., 1965	Ox femoral shaft	Fixed in neutral formaldehyde and ground	Microradiographs from polarizing microscope	Needle-shaped crystallites, reach a maximum width of 40-50 Angstroms, calcium salts, parallel oriented bands having average width of 40 nm, interbands reach 25 nm.
Ascenzi et al., 1978	Human/Ox femoral shaft	Cross sectioned	Low and Wide angle XRD and EM	Needle-shaped granules with maximum width 40-45 A, bands of 400 A
Kim, Rey, Glimcher, 1995	Bone crystals of fish, chicken, mouse, and bovine	100% ethanol, frozen in liquid nitrogen, stored at -20C, lyophilized to bone powder, 3 hours at 4C in chloroform and methanol (2:1), ethanol, ethyl acetate, dried, nonaqueous hydrazine for 12 hours, ultrasoincation, 100% ethanol, guanidine hydrochloride and SDS, plasma ashing	XRD, FTIR, TEM	Average dimensions bovine bone 15.8 ± 7.3 nm, 27.3 ± 11.4 nm, 0.59 ± 0.18 nm
Fratzl, 1992	Mineralized turkey leg tendon, calvarial/femur/iliac crest bone	Formaldehyde fixation, ethanol, and sodium barbital buffer at pH 7.4 and glucose	SAXS	plate and needle-like crystals 2-4 nm
Wachtel and Weiner, 1994	Mineralized turkey tendon	NaOCl (5%), water, acetone	SAXS	17 A thickness of plates, bone crystals are needle shaped, shapes irregular
Hohling et al., 1971	Rat incisor dentine	Glutaraldehyde-fixed	EM	6.5 ± 1.2 nm
Bertazzo and Bertran, 2006	Parietal and femoral bone from Wistar rats	Hydrazine deproteination	XRD	19.2 ± 0.4 (PD), 21 ± 2 (PM), 22.3 ± 0.6 (PY), 19 ± 1 (FD), 18.6 ± 0.6 (FM), 22 ±2 (FY)
Bertazzo and Bertran, 2006	Parietal and femoral bone from Wistar rats	Hydrazine deproteination	SEM	Globular structures ranging between 70-90 nm
Danilchenko et al., 2003	Bovine bone femur	Untreated	XRD	33.34 ± 48.0
Baud and Very, 1982	Femoral ox shaft		EM and XRD	10 x 50 x 120 nm; plate crystals 5 x 40 x 40 nm
Kuhn-Spearing et al., 1996	Bovine bone	Organic phase removed, bone powder prepared non-aqueously by milling and sieving, solvent extraction of lipids by chloroform:methanol, anhydrous hydrazine, low power plasma ashing, ethanol, vacuum dried	TEM, XRD	~30 nm
Miller and Burnell, 1977	Synthetic HA formed from the salts of CaCl2, K2HPO4, Na2CO3	Aged for 6 days at 23 and 45 degrees	XRD	Specific crystal sizes not given
Jackson et al., 1978	Rabbit, ox, human bone cortical, midfemoral region	Unfixed, unembedded bone, cemented into an epoxy resin block for support	EM, XRD	32.4 ± 16.3 nm from EM, XRD shows 32.2 ± 1.1
Burnell et al., 1980	Rat tibia bone	Defatted with petroleum:ethyl ether, hydrazine deproteinization	XRD measured ratios of Ca, Mg, Na, HCO3, P	Only ratios reported, not specific sizes
Fratzl et al., 1996	Cranial and caudal zones in the transverse	Untreated	SAXS	Crystals elongated average thickness of 3.17 ± 0.15 nm in caudal region, 3.79 ± 0.20 nm in cranial region.

	midshaft section of the equine radius			
Ghezzo et al., 1996	Rat femur	Weiner/Price deproteinization technique, defatted, NaOCl, dried at 50C	XRD	sizes not recorded; crystallinity not changed significantly with ipriflavone-treated rats (previously it would increase bone density and improve biomechanical properties)
Weiner and Price, 1986	Whale bulla, bovine tibial cortical bone, rat tibia, human femur, turkey tendon, bluefin tuna bone	NaOCl, EtOH drying	TEM	Plate-shaped, tabular crystals, fused aggregates 29 ± 10.6 nm, 16.5 ± 5.4 nm for turkey tendon; 55 ± 25 nm, 30 ± 10 nm for human femur
Boskey et al., 2006 (review)	Mouse tibia	Sectioned and embedded	Infrared spectroscopic imaging	Sizes not recorded
Bozec et al., 2005	Dentin, bovine cortical bone	Polished	AFM, contact mode (Dimension)	225 nm spherites
Wopenka et al., 2005 (review)			Raman spectroscopy, FTIR	size not reported, Ca/P ratio, crysallographic clusters
Fratzl et al., 2004 (review)	Human bone		TEM, SAXS	Platelets and needles; 2-7 nm thick, 15-200 nm long, 10-80 nm wide
Danilchenko et al., 2004	Femur of mature cow	Modification in the bioapatite crystals observed in the bone subjected to demineralization in a 0.1 N HCl; boiled in water, dried in air	XRD and fourier analysis	21 ± 1 nm crystallite size, decreasing with further demineralization
Boskey, 2003 (review)			XRD, IR, TEM	Effects shown on crystal size, size range not reported
Hiller et al., 2003	Fresh cortical bone from sheep long bones	Controlled heating at 500C, 700C, 900C for 15 or 45 minutes	XRD, SAXS	2.3 - 2.8 nm is control; 5.24 - 31.26 nm thicknesses for heated samples which grew in thickness upon heating
Tong et al., 2003	Isolated mineralites from cortical bone of mid-diaphysis of 3-5 week old bovine tibia and femurs	Same process as Kim/Rey/Glimcher 1995	AFM	Small mineralites: 9 ± 3 nm x 6 ± 2 nm x 2 ± 1.2 nm; Large mineralites: 110 ± 61 nm x 72 ± 41 nm x 34 ± 29 nm
Zizak et al., 2003	Normal human bone at the interface between bone and cartilage; patella, fourth lumbar vertebral midbody male and female	Fixed in ethanol/formalin solution and dehydrated in ethanol before being embedded in polymethyl methacrylate.	Scanning small-angle X-ray scattering and quantitative backscattered electron imaging	3.4 ± 0.4 and 2.5 ± 0.4 nm platelets
Danilchenko et al., 2002	Femoral bovine bone	Boiled in water, cleaned and dried in air.	Fourier analysis and approximation with threefold convolution of X-ray lines	Rod-shaped or elongated platelets with 20-30 A thickness, and 200-400 A length: 210.8 ± 13.4 A, 288.2 ± 62.1 A, 186.2 ± 18.0, 164.4 ± 20.4 A
Eppell et al., 2001	Tibial bovine bone	Frozen, ethanol, ether, ground in liquid nitrogen-cooled mill, defatted particles in chloroform and methanol; repeated cycles of hydrazine extraction and plasma ashing	AFM in tapping mode	Large mineralites: thickness 12-115 nm, mean 37 nm; width ranged from 27-172 nm, mean of 64 nm; length ranged from 43-226 nm, mean of 90 nm. Small mineralites: thickness 0.61 ± 0.19 nm, width 10 ± 3 nm, length 15 ± 5 nm; thin plate shapes
Peters et al., 2000	Cancellous bone from femoral head, cancellous bone from distal femur, newly	Embedding in PMMA, rinsed with ethanol, dried in vacuo, ground in agate mortar	Differential thermal analysis-mass spectrometry, x-ray powder diffraction (synchrotron), x-ray	From high resolution x-ray powder diffractograms (Scherrer equation) 19, 23, 18, 29 nm

	formed callus bone after fracture, tumor bone		absorption spectroscopy, infrared spectroscopy.	
Zizak et al., 2000	Human femoral head	Fixed in ethanol/formalin solution, dehydrated in a graded series of ethanol before embedding in PMMA	SAXS, WAXD	3.1 to 3.9 nm
Henning http://www1.medizin.uni-halle.de/biomechanik/acas99/abstracts/henning.htm	Cortical bone femur	Dehydrated through alcohol, embedded in PMMA	TMAFM	Length 91 nm, width 53 nm, thickness 17 nm
Landis et al., 1996	Tibiae from embryonic chicks	100% ethylene glycol, embedded in Spurr resin, trimmed, cut to 0.25 um thick sections.	high voltage electron microscopy	80 x 30 x 8 nm length, width, thickness
Fratzl et al., 1996	Mouse femurs and tibiae	Ethylene glycol and cellosolve and embedded in epon resin	SAXS	Mineral blocks, dimensions typically exceeding 50 nm
Landis et al., 1993	Mineralizing tendons from domestic turkey	2.5% glutaraldehyde, 1% osmium tetroxide, 100% ethylene glycol, dehydrated, embedded in Spurr or Epon resin	High voltage electron tomography, 3-D reconstructions	Length up to 170 nm, width 30-45 nm, thickness 4-6 nm
Weiner and Traub, 1991	Diaphyses of rat tibia, cortical	Cut, washed with deionized water, sonicated, dried under vacuum, coated with gold	SEM and TEM	Distance between parallel layers viewed edge on is ~5 nm, no information about size of mineralites
Weiner and Traub, 1986	Calcified leg tendons	Ethanol, sonicated, frozen, vacuum dried, embedded in epon	TEM	Length 334 ± 106 A, width 185 ± 106 A
Matsushima et al., 1981	Compact bone from rat and rabbit femurs	Washing with distilled water and drying at 50 C after grinding	SAXS	43-50 A
Robinson, 1952	Human cortical bone	Autoclaved, blended, re-autoclaved	TEM	20-150 nm length, 10-80 nm width
Kindt et al., 2005	Bovine trabecular bone	Wet samples stored in -20C Na-buffer (150mN NaCl, 10mM Hepes, pH 7.0) before fractured in tension, rinsed in Ca-buffer (110mM NaCl, 40mM CaCl2, 10mM Hepes, pH 7.0) smooth fracture surface embedded in epoxy resin	TMAFM	Particle dimensions measured ranged 70 ± 35 nm, 53 ± 14 nm, and 25 ± 15 nm.
Thurner et al., 2006	Human trabecular bone	Compressed in buffer 150mM NaCl, 10mM Hepes, pH 7.0, rinsed in water and ethanol, coated with gold	SEM	72 ± 17 nm

Table G-1. Literature review of mineral cluster sizes and morphologies based on various treatments and measurement techniques.

The results of the table show that in general, the mineralite morphologies are predominantly platelet in shape with needle-like formations also. The length, width, and thickness dimensions also vary for each crystallite. Typical lengths range from 20 – 120

nm (even as high as 225 nm). Thicknesses will range from 2 – 10 nm. Widths will vary depending on the overall morphology of the crystals, but will typically be in between that of the lengths and thicknesses reported from the various studies. In general, from high resolution TEM imaging, the typical average dimensions observed in crystallite formation through independent preparation methods are 30-70 nm.

Appendix H

Effect of Strain Hardening on Indentation Behavior

A strain hardening sensitivity analysis was performed using FEA to compare between different hardening cases for undemineralized bone. Relative curve fits to indentation unloading curves yielded a modulus of E = 9 GPa (Figure H-1). In this case, values of strain hardening used were n = 0.0, 0.1, 0.2, and 0.3. Corresponding values of yield stress were Y = 210, 185, 160, and 135 MPa. Here, for each increase of 0.1 in the hardening exponent, for similar indentation behavior (that would also match the experimental indent curve as closely as possible), the yield stress would decrease accordingly by 25 MPa. Given this result, when n is fluctuating, it is difficult to predict accurate trends for yield stress. However, if n is constant, it is not expected for the overall trend to be affected. For a strain hardening/softening law, the elastic-perfectly plastic average yield stress prediction is much more suitable given that the parameters are manageable and that the nanoindentation behavior can still be captured.

An independent method for determining the strain hardening and constitutive law is needed. The first approximation is to assume that macro=nano behavior, which produces n=0.3. This assumption is considered to be inaccurate due to the many structures (e.g. lacuno-canalicular canals, osteons, lamellae) that exist above the length scale that is being probed and the fact that damage accumulation is also not observed. Also, softening is a phenomenon that occurs at the macroscale which is not captured in the exponential strain hardening model. As a result, it is expected for the nanoscale

mechanical properties to be different than at the macroscale. In addition to this statement, the smaller the length scale that is tested, fundamentally, the more ideal (i.e. less defects, cracking) the material will perform.

The paper, "Computational modeling of the forward and reverse problems in instrumented sharp indentation", by Dao et al., 2001 [40] gives validation from a wide array of FEA indentation simulations to determine the "forward analysis" problem, being the degree to which indentation curves can be predicted from macroscopic elastic-plastic properties, and the "reverse analysis" problem (local mechanical properties extracted from indentation curves). The properties of interest are the modulus (E), yield strength (Y), and hardening exponent (n). The "reverse analysis" algorithm was applied to a set of indentation curves on bone, utilizing a set of dimensionless functions (P1-P5) that are set forth in Figures 8, 10, and 11 of the paper. In short, the strain hardening exponent was found to be n = 0 for bone at mineral contents both above and below the percolation threshold. As stated before, there is no reason why the mechanical properties at the nanoscale should necessarily reflect the behavior of macroscopic testing.

Using the dimensionless functions found in Dao et al. for undemineralized bone (58 wt.%):

1) The W_p/W_t ratio came out to 0.76, which corresponds to a h_r/h_m ratio (from P5) of 0.82.
2) The E* value is 14 GPa from P4.
3) The C value is 13 GPa from fitting to $P = Ch^2$.
4) The $Y_{0.033}$ value is 250 MPa from using P1 where the plastic strain of 0.033 is independent of n
5) Using P2, comparing the $E^*/Y_{0.033}$ ratio of 56 to the $(dP/dh)/(E^*h_m)$ ratio of 5.78, the strain hardening exponent comes to n = 0.
6) Using P3, comparing the $Y_{0.033}/E^*$ ratio of 0.0178 to the h_r/h_m ratio of 0.82 from 1), the strain hardening exponent comes to n = 0.

For bone that was partially demineralized for 1 sec. in phosphoric acid and rehydrated (37 wt.%):

1) The W_p/W_t ratio came out to 0.8, which corresponds to a h_r/h_m ratio (from P5) of 0.85.
2) The E* value is 8.6 GPa from P4.
3) The C value is 5 GPa from fitting to $P = Ch^2$.
4) The $Y_{0.033}$ value is 100 MPa from using P1 where the plastic strain of 0.033 is independent of n
5) Using P2, comparing the $E^*/Y_{0.033}$ ratio of 50 to the $(dP/dh)/(E^*h_m)$ ratio of 5.84, the strain hardening exponent comes to n = 0.
6) Using P3, comparing the $Y_{0.033}/E^*$ ratio of 0.012 to the h_r/h_m ratio of 0.85 from 1), the strain hardening exponent comes to n = 0.

Further evidence for a lack of hardening is that there is no increase in the hardness (the material's resistance to plasticity) with increasing maximum load (Figure H-2). There is a statistically significant lack of trend based on ANOVA (F = 0.3844, shows no significant differences), which shows that as the material is deformed at greater depths, there is no hardening or softening effect occurring at the length scale which is probed.

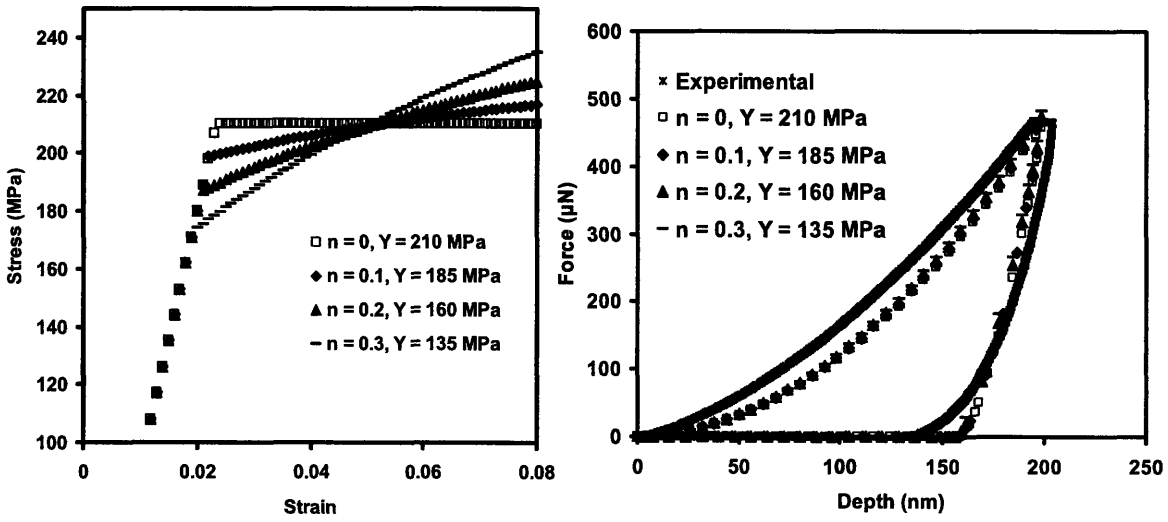

Figure H-1. Sensitivity analysis carried out with varying values of strain hardening exponent and yield stress using FEA to generate similar indentation behavior compared to indentation on undemineralized bone.

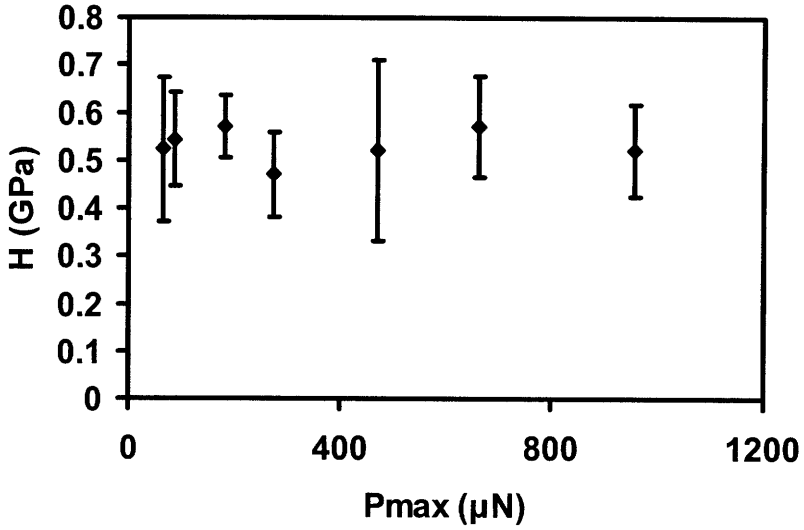

Figure H-2. Plot is given of the hardness with increasing maximum load. The hardness is relatively constant as the maximum indentation load increases.

References

[1] D. M. Tsai and B. Hsiao. Automatic surface inspection using wavelet reconstruction *Pattern Recogn.*, 34(6):1285-1305, 2001.

[2] W. C. Oliver and G. M. Pharr. An improved technique for determining hardness and elastic modulus using load and displacement sensing indentation experiments *J. Mater. Res.*, 7(1564, 1992.

[3] J. D. Currey, "The structure of bone tissue," in *Bones: Structure and Mechanics*: Princeton University Press, 2002, pp. 3-26.

[4] P. Bianco and P. G. Robey. Marrow stromal stem cells *J. Clin. Invest.*, 105(12):1663-1668, 2000.

[5] Americans over 50 at risk for bone fractures *FDA Consumer Magazine*, 39(1):2005.

[6] "FAQs about osteoporosis," D. o. P. H. a. Enviornment, Ed.

[7] S. C. Cowin, *Bone Mechanics*: CRC Press, 1989.

[8] K. Tai, H. J. Qi, and C. Ortiz. Effect of mineral content on the nanoindentation properties and nanoscale deformation mechanisms of bovine tibial cortical bone *Journal of Materials Science - Materials in Medicine*, 16(947-959., 2005.

[9] R. S. Lakes. Materials with Structural Hierarchy *Nature*, 361(511-515, 1993.

[10] W. J. Landis. The strength of a calcified tissue depends in part on the molecular structure and organization of its constituent mineral crystals in their organic matrix *Bone*, 16(5):533-44, 1995.

[11] J. Y. Rho, L. Kuhn-Spearing, and P. Zioupos. Mechanical Properties and the Hierarchical Structure of Bone *Medical Engineering and Physics*, 20(92-102, 1998.

[12] S. Weiner and H. D. Wagner. The material bone: Structure-mechanical function relations *Ann. Rev. Mater. Sci.*, 28(271-298, 1998.

[13] R. M. Biltz and E. D. Pellegrino. The Chemical Anatomy of Bone I. A Comparative Study of Bone Composition in Sixteen Vertebrates *J. Bone Joint Surg.*, 51-A(3):456-466, 1969.

[14] S. Mann, "Organic matrix-mediated biomineralization," in *Biomineralization: Principles and Concepts in Bioinorganic Materials Chemistry*: Oxford Chemistry Masters, 2001, pp. 89-124.

[15] M. Nordin and V. Frankel, "Biomechanics of Bone," in *Basic Biomechanics of the Musculoskeletal System*. Philadelphia: Lea & Febiger, 1989, pp. 3-29.

[16] J. Y. Rho and G. M. Pharr, *Nanoindentation Testing of Bone*, Boca Raton, FL: CRC Press, 2000.

[17] S. Hengsberger, A. Kulik, and P. Zysset. A combined atomic force microscopy and nanoindentation technique to investigate the elastic properties of bone structural units *Euro. Cells Mater.*, 1(12-17, 2001.

[18] S. J. Eppell, W. Tong, J. L. Katz, L. Kuhn, and M. J. Glimcher. Shape and size of isolated bone mineralites measured using atomic force microscopy *J. Orthop. Res.*, 19(1027-1034, 2001.

[19] T. Hassenkam, G. E. Fantner, J. A. Cutroni, J. C. Weaver, D. E. Morse, and P. K. Hansma. High-resolution AFM imaging of intact and fractured trabecular bone *Bone*, 35(1):4-10, 2004.

[20] V. Baranauskas, I. Garavello-Freitas, Z. Jingguo, and M. A. Cruz-Hofling. Observation of the bone matrix structure of intact and regenerative zones of tibias by atomic force microscopy *J. Vac. Sci. Technol.*, 19(4):1042-1045, 2001.

[21] J. B. Thompson, J. H. Kindt, B. Drake, H. HANSMa, D. E. Morse, and P. K. Hansma. Bone indentation recovery time correlates with bond reforming time *Nature*, 414(773-776, 2001.

[22] J. Y. Rho, M. E. Roy, T. Y. Tsui, and G. M. Pharr. Elastic properties of microstructural components of human bone measured by nanoindentation *J. Biomed. Mater. Res.*, 45(48, 1999.

[23] J. Y. Rho, T. Y. Tsui, and G. M. Pharr. Elastic properties of human cortical and trabecular lamellar bone measured by nanoindentation *Biomaterials*, 8(1325, 1997.

[24] J. Y. Rho, P. Zioupos, J. D. Currey, and G. M. Pharr. Variations in the Individual Lamellar Properties within Osteons by Nanoindentation *Bone*, 25(3):296, 1999.

[25] Z. Fan, J. G. Swadener, M. E. Rho, and G. M. Pharr. Anisotropic properties of human tibial cortical bone as measured by nanoindentation *J. Orthop. Res.*, 4(806-810, 2002.

[26] V. L. Ferguson, A. J. Bushby, and A. Boyde. Nanomechanical properties and mineral concentration in articular calcified cartilage and subchondral bone *J. Anat.*, 203(191-202, 2003.

[27] K. J. Bundy, "Composite materials models for bone," in *Bone Mechanics*, S. C. Cowin, Ed. Boca Raton, Florida: CRC Press, 1989, pp. 197-210.

[28] F. E. Feninat, T. H. Ellis, E. Sacher, and I. Stangel. Moisture-dependent renaturation of collagen in phosphoric acid etched human dentin *J. Biomed. Mater. Res.*, 42(4):549-553, 1998.

[29] J. D. Currey. Tensile yield in compact bone is determined by strain, post-yield behaviour by mineral content *J. Biomech.*, 37(4):549-556, 2004.

[30] L. K. Bachrach, T. Hastie, M. Wang, B. Narasimhan, and R. Marcus. Bone Mineral Acquisition in Healthy Asian, Hispanic, Black, and Caucasian Youth: A Longitudinal Study *J. Clin. Endocrin. Metab.*, 84(12):4702-4712, 1999.

[31] D. P. Nicolella, D. E. Moravitis, A. J. Siller-Jackson, R. J. Railsback, S. F. Timmons, K. J. Jepson, D. T. Davy, and J. Lankford, "Ultrastructural Characterization of Damaged Cortical Bone Using Atomic Force Microscopy," Proceedings of the 1999 American Society of Mechanical Engineering (ASME) Bioengineering Conference, Big Sky, Montana June 16-20, 1999 1999.

[32] M. Akao, H. Aoki, and K. Kato. Mechanical properties of sintered hydroxyapatite for prosthetic applications *J. Mater. Sci.*, 16(809-812, 1981.

[33] G. E. Lloyd. Atomic number and crystallographic contrast images with the SEM: a review of backscattered electron techniques *Mineralogical Magazine*, 51(3-19, 1987.

[34] J. G. Skedros, R. D. Bloebaum, and K. N. Bachus. The meaning of graylevels in backscattered electron images of bone *Journal of Biomedical Materials Research*, 27(47-56, 1993a.

[35] J. G. Skedros, R. D. Bloebaum, K. N. Bachus, T. M. Boyce, and B. Constantz. Influence of mineral content and composition on graylevels in backscattered electron images of bone *Journal of Biomedical Materials Research*, 27(57-64, 1993.

[36] T. M. Boyce, R. D. Bloebaum, K. N. Bachus, and J. G. Skedros. Reproducible method for calibrating the backscattered electron signal for quantitative assessment of mineral content in bone *Scanning*, 4(3):591-603, 1990.

[37] A. Boyde and S. J. Jones. Back-scattered electron imaging of skeletal tissues *Metab. Bone Dis. and Rel. Res.*, 5(145-150, 1983.

[38] H. Hertz. *J. Reine Angew Math*, 92(156-171, 1881.

[39] R. G. Munro, "Elastic moduli data for polycrystalline ceramics," National Institute of Standards and Technology, Gaithersburg, Maryland 20899 2002.

[40] M. Dao, N. Chollacoop, K. J. Van Vliet, T. A. Venkatesh, and S. Suresh. Computational modeling of the forward and reverse problems in instrumented sharp indentation *Acta Mater.*, 49(3899-3918, 2001.

[41] S. Weiner and W. Traub. Bone structure: from angstroms to microns *The FASEB Journal*, 6(879-885, 1992.

[42] M. J. Glimcher, "The nature of the mineral component of bone and the mechanism of calcification," in *Physiology of Bone: Chapter 3*, 1987, pp. 49-69.

[43] E. P. Katz and S. Li. Structure and Function of Bone Collagen Fibrils *Journal of Molecular Biology*, 80(1-15, 1973.

[44] V. B. Rosen, L. W. Hobbs, and M. Spector. The Ultrastructure of Anorganic Bovine Bone and Selected Hydroxyapatites used as Bone Graft Substitutes *Biomaterials*, 1-8, 2001.

[45] C. P. Tarnowski, M. A. Ignelzi, and M. D. Morris. Mineralization by Developing Mouse Calvaria as Revealed by Raman Microspectroscopy *Journal of Bone and Mineral Research*, 17(6):1118-1126, 2002.

[46] A. Courtney, W. C. Hayes, and L. J. Gibson. Age-related differences in post-yield damage in human cortical bone. Experiment and model *J. Biomech.*, 29(11):1463-1471, 1996.

[47] S. P. Kotha and N. Guzelsu. Effect of bone mineral content on the tensile properties of cortical bone: experiments and theory *J Biomech Eng*, 125(6):785-93, 2003.

[48] R. T. Hart, "The Finite Element Method," in *Bone Mechanics*, S. C. Cowin, Ed. Boca Raton, Florida: CRC Press, 1989, pp. 54-73.

[49] Z. Fan and J. Y. Rho. Effects of viscoelasticity and time-dependent plasticity on nanoindentation measurements of human cortical bone *J. Biomed. Mater. Res.*, 67A(208-214, 2002.

[50] J. Y. Rho, P. Zioupos, J. D. Currey, and G. M. Pharr. Microstructural elasticity and regional heterogeneity in human femoral bone of various ages examined by nano-indentation *J. Biomech.*, 35(189-198, 2002.

[51] D. T. Reilly and A. H. Burstein. Review article. The mechanical properties of cortical bone *J. Bone Joint Surg. Am.*, 56(5):1001-1022, 1974.

[52] J. D. Currey. The effect of porosity and mineral content on the Young's modulus elasticity of compact bone *J. Biomech.*, 21(131-139, 1988.

[53] S. N. Danilchenko, C. Moseke, L. F. Sukhodub, and B. Sulkio-Cleff. X-ray diffraction studies of bone apatite under acid demineralization *Cryst. Res. Technol.*, 39(1):71-77, 2004.

[54] K. J. Van Vliet, J. Li, T. Zhu, J. Yip, and S. Suresh. Quantifying the early stage of plasticity through nanoscale experiments and simulations. *Physical Review*, B67(104105, 2003.

[55] Z. Fan, J. J. Swadener, J. Y. Rho, M. E. Roy, and G. Pharr, "Anisotropy nanoindentation properties of human cortical bone," Transactions of the Annual Meeting of the Orthopaedic Research Society 2001.

[56] T. Gutsmann, G. E. Fantner, M. Venturoni, E.-N. A., J. B. Thompson, J. H. Kindt, D. E. Morse, D. K. Fygenson, and H. G. Hansma. Evidence that collagen fibrils in tendons are Inhomogeneously structured in a tube-like manner *Biophys. J.*, 84(2593-2598, 2003.

[57] S. K. Sarkar, Y. Hiyama, C. H. Niu, P. E. Young, J. T. Gerig, and D. A. Torchia. Molecular dynamics of collagen side chains in hard and soft tissues. A multinuclear magnetic resonance study *Biochemistry*, 26(6793-6800, 1987.

[58] S. N. Vaidya, C. Karunakaran, B. M. Pande, N. M. Gupta, R. K. Iyer, and S. B. Karweer. Pressure-induced crystalline to amorphous transition in hydroxylapatite *Journal of Materials Science*, 32(3213-3217, 1997.

[59] M. C. Boyce, S. Socrate, O. C. Yeh, K. Kear, and K. Shaw. Micromechanisms of deformation and recovery in thermoplastic vulcanizates *J. Mech. Phys. Solids*, 49(1073-1098, 2001a.

[60] M. C. Boyce, O. C. Yeh, S. Socrate, K. Kear, and K. Shaw. Micromechanisms of the cyclic softening in thermoplastic vulcanizates *J. Mech. Phys. Solids*, 49(1343-1360, 2001b.

[61] K. Tai, F.-J. Ulm, and C. Ortiz. Nanogranular origins of the strength of bone *Nano Lett.*, in press, 2006.

[62] G. E. Fantner, T. Hassenkam, J. H. Kindt, G. Weaver, H. Birkedal, L. Pechenik, J. A. Cutroni, A. Cidade, G. Stucky, D. E. Morse, and H. G. Hansma. Sacrificial bonds and hidden length dissipate energy as mineralized fibrils separate during bone fracture *Nat. Mater.*, 4(612-616, 2005.

[63] H. S. Gupta, W. Wagermaier, G. A. Zickler, D. Raz-Ben Aroush, S. S. Funari, P. Roschger, H. D. Wagner, and P. Fratzl. Nanoscale deformation mechanisms in bone *Nano Lett.*, 5(10):2108-2111, 2005.

[64] R. K. Nalla, J. H. Kinney, and R. O. Ritchie. Mechanistic fracture criteria for the failure of human cortical bone *Nat. Mater.*, 2(164-168, 2003.

[65] G. V. B. Cochran, *A primer of orthopaedic biomechanics*, New York, NY: Churchill Livingstone, 1982.

[66] A. A. Biewener. Safety factors in bone strength *Calcif. Tiss. Int.*, 53 Suppl 1(S68-74, 1993.

[67] D. Vashishth, J. Koontz, S. J. Qiu, D. Lundin-Cannon, Y. N. Yeni, M. B. Schaffler, and D. P. Fyhrie. In vivo diffuse damage in human vertebral trabecular bone *Bone*, 26(2):147-52, 2000.

[68] K. M. Fine, J. J. Vegso, B. Sennett, and J. S. Torg. Prevention of cervical spine injuries in football: A model for other sports *Phys. Sportsmed.*, 19(54-62, 1991.

[69] Y. N. Yeni, X. N. Dong, D. P. Fyhrie, and C. M. Les. The dependence between the strength and stiffness of cancellous and cortical bone tissue for tension and compression: extension of a unifying principle *Biomed. Mater. Eng.*, 14(3):303-10, 2004.

[70] G. E. Fantner, O. Rabinovych, G. Schitter, P. Thurner, J. H. Kindt, M. M. Finch, J. C. Weaver, L. S. Golde, D. E. Morse, E. A. Lipman, I. W. Rangelow, and P. K. Hansma. Hierarchical interconnections in the nano-composite material bone: Fibrillar cross-links resist fracture on several length scales *Comp. Sci. Tech.*, 66(9):1205-1211, 2005.

[71] N. J. Wachter, G. D. Krischak, M. Mentzel, M. R. Sarkar, T. Ebinger, L. Kinzl, L. Claes, and P. Augat. Correlation of bone mineral density with strength and microstructural parameters of cortical bone in vitro *Bone*, 31(1):90-5, 2002.

[72] O. Louis, F. Boulpaep, J. Willnecker, P. Van den Winkel, and M. Osteaux. Cortical mineral content of the radius assessed by peripheral QCT predicts compressive strength on biomechanical testing *Bone*, 16(3):375-9, 1995.

[73] J. C. Lotz, T. N. Gerhart, and W. C. Hayes. Mechanical properties of trabecular bone from the proximal femur: a quantitative CT study *J. Comput. Assist. Tomogr.*, 14(1):107-14, 1990.

[74] C. Hellmich and F. J. Ulm. Average hydroxyapatite concentration is uniform in the extracollagenous ultrastructure of mineralized tissues: evidence at the 1-10-micron scale *Biomech. Model. Mechanobiol.*, 2(1):21-36, 2003.

[75] J. D. Currey. Effects of differences in mineralization on the mechanical properties of bone *Phil. Trans. R. Soc. Lond. B*, 304(509-518, 1984.

[76] P. J. Thurner, B. Erickson, R. Jungman, Z. Schriock, J. C. Weaver, G. E. Fantner, G. Schitter, D. E. Morse, and P. K. Hansma. Photography of compressed human trabecular bone correlates whitening to microscopic damage *Eng. Fracture Mech.*, Special Issue: Mechanics of Biomaterials):doi:10.1016/j.engfracmech.2006.05.024, 2006.

[77] N. Mitarai and F. Nori. Wet granular materials *Adv. Phys.*, 55(1-2):1-45, 2006.

[78] C. A. Coulomb. *Mem. de Math. de l'Acad. Royale des Sciences*, 7(343, 1773.

[79] F. Ganneau, G. Constantinides, and F.-J. Ulm. Dual-indentation technique for the assessment of strength properties of cohesive-frictional materials *Int. J. Solids Struct.*, 43(4):1727-1745, 2006.

[80] Z. Fan, J. Y. Rho, and J. G. Swadener. Three-dimensional finite element analysis of the effects of anisotropy on bone mechanical properties measured by nanoindentation *J. Mater. Res.*, 19(1):114-123, 2004.

[81] E. Wachtel and S. Weiner. Small-angle x-ray scattering study of dispersed crystals from bone and tendon *Journal of Bone and Mineral Research*, 9(10):1651-5, 1994.

[82] U. Raviv, S. Giasson, N. Kampf, J. F. Gohy, R. Jerome, and J. Klein. Lubrication by charged polymers *Nature*, 425(163-165, 2003.

[83] W. R. Walsh, H. D. Kim, D. P. Labrador, and N. Guzelsu. Mineral-organic interfacial bonding: effect of strain rate on the mechanical properties of bone *Hydroxyapatite Relat. Mater.*, 289-93, 1994.

[84] D. R. Eyre and J. J. Wu. Collagen crosslinks *Top. Curr. Chem.*, 247(207-229, 2005.

[85] L. Knott and A. J. Bailey. Collagen Cross-Links in Mineralizing Tissues: A Review of Their Chemistry, Function, and Clinical Relevance *Bone*, 22(3):181-187, 1998.
[86] G. E. Fantner, E. Oroudjev, G. Schitter, L. S. Golde, P. Thurner, M. M. Finch, P. Turner, T. Gutsmann, D. E. Morse, H. Hansma, and P. K. Hansma. Sacrificial bonds and hidden length: unraveling molecular mesostructures in tough materials *Biophys. J.*, 90(4):1411-1418, 2006.
[87] R. T. Ingram, B. L. Clarke, L. W. Fisher, and L. A. Fitzpatrick. Distribution of noncollagenous proteins in the matrix of adult human bone: evidence of anatomic and functional heterogeneity *J. Bone Miner. Res.*, 8(9):1019-1029, 1993.
[88] S. Weinbaum, S. C. Cowin, and Y. Zeng. A model for the excitation of osteocytes by mechanical loading-induced bone fluid shear stresses *J. Biomech.*, 27(3):339-360, 1994.
[89] A. N. Schofield and C. P. Wroth, *Critical state soil mechanics*: McGraw Hill, 1968.
[90] Y. Braiman, J. Barhen, and V. Protopopescu. Control of friction at the nanoscale *Phys. Rev. Lett.*, 90(9):094301, 2003.
[91] R. Z. Wang, Z. Suo, A. G. Evans, N. Yao, and I. A. Aksay. Deformation mechanisms in nacre *J. Mat. Res.*, 16(9):2485-2493, 2001.
[92] M. Hirano. Atomistics of friction *Surf. Sci. Rep.*, 60(159-201, 2006.
[93] M. Urbakh, J. Klafter, D. Gourdon, and J. Israelachvili. The nonlinear nature of friction *Nature*, 430(525-528, 2004.
[94] T. A. L. Wren, S. A. Yerby, G. S. Beaupre, and D. R. Carter. Influence of bone mineral density, age, and strain rate on the failure mode of human Achilles tendons *Clin. Biomech.*, 16(529-534, 2001.
[95] J. Aerssens, S. Boonen, J. Joly, and J. Dequeker. Variations in trabecular bone composition with anatomical site and age: potential implications for bone quality assessment *J. Endocrinol.*, 155(3):411-421, 1997.
[96] K. Raum, I. Leguerney, F. Chandelier, M. Talmant, A. Saied, F. Peyrin, and P. Laugier. Site-matched assessment of structural and tissue properties of cortical bone using scanning acoustic microscopy and synchrotron radiation muCT *Phys Med Biol*, 51(3):733-46, 2006.
[97] E. F. Morgan, H. H. Bayraktar, O. C. Yeh, S. Majumdar, A. Burghardt, and T. M. Keaveny. Contribution of inter-site variations in architecture to trabecular bone apparent yield strains *J. Biomech.*, 37(9):1413-20, 2004.
[98] D. B. Burr, M. R. Forwood, D. P. Fyhrie, R. B. Martin, M. B. Schaffler, and C. H. Turner. Bone microdamage and skeletal fragility in osteoporotic and stress fractures *J. Bone Miner. Res.*, 12(1):6-15, 1997.
[99] B. R. Lawn, T. P. Dabbs, and C. J. Fairbanks. Kinetics of shear-activated indentation crack initiation in soda-lime glass *J. Mater. Sci.*, 18(9):2785-2797, 1983.
[100] J. Currey. Structural heterogeneity in bone: good or bad? *J Musculoskelet. Neuronal Interact.*, 5(4):317, 2005.
[101] E. F. Morgan, H. H. Bayraktar, and T. M. Keaveny. Trabecular bone modulus-density relationships depend on anatomic site *J. Biomech.*, 36(7):897-904, 2003.

[102] M. H. Pope and J. O. Outwater. Mechanical properties of bone as a function of position and orientation *J. Biomech.*, 7(61-66, 1974.
[103] J. G. Skedros, S. M. Sorenson, Y. Takano, and C. H. Turner. Dissociation of mineral and collagen orientations may differentially adapt compact bone for regional loading environments: results from acoustic velocity measurements in deer calcanei *Bone*, 39(1):143-151, 2006.
[104] H. S. Gupta, U. Stachewicz, W. Wagermaier, P. Roschger, H. D. Wagner, and P. Fratzl. Mechanical modulation at the lamellar level in osteonal bone *J. Mater. Res.*, 21(8):1913-1921, 2006.
[105] R. B. Martin and D. B. Burr, *Structure, Function and Adaptation of Compact Bone*, New York, NY: Raven Press, 1989.
[106] P. K. Zysset, X. E. Guo, C. E. Hoffler, K. E. Moore, and S. A. Goldstein. Elastic modulus and hardness of cortical and trabecular bone lamellae measured by nanoindentation in the human femur *J Biomech*, 32(10):1005-12, 1999.
[107] J. Catanese, 3rd, E. P. Iverson, R. K. Ng, and T. M. Keaveny. Heterogeneity of the mechanical properties of demineralized bone *J. Biomech.*, 32(12):1365-1369, 1999.
[108] H. Peterlik, P. Roschger, K. Klaushofer, and P. Fratzl. From brittle to ductile fracture of bone *Nat. Mater.*, 5(1):52-55, 2006.
[109] J. B. Phelps, G. B. Hubbard, X. Wang, and C. M. Agrawal. Microstructural heterogeneity and the fracture toughness of bone *J. Biomed. Mater. Res.*, 51(4):735-741, 2000.
[110] T. Jamsa, J. Y. Rho, Z. Fan, C. A. MacKay, S. C. Marks, and J. Tuukkanen. Mechanical properties in long bones of rat osteopetrotic mutations *Journal of Biomechanics*, 35(161-165, 2002.
[111] H. Gao, B. Ji, I. L. Jager, E. Arzt, and P. Fratzl. Materials become insensitive to flaws at nanoscale: lessons from nature *Proc. Natl. Acad.Sci. U. S. A.*, 100(10):5597-5600, 2003.
[112] L. D. You, S. Weinbaum, S. C. Cowin, and M. B. Schaffler. Ultrastructure of the osteocyte process and its pericellular matrix *Anat. Rec. A Discov. Mol. Cell Evol. Biol.*, 278(2):505-513, 2004.
[113] J. Vesenka, S. Manne, R. Giberson, T. Marsh, and E. Henderson. Colloidal gold particles as an incompressible atomic force microscope imaging standard for assessing the compressibility of biomolecules *Biophys. J.*, 65(3):992-997, 1993.
[114] J. Seog, D. Dean, A. Plaas, A. Wong-Palms, A. Grodzinsky, and C. Ortiz. Direct Measurement of Glycosaminoglycan Intermolecular Interactions via High-Resolution Force Spectroscopy *Macromolecules*, 35(14):5601-5615, 2002.
[115] W. C. Oliver and G. M. Pharr. Measurement of hardness and elastic modulus by instrumented indentation: Advances in understanding and refinements to methodology *J. Mater. Res.*, 19(3-20, 2004.
[116] G. Constantinides, R. C. K. S., F.-J. Ulm, and K. J. Van Vliet. Grid indentation analysis of composite microstructure and mechanics: Principles and validation *Mater. Sci. and Eng. A*, 430(189-202, 2006.
[117] G. Strang and T. Nguyen, *Wavelets and Filter Banks*, Wellesley, MA: Wellesley-Cambridge, 1996.

[118] M. M. Giraudguille. Twisted plywood architecture of collagen fibrils in human compact-bone osteons *Calcif. Tissue Int.*, 42(167-180, 1988.
[119] T. Hofmann, F. Heyroth, H. Meinhard, W. Franzel, and K. Raum. Assessment of composition and anisotropic elastic properties of secondary osteon lamellae *J. Biomech.*, 39(12):2282-2294, 2006.
[120] M. Kazanci, P. Roschger, E. P. Paschalis, K. Klaushofer, and P. Fratzl. Bone osteonal tissues by Raman spectral mapping: Orientation-composition *J. Struct. Biol.*, doi:10.1016/j.jsb.2006.06.011):2006.
[121] W. Wagermaier, H. S. Gupta, A. Gourrier, M. Burghammer, P. Roschger, and P. Fratzl. Spiral twisting of fiber orientation inside bone lamellae *Biointerphases*, 1(1):1-5, 2006.
[122] A. Ardizzoni. Osteocyte lacunar size-lamellar thickness relationships in human secondary osteons *Bone*, 28(2):215-219, 2001.
[123] S. Mallat, *A Wavelet Tour of Signal Processing.*, San Diego, CA: Academic Press, 1998.
[124] T. Nakamura and S. Suresh. Effects of thermal residual-stresses and fiber packing on deformation of metal-matrix composites *Acta. Metal. et Mater.*, 41(6):1665-1681, 1993.
[125] M. J. Jaasma, H. H. Bayraktar, G. L. Niebur, and T. M. Keaveny. Biomechanical effects of intraspecimen variations in tissue modulus for trabecular bone *J. Biomech.*, 35(2):237-246, 2002.
[126] P. J. Ehrlich and L. E. Lanyon. Mechanical strain and bone cell function: a review *Osteoporos Int.*, 13(9):688-700, 2002.
[127] L. You, S. C. Cowin, M. B. Schaffler, and S. Weinbaum. A model for strain amplification in the actin cytoskeleton of osteocytes due to fluid drag on pericellular matrix *J. Biomech.*, 34(11):1375-1386, 2001.
[128] E. H. Burger and J. Klein-Nulend. Mechanotransduction in bone--role of the lacuno-canalicular network *Faseb J.*, 13 Suppl(S101-12, 1999.
[129] C. Hellmich and F. J. Ulm. Are mineralized tissues open crystal foams reinforced by crosslinked collagen? Some energy arguments *J. Biomech.*, 35(9):1199-1212, 2002.
[130] C. Hellmich and F. J. Ulm. MIcromechanical Model for Ultrastructural Stiffness of Mineralized Tissues *J. Eng. Mech.*, 128(8):898-908, 2002.
[131] S. Lees, K. S. Prostak, V. K. Ingle, and K. Kjoller. The loci of mineral in turkey leg tendon as seen by atomic force microscope and electron microscopy *Calcif. Tissue Int.*, 55(3):180-9, 1994.
[132] K. S. Prostak and S. Lees. Visualization of crystal-matrix structure. In situ demineralization of mineralized turkey leg tendon and bone *Calcif Tissue Int*, 59(6):474-9, 1996.
[133] J. Y. Rho. An ultrasonic method for measuring the elastic properties of human tibial cortical and cancellous bone *Ultrasonics*, 34(8):777-83, 1996.
[134] S. Lees. Considerations regarding the structure of the mammalian mineralized osteoid from viewpoint of the generalized packing model. *Connective Tissue Research*, 16(281-303, 1987.
[135] J. D. Currey. The relationship between the stiffness and the mineral content of bone *J. Biomech.*, 2(4):477-480, 1969.

[136] R. M. V. Pidaparti, A. Chandran, Y. Takano, and C. H. Turner. Bone mineral lies mainly outside collagen fibrils predicions of a composite model for osteonal bone *J. Biomech.*, 29(7):909-916, 1996.
[137] J. Bryant. On the mechanical function of marrow in long bones *Eng. Med.*, 17(2):55-58, 1988.
[138] E. Guth. Theory of filler reinforcement *J. Appl. Phys.*, 16(20, 1945.
[139] S. Lees. A mixed packing model for bone collagen *Calcif. Tissue Int.*, 33(6):591-602, 1981.
[140] Z. Fan and J. Y. Rho. Effects of viscoelasticity and time-dependent plasticity on nanoindentation measurements of human cortical bone *J. Biomed. Mater. Res.*, 67(1):208-214, 2003.
[141] W. R. Walsh and N. Guzelsu. The role of ions and mineral-organic interfacial bonding on the compressive properties of cortical bone *Bio-Med. Mater. and Eng.*, 3(2):75-84, 1993.
[142] R. T. Ingram, B. L. Clarke, L. W. Fisher, and L. A. Fitzpatrick. Distribution of noncollagenous proteins in the matrix of adult human bone: Evidence of anatomic and functional heterogeneity *J. Bone Min. Res.*, 8(9):1019-1029, 1993.
[143] S. Li and E. P. Katz. On the state of anionic groups of demineralized matrices of bone and dentine *Calcif. Tissue Int.*, 22(1):275-284, 1977.
[144] W. R. Walsh, H. D. Kim, D. P. Labrador, and N. Guzelsu. Mineral-organic interfacial bonding: effect of strain rate on the mechanical properties of bone *Hydroxyapatite Relat. Mater.*, 289-293, 1994.
[145] W. R. Walsh, M. Ohno, and N. Guzelsu. Bone composite behaviour: effects of mineral-organic bonding *J. Mater. Sci.*, 5(72-79, 1994.
[146] W. R. Walsh and N. Guzelsu. Compressive properties of cortical bone: mineral-organic interfacial bonding. *Biomaterials*, 15(2):137-145, 1994.
[147] M. W. Otter, V. R. Palmieri, and G. V. Cochran. Transcortical streaming potentials are generated by circulatory pressure gradients in living canine tibia *J. Orthop. Res.*, 8(1):119-126, 1990.
[148] M. Otter, S. Goheen, and W. S. Williams. Streaming potentials in chemically modified bone *J. Orthop. Res.*, 6(3):346-359, 1988.
[149] C. Eriksson. Surface energies and the bone induction principle *J. Biomed. Mater. Res.*, 19(7):833-849, 1985.
[150] S.-H. Rhee and J. D. Lee. Nucleation of hydroxyapatite crystal through chemical interaction with collagen *J. Am. Ceram. Soc.*, 83(11):2890-2892, 2000.
[151] M. J. Glimcher. Recent studies of the mineral phase in bone and its possible linkage to the organic matrix by protein-bound phosphate bonds *Phil. Trans. R. Soc. Lond. B*, 304(479-508, 1984.
[152] S. Weiner and W. Traub. Bone structure: from angstroms to microns *FASEB J.*, 6(879-885, 1992.
[153] R. W. Romberg, P. G. Werness, B. L. Riggs, and K. G. Mann. Inhibition of hydroxyapatite crystal growth by bone-specific and other calcium-binding proteins *Biochemistry*, 25(1176-1180, 1986.
[154] J. D. Termine, H. K. Kleinman, S. W. Whitson, K. M. Conn, M. L. McGarvey, and G. R. Martin. Osteonectin, a bone-specific protein linking mineral to collagen *Cell*, 26(99-105, 1981.

[155] R. W. Romberg, P. G. Werness, P. Lollar, B. L. Riggs, and K. G. Mann. Isolation and characterization of native adult osteonectin *J. Biol. Chem.*, 260(5):2728-2736, 1985.
[156] P. V. Hauschka and S. A. Carr. Calcium-dependent alpha-helical structure in osteocalcin *Biochemistry*, 21(2538-2547, 1982.
[157] P. V. Hauschka, J. B. Lian, and P. M. Gallop. Direct identification of the calcium-binding amino acid, gamma-carboxyglutamate, in mineralized tissue *Proc. Nat. Acad. Sci. USA*, 72(10):3925-3929, 1975.
[158] C. E. Tye, G. K. Hunter, and H. A. Goldberg. Identification of the type I collagen-binding domain of bone sialoprotein and characterization of the mechanism of interaction *J. Biol. Chem.*, 280(14):13487-13492, 2005.
[159] C. E. Tye, K. R. Rattray, K. J. Warner, J. A. R. Gordon, J. Sodek, G. K. Hunter, and H. A. Goldberg. Delineation of the hydroxyapatite-nucleating domains of bone sialoprotein *J. Biol. Chem.*, 278(10):7949-7955, 2003.
[160] W. G. Stetler-Stevenson and A. Veis. Type I collagen shows a specific binding affinity for bovine dentin phosphophoryn *Calcif. Tissue Int.*, 38(135-141, 1986.
[161] C. Werner, R. Zimmermann, and T. Kratzmuller. Streaming potential and streaming current measurements at planar solid/liquid interfaces for simultaneous determination of zeta potential and surface conductivity *Colloids Surf. A*, 192(1):205-213, 2001.
[162] R. M. Kowalchuk, T. A. Corcoran, S. R. Pollack, and M. E. Steinberg. Effects of etidronate and oophorectomy on the zeta potential of rat bone *Clin. Orthop. Relat. Res.*, 328):241-249, 1996.
[163] P. Ducheyne, C. S. Kim, and S. R. Pollack. The effect of phase differences on the time-dependent variation of the zeta potential of hydroxyapatite *J. Biomed. Mater. Res.*, 26(2):147-168, 1992.
[164] J. W. Thornton, M. J. Morykwas, and R. H. Bartlett, "Adherence of skin prosthesis: collagen, elastin, fibrin, and net surface charge.," in *Burn Wound Coverings*, 1984, pp. 147-159.
[165] W. R. Walsh and N. Guzelsu. Electrokinetic behavior of intact wet bone: compartmental model *J. Orthop. Res.*, 9(5):683-692, 1991.
[166] R. M. Kowalchuk, S. R. Pollack, P. Ducheyne, and L. A. King. Particle microelectrophoresis of calcium-deficient hydroxyapatite: solution composition and kinetic effects *J. Biomed. Mater. Res.*, 27(6):783-790, 1993.
[167] R. M. Kowalchuk and S. R. Pollack. Stress-generated potentials in bone: effects of bone fluid composition and kinetics *J. Orthop. Res.*, 11(6):874-883, 1993.
[168] D. A. Berretta and S. R. Pollack. Ion concentration effects on the zeta potential of bone *J. Orthop. Res.*, 4(3):337-345, 1986.
[169] C. N. Wilson and A. D. Miller. The effects of polyvalent salts on zeta potential of bone *J. Biomed. Mater. Res.*, 9(3):265-272, 1975.
[170] R. Brommage and W. F. Neuman. Passive accumulation of magnesium, sodium, and potassium by chick calvaria *Calcif. Tissue Int.*, 28(1):57-63, 1979.
[171] R. M. Kowalchuk, S. R. Pollack, and T. A. Corcoran. Zeta potential of bone from particle electrophoresis: solution composition and kinetic effects *J. Biomed. Mater. Res.*, 29(1):47-57, 1995.

[172] I. O. Smith, M. J. Baumann, and L. R. McCabe. Electrostatic interactions as a predictor for osteoblast attachment to biomaterials *J. Biomed. Mater. Res.*, 70(3):436-441, 2004.
[173] D. A. Oppermann, M. J. Crimp, and D. M. Bement. In vitro stability predictions for the bone/hydroxyapatite composite system *J. Biomed. Mater. Res.*, 42(3):412-416, 1998.
[174] K. J. Bundy. Determination of Mineral-Organic Bonding Effectiveness in Bone-Theoretical Considerations *Ann. Biomed. Eng.*, 13(119-135, 1985.
[175] A. L. Boskey. Mineral-matrix interactions in bone and cartilage *Clin. Orthop. Relat. Res.*, 281(244-274, 1992.
[176] S. M. Bowman, J. Zeind, L. J. Gibson, W. C. Hayes, and T. A. McMahon. The Tensile Behavior of Demineralized Bovine Cortical Bone *J. Biomech.*, 29(11):14971501, 1996.
[177] M. Akao, H. Aoki, and K. Kato. Flexural strength of mixed hydroxyapatite-tricalcium phosphate ceramics *Tokyo Ika Shika Daigaku Iyo Kizai Kenkyusho Hokoku*, 15(17-22, 1981.
[178] K. Tai, H. J. Qi, and C. Ortiz. Effect of mineral content on the nanoindentation properties and nanoscale deformation mechanisms of bovine tibial cortical bone *J. Mater. Sci. Mater. Med.*, 16(947-959, 2005.
[179] J. G. Skedros, R. D. Bloebaum, K. N. Bachus, T. M. Boyce, and B. Constantz. Influence of mineral content and composition on graylevels in backscattered electron images of bone *J. Biomed. Mater. Res.*, 27(57-64, 1993.
[180] J. G. Skedros, R. D. Bloebaum, and K. N. Bachus. The meaning of graylevels in backscattered electron images of bone *J. Biomed. Mater. Res.*, 27(47-56, 1993.
[181] G. E. Lloyd. Atomic number and crystallographic contrast images with the SEM: a review of backscattered electron techniques *Mineral. Mag.*, 51(3-19, 1987.
[182] J. Seog, D. Dean, A. Plaas, S. Wong-Palms, A. Grodzinsky, and C. Ortiz. Direct Measurement of Glycosaminoglycan Intermolecular Interactions via High-Resolution Force Spectroscopy *Macromolecules*, 35(14):5601-5615, 2002.
[183] D. Dean, J. Seog, C. Ortiz, and A. Grodzinsky. Molecular-Level Theoretical Model for Electrostatic Interactions within Polyelectrolyte Brushes: Applications to Charged Glycosaminoglycans *Langmuir*, 19(5526-5539, 2003.
[184] M. Rixman, D. Dean, C. Macias, and C. Ortiz. Nanoscale Intermolecular Interactions Between Human Serum Albumin and Alkanethiol Self-Assembling Monolayers *Langmuir*, 19(15):6202-6218, 2003.
[185] Y. W. Kim, J. J. Kim, Y. H. Kim, and J. Y. Rho. Effects of organic matrix proteins on the interfacial structure at the bone-biocompatible nacre interface in vitro *Biomaterials*, 23(9):2089-2096, 2002.
[186] H. Baumann, R. Keller, and E. Ruzicka. Partially cationized cellulose for non-thrombogenic membrnae in the presence of heparin and endothelial-cell-surface-heparansulfate (ES-HS) *J. Membr. Sci.*, 61(253-268, 1991.
[187] K. S. Hwang, J. E. Song, J. W. Jo, H. S. Yang, Y. J. Park, J. L. Ong, and H. R. Rawls. Effect of poling conditions on growth of calcium phosphate crystal in ferroelectric BaTiO3 ceramics *J. Mater. Sci. Mater. Med.*, 13(133-138, 2002.
[188] J. Vandiver, D. Dean, N. Patel, W. Bonfield, and C. Ortiz. Nanoscale Variation in Surface Charge of Synthetic Hydroxyapatite Detected by Chemically and

Spatially Specific High Resolution Force Spectroscopy *Biomaterials*, 26(3):271-283, 2005.

[189] A. Veis, *The macromolecular chemistry of gelatin*, New York, NY: Academic Press, 1964.

[190] P. Zioupos, J. D. Currey, and A. J. Hamer. The role of collagen in the declining mechanical properties of aging human cortical bone *J. Biomed. Mater. Res.*, 45(2):108-116, 1999.

[191] N. Guzelsu and R. L. Regimbal. The origin of electrokinetic potentials in bone tissue: the organic phase *J. Biomech.*, 23(7):661-672, 1990.

[192] S. R. Pollack, R. Salzstein, and D. Pienkowski. The electric double layer in bone and its influence on stress-generated potentials *Calcif. Tissue Int.*, 36 Suppl 1(S77-81, 1984.

[193] H. M. Kim, T. Himeno, T. Kokubo, and T. Nakamura. Process and kinetics of bonelike apatite formation on sintered hydroxyapatite in a simulated body fluid *Biomaterials*, 26(21):4366-4373, 2005.

[194] J. D. de Bruijn, C. A. van Blitterswijk, and J. E. Davies. Initial bone matrix formation at the hydroxyapatite interface in vivo. *J. Biomed. Mater. Res.*, 29(1):89-99, 1995.

[195] G. Pelled, K. Tai, D. Sheyn, Y. Zilberman, D. Gazit, and C. Ortiz. Structural and nanoindentation studies of stem cell-based tissue engineered bone *Journal of Biomechanics, submitted.*, 2005.

[196] J. R. Lieberman, L. Q. Le, L. Wu, G. A. Finerman, A. Berk, O. N. Witte, and S. Stevenson. Regional gene therapy with a BMP-2-producing murine stromal cell line induces heterotopic and orthotropic bone formation in rodents. *Journal of Orthopedic Research*, 16(3):330-339, 1998.

[197] J. R. Lieberman, A. Daluiski, S. Stevenson, L. Wu, P. McAllister, Y. P. Lee, J. M. Kabo, G. A. Finerman, A. J. Berk, and O. N. Witte. The effect of regional gene therapy with bone morphogenetic protein-2-producing bone-marrow cells on the repair of segmental femoral defects in rats. *Journal of Bone and Joint Surgery*, 81(7):905-917., 1999.

[198] D. Gazit. Engineered pluripotent mesenchymal cells integrate and differentiate in regenerating bone: A novel cell mediated gene therapy *J. Gene Med.*, 1(121-133, 1999.

[199] G. Turgeman, D. D. Pittman, R. Muller, B. G. Kurkalli, S. Zhou, G. Pelled, A. Peyser, Y. Zilberman, I. K. Moutsatsos, and D. Gazit. Engineered human mesenchymal stem cells: a novel platform for skeletal cell mediated gene therapy *J Gene Med.*, 3(3):240-51, 2001.

[200] I. K. Moutsatsos, G. Turgeman, S. Zhou, B. G. Kurkalli, G. Pelled, L. Tzur, P. Kelley, N. Stumm, S. Mi, R. Muller, L. Zilberman, and D. Gazit. Exogenously regulated stem cell-mediated gene therapy for bone regeneration *Molecular Therapy*, 3(4):449-461, 2001.

[201] R. J. Dumont, H. Dayoub, L. J.Z., A. S. Dumont, D. F. Kallmes, G. R. Hankins, and G. A. Helm. Ex vivo bone morphogenetic protein-9 gene therapy using human mesenchymal stem cells induces spinal fusion in rodents. *Neurosurgery*, 51(5):1239-1244, 2002.

[202] Y. Zilberman, G. Turgeman, G. Pelled, N. Xu, I. K. Moutsatsos, G. Hortelano, and G. D. Polymer encapsulated engineered mesenchymal stem cells secrete exogenously regulated rhBMP-2, and induce osteogenic and angiogenic tissue formation *Polymers for Advanced Technologies*, 13(863-870, 2002.

[203] J. L. Dragoo, J. Y. Choi, J. R. Lieberman, J. Huang, P. A. Zuk, J. Zhang, M. H. Hedrick, and P. Benhaim. Bone induction by BMP-2 transduced stem cells derived from human fat *J. Orthop. Res.*, 21(4):622-629, 2003.

[204] J. L. Dragoo, J. R. Lieberman, R. S. Lee, D. A. Deugarte, Y. Lee, P. A. Zuk, M. H. Hedrick, and P. Benhaim. Tissue-engineered bone from BMP-2-transduced stem cells derived from human fat. *Plastic and Reconstructive Surgery*, 115(6):1665-1673, 2005.

[205] H. Dayoub, R. J. Dumont, L. J.Z., A. S. Dumont, G. R. Hankins, D. F. Kallmes, and G. A. Helm. Human mesenchymal stem cells transduced with recombinant bone morphogenetic protein-9 adenovirus promote osteogenesis in rodents. *Tiss. Eng.*, 9(2):347-356., 2003.

[206] O. Sugiyama, D. S. An, S. P. Kung, B. T. Feeley, S. Gamradt, N. Q. Liu, I. S. Chen, and J. R. Lieberman. Lentivirus-mediated gene transfer induces long-term transgene expression of BMP-2 in vitro and new bone formation in vivo. *Molecular Therapy.*, 11(3):390-398, 2005.

[207] B. Peterson, J. Zhang, R. Iglesias, M. Kabo, M. Hedrick, P. Benhaim, and J. R. Lieberman. Healing of critically sized femoral defects, using genetically modified mesenchymal stem cells from human adipose tissue. *Tissue Engineering*, 11(1-2):120-129, 2005.

[208] A. Hasharoni, Y. Zilberman, G. Turgeman, G. A. Helm, M. Liebergall, and D. Gazit. Murine spinal fusion induced by engineered mesenchymal stem cells that conditionally express bone morphogenetic protein-2. *J. Neurosurgery:Spine*, 3(1):47-52, 2005.

[209] W. J. Li, C. T. Laurencin, E. J. Caterson, R. S. Tuan, and F. K. Ko. Electrospun nanofibrous structure: a novel scaffold for tissue engineering *Journal of Biomedical Materials Research*, 60(4):613-621, 2002.

[210] G. E. Fantner, H. Birkedal, J. H. Kindt, T. Hassenkam, J. C. Weaver, J. A. Cutroni, B. L. Bosma, L. Bawazer, M. M. Finch, G. A. Cidade, D. E. Morse, G. D. Stucky, and P. K. Hansma. Influence of the degradation of the organic matrix on the microscopic fracture behavior of trabecular bone *Bone*, 35(5):1013-1022, 2004.

[211] J. Xu, J. Y. Rho, S. R. Mishra, and Z. Fan. Atomic force microscopy and nanoindentation of human lamellar bone prepared by microtome sectioning and mechanical polishing technique. *Journal of Biomedical Materials Research*, 67(3):719-726, 2003.

[212] J. D. Currey. Biomaterials: Sacrificial bonds heal bone *Nature*, 414(699-699, 2001.

[213] M. J. Silva, M. D. Brodt, Z. Fan, and J. Y. Rho. Nanoindentation and whole-bone bending estimates of material properties in bones from the senescence accelerated mouse SAMP6 *Journal of Biomechanics*, 37(1639-1646, 2004.

[214] J. Y. Rho and G. M. Pharr. Effects of drying on the mechanical properties of bovine femur measured by nanoindentation *Journal of Materials Science: Materials in Medicine*, 10(485-488, 1999.
[215] R. K. Nalla, J. S. Stolken, J. H. Kinney, and R. O. Ritchie. Fracture in human cortical bone: local fracture criteria and toughening mechanisms *J. Biomech.*, 38(7):1517-25, 2005.
[216] B. Kavukcuoglu, C. West, D. T. Denhardt, and A. B. Mann, "Effects of osteopontin deficiency and aging on nanomechanics of mouse bone.," presented at Materials Research Society Symposium Proceedings, Boston, MA, 2003.
[217] J. Malzbender. Letter to the editor comment on "Nanoindentation and whole-bone bending estimates of material properties in bones from senescence accelerated mouse SAMP6" *Journal of Biomechanics*, 1191-1192, 2005.
[218] R. Muller and P. Ruegsegger. Micro-tomographic imaging for the nondestructive evaluation of trabecular bone architecture *Studies in Health Technology and Informatics*, 40(61-79, 1997.
[219] T. Hildebrand, R. Muller, A. Laib, J. Dequeker, and P. Ruegsegger. Direct 3-D morphometric analysis of human cancellous bone: Microstructural data from spine, femur, iliac crest, and calcaneus *J. Bone Miner. Res.*, 14(1167-1174, 1999.
[220] P. Fratzl, M. Groschner, G. Vogl, G. Plenk, J. Eschberger, N. Fratxl-Zelman, K. Koller, and K. Klaushofer. Mineral crystals in calcified tissues: a comparative study by SAXS *J. Bone Miner. Res.*, 7(3):329-334, 1992.
[221] D. Dean, L. Han, A. J. Grodzinsky, and C. Ortiz. Compressive nanomechanics of opposing aggrecan macromolecules *accepted for publication, J. Biomech.*, 2005.
[222] D. Dean, L. Han, C. Ortiz, and A. J. Grodzinsky. Nanoscale conformation and compressibility of cartilage aggrecan using micro-contact printing and atomic force microscopy *Macromolecules*, 38(10):4047-4049, 2005.
[223] T. A. Einhorn, J. M. Lane, A. H. Burstein, C. B. Kopman, and V. J. Vigorita. The healing of a segmental defect induced by demineralized bone matrix *J. Bone Joint Surgery*, 66A(274-279, 1984.
[224] D. W. Wolff, V. M. Goldberg, and S. Stevenson. Histomorphometric analysis of the repair of a segmental diaphyseal defect with ceramic and fiber metal implants: effects of bone marrow *J. Orthop. Res.*, 12(3):439-446, 1994.
[225] L. Breschi, J. Perdiago, P. Gobbi, G. Mazzotti, M. Falconi, and M. Lopes. Immunocytochemical identification of type I collagen in acid-etched dentin *J. Biomed. Mater. Res.*, 66A(749-764):2003.
[226] A. V. Ritter, E. Swift, and M. Yamauchi. Effects of phosphoric acid and glutaraldehyde-hema on dentin collagen *Eur. J. Oral Sci.*, 109(348-353, 2001.
[227] G. Eliades, G. Palaghias, and G. Vougiouklakis. Effect of acidic conditioners on dentin morphology, molecular composition and collagen conformation in situ *Dent. Mater.*, 13(24-33, 1997.
[228] A. Oyarzun, H. Rathkamp, and E. Dreyer. Immunohistochemical and ultrastructural evaluation of the effects of phosphoric acid etching on dentin proteoglycans *Eur. J. Oral Sci.*, 108(546-554, 2000.
[229] K. Lewandrowski, V. Venugopalan, W. W. Tomford, K. T. Schomacker, H. J. Mankin, and T. F. Deutsch. Kinetics of cortical bone demineralization: Controlled

demineralization - a new method for modifying cortical bone allografts *J. Biomed. Mater. Res.*, 31(365-372, 1996.
[230] N. Natsir, K. Wakasa, Y. Yoshida, N. Satuou, and H. Shintani. Effect of tannic acid solution on collagen structures for dental restoration *J. Mater. Sci. Mater. Med.*, 10(489-494, 1999.
[231] Y. Okamoto, J. D. Heeley, I. L. Dogon, and H. Shintani. Effects of phosphoric acid and tannic acid on dentine collagen. *J. Oral Rehab.*, 18(507-512, 1991.
[232] F. E. Feninat, T. H. Ellis, E. Sacher, and I. Stangel. A tapping mode AFM study of collapse and denaturation in dentinal collagen *Dent. Mater.*, 17(284-288, 2001.
[233] J. Perdigao, P. Lambrechts, B. Van Meerbeek, A. R. Tome, G. Vanherle, and A. B. Lopes. Morphological field emission-sem study of the effect of six phosphoric acid etching agents on human dentin *Dent. Mater.*, 12(262-271, 1996.
[234] G. W. Marshall, N. Inai, I. C. Wu Magidi, M. Balooch, J. H. Kinney, J. Tagami, and S. J. Marshall. Dentin demineralization: Effects of dentin depth, pH and different acids *Dent. Mater.*, 13(343-388, 1997.
[235] K. Lewandrowski, W. W. Tomford, N. A. Michaud, K. T. Schomacker, and T. F. Deutsch. An electron microscopic study on the process of acid demineralization of cortical bone *Calcif. Tissue Int.*, 61(294-297, 1997.
[236] M. Farid, A. F. El-Daoushy, I. U. Olsson, and F. H. Oro. The EDTA and HCl methods of pre-treating bones *GFF*, 100(213-219, 1978.
[237] M. R. Urist and B. S. Strates. Bone formation in implants of partially and wholly demineralized bone matrix. *Clin. Orthop. Relat. Res.*, 71(271-278, 1970.
[238] K. Lewandrowski, W. W. Tomford, A. Yeadon, T. F. Deutsch, H. J. Mankin, and H. K. Uhthoff. Flexural rigidity in partially demineralized diaphyseal bone grafts *Orthop. Rel. Res.*, 317(254-262, 1995.
[239] F. Schajowicz and R. L. Cabrini. The effect of acids (decalcifying solutions) and enzymes on the histochemical behavior of bone and cartilage *J. Histochem. Cytochem.*, 3(122-129, 1954.
[240] J. J. Vandersteenhoven and M. Spector. Histological investigation of bone induction by demineralized allogeneic bone matrix: A natural biomaterial for osseous reconstruction *J. Biomed. Mater. Res.*, 17(1003-1014, 1983.
[241] I. R. Dickson and S. S. Jande. Effects of demineralization in an ethanolic solution of triethylammonium EDTA on solubility of bone matrix components and on ultrastructural preservation *Calcif. Tissue Int.*, 32(175-179, 1980.
[242] R. M. Carvalho, F. Tay, H. Sano, M. Yoshiyama, and D. H. Pashley. Long-term mechanical properties of edta-demineralized dentin matrix *J. Adhes. Dent.*, 2(193-199, 2000.
[243] N. Sasaki, A. Tagami, T. Goto, M. Taniguchi, M. Nakata, and K. Hikichi. Atomic force microscopic studies on the structure of bovine femoral cortical bone at the collagen fibril-mineral level *J. Mater. Sci. Mater. Med.*, 13(333-337, 2002.
[244] M. Fois, A. Lamure, M. J. Fauran, and C. Lacabanne. Study of human cortical bone and demineralized human cortical bone viscoelasticity *J. Appl. Polymer Sci.*, 79(2527-2533, 2001.
[245] I. U. Olsson. Further tests of the edta treatment of bones *Radiocarbon*, 42(49-52, 2000.

[246] P. J. Makarewicz, L. Harasta, and S. L. Webb. Kinetics of acid diffusion and demineralization of bone *J. Photograph. Sci.*, 28(177-184, 1980.
[247] X. Wang, X. Li, R. A. Bank, and C. M. Agrawal. Effects of Collagen Unwinding and Cleavage on the Mechanical Integrity of the Collagen Network in Bone *Calcified Tissue International*, 71(186-192, 2002.
[248] J. Catanese, J. D. B. Featherstone, and T. M. Keaveny. Characterization of the mechanical and ultrastructural properties of heat-treated cortical bone for use as a bone substitute *J. Biomed. Mater. Res.*, 45(327-336, 1999.
[249] N. Kumagai, T. Kadota, R. C. Goris, and R. Kishida. Decalcification with ethylenediaminetetraacetic acid does not affect immunohistochemical activity *Yokohama Medical Bulletin*, 40(31-35, 1989.
[250] I. Kiviranta, M. Tammi, R. Lappalainen, T. Kuusela, and H. J. Helminen. The rate of calcium extraction during EDTA decalcification from thin bone slices as assessed with atomic absorption spectrophotometry *Histochemistry*, 68(119-127, 1980.
[251] G. Nikiforuk and L. Sreebny. Demineralization of hard tissues by organic chelating agents at neutral pH *J. Dent. Res.*, 32(859-867, 1953.
[252] J. Charman and L. Reid. The effect of decalcifying fluids on the staining of epithelial mucins by alcian blue. *Stain Tech.*, 47(173-177, 1972.
[253] K. M. Daumer, A. U. Khan, and M. J. Steinbeck. Chlorination of pyridinium compounds *J. Biol. Chem.*, 275(34681-34692, 2000.
[254] V. d. P. A. Saboia, L. A. F. Pimenta, and G. M. B. Ambrosano. Effect of collagen removal on microleakage of resin composite restorations *Oper. Dent.*, 27(38-43, 2002.
[255] J. J. Broz, S. J. Simske, W. D. Corley, and A. R. Greenberg. Effects of deproteinization and ashing on site-specific properties of cortical bone *J. Mater. Sci. Mater. Med.*, 8(395-401, 1997.
[256] M. Toledano, R. Osorio, J. Perdigao, J. Rosales, J. Thompson, and M. A. Cabrerizo-Wilchez. Effect of acid etching and collagen removal on dentin wettability and roughness *J. Biomed. Mater. Res.*, 47(198-203, 1999.
[257] D. H. Carter, A. J. Scully, D. A. Heaton, M. P. J. Young, and J. E. Aaron. Effect of deproteination of bone mineral morphology: Implications for biomaterials and aging *Bone*, 31(389-395, 2002.
[258] M. Raspanti, S. Guizzardi, V. De Pasquale, D. Martini, and A. Ruggeri. Ultrastructure of heat-deproteinated compact bone *Biomaterials*, 15(6):433-436, 1993.
[259] S. Guizzardi, M. Raspanti, D. Martini, R. Scandroglio, P. Govoni, and A. Ruggeri. Low-temperature heat-deproteinated compact bone to heal large bone defects *Biomaterials*, 16(931-936, 1995.
[260] J. L. Holden, J. G. Clement, and P. P. Phakey. Age and Temperature Related Changes to the Ultrastructure and Composition of Human Bone Mineral *J. Bone Miner. Res.*, 10(9):1400-1409, 1995.
[261] I. Mayer, R. Schlam, and J. D. B. Featherstone. Magnesium-containing carbonate apatites. *J. Inorganic Biochem.*, 66(1-6, 1997.